THE UNIVERSITY *of* EDINBURGH

Suspension rheology and extrusion

A discrete element method study

Christopher John Ness

School of Engineering
University of Edinburgh

This dissertation is submitted for the degree of
Doctor of Philosophy

May 2016

This thesis is dedicated to Kathleen Ness
11 August 1932 - 15 January 2016

Summary

Suspensions of microscopic particles in liquid, such as pastes and slurries, are found all over nature and industry, yet a thorough knowledge of how they respond to applied forces and flows is lacking. Such understanding could be used to design superior food and cosmetic spreads, to optimise industrial cement and clay processing, or to predict and mitigate the effects of rapid geophysical flows. In the present work, we use particle based simulations to capture suspension flow behaviour under well defined conditions, in simple shear and two engineering geometries. We reveal distinct contributions of particle-particle contacts and particle-fluid interactions to the resulting stresses across flow regimes, and explore the roles of the liquid viscosity and the particle concentration, hardness and roughness. The results help to settle ongoing disputes about the origins of the high viscosity of such materials, and establish an improved framework for modelling suspension flows in an industrial setting.

Declaration

I hereby declare that except where specific reference is made to the work of others, the contents of this dissertation are original and have not been submitted in whole or in part for consideration for any other degree or qualification in this, or any other university. This dissertation is my own work and contains nothing which is the outcome of work done in collaboration with others, except as specified in the text and Acknowledgements.

This thesis includes work that has been published elsewhere:

1 **C. Ness** and J. Sun. Flow regime transitions in dense non-Brownian suspensions. *Physical Review E*, 91(1) 012201, 2015.

2 N. Lin, B. Guy, M. Hermes, **C. Ness**, J. Sun, W. Poon and I. Cohen. Hydrodynamic and contact contributions to shear thickening in colloidal suspensions. *Physical Review Letters*, 115:228304, 2015.

3 **C. Ness** and J. Sun. Two-scale evolution during shear reversal in dense suspensions. *Physical Review E*, 93(1) 012604, 2016.

4 **C. Ness** and J. Sun. Shear thickening regimes of dense non-Brownian suspensions. *Soft Matter*, 12(3), 914-924, 2016.

Christopher John Ness
May 2016

Acknowledgements

This work would not have been possible without the unceasing dedication and support offered by Jin Sun. He has been highly committed to the success of this project and to my personal and professional development as a researcher, and I hope we remain colleagues and friends for the rest of our careers. My research has benefitted greatly from enlightening discussions with Ben Guy, Michiel Hermes, Wilson Poon, Mike Cates, Neil Lin, Jin Ooi, Michele Marigo, Paul McGuire, Hugh Stitt, Han Xu, my colleagues in the Alexander Graham Bell Building, and the numerous researchers I have had the pleasure of meeting at conferences around the world, for which I am grateful.

Abstract

A suspension is a fully saturated mixture of discrete solid particles and interstitial liquid. Examples of suspensions include pastes, slurries, cement, food-spreads, drilling fluids and some geophysical flows. The present work focusses on *granular* (as opposed to *colloidal*) suspensions, which we define as those for which the thermal motion of the solid particles is negligible. Despite such ubiquity in industry and nature, our understanding of the mechanical properties of suspensions lags behind that of their constituent solid and liquids. In this thesis, the discrete element method is used to simulate suspension flow in shear, capillary and constriction geometries, mapping and characterising the fundamental flow, or *rheological*, regimes.

As a starting point (Chapter 2), we consider an established regime map for dry granular materials, appropriate for flows of sand, grains and dry debris. Taking guidance from shear flow simulations that consider the lubricating effect of an interstitial liquid, we recast the regime map for a general suspension, elucidating flows comparable to the dry material or to a viscous liquid, dependent on the shear rate, liquid viscosity and particle stiffness. We give an account of the microstructural traits associated with each regime.

Motivated by recent groundbreaking theoretical, computational and experimental work, we incorporate the emerging picture of *frictional shear thickening* into our regime map (Chapter 3). Our shear flow simulations capture the shear thickening behaviour and demonstrate that it may, in principle, occur in any of the identified flow regimes.

Our simulations of time-dependent shear flows (Chapter 4), specifically flow reversal, provide a detailed micro-mechanical explanation of a longstanding and previously unexplained experimental finding, guiding future experimentalists in decomposing the particle and liquid contributions to the viscosity of any suspension. Indeed, the findings have already been exploited in the devising of an experimental protocol that has successfully proven the dominance of particle contacts in driving shear thickening.

We next consider suspension flow in a microchannel (Chapter 5), finding that the identified shear flow regimes are locally applicable to flows in complex geometries under inhomogeneous stress conditions only when the local mean shear rate exceeds temporal velocity fluctuations. A more comprehensive description is therefore required to fully characterise the flow behaviour in this geometry.

Finally (Chapter 6), we simulate pressure driven suspension flow through a constriction geometry, observing highly inhomogeneous stress distributions and velocity profiles. The roles of particle and fluid properties are considered in the context of an industrial paste extrusion process.

Table of contents

List of figures

Introduction

Every day we surround ourselves with granular materials: the sugar we sweeten our coffee with, the cornflakes we eat, the toothpaste we brush our teeth with and the gravel on our driveways being just a few examples. Granular materials, assemblies of discrete macroscopic particles surrounded by an interstitial fluid (either gaseous or liquid), have been ubiquitous in human life for centuries (Jaeger et al., 1996). From transporting rice across 10th century China, to designing particulate filling agents to optimise the properties of speciality plastics, the engineering challenges associated with granular materials have been studied by academics and industrialists for generations. Today, granular materials remain a prominent component in many fields of agriculture, mining, processing, pharmaceuticals and manufacturing, and represent tens of billions of pounds of revenue worldwide annually (Nedderman, 2005). In addition to their widespread presence in industry, granular materials have geological significance, with the study of their mechanics being applicable to soils, sands and natural phenomena such as avalanches and landslides (Wu et al., 2009; Vedachalam, 2011). A thorough understanding of the behaviour of granular matter is therefore imperative, not just to satisfy academic curiosity, but to allow prediction, description and control of these interesting materials in the real world.

Experience tells us that granular matter can be observed to behave in either a solid-like or fluid-like way. For example, a pile of dry sand can sit at rest on a surface and appear to be solid even though it is subject to the forces of gravity, while grain flowing out of an agricultural silo could be considered to be behaving like a liquid. As such, the analyses of these systems have historically evolved from those of static and flowing systems respectively. From a solid-like point of view, the most simple description of the static behaviour is that proposed by Coulomb (Shield, 1955), who described a yield criterion for granular solids in terms of a linear relationship between shear and normal stresses on a yield plane. Fluid-like descriptions ultimately began with the work of Newton (Guicciardini, 2005) and later Navier and Stokes (Drazin and Riley, 2006), who described liquids as a continuum, giving them a constant resistance to flow called a viscosity. Indeed, the relationship $\sigma = \eta\dot{\gamma}$, relating the shear stress to the viscosity and shear rate of a fluid represents the most basic of constitutive relations for fluids. Einstein's proposal (Einstein, 1906) for the increase in this viscosity with solid volume fraction upon adding suspended particles (for dilute suspensions) was an early attempt to incorporate the effect of suspended solids into a continuum description of flow. While there has been sustained progress over the past century in extending these early descriptions (Lin, 1970; Batchelor, 1977; Ryskin, 1980), and much effort in bridging the gaps between models for low and high particle volume fractions (Liu

and Nagel, 1998; O'Hern et al., 2002; Song et al., 2008), small and large particles and flowing and static systems, (Mewis and Spaull, 1976; Stickel and Powell, 2005), a unified, continuum description of granular material remains elusive.

Computational work has long played a key role in the analysis of granular materials (Cundall and Strack, 1979; Bossis and Brady, 1984; Hu and Joseph, 1992). Technological advances in the past 30 years have facilitated a surge of activity in this field, with discrete element method (DEM) simulations (Cundall and Strack, 1979; Plimpton, 1995) recently earning a central role in the analysis of granular systems. In recent literature, the approach has been to study granular materials in a rheological framework (Hatano, 2008; Otsuki and Hayakawa, 2009; Sun and Sundaresan, 2011), the ultimate goal being to develop a numerically stable, micromechanically based, constitutive equation to relate stresses to strain rates, encompassing a full range of solid volume fractions, particle sizes and shear rates, and taking the evolution of microstructural properties with shear into account. Particular emphasis has been on developing unifying theories that bridge Brownian and non-Brownian materials (Ikeda et al., 2012), dry and wet systems (Isa et al., 2007), and jammed and unjammed states (Chialvo et al., 2012). While numerous publications have proposed constitutive models and unifying theories for specific materials or geometries (Hu and Joseph, 1992; Yuan et al., 2001; Rough et al., 2002; Patil et al., 2006), a single all-emcompassing description is still lacking.

This project addresses the present shortcomings of modelling techniques by using particle-level simulations of granular systems to understand how both particle-particle and particle-fluid interactions contribute to the bulk stresses under flow. We show that the most important hydrodynamic effects in these materials can be captured by coupling a fluid film lubrication model with a frictional spring-dashpot model, to computationally account for the particle-fluid and particle-particle interactions respectively. We implement such a model in a discrete element code, allowing us to probe the shear rheology of suspensions. The model is then implemented in channel and constriction geometries, to assess the compatibility of a description of shear flow with flow in real processing conditions.

We propose regime maps (built upon those for dry granular materials) that successfully combine multiple aspects of granular suspension flow, namely viscous and inertial dissipation, jammed and flowing behaviour, and frictional shear thickening, offering a unified framework for understanding suspension rheology. This understanding is extended to non-steady flows, where we present a shear reversal protocol that has successfully been employed to isolate contact and hydrodynamic stress contributions, and offers prospects as a diagnostic tool for characterising surface and contact force properties of suspended particles.

Chapter 1

Literature review

In Section 1.1, the characteristics and terminology used in classifying different types of granular media are introduced. The two following sections will give an overview of the classical analysis of granular materials (Section 1.2) and the classical rheological framework (Section 1.3). In Section 1.4, a review will be given of theoretical, experimental and computational work that endeavours to construct rheological descriptions of granular materials. We will then discuss (Section 1.5) recent literature that aims to use this rheological framework to unify seemingly distinct granular phenomena such as the jamming and glass transitions and dry and wet system behaviour.

1.1 Characterising particulate materials

In this work, we consider assemblies of a large number of finite sized, microscopic, solid particles, the discrete phase, fully surrounded by an interstitial fluid, the continuous phase, which may be either gaseous or liquid. Materials with gaseous interstitial fluids will be referred to as dry granular materials while those with interstitial liquids will be referred to as suspensions.

The discrete particles may be either hard or soft. Hard particles, such as grains of sand, are not able to deform (represented numerically as an overlap in space) and have zero interaction potential, except when surfaces contact, when they exhibit extremely strong repulsion. Soft particles, such as some biological cells (Gross et al., 2014), are able to deform, and exhibit repulsive forces that are proportional to the extent of deformation (represented as particle surface overlap numerically).

The relative volume of solid present in the system is quantified by the volume fraction ϕ, defined according to Equation 1.1, where $V_{particles}$ is the total volume of the

particles, and V_{fluid} is the total volume of the fluid.

$$\phi = \frac{V_{particles}}{V_{particles} + V_{fluid}} \tag{1.1}$$

The volume fraction can vary from 0 (*i.e.* pure solvent with no solids present) to an upper limit that depends on the maximum packing fraction of the particles, which is intimately linked with particle geometry, particle size distribution and particle surface details. For low volume fractions ($\phi \lesssim 0.1$), the behaviour of the system will be dominated by the fluid viscosity plus the particle-fluid interactions, and the particles are assumed not to "see" each other. For intermediate volume fractions, particle-particle interactions will be more common and will make a significant contribution to the properties of the system. For high volume fractions ($\phi \gtrsim 0.6$), sustained particle-particle contacts will be prevalent and will govern the material properties of the system.

1.1.1 Force scales in particulate systems

Granular materials exhibit bulk properties that are dependent on particle level interactions. The particle level interactions that most contribute to the bulk properties are dependent on the size of the particles and the properties of the interstitial fluid. Forces potentially significant in particulate systems include, for example, buoyancy and drag, Van der Waals, electrostatic interactions and transient or sustained particle-particle contact forces. Three-phase interactions such as liquid bridge formation (Fisher, 2009) can also contribute significantly to bulk behaviour, but in this work we consider systems that are either completely dry or fully wetted systems, and as such the opportunity for liquid bridge formation is assumed not to arise.

Depending on the magnitude of particle thermal motion relative to that of the driving flow (quantified as the Péclet number *Pe*, as defined later), the system can be described as Brownian or non-Brownian. For very small particles ($< 1\mu m$ (Einstein, 1956), $Pe < 1$), the translational particle movement as a result of thermal energy k_bT (Brownian motion) is sufficient to homogenise the system against sedimentation or inhomogeneities resulting from externally applied forces such as during shear flow. These are referred to as colloidal or Brownian systems. For large *Pe*, Brownian motion is too slow to maintain equilibrium, so particle motion results from bulk flow of the material and buoyancy effects, and the suspension is described as non-Brownian, or granular. Van der Waals forces contribute to the overall particle-particle interaction in colloids, and any two molecules with separation r in these suspensions are subject to a

Lennard-Jones potential given by Equation 1.2

$$w(r) = 4\upsilon \left[\left(\frac{\sigma}{r} \right)^{12} - \left(\frac{\sigma}{r} \right)^{6} \right] \tag{1.2}$$

for a potential well of depth υ and a characteristic molecule separation at which the potential is zero σ. This potential can then be integrated over each particle volume to find a very short range particle-particle repulsive force and a longer range attractive force. Particle-liquid interactions are also important in colloidal suspensions. Electrostatic interactions between the colloidal particles and the interstitial liquid result in a gradient of charge density at the particle surfaces, leading to particle-particle repulsion described by the Poisson-Boltzmann Equation 1.3

$$\nabla_2 \Psi = -\frac{F}{\varepsilon} \sum_i \left(c_{i\infty} z_i \exp\left(-\frac{z_i F \Psi}{RT} \right) \right), \tag{1.3}$$

for electrostatic potential Ψ, Faraday's constant F, dielectric constant ε, bulk ion concentration $c_{i\infty}$, ion valence z_i, gas constant R and temperature T.

This repulsion occurs over a length scale derived from the Poisson-Boltzmann equation, called the Debye length κ. DLVO theory describes the resultant particle-particle force by simply adding the contributions from Van der Waals and electrostatic forces. As such, the properties of Brownian, colloidal suspensions may be characterised by thermal motion, Van der Waals, and electrostatic interactions.

For systems of large particles, the $k_b T$ energy is not sufficient to cause Brownian motion. The particle motion is therefore determined by their buoyancy and drag and by external forces applied to the material. The magnitude of the Van der Waals and electrostatic forces is typically much smaller than that of the forces arising from the momentum of the particles, and as such they are neglected in any analysis. Force transmission between particles is therefore by momentum transfer during particle-particle collisions and sustained particle contacts. Such non-Brownian systems will be referred to as granular (rather than colloidal) materials.

Non-Brownian systems may be further characterised according to whether their flow is viscous or inertial. For viscous flows, the forces on all particles are balanced, so their motion is assumed to be entirely governed by the local motion of the surrounding fluid. For inertial flows, particles may be accelerating or decelerating with respect to their local suspending fluid, and may take part in inertial collisions that resemble those occurring in dry granular materials. The viscous-inertial transition is delineated by the Stokes number St (defined later), and will be considered in greater depth in subsequent chapters.

Krieger (Krieger and Dougherty, 1959) proposed that the viscosity of a particulate suspension is a function of the particle radius r, density ρ_p and volume fraction ϕ, the interstitial fluid viscosity η_f and density ρ, the thermal energy k_bT, and the shear rate $\dot{\gamma}$. Using dimensional analysis and assuming neutrally buoyant particles, Krieger obtained $\eta = f(\phi, Pe, St)$.

1.1.2 Jamming of granular materials

A granular suspension can be observed to flow like a liquid, in the case of dry grains flowing out of a hopper (Nedderman, 2005), or to behave as a solid under an applied load, such as soil (Schofield and Wroth, 1968). In the case of soil, the material might be referred to as "*jammed*", having a yield stress that gives rise to elasticity (analogous to an elastic solid), whereas the flowing system could be described as having a viscosity, like that of a liquid. At the interface between the flowing regime and the solid regime is the jamming transition (Liu and Nagel, 1998), a critical point at which the rheological properties of the material change dramatically (Wang and Brady, 2015). In the jammed state the particles are tightly packed and in persistent contact with one another meaning their motions are restricted and they cannot explore alternative configurations and as such the system is not at equilibrium, or is non-ergodic. It has been proposed that the jamming transition in granular suspensions can be described under the same framework as the glass transition in colloids (Liu and Nagel, 1998) using a three-dimensional phase diagram with axes of Temperature, Inverse Volume Fraction and Applied Stress, however recent work has suggested that they are infact distinct phenomena (Ikeda et al., 2012). For strictly non-Brownian systems, the Temperaure axis can be neglected and the state of jamming can be described by the volume fraction and applied stress. Under zero applied stress, the system is jammed at volume fractions above approximately 0.64 (Song et al., 2008) (for frictionless particles - for frictional particles this value is reduced, as will be seen later (Chialvo et al., 2012)). A system that is in the jammed state under zero applied stress will then "*unjam*" if a stress is applied that exceeds the yield stress. The nature of the microstructural properties and bulk rheological properties of granular materials above and below the jamming transition will be a central discussion point of this work.

1.1.3 Microstructural properties

In this work, the micromechanical properties of granular materials will be probed using microstructural properties such as the coordination number and the fabric tensor. The extent of sustained particle-particle interaction in a granular suspension can be

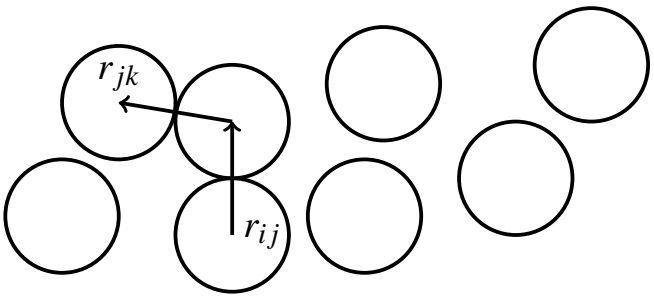

Fig. 1.1 Contact vectors r in a granular material

quantified using the coordination number Z, the average number of particle contacts that each particle in the material has. For dilute suspensions, particles mainly interact with the interstitial fluid, and as such the coordination number is approximately zero, with particles interacting only occasionally, by transient, dissipative collisions. The jamming transition has been associated with a sharp increase in the coordination number of the suspension (Siemens and Van Hecke, 2010). An increase in coordination number means there is an increase in the number of sustained particle-particle contacts. Forces applied to the material such as those due to shearing or to an applied load are transmitted through these sustained contacts, giving rise to force chains (Majmudar and Behringer, 2005; Vanel et al., 1999) which propagate through the material. Length scales associated with force transmission through granular media are found to diverge (Zhang et al., 2009) at the jamming transition, corresponding to the increased coordination number.

Depending on the nature of an external force applied to the granular media, such force chains may align in a certain direction. For example, in a pile of sand on a flat surface under the influence of gravity, the force chains will tend to be aligned with the vertical axis (Vanel et al., 1999). Isotropically compressed systems tend to show no net alignment, while systems under shear show strong alignment of force chains in the direction of shearing (Majmudar and Behringer, 2005), i.e. along the compressive axis. The anisotropy of a granular suspension may be quantified using the fabric tensor $\mathbf{A}$, defined in Equation 1.4 (Sun and Sundaresan, 2011; Shertzer, 2011).

$$\mathbf{A} = \frac{1}{N_c} \sum_{\alpha=1}^{N_c} \mathbf{n}_\alpha \mathbf{n}_\alpha - \frac{1}{3}\mathbf{I} \tag{1.4}$$

The unit vectors $\mathbf{n}_\alpha$ are given by $\frac{\mathbf{r}_{ij}}{|\mathbf{r}_{ij}|}$, where $\mathbf{r}_{ij}$ are the vectors between centres of contacting particles, as shown in Figure 1.1, and N_c is the total number of such contacts in the system. The use and interpretation of the fabric tensor will be illustrated throughout the later Chapters of this thesis.

1.2 Analysis of dry granular materials

In this section we introduce some key features of the analysis of *dry granular materials*, systems of discrete solid particles in an interstitial fluid of low enough density and viscosity (*i.e.* air) that its influence on particle behaviour can be neglected. Static dry granular materials were famously described by Coulomb in the 18th century (Coulomb, 1773) as continuous media with a frictional yield criterion. Coulomb was interested in the prediction of static soil failures for structural engineering work. His model for the yield stresses in bulk granular materials is still the basis of many analyses of granular systems in industry, and is considered to be the most fundamental and simple approach to describing these materials. The brief analysis of static systems and explanation of the Coulomb yield criterion presented in Section 1.2.1 follows that of Schofield and Wroth (Schofield and Wroth, 1968) and Nedderman (Nedderman, 2005). Section 1.2.2 introduces some of the more unusual properties of static granular systems that distinguish them from typical solids, and in Section 1.2.3 some descriptions and properties of dry granular material under flow are presented.

1.2.1 Coulomb Yield Criterion

An element of elastic solid subjected to an applied force will deform elastically, with the extent of the deformation being related to the applied shear and normal stresses. The most simple case of this relationship is given by Hooke's Law, in which the relationship between the strain γ and the shear stress τ is linear, and characterised by the shear modulus G, $\tau = G\gamma$.

For granular materials or materials that can undergo plastic deformation, this relationship may hold for very small forces or strains, but experience tells us that applying a sufficiently large force of this type is likely to result in failure of the material along a dividing plane. The shear stress on the failure plane is independent of γ and $\frac{d\gamma}{dt}$ and as such the separated parts of the material can be considered to be rigid blocks, and the depth of the failure plane can be considered to be infinitesimally small.

To study this failure behaviour further, we consider the stresses acting on a volume element of granular material in static equilibrium, as shown in Figures 1.2 and 1.3, for the 3-dimensional and 2-dimensional cases, respectively. Since Coulomb's analysis typically refers to materials with a compressive strength that greatly exceeds the tensile strength, most authors take compressive stresses to be positive in their sign conventions, and we follow this convention here. σ_{ij} is used to represent normal and shear stresses, and we construct the stress tensor for the system as shown in Equation 1.5.

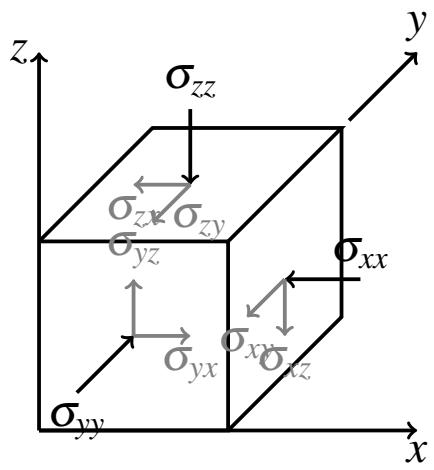

Fig. 1.2 Normal and shear forces acting on a volume element of material

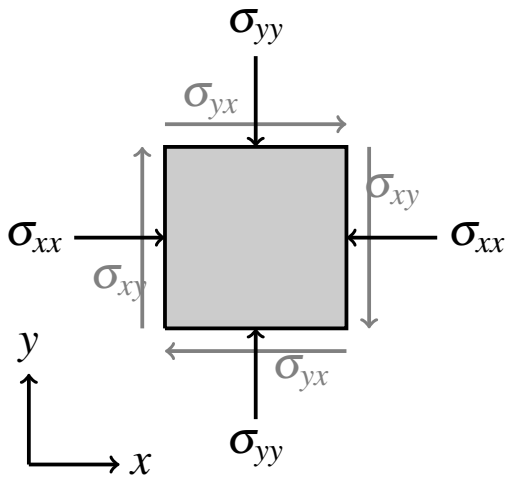

Fig. 1.3 Normal and shear forces acting on a 2D element of granular material

$$\sigma = \begin{pmatrix} \sigma_{xx} & \sigma_{xy} & \sigma_{xz} \\ \sigma_{yx} & \sigma_{yy} & \sigma_{yz} \\ \sigma_{zx} & \sigma_{zy} & \sigma_{zz} \end{pmatrix} \tag{1.5}$$

Equation 1.5 describes the stresses acting on a volume element of granular material in the global reference frame. It is possible to determine the components of these stresses in any other co-ordinate frame using matrix manipulations. In order to simplify the analysis, the problem can be reduced to two dimensions, with the corresponding forces acting on a unit square of the granular material in static equilibrium being shown in Figure 1.3.

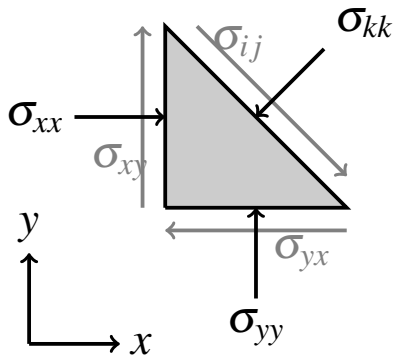

Fig. 1.4 Normal and shear forces acting on an arbitrary plane in the granular material

The internal stresses acting on an arbitrary plane within this unit square as a result of the normal and shear forces acting on the square are shown in Figure 1.4. This Figure highlights that on any arbitrary plane within the granular material, there will be a normal and a shear stress contribution to the total stress acting on that plane. If σ_{xx}, σ_{yy}, σ_{xy} and σ_{yx} are known for the solid element, Mohr's Circle can be used to obtain the values of σ_{ij} for any plane within the material. Mohr's Circle is a graphical construction method, commonly used for two-dimensional reference frame manipulations, allowing determination of the normal and shear stresses on any plane within a material, such as the arbitrary plane shown in Figure 1.4.

As mentioned previously, the shear stress acting on the failure plane of the granular material is independent of the strain and strain rate, but is dependent on the normal stress acting on that plane, $\sigma_{ij} = f(\sigma_{kk})$.

The yield criterion proposed by Coulomb states that a linear relationship between normal and shear stress is a good approximation for many granular materials, subsequently referred to as "Coulomb materials". The relationship can be described by a coefficient of friction μ, so that on the yield plane $\sigma_{ij} = \mu\sigma_{kk}$. The addition of a constant, c, can be used to take cohesive forces between granular particles into account, resulting in the Coulomb yield criterion $\sigma_{ij} = \mu\sigma_{kk} + c$.

If on all planes within the granular material $\sigma_{ij} < \mu\sigma_{kk} + c$, then the system will not fail. If there exists a plane within the granular material where the Coulomb yield criterion holds, then yield will occur with the angle of friction ϕ given by $\mu = \tan\phi$. It is not possible for the situation where $\sigma_{ij} > \mu\sigma_{kk} + c$, except transiently, as yield would have occurred within the material before this point was reached. Mohr's Circle can be used to determine whether or not the Coulomb yield criterion holds on any plane within the material, and hence whether or not the material will fail.

While the Coulomb yield criterion is a simple and well-used rule to determine the location of a failure plane in a static granular system, its assumptions have fundamental shortcomings and therefore are not broadly applicable without justification.

In order to study a discrete system in a continuum framework, it is essential that we can consider forces and velocities on a length scale that is significantly greater than that of the particles. For many granular systems that we may come across in industry, for example silo storage and discharge, it is easy to think of a case where the length scale of the domain may only be 10s or 100s of particle diameters, in which case a continuum based analysis is unlikely to represent the behaviour of the system.

In applying the Coulomb yield criterion, we treat the granular material as a single phase bulk plastic solid, and as such we fail to take into account the randomness or disorder of the distribution of the discrete solid particles, as well as the potential anisotropy in the system. As a result of this, our assumptions that the failure will occur along a single, uniform plane and that that plane will be of infinitesimal thickness are likely to be incorrect in most applications, since significant velocity variations are possible between adjacent particles upon yield.

The Coulomb yield criterion is, however, a historically significant analysis of static granular systems and forms the basis of contemporary models.

1.2.2 Static granular systems

Static granular systems behave unlike other solids, with properties that are both unusual and unexpected, distinguishing them from typical continuum solids. A few of these properties are introduced below.

A fundamental parameter of granular materials, the volume occupied by a certain mass of material, has been studied for centuries, with packing fractions in static granular systems found to vary from approximately 0.50 to 0.64 (O'Hern et al., 2002). Unlike thermal systems, *i.e.* systems where the energy scale k_bT is significant, dry granular systems are not able to change configuration without the input of energy from an external source. The volume occupied by a dry granular material is therefore dependent on the packing history of that material and on externally applied forces such as container motion (Jaeger et al., 1996).

Another unusual property of dry granular systems is their ability to maintain a free surface that is inclined to the horizontal, at an angle called the angle of repose. Analysis of the angle of repose is essential in determining the surface area that will be occupied by a heap of process material and in determining the maximum force exerted on the wall of a storage bunker by a granular material (Nedderman, 2005). Further work in this area has been done to determine the stress distribution on a surface on which a

heap of static granular material sits (Majmudar and Behringer, 2005; Behringer et al., 1999). The result is surprising and again demonstrates the non-continuum behaviour of granular materials. It is found that the greatest pressure on the ground does not occur below the peak of the heap, but that the stress is distributed throughout the material in aligned force chains (Vanel et al., 1999). The resulting force on the ground is therefore spread across a wide area below the heap.

When granular matter is stored in a cylinder with a vertical axis, the pressure at the base of the cylinder is found not to increase with depth of material as would be expected in a liquid system, but is observed to have a maximum value (Sperl, 2006). The classical analysis of this phenomenon by Janssen, and subsequent refinement by Walker (Nedderman, 2005) describes how the pressure at the bottom of the container increases towards an asymptotic value. The weight of additional material is then supported by the walls of the container, enabled by the frictional properties of the particles and wall. The force distributions associated with dry granular material under gravity are responsible for unusual phenomena such as this.

In the past 20 years, increasing attention has been given to the concept of jamming (Liu and Nagel, 1998). The jamming phase diagram proposed by Liu *et al*. postulates that for a non-thermal material at a given density, the system will be in a jammed state for low enough applied stresses. Static, dry, granular systems such as heaps of sand would be considered to be in the jammed state since they appear to be solid-like. For systems such as this, the transitions in to and out of the jammed state are stress-dependent (Siemens and Van Hecke, 2010). For example, if a very small tensile stress is applied to the sand pile, *e.g*. by tilting the surface, the system will "unjam" and flow down the inclination. Describing granular systems according to a jamming phase diagram is an attractive prospect as it would give a modelling framework that unifies volume fraction, applied forces and temperature effects. Numerous attempts have been and are being made to shed light on jamming (Ikeda et al., 2012; Song et al., 2008), some of which will be considered in this work.

1.2.3 Flowing granular systems

There are many circumstances under which dry granular material is observed to flow like a liquid. In many industrial and agricultural processes, material storage and transportation are dominated by both gravity-driven and mechanically-driven flow of granular materials (Campbell, 2006). Furthermore, natural phenomenon such as landslides can be considered to be gravity-driven flow of a granular material (Aranson and Tsimring, 2006). The Coulomb Yield Criterion discussed above gives an approximation of the

conditions under which a static, dry, granular solid will yield and begin to flow, but it gives no account of the nature or properties of that flow.

Much of the traditional analysis of granular flow has focussed on development of empirical correlations to predict flow rates in specific pieces of process and storage equipment (Nedderman, 2005). For example, discharge rates from silos have received much attention (Beverloo et al., 1961) owing to their implications for storage, transportation, residence time distributions, mixing efficiency and rate of silo wall wear. By analysis of the variables of silo discharge, and with consideration of Janssen's analysis discussed previously, Beverloo *et al*. (Beverloo et al., 1961) identified the salient parameters in determining the flow rate W of a cohesionless material to be the bulk density ρ_b, gravitational acceleration g, orifice diameter D_0 and particle diameter d. Comparison with experimental results lead them to the empirical relationship in Equation 1.6, for empirical coefficients C and k.

$$W = C\rho_b g^{1/2}(D_0 - kd)^{5/2} \tag{1.6}$$

This result has been refined by the inclusion of previous work to account for non-circular orifices (Fowler and Glastonbury, 1959) and with later work aimed at more closely matching experimental data for cohesionless flow (Al-Din and Gunn, 1983; Johanson, 1965), to give correlations for discharge flow rates that have been utilised for decades. The ongoing work by Janda et al (e.g. (Mankoc et al., 2007)) represents a continuation of this classical analysis of discharging systems.

An assimilation of granular flow data carried out by Groupement De Recherche Milieux Divises (MiDi, 2004) has elucidated the parameters most important to a variety industrial granular flows, such as annular shear flow, chute flow and heap flow. The governing parameter in determining the nature of granular flow identified by this work and others is the Inertial Number (Jop et al., 2006; Forterre and Pouliquen, 2008), defined in Equation 1.7 for hard spheres, for shear rate $\dot{\gamma}$, particle diameter d, confining pressure P and particle density ρ.

$$I = \frac{\dot{\gamma}d}{\sqrt{P/\rho}} \tag{1.7}$$

Three flow regimes are observed for different inertial numbers:

$$\begin{array}{cc} I < 10^{-3} & quasistatic \\ 10^{-3} < I < 10^{-1} & intermediate flow \\ I > 10^{-1} & inertial \end{array}$$

In the quasistatic regime, flow is arrested and the jammed material behaves as an elastic solid, and could potentially be analysed according to the static yield criterion discussed previously. In the intermediate regime, the stress transmission during granular flow is dominated by continuous particle-particle contacts, though particle rearrangements can occur, allowing flow. An example of this flow is the internal flow and discharge of grain from a hopper, as discussed above. To analytically describe flows of this type, plasticity theory has been applied and extended to account for very large effective strains present in non-static systems. In the inertial regime, the stress transmission is dominated by transient particle-particle collisions resulting in significant momentum transfer occurring during flow (Jackson, 1986). As such, the stresses in flow of high inertial number are rate-dependent with $\sigma \propto \dot{\gamma}^2$ (Savage et al., 1983), unlike those in slower and static systems.

Theoretical continuum models exist to describe the flows in these regimes (Jaeger et al., 1996). These models use temporal and spatial averaging to develop a continuum from the discrete system that is analogous to that used in modifying the Navier-Stokes equations for turbulent liquid flow. As mentioned for static systems, these averaged scales must be sufficiently greater than the particle dimensions. There are many models for flow in the quasistatic, intermediate and inertial regimes, and much discussion as to how to combine these for dry granular systems (Savage, 1988; Fan and Chen, 1990; Jop et al., 2006; Forterre and Pouliquen, 2008; DeGiuli et al., 2015; Lerner et al., 2012).

1.3 Principles of rheology

Rheology, the study of the deformation and flow of matter, has been at the heart of material processing since the 1930s (Barnes, 1989). Rheological studies aim to establish relationships between deformations and stress, to describe the non-Newtonian behaviour of plastic, elastic and viscoelastic materials. A truly interdisciplinary area of engineering, principles of rheology are applied to the characterisation of rubbers, plastics, drilling muds, food products and paints to name a few. Research work in rheology was an area of excitement, plentiful funding and great industrial interest around the middle of the 20th century, when a boom in plastics and polymer processing meant there was a real need for predictive rheological models of complex fluids at the downstream end of the oil and gas industry. Subsequently, the rheological framework has been applied to particle suspensions, colloidal systems, biological systems, and many other realms of engineering (Mackley, 2009).

In this Section, an overview of the fundamental principles of rheology is presented. Much recent work in granular rheology that will be discussed later is built directly upon

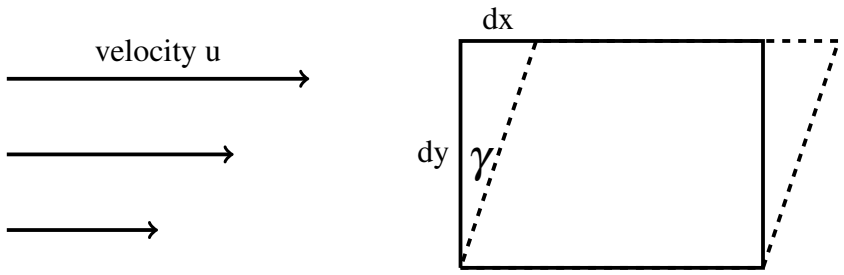

Fig. 1.5 Simple shear flow deformation resulting in a strain γ

the principles given here. The analysis is taken from a lecture course given by Professor Malcolm Mackley in the Department of Chemical Engineering at the University of Cambridge, between October 2010 and May 2011.

1.3.1 Strain rates and constitutive equations

For an initial analysis, it is prudent to consider the case of simple shear flow, *i.e.* an incompressible fluid contained between infinite parallel plates, the upper plate moving at a constant velocity U (usually called Couette flow). The velocity profile obtained in this configuration and the subsequent deformation of a differential volume of fluid is shown in Figure 1.5. It can be seen that in the case of simple shear flow and assuming there is no slip at the plate walls, the direction of velocity increase is perpendicular to the direction of flow. In this configuration, the strain γ is given by $\tan\gamma = dx/dy$. For small strains we approximate this to $\gamma = dx/dy$. Equation 1.8 demonstrates that in this geometry, the rate of strain is equal to the velocity gradient in the y direction.

$$\dot{\gamma} = \frac{\partial \gamma}{\partial t} = \frac{\partial \left(\frac{\partial x}{\partial y}\right)}{\partial t} = \frac{\partial \left(\frac{\partial x}{\partial t}\right)}{\partial y} = \frac{\partial u}{\partial y} \tag{1.8}$$

Rheology aims to relate this strain rate $\dot{\gamma}$ to the shear stress σ exerted by the plate walls on the fluid. The most simple relationship is given by the Newtonian constitutive equation, in which the stress is a linear function of the instantaneous strain rate, $\sigma = \eta\dot{\gamma}$.

This is the most basic and widespread of the constitutive equations and can be applied to water, organic solvents and many other single phase fluids over a wide range of pressures and strain rates. The simplicity of this constitutive equation stems from the fact that the viscosity η is not a function of the strain γ or strain rate $\dot{\gamma}$. In many cases, however, the viscosity may be found to be a function of temperature T, showing

a dependence such as $\eta = \eta_0 e^{k/T}$, for constants η_0 and k. Though the viscosity of a Newtonian fluid is independent of the nature of the flow, it is not necessarily a constant under all circumstances.

While the Newtonian constitutive equation is a simple and robust model for some liquids, experience tells us that many fluids such as toothpaste, paint and shampoo behave in more complex ways. Liquids such as these are described as "non-Newtonian", as their behaviour under an applied shear stress cannot be characterised by a single strain and strain-rate independent viscosity.

An early constitutive equation describing non-Newtonian flow is the Bingham plastic model (Bingham, 1925), named for Professor Bingham of Lafayette College Pennsylvania, an early pioneer of rheology (Barnes, 1989). The Bingham plastic constitutive model is given by $\sigma = \sigma_y + \eta\dot{\gamma}$. This model assigns the fluid a strain rate independent viscosity, as for a Newtonian fluid, but states that below a certain shear stress, called the yield stress σ_y, this viscosity will not be observed, but rather, the fluid will be observed to behave as a solid. Heavy engine grease is an example of a Bingham plastic fluid. Under no applied stress, a "blob" of grease can maintain its shape indefinitely as if it were a solid, but when a sufficient shear stress is applied, the grease will flow like a liquid.

More recent constitutive equations take into account *shear thinning* and *shear thickening* behaviour of complex materials. These are materials whose viscosity is a function of strain rate, for example polymer melts, slurries, corn flour in water and colloidal suspensions such as paints. The most simple of these models is the power law fluid, with constitutive model $\sigma = k\dot{\gamma}^n$. The apparent viscosity of a power law fluid is given by $\eta = k\dot{\gamma}^{n-1}$. For these fluids, the exponent n may determined empirically, and characterises whether the fluid shear thins (viscosity reduces with shear rate) or shear thickens (viscosity increases with shear rate). For $n = 1$ it is clear that the power law constitutive equation reduces to the standard Newtonian one, and as expected the viscosity η is not a function of the strain rate.

Mechanisms for shear thinning and thickening are the subject of debate, with various models being proposed for each. The shear thinning behaviour of polymer melts has been explained in terms of polymer chain disentanglement and stretching under shear, resulting in a history-dependent reduced viscosity. Shear thinning behaviour in colloids (Guy et al., 2015) may be attributed to an increasing dominance of shear induced order over thermally activated rehomogenisation as the shear rate is increased. A detailed review of shear thickening behaviour is given later.

Further examples of constitutive models for shear thinning flow are the Carreau (Carreau, 1972) and Cross (Cross, 1965) equations, the apparent viscosities for which

are shown respectively in Equations 1.9 and 1.10, where η_0 is the zero shear viscosity, η_∞ is the high shear viscosity, and α, λ and p are constants.

$$\eta_a = \eta_0 \left[1 + (\lambda \dot{\gamma})^2\right]^{-p} \tag{1.9}$$

$$\eta_a = \eta_\infty + \frac{\eta_0 - \eta_\infty}{1 + \alpha \dot{\gamma}^n} \tag{1.10}$$

Both models predict Newtonian behaviour at low shear rates, with the viscosity being given by η_0. The Carreau model then predicts power law shear thinning for higher shear rates. The Cross model also predicts shear thinning for intermediate shear rates, but exhibits a Newtonian plateau at high shear rates, with a constant viscosity η_∞. For a particle suspension, it has been proposed that the high shear viscosity η_∞ is approximately the viscosity of the interstitial fluid.

In this Section we have introduced the concepts of strain rates, shear stresses and constitutive equations. The basic Newtonian constitutive equation has been presented along with examples of constitutive equations describing non-Newtonian behaviour in complex fluids. Characterising the relationship between particle level interactions and bulk rheological models is an area of great interest, and will form the intellectual heart of this work.

1.3.2 Viscoelasticity

Materials such as polymers and some particulate systems, may exhibit both viscous and elastic properties. For example, under very low shear strain they may deform elastically, like a solid, while under high shear strain they may deform greatly like a viscous liquid. In order to describe this behaviour quantitatively, we introduce the concept of *viscoelasticity*. Viscoelasticity can be the cause of significant industrial paste and polymer extrusion processing instabilities such as die swell and sharkskin (Benbow and Bridgwater, 1993), so it is essential that the properties of viscoelastic materials are well understood. In order to introduce the analysis of viscoelastic materials, it is convenient to consider the behaviour of such a material under oscillatory shear, for example between two parallel plates, the upper plate oscillating backwards and forwards sinusoidally, parallel to the lower plate, with fixed gap between the plates. The material is subjected to an oscillating strain given by $\gamma = \gamma_0 \sin(\omega t)$, and consequently the strain rate is given by $\dot{\gamma} = \gamma_0 \omega \cos(\omega t)$. The property that we measure is the stress, which for a viscoelastic material is found to oscillate out of phase with the strain and strain rate, so is given by $\sigma = \sigma_0 \sin(\omega t + \delta)$, which can be expanded to give that shown in

Equation 1.11.

$$\sigma = \sigma_0 \sin(\omega t)\cos(\delta) + \sigma_0 \cos(\omega t)\sin(\delta) \tag{1.11}$$

There are now two components of σ, one in phase with the strain ($\sin(\omega t)$ part), and one in phase with the strain rate ($\cos(\omega t)$ part). We may build a constitutive equation for the material that characterises the relative contributions from each phase with two parameters, the storage and loss moduli G' and G'' respectively, as shown in Equation 1.12.

$$\sigma = G'\gamma_0 sin(\omega t) + G''\gamma_0 cos(\omega t) \tag{1.12}$$

The storage modulus characterises the elastic behaviour of the material in the form of $\sigma = G\gamma$ and the loss modulus characterises the viscous behaviour in the form of $\sigma = \eta\dot{\gamma}$.

Maxwell proposed that a linear spring and dashpot in series could describe this behaviour. The left spring part is given an elastic constant G, while the right dashpot is given a viscosity η. Applying stress continuity ($\sigma = \sigma_{spring} = \sigma_{dashpot}$) and strain additivity ($\gamma = \gamma_{spring} + \gamma_{dashpot}$) allows us to derive the Maxwell equation (1.13), the governing ordinary differential equation for linear viscoelasticity:

$$G\frac{d\gamma}{dt} = \frac{d\sigma}{dt} + \frac{\sigma}{\eta} \tag{1.13}$$

Solution of this equation allows the prediction of the time dependent response of a viscoelastic material to applied shear rates. We have thus shown how the basic principles of rheology can be applied to determine relationships describing the time dependent flow of complex viscoelastic materials. The Maxwell model can be enhanced to account for more complex viscoelasticity, for example by modelling the material as a parallel rather than series spring-dashpot, and by introducing multiple parallel springs and dashpots, with a range of elasticities and viscosities.

1.3.3 General deformations

In this Section we discuss the extension of the above rheological analysis to three dimensional flows, and consider how the Newtonian constitutive equation can be generalised to three dimensions for simple shear flow.

The forces on an element of fluid at static equilibrium are shown in Figure 1.2. As in the previous analysis of dry granular material, the stress tensor describing this state is given in Equation 1.5. In addition to the normal stresses acting on the fluid element as a result of its flow and deformation, we must also take into account the hydrostatic pressure acting on the volume element of material. The stress tensor in Equation 1.5 is

therefore broken down into two parts, one contribution from the hydrostatic pressure, and the other is referred to as the deviatoric stress, shown in Equation 1.14

$$\begin{pmatrix} \sigma_{xx} & \sigma_{xy} & \sigma_{xz} \\ \sigma_{yx} & \sigma_{yy} & \sigma_{yz} \\ \sigma_{zx} & \sigma_{zy} & \sigma_{zz} \end{pmatrix} = \begin{pmatrix} p & & \\ & p & \\ & & p \end{pmatrix} + \begin{pmatrix} \sigma'_{xx} & \sigma'_{xy} & \sigma'_{xz} \\ \sigma'_{yx} & \sigma'_{yy} & \sigma'_{yz} \\ \sigma'_{zx} & \sigma'_{zy} & \sigma'_{zz} \end{pmatrix} \tag{1.14}$$

where p is such that the deviatoric stress tensor is traceless, $\sigma'_{xx} + \sigma'_{yy} + \sigma'_{zz} = 0$. The deviatoric stress is the stress that is available to deform the material. The above expression is abbreviated to $\sigma_{ij} = pI + \sigma'_{ij}$, where I is the identity matrix. Under a general deformation, the above deviatoric stress will lead to the strain rate matrix given in Equation 1.15.

$$\begin{pmatrix} \dot{\gamma}_{xx} & \dot{\gamma}_{xy} & \dot{\gamma}_{xz} \\ \dot{\gamma}_{yx} & \dot{\gamma}_{yy} & \dot{\gamma}_{yz} \\ \dot{\gamma}_{zx} & \dot{\gamma}_{zy} & \dot{\gamma}_{zz} \end{pmatrix} \tag{1.15}$$

It is found that a non-symmetric strain rate matrix such as this describes a flow that has both deformational and rotational components. In order to obtain the strain rate matrix that contributes to the deformation of the material, it is necessary to write down the above strain rate matrix as the sum of a symmetric matrix (the deformational part), and an anti-symmetric matrix (the rotational part). The components of the symmetric ($\dot{\varepsilon}$) and anti-symmetric ($\dot{\omega}$) matrices are given in Equations 1.16 and 1.17 respectively.

$$\dot{\varepsilon}_{ij} = \frac{1}{2}(\dot{\gamma}_{ij} + \dot{\gamma}_{ji}) \tag{1.16}$$

$$\dot{\omega}_{ij} = \frac{1}{2}(\dot{\gamma}_{ij} - \dot{\gamma}_{ji}) \tag{1.17}$$

We have thus extracted the relevant deformational strain rate matrix $\dot{\varepsilon}$ that we wish to relate to the deviatoric part of the stress tensor. We will now look at the case of simple shear flow.

The strain rate derived at the beginning of this chapter for simple shear flow, can be written in the form of a strain rate matrix as in Equation 1.18.

$$\begin{pmatrix} 0 & 0 & 0 \\ \dot{\gamma}_{yx} & 0 & 0 \\ 0 & 0 & 0 \end{pmatrix} \tag{1.18}$$

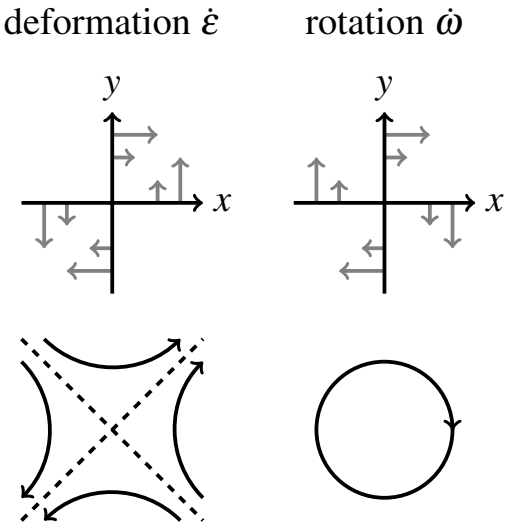

Fig. 1.6 Plots of the direction of strain and subsequent deformation and rotation of a volume element of fluid under simple shear.

The symmetric and anti-symmetric strain rate matrices are therefore:

$$\dot{\varepsilon} = \begin{pmatrix} 0 & \frac{\dot{\gamma}_{yx}}{2} & 0 \\ \frac{\dot{\gamma}_{yx}}{2} & 0 & 0 \\ 0 & 0 & 0 \end{pmatrix} \tag{1.19}$$

$$\dot{\omega} = \begin{pmatrix} 0 & -\frac{\dot{\gamma}_{yx}}{2} & 0 \\ \frac{\dot{\gamma}_{yx}}{2} & 0 & 0 \\ 0 & 0 & 0 \end{pmatrix} \tag{1.20}$$

Figure 1.6 shows the corresponding velocity gradients in x and y for the $\dot{\varepsilon}$ and $\dot{\omega}$ matrices, and the subsequent streamlines of the deformational and rotational flows. It can be seen that the flow given by $\dot{\varepsilon}$ represents pure deformation and that given by $\dot{\omega}$ represents pure rotation.

In constructing a constitutive equation for this flow, the deviatoric stress σ'_{ij} must be related to the pure deformation part of the strain rate matrix, so for the Newtonian case, one obtains $\sigma'_{ij} = 2\eta\dot{\varepsilon}_{ij}$, where η is the Newtonian viscosity. The factor of 2 is included to ensure self-consistency, as the individual components of $\dot{\varepsilon}$ are $\frac{\dot{\gamma}_{yx}}{2}$. This expression for σ'_{ij} can now be included in the expression for the total stress acting on the volume element, to give the complete generalised definition of Newtonian flow, in Equation 1.21.

$$\sigma_{ij} = pI + 2\eta\dot{\varepsilon}_{ij} \tag{1.21}$$

In this Chapter some fundamental concepts of rheology have been introduced. The notion of a constitutive equation is presented, along with examples of constitutive equations describing Newtonian and non-Newtonian materials. The analysis was then extended to viscoelastic materials, whose flow properties were described in terms of an elastic and a viscous effect. Finally, the discussion was extended to three dimensions, with the Newtonian constitutive equation for three dimensional simple shear being derived.

1.4 Rheology of granular suspensions

When solid particles are suspended in a liquid, the flow properties of the liquid change (Mewis and Spaull, 1976). For low solids volume fractions, the change is due to hydrodynamic interactions. That is, the interaction of the continuous, interstitial fluid with the particles leads to enhanced dissipation. At intermediate volume fractions, both hydrodynamic interactions and transient particle-particle collisions contribute to the change in flow properties. For dense suspensions, force transmission through prolonged particle-particle contacts and interactions pays a significant contribution to the system properties (de Bruyn, 2011). The term "dense" can be interpreted in a number of ways, i.e. in terms of the average separation between particles, in terms of proximity to the jamming transition, or simply in terms of significant observed deviation from Newtonian flow behaviour (Stickel and Powell, 2005).

The past century has seen numerous attempts to develop models to predict the bulk flow properties of the above regimes based on particle-fluid, particle-particle and particle-boundary interactions associated with increasing volume fractions. This review will cover the theoretical development from early predictive models for dilute particulate systems to proposed constitutive relations for dense granular flow. Experimental and computational studies of dense granular materials will then be discussed.

1.4.1 Theoretical Development

Dilute suspensions

Initial work in suspension rheology considered dilute suspensions of Brownian (*i.e.* $Pe < 1$) hard spheres, and assumed that they behaved in a Newtonian manner, with the shear stress being proportional to a rate independent viscosity. This set the grounding for a first approximation of the variation of viscosity η with volume fraction ϕ to be determined analytically. Expressions for viscosity could then be used in a Newtonian constitutive equation of the form $\tau = \mu(\phi)\dot{\gamma}$. Based on the following assumptions,

Einstein (Einstein, 1906) determined analytically the increase in bulk fluid viscosity with volume fraction to a first order approximation, for volume fractions up to approximately 0.02, as $\eta = (1+2.5\phi)\eta_0$:

- The continuous phase is a Newtonian fluid
- Low Reynolds number, *i.e.* creeping flow regime
- Neutrally buoyant, rigid particles
- No particle-particle or particle-boundary interactions
- No slip at particle surface

Batchelor (Batchelor, 1977) considered particle-particle interactions and extended this to a second order approximation ($\eta = (1+2.5\phi+6.2\phi^2)\eta_0$), allowing viscosity to be predicted for volume fractions up to 0.1. At large Reynolds numbers, the flow field around a spherical particle will be different to that at low Reynolds numbers, so one would expect the variation of suspension viscosity with volume fraction to be dependent upon whether the flow is inertial. As such, Einstein's expression for viscosity has been developed semi-empirically to include Reynolds number dependence, accounting for inertial flow (Lin, 1970; Ryskin, 1980) in dilute systems, allowing the assumption of creeping flow to be relaxed somewhat.

Dense suspensions

The relationships between suspension viscosity and volume fraction above have been further extended by Krieger and Dougherty (Krieger and Dougherty, 1959), to calculate the viscosity of suspensions with volume fractions up to the maximum packing fraction ϕ_c, according to Equation 1.22

$$\eta = \eta_0 \left(1 - \frac{\phi}{\phi_c}\right)^{-2.5\phi_c} \tag{1.22}$$

for a suspending liquid of viscosity η_0. This critical packing fraction ϕ_c represents the solids volume fraction at which the system transitions from liquid-like to solid-like. It is related to the efficiency with which particles can occupy a control volume, and depends acutely on their shape, size distribution and surface properties. For example, rough particles have a lower ϕ_c than smooth particles, as the increased resistance to sliding and rolling allows the particle assembly to achieve structural rigidity with fewer particle-particle contacts (Song et al., 2008; Chialvo et al., 2012).The precise value of the exponent determines the rate at which the viscosity diverges with volume fraction

and remains contested. Its true dependence on ϕ_c and on the particular surface details of the suspended system in question is unclear (Guy et al., 2015). As the volume fraction approaches the maximum allowed volume fraction (based on the maximum packing at a given shear rate and dependent on particle surface details), the viscosity of the system diverges. While this predicts the volume fraction dependence of the viscosity, it does not take into account how the viscosity behaves at a given volume fraction, for example with respect to shear rate.

So far we have assumed that suspensions behave as Newtonian fluids, with a constant viscosity for a given volume fraction. This is not the case for the viscosity of dense suspensions, which can exhibit complex shear rate dependence (Stickel and Powell, 2005). Shear thinning behaviour has been thoroughly studied theoretically and experimentally (Krieger, 1972; Barnes, 1989; Roberts et al., 2001). Shear thickening has also been observed classically (Barnes, 1989), and will be discussed at great length throughout this work. Predictive models for suspension rheology must therefore account for shear rate dependence of viscosity.

Predicting the viscosity of increasingly dense suspensions becomes difficult once the hydrodynamic interactions alone are not sufficient to describe the momentum transfer in the material. For the dilute systems above, it was assumed that there were either no particle-particle interactions, or only simple two-particle interactions, meaning that the particle-fluid interaction could be solved analytically. For dense suspensions, particle collisions and sustained particle contacts will be ubiquitous in addition to hydrodynamic interactions, and will have a significant effect on momentum transfer. In dense systems the viscosity is, therefore, dependent on the microstructure of the particle network, which may have very complex shear rate dependence, making particle based analytical solutions difficult in practice.

Kinetic theory for gases has been extended (Lun et al., 1984; Garzó and Dufty, 1999) to account for inelastic (*i.e.* dissipative) collisions of frictionless, finite volume disks (Jenkins and Richman, 1985), and there has been some success in developing constitutive models for granular flow based on this work (Goddard, 1986). Original extensions of kinetic theory assume that particle-particle collisions are entirely uncorrelated, and that the Peclet number is low. These assumptions are clearly invalid for particulate systems at or near the jamming or glass transitions, as the non-ergodic, "caged" or crowded, nature of such systems means particle contacts will be enduring and usually history dependent. As such, these models are typically suitable for dilute, inertial flows. This particle based approach is therefore able to predict flow behaviour of dilute granular materials, and has shown some agreement with experimental data. More recently, this extension of kinetic theory has been further built upon (Chialvo

and Sundaresan, 2013) to allow prediction of dense flows ($0.5 < \phi < \phi_c$) of frictional granular material. Initial results show quantitative agreement with molecular dynamics simulations of these types of flow.

A number of micromechanical approaches (Johnson and Jackson, 1987; Stickel et al., 2006; Seth et al., 2011) have led to the development of numerous constitutive equations for dense suspensions (Harris, 1995) in the regimes where particle collisions and sustained particle contacts are important. Harris (Harris, 2010) has argued that many existing models are ill-posed in that for some initial conditions small flow perturbations will lead to unbounded growth in flow instabilities that do not correspond to physical behaviour. Harris goes on to describe a protocol for stability analysis and presents a model for slow flow of dense material, where sustained particle contacts are important, that is numerically stable in some cases (Harris, 2006). It is crucial therefore, that before any micromechanical model is implemented it is rigorously checked for stability with respect to the initial conditions and flow geometry under consideration.

A particularly noteworthy constitutive equation is that proposed by Phillips (Phillips et al., 1992). This model predicts the volume fraction and velocity components in dense monodisperse suspensions, taking into account shear-induced phase migration. There are two components, a Newtonian constitutive model for the liquid phase that relates the viscosity to the local volume fraction, and a diffusive model that determines the particle motion induced by the fluid flow. This model has shown considerable agreement with experimental data, for dense suspensions of volume fractions up to 0.6. Phase migration causes significant problems in industrial extrusion processes, where localised pressure gradients drive liquid out of a region, causing a localised increase in volume fraction (Benbow and Bridgwater, 1993). The flow properties in these regions will therefore differ considerably, leading to instabilities in extrusion flow. It is therefore highly desirable to include such particle phenomenon in constitutive equations for dense suspensions.

Although there has been much work in extending kinetic theories for granular flow, and in coupling fluid flow and particle properties in micromechanical models, the constitutive models adopted in industry have traditionally stemmed from continuum models based on empirical studies of bulk non-Newtonian flows. Such constitutive equations take into account yield behaviour (Bingham plastic (Bingham, 1925), Herschel-Bulkley (Bulkley and R., 1926)), shear thinning and thickening (Power law), and high and low shear rate Newtonian plateaus (Cross (Cross, 1965), Carreau (Carreau, 1972)), over a wide range of shear stresses (Roberts et al., 2001), and can be implemented into a numerical solution of the Navier-Stokes equations (Harris, 2010).

While the constitutive equations above have been common in industry for decades for modelling dense suspensions, each is typically applied to a specific process or product and none have general applicability. The challenge of extending the static analysis of dry granular materials to post-failure (Jop et al., 2006), where the material flows like a high viscosity liquid has persisted.

1.4.2 Experimental work

Rheological measurements

Dry granular materials have been studied experimentally using common rheological measurements such as Couette and Poiseuille flow rheometry, cone and plate rheometry and concentric cylinder rheometry (MiDi, 2004). These techniques involve applying a stress, strain or pressure gradient to a material in a well defined geometry, and measuring the resulting strain, stress or velocity profile, respectively, in order to obtain information about the viscosity and elasticity of the material. The French research group Groupement De Recherche Milieux Divises published an assimilation of rheological techniques for granular flow, identifying the critical parameters and measurable properties for a number of geometries (MiDi, 2004). A particular challenge in experimental studies of dense granular flows is obtaining stable samples at very high, and very precisely known, volume fractions.

Researchers have found that under Couette and Poiseuille flow (Arp and Mason, 1977) viscous Newtonian fluids with low solids volume fractions ($\phi < 0.1$) behave like Newtonian fluids. This corresponds well with early theoretical models (Einstein, 1906; Batchelor, 1977) that describe dilute suspension viscosities as functions of volume fraction only.

For higher volume fractions, non-Newtonian behaviour is observed under these flows (Arp and Mason, 1977; Gadala-Maria and Acrivos, 1980). In Poiseuille flow, partial plug flow is observed, with apparent wall slip due to hydrodynamic forces resulting in a reduced particle concentration and apparent reduced viscosity at the walls. In Couette flows, the fluid is observed to have a stagnant region adjacent to the stationary boundary and a flowing region at the moving boundary (Bocquet et al., 2001), with the interface location being dependent on the velocity of the upper plate. This has been described as yield stress behaviour (Jop et al., 2006), with the yield stress not being dependent on the interstitial fluid viscosity, but on the physical details of the particles (Divoux and Géminard, 2007).

Nordstrom and co-workers have characterised dense aqueous suspensions of *N*-isopropylacrylamide particles using centrifugal compression (Nordstrom et al., 2010a,b).

They were able to precisely control the volume fraction by changing the temperature of the system. Stress versus strain rate data were then obtained over a very wide range of strain rates, and for volume fractions above and below the jamming transition. The data were then collapsed based on the distance of the volume fraction from the critical volume fraction at which jamming occurs (Olsson and Teitel, 2007; Hatano, 2008), and the stress versus strain rate data were found to lie on a master curve with three regimes - the quasistatic, intermediate and flowing regimes. Below the critical volume fraction, the material flows (in a viscous or inertial regime, dependent on shear rate and interstitial fluid viscosity), with non-Newtonian shear thinning rheology observed at very high shear rates. Above the critical volume fraction, the material is static and described by a yield stress. At very high shear rates, these behaviours converge in the so-called *intermediate* regime. These regimes have been well documented in computational work (Olsson and Teitel, 2007; Hatano, 2008; Sun and Sundaresan, 2011; Ikeda et al., 2012) and appear to be generally consistent across viscous and inertial, Brownian and non-Brownian, soft and hard particle flows. This framework for unifying granular flow regimes will be utilised and built upon in the following Chapter.

Stress transmission in dense systems

Experimental micromechanical work by Behringer and co-workers at Duke University has looked at force distributions in granular media, and how frictional forces between particles in contact influence these distributions (Behringer et al., 1999). Photoelastic disks, two dimensional plastic disks whose light transmission properties are dependent on the compressive force applied to them, are poured into piles (Vanel et al., 1999), and the resulting distribution of force chains is observed visually. In this instance it is found that the force chains are predominately aligned in the vertical axis, as expected, and they distribute the weight of the pile in such a way that it is spread across the ground surface area rather than localised below the centre of mass. Analyses such as these contribute to our understanding of dense suspensions, since for high volume fractions the flow behaviour is dominated by persistent particle-particle contacts, meaning force chains will be established.

Later work by this group found that when these disks are sheared, long-range uni-directional force chains are established that are not present in isotropically compressed systems (Majmudar and Behringer, 2005). Furthermore, it was found that at a critical volume fraction (thought to correspond to the jamming point), there was a non-linear and rapid increase in the coordination number of the system, suggesting that at this point the force transmission through sustained particle-particle contacts becomes significantly more important (Majmudar and Behringer, 2005).

Imaging granular systems

Individual particle data such as location and velocity components have traditionally been very difficult to extract from experiments of granular media. The recent development of confocal rheometry (Isa et al., 2009) has allowed a 3D particle scale imaging technique, confocal microscopy, to be coupled with real time rheological measurements. This procedure can be implemented in some of the traditional rheological geometries, including Couette flow, Poiseuille flow and cone and plate rheometry. Algorithms have been developed that are able to determine the location, velocity and size of every particle in a suspension under shear, at frame rates of 5-100 Hz. These data now offer unparalleled levels of simulation validation.

1.4.3 Computational work

Computational work in the field of suspension rheology can be broadly split into two categories; particle based and continuum based simulations.

Particle Simulations Particle based simulations involve the explicit calculation of particle properties such as position, velocity and contact force, for a particle assembly or suspension. A classical particle simulation technique is Stokesian Dynamics (Bossis and Brady, 1984; Brady and Bossis, 1985), in which the Langevin Equation (Langevin, 1908) is solved numerically for the motion of particles in a continuous interestitial fluid. This technique captures long and short range hydrodynamic forces and non-hydrodynamic interaction forces for non-equilibrium flows, such as simple shear.

Another particle simulation method used in suspension rheology is the Discrete Element Method (DEM) (Cundall and Strack, 1979). DEM is a branch of traditional molecular dynamics simulations, in which the motion and interactions of individual particles are solved explicitly. DEM is able to model Brownian and non-Brownian particles that have a volume and rotational velocity components. Particle based simulations are computationally expensive as the momentum equations must be solved for every particle.

Continuum Simulations Alternatively, the particle properties can be averaged across a large number of particles and the material treated as a continuum. In the case of very dense suspensions, the system may be treated as an elastic solid, with a yield criterion-type constitutive equation. This constitutive equation is then incorporated into, for example, a Finite Element Method (FEM) (Bathe et al., 1975; Bathe and Zhang, 2004) solver, and the bulk behaviour analysed (Ooi and She, 1997; Rotter et al., 1998).

For less dense suspensions, the material may be treated as a liquid, and described by a Newtonian or non-Newtonian constitutive equation, which can then be incorporated into a Computational Fluid Dynamics (CFD) (Wendt, 2009) solver, and the bulk flow studied. These simulations are potentially less computationally expensive as the solver does not solve individual particles, but solves the continuous flow field across the domain. Optimisations to these techniques can make them more suited to simulations of the complex and moving boundaries associated with particulate flows. For example, the immersed boundary method (Mittal and Iaccarino, 2005) is a procedure for solving such flows whereby instead of solving the flow field on a geometry-conformal mesh (which is slow to generate and is associated with complex reference frame transformations), a cartesian mesh is rapidly generated, and the particle boundaries lie within the mesh. This has the advantage of not requiring remeshing at each step, but rather updating the locations of the immersed boundaries to account for particle convection through the interstitial fluid.

DEM simulations provide a level of solution detail that cannot be paralleled by continuum methods. For example, at any point in time during a DEM simulation, the precise coordinates, velocity components and force components of every particle being simulated can be obtained and used for calculation. Furthermore, the particle interaction forces can be refined and developed to accurately model additional forces such as particle cohesion and friction. The computational power required by DEM is related to the number of particles being simulated, and the length of the simulation. The desire to simulate very large systems of particles in complex geometries means that even with today's high performance computers, DEM has significant limitations. As a consequence, there remains a massive drive in developing constitutive equations for granular materials, facilitating computationally less intensive continuum simulations.

Discrete Element Simulations

Computational advances in the past 20 years have led to a surge in the application of DEM simulations to granular problems. DEM has been used extensively to study the behaviour of dense granular materials under shear, in periodic domains (Campbell, 2002; Aarons and Sundaresan, 2006; Olsson and Teitel, 2007). In these simulations, a domain is defined and filled with particles (typically 2D circles or 3D spheres but not exclusively (Azema et al., 2009)) at a desired volume fraction (O'Hern et al., 2002; Luding and Herrmann, 1999; Miller and Luding, 2004). The boundaries of the domain are periodic, meaning that there are "image" boxes in x, y and z, as shown in Figure 1.7. When a particle exits the domain through the left boundary, an identical particle

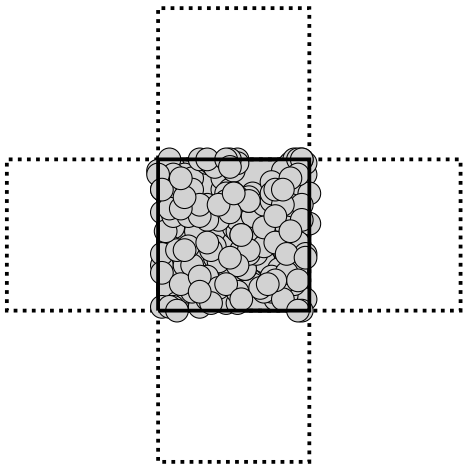

Fig. 1.7 Front view of simulation box showing image boxes

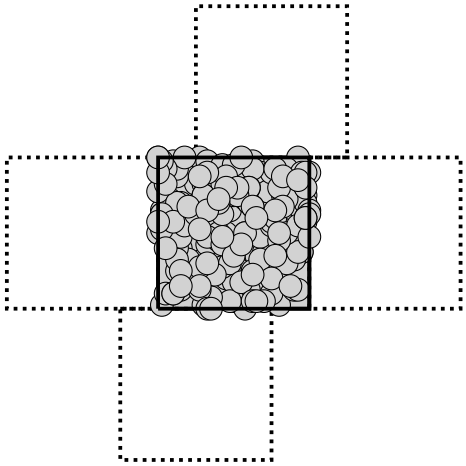

Fig. 1.8 Front view of simulation box showing Lees-Edwards boundary conditions

will enter at the same point on the right boundary, simulating an infinite domain. Lees-Edwards boundary conditions (Lees and Edwards, 1972) are then applied to simulate simple shear, as shown in Figure 1.8, and the resulting stress response analysed. These boundary conditions effectively shift the image boxes in the direction of shearing, simulating a velocity gradient or shear rate in that direction. The focus of recent work has been to characterise the stress response in various flow regimes, with the aim of understanding the constitutive properties of the material

Campbell (Campbell, 2002) studied this configuration for steady shear. It was predicted that for cohesionless, elastic, non-Brownian particles in the absence of gravity, there is a critical volume fraction above which the material is in the quasistatic, jammed regime, and below which it is in the inertial regime. This transition was observed to occur at around $\phi = 0.62 \pm 0.02$. In the quasistatic regime the stresses were found to

scale purely elastically, with yield behaviour, while in the inertial regime the stresses were found to scale with $\dot{\gamma}^2$. This work has been extended by Aarons and co-workers (Aarons and Sundaresan, 2006) to account for cohesive particles, finding that cohesion extends the values of ϕ for which quasistatic behaviour is observed.

Later, Campbell found (Campbell, 2005) significant differences in behaviour if the domain is defined by constant pressure at the boundaries, rather than constant volume. For the former case, at very high shear rates, the volume was found to increase slightly, reducing ϕ to accommodate the applied stress, an effect referred to as dilatancy. This meant that for fixed applied stress cases, high stresses resulted in a transition from quasistatic to inertial regime. Later work by Aarons (Aarons and Sundaresan, 2008) somewhat contradicts this result, finding that the steady state stress response for cohesive particles in this configuration is independent of whether the domain is defined by constant volume or constant applied normal stress, suggesting that one role of cohesive particle-particle interactions may be to mitigate dilatant rheology.

The evolution of the microstructure during shearing is critical to the rheological behaviour (Sun and Sundaresan, 2011). For, initially isotropic, dense materials under shear, the rate of breaking of particle-particle contacts is greater than the rate of creating them, while for dilute suspensions, the opposite is true (Rothenburg, 2004; Aarons and Sundaresan, 2006). Anisotropies that form during shearing simulations have been quantified (Aarons et al., 2009) through the fabric tensor, which has been incorporated into constitutive models for granular materials (Sun and Sundaresan, 2011).

The volume fraction at which the system moves from the inertial to the quasistatic regime as observed by Campbell (Campbell, 2002) has been given much attention (O'Hern et al., 2003; Zhang et al., 2005; Song et al., 2008; Chaudhuri et al., 2010). There is some debate as to whether this transition, the jamming transition, can be defined by a single volume fraction for a single system, or whether it is dependent on the precise history and microstructure of the system. Song (Song et al., 2008) argued that for frictionless particles, the jamming transition occurs at a single point, regardless of history. Chaudhuri (Chaudhuri et al., 2010) has proposed that the jamming transition is a sharp transition, but that it can occur along a continuous range of volume fractions, depending on history. Earlier results (O'Hern et al., 2002) suggest that as the number of particles simulated in the periodic domain is increased, this range of volume fractions is found to narrow. For frictional particles, Zhang (Zhang et al., 2005) found that the jamming transition occurs between $\phi = 0.576$ and $\phi = 0.604$, and suggested that the exact value is dependent on the microstructure and hence the history of the material.

Olsson (Olsson and Teitel, 2007) studied bidisperse, two-dimensional, non-Brownian frictionless disks under simple shear and similarly found two different flow regimes

at low and high volume fractions. Just as rheological experiments aim to obtain flow curves based on the relationship between stress and strain for complex fluids, so recent computational work in granular materials has focussed on developing scaling relationships allowing analogous relationships to be obtained. Olsson computed the shear viscosity η as a function of applied stress σ for a large range of volume fractions ϕ, spanning the jamming transition. As with previous work (Campbell, 2002; Aarons and Sundaresan, 2006), different behaviour was observed above and below a critical volume fraction. Olsson proposed the scaling variables $\sigma/|\phi_c - \phi|^{\Delta}$ and $\eta^{-1}/|\phi - \phi_c|^{\beta}$ where ϕ_c is the volume fraction at which the transition occurs and Δ and β are constants. Scaled in this way, the data were found to collapse onto two master curves, above and below the critical volume fraction, for $\Delta = 1.2$ and $\beta = 1.65$.

Hatano (Hatano, 2008) extended these scaling laws to include the pressure and kinetic temperature, but found that while scaling using distance from critical volume fraction suggests that jamming is a conventional critical phenomenon, the exponential constants associated with the scaling expressions are dependent on the choice of force model (O'Hern et al., 2003). Experimental work, for example in emulsions (Nordstrom et al., 2010a), has shown agreement with the scaling relations discussed by Olsson (Olsson and Teitel, 2007) and Hatano (Hatano, 2008).

Scaling of the form used by Olsson and Hatano has since been predicted phenomenologically (Otsuki and Hayakawa, 2009), with the theoretically predicted critical exponents being verified using similar simulations (Otsuki and Hayakawa, 2008). Furthermore, the simulations have been carried out for frictional particles (Otsuki and Hayakawa, 2011) and it is found that although the jamming transition occurs over a range of volume fractions dependent on history, making the choice of the critical volume fraction somewhat dubious, the scaling rules for frictionless particles still broadly apply for frictional systems. At high shear rates, it is found that the quasistatic and inertial master curves share a common asymptote that is independent of interparticle friction coefficient (Chialvo et al., 2012). This is surprising given that earlier work (Zhang et al., 2005) found that the critical volume fraction itself is a function of friction. The common high shear asymptote is called the intermediate regime. For systems at $\phi > \phi_c$, the behaviour as the shear rate is increased and the system moves from the quasistatic to the intermediate regime has been described as Herschel-Buckley form (Bulkley and R., 1926; Nordstrom et al., 2010a; Seth et al., 2011). Chialvo (Chialvo et al., 2012) proposed a blending function to combine the scaled behaviour in the three regimes (quasistatic, inertial and intermediate) under a common framework, and again found Herschel-Bulkley behaviour at high volume fractions. Although the exact values used in the scaling variables vary between authors and precise simulation settings (choice of

friction coefficient etc), there is widespread agreement that the flow curve data can be seen to collapse onto the quasistatic, inertial and intermediate regimes in all cases. In fact, it has been suggested (Tighe et al., 2010) that the disparity in scaling exponents is due to the presence of a third rate-dependent regime, and that current literature data may potentially be collapsed to a single flow curve with four, rather than three, flow regimes.

In addition to shearing in periodic domains, discrete element simulations have also been used to study boundary effects and flows in simple and complex geometries.

Building upon simple shearing simulations in periodic domains, there has long been research in plane shearing of granular materials between parallel walls, aiming to demonstrate the non-Newtonian behaviour of suspensions in geometries that more closely represent engineering scenarios (Zhou and Pozrikidis, 1993). Although the parallel plate case is a highly simplified geometry, it has been used to extract rheological information about granular materials which compliments that acquired through periodic domain simulations and that can be applied to more complex geometries. Da Cruz and co-workers (Da Cruz et al., 2005) simulated two dimensional disks in plane shear flow between rough (the surface is made up of stationary particles), parallel plates, bound by a constant applied pressure. The same increasing volume effect as for periodic simulations (Campbell, 2005) was found at high shear rates under the constant pressure condition. Furthermore, it was found that the salient variables of the simulation could be combined as in earlier experimental work (MiDi, 2004), leaving a single relevant variable to determine the shear state - the Inertial number. Plane shear simulations have been used to characterise the yield behaviour of granular systems (Xu and O'Hern, 2006; Rognon et al., 2008). For frictionless, cohesionless systems it is found that the granular material in plane shear can be described as an ideal Coulomb material, with a single static yield stress (Xu and O'Hern, 2006), while for cohesive systems it is possible to characterise the material by a simple friction law, but the yield stress of the material is significantly enhanced (Rognon et al., 2008).

Particle simulations have been used to study velocity profiles in pressure driven flows of suspensions (Nott and Brady, 1994; Morris and Brady, 1998; Silbert et al., 2001; Pozrikidis, 2002). A recurring observation (Nott and Brady, 1994) is the effect known as apparent wall slip (Elhweg et al., 2009), in which the material appears to exhibit an extreme shear-induced reduction in viscosity (shear-thinning) in very close proximity to the boundary. This affect has been observed both in the presence and absence of particle buoyancy effects (Nott and Brady, 1994; Morris and Brady, 1998). This phenomenon is actually a consequence of hydrodynamic particle migration (Nott and Brady, 1994; Pozrikidis, 2002), in which the flow field established around the

surface of a particle results in a wall interaction that drives the particle away from the wall, resulting in a particle-deficient region of material near the boundary. Rather than being a particle interaction or effect causing shear thinning, the apparent wall slip is therefore an exhibition of the viscosity of the interstitial fluid, hence the phrase "apparent" (Pozrikidis, 2002). Furthermore, the particle concentration in the bulk of the material will be slightly increased as a result of this migratory affect, with potentially significant implications for the rheology of the bulk. It is therefore important in any particle simulation which includes wall effects that migratory behaviour is characterised and accounted for.

Gravitationally driven, inclined-plane, free-surface particle flows have been simulated (Silbert et al., 2001; Reddy and Kumaran, 2010), finding that for angles even very slightly greater than the angle of repose, the steady-state velocity profile is well predicted by the traditional Bagnold scaling (Bagnold, 1954; Hunt et al., 2002).

Constitutive models for granular flow

Constitutive equations provide a computationally cheap means of characterising the bulk material properties of granular systems. Practical and industrial applications of granular materials often involve length scales of thousands or tens of thousands of particle diameters, so a bulk, continuum description of their flow is clearly preferable to a particle by particle solution (Goddard, 1998). Such continuum descriptions aim to describe the quasi-static regime (traditionally described by Coulomb yield type constitutive equation (Schofield and Wroth, 1968; Goddard, 1998)) as well as the inertial, fluid-like regime, where the material behaves like a viscous liquid. Furthermore, there is a drive to characterise potentially unexpected interfaces between these regimes, such as those arising due to shear-banding (Schall and Van Hecke, 2010; Anand and Gu, 2000) and phase migration.

Works have focussed on correlating particle level (micromechanical) properties such as coordination number (Sun and Sundaresan, 2011), anisotropy (fabric tensor) and the development of force chains (Nemat-Nasser, 2000; Nemat-nasser and Zhang, 2002; Zhu et al., 2006; Sun and Sundaresan, 2011), local volume fraction (Daniel et al., 2007), friction (Daniel et al., 2007; Nemat-nasser and Zhang, 2002) and local dilatancy (Nemat-Nasser, 2000) with continuum level rheological characteristics. These correlations can be elucidated experimentally (Nemat-Nasser, 2000) by observing the development of particle level properties under shearing in standard rheological apparatus, for example. Alternatively, DEM simulations can be used to develop, and subsequently calibrate, relationships between particle level properties and bulk material properties (Sun and Sundaresan, 2011). These relationships can then be assimilated into a constitutive

equation, allowing it to take account of the evolution of the microstructural properties of the material as the shearing progresses. There has therefore been some success in developing constitutive equations that use micromechanical properties to describe the behaviour of dense granular materials at and near the transition between inertial and quasistatic regimes. It is still essential that these models be expanded to account for a broader range of shear states, both well above and well below the jamming transition. Many other physical effects are yet to be incorporated into such a constitutive equation, such as the lubrication and hydrodynamic effects of an interstitial fluid (as attempted by (Goddard, 2006), though without a deep mechanistic understanding), more complex particle-particle cohesive/repulsive forces and phase migration, for example, so there is still a great way to go in developing continuum models for granular material.

1.5 Unifying theories

Particulate material research has traditionally been split fairly clearly into dry, wet, Brownian and non-Brownian. In terms of applications, these separations may remain relevant (for example dry grains and pastes are distinct engineering materials with substantially differing processing requirements), but the theoretical understanding of such materials is converging, with the boundaries between fields becoming less apparent and less meaningful (Cates et al., 2009). In the past two decades there has been an increased drive to unify previously distinct areas of understanding in particulate materials and disordered systems in general, in order that a common framework becomes apparent under which all such systems can be described (Sollich et al., 1997; Cates et al., 1998). Researchers have aimed to bridge understanding between wet and dry granular systems (Isa et al., 2007; Lemaître et al., 2009; Dijksman et al., 2010; Boyer et al., 2011; de Bruyn, 2011; Lerner et al., 2012), and between Brownian and non-Brownian suspensions (Cates et al., 2009; Xu et al., 2009; Haxton et al., 2011; Ikeda et al., 2012; Guy et al., 2015).

An analogy was drawn between wet and dry systems in experimental work by Isa *et.al*. (Isa et al., 2007), who found that for pressure driven capillary flow of a dense, colloidal, suspension, the plug-flow velocity profile observed using confocal-microscopy is better described by typical dry granular yield stress behaviour than by the expected Herschel-Bulkley model. Rather than observing a decreasing plug-width with increasing flow rate (as would be expected with a Herschel-Bulkley fluid), it was found that the shear zone width was not a function of flow rate. This corresponds well with a yield stress model proposed previously for chute flow of dry granular materials (Pouliquen and Gutfraind, 1996). For high volume fraction, colloidal suspensions of frictional

particles in narrow geometries, it may therefore be possible describe the shear state and hence the velocity profile by analogy with dry granular flow.

Theoretical work (Lemaître et al., 2009) has since shown through dimensional analysis that the parameters characterising dry granular flow, most importantly the Inertial Number I (MiDi, 2004), can be extended to the case of non-Brownian suspension flow. Rheological measurements of non-density matched (and non-Brownian) suspensions have demonstrated behaviour characteristic of both dry and wet granular systems (Dijksman et al., 2010) in the same material. At low shear rates, the flow is such that the particles are able to settle during the measurement, forming a region of increased volume fraction at the bottom of the apparatus. The shear banding observed in this region is the same as would be predicted for a dry granular material. At high shear rates, the flow is such that the settling is slow compared to the particle convection induced by shearing, and as such the material behaves as would be expected for a viscous granular suspension.

Boyer *et.al*. (Boyer et al., 2011; de Bruyn, 2011) extended analysis of the Inertial number for dry granular systems by showing experimentally its similarity with the Viscous number (proposed earlier by Cassar (Cassar et al., 2005)) for suspensions. Constitutive equations for frictional granular media that predict the shear stress and volume fraction as a function of the Inertial number have been modified to successfully show the shear rate and volume fraction dependence of the Viscous number in suspensions, showing that the two systems can be considered to be analogous (Trulsson et al., 2012).

Recent computational work (Lerner et al., 2012) has focussed on drawing an analogy between the rheology of suspensions very near to the jamming transition and the elasticity of amorphous, dry, granular solids very near to the unjamming transition, using the operator $\mathscr{N}$, a micromechanical tensor containing information about the contact network and coordination number of the system. Very close to the jamming and unjamming transitions, the contact forces and effective viscosity for both types of system can be obtained from constitutive equations based on this operator.

Brownian and non-Brownian systems have traditionally been studied under separate frameworks, due to their seemingly very different underlying dominant particle interactions. Brownian systems are described by equilibrium statistical mechanics, while non-Brownian systems are in a state of thermodynamic non-equilibrium. Recent experimental developments have allowed visualisation of both colloidal and granular suspensions (Besseling et al., 2010; Isa et al., 2009, 2007), allowing precise micromechanical comparisons to be made between previously distinct materials. Furthermore, computational advances have allowed a dramatic improvement in both analysis of

experimental data, and in simulation techniques, which enable yet more comparison to be drawn between Brownian and non-Brownian systems.

The non-equilibrium behaviour of colloids (*i.e.* caged dynamics associated with the glass transition) has offered even more scope for unifying theories, with phase diagrams being proposed (Xu et al., 2009; Haxton et al., 2011) that suggest jamming and glass transitions can be entirely described under a common framework (Liu and Nagel, 1998; Song et al., 2008; Ikeda et al., 2012). A phase diagram with axes of Inverse Volume Fraction, Temperature and Applied Stress is proposed (Liu and Nagel, 1998), where the jamming transition lies in the zero temperature plane, and the glass transition lies in the zero Applied Shear Stress plane, these being the extreme cases. Intermediate non-equilibrium states (*i.e.* something that resembles jamming and a glass transition) have been considered, for example a glass transition occurring under an applied stress (Haxton et al., 2011) (the example of stress-induced solidification in cornstarch has been given (Cates et al., 2009)). Some proteins have also been suggested (Jose and Andricioaei, 2012) as a class of suspension that can exhibit both glassy and jamming transitional properties, with the extent of folding and unfolding determining the nature of arrest at high volume fraction.

The rheology of glass and jamming transitions is qualitatively similar, both being associated with non-Newtonian flow just below the critical volume fraction, and yield-stress, quasistatic behaviour just above. However, recent computational work (Ikeda et al., 2012) has demonstrated that while they are distinct at low temperature, the jamming and glass transitions can be observed to coexist at a precise set of conditions of volume fraction, temperature and shear stress, *i.e.* at a specific set of points on the jamming phase diagram. This emphasises that while the two phenomenon are distinct in the pure jamming and pure glass transitions, at intermediate points in the jamming phase diagram, the observed rheological flow curve is the result of a melange of both. In addition to assimilating both glassy and jamming dynamics, this work uses a particle-particle interaction based simulation method to approximate suspensions and emulsions, further exemplifying the corespondance between wet and dry system dynamics at high volume fraction.

It is likely that there will continue to be a great deal of interest and future development in unifying theories for particulate systems.

Chapter 2

Flow regime transitions in dense non-Brownian suspensions

In this chapter, simple shear flow of dense, non-Brownian suspensions is simulated using the discrete element method (DEM), taking into account direct particle-particle contacts and short-range hydrodynamic lubrication forces. The resulting stress responses are assigned to distinct flow regimes, mapped in the parametric space of solid volume fraction ϕ, shear rate $\dot{\gamma}$, fluid viscosity η_f and particle stiffness k_n. Below a critical solids volume fraction ϕ_c, the rheology is governed by the Stokes number, which distinguishes between viscous and inertial flow regimes. Above ϕ_c, a quasistatic regime exists for low and moderate shear rates. At very high shear rates, the ϕ dependence is lost and soft particle rheology is explored. The transitions between rheological regimes are associated with the evolving contribution of lubrication to the suspension stress, and the relative deformability of the particles. Transitions in microscopic quantities such as inter-particle spatial force distribution, fabric and velocity correlation length are found to correspond to those in the macroscopic flow. Motivated by the observed bulk rheology, a constitutive model is proposed combining a viscous stress term with a dry granular model presented by Chialvo, Sun and Sundaresan [Phys. Rev. E. **85**, 021305 (2012)]. The model successfully predicts the flow regime transitions.

2.1 Introduction

Dense suspensions of solid, non-Brownian particles in Newtonian fluid, such as slurries and pastes, are ubiquitous in nature and industry, and present a wealth of complex and surprising flow behaviour (Stickel and Powell, 2005). The rheology of such suspensions is highly challenging, as the viscosity (shear stress divided by shear rate) is highly

sensitive to the solid volume fraction (Liu and Nagel, 1998; Chialvo et al., 2012), the shear rate, the preparation and shear history, and the particle properties.

Inspiration from granular mechanics (Forterre and Pouliquen, 2008) has recently shed light on suspension rheology near the critical volume fraction, ϕ_c. Experimental work (Boyer et al., 2011) demonstrates that under simple shear flow, dense suspensions can be constitutively characterised analogously to dry granular materials at low Reynolds numbers and below ϕ_c by adopting an approach analogous to the popular $\mu(\mathrm{I})$ rheology (MiDi, 2004). A suitable dimensionless control parameter, the viscous number $\mathrm{I_V} = \eta_f \dot{\gamma}/\mathrm{P}$ for wet systems with interstitial fluid viscosity η_f, confining pressure P at a shear rate $\dot{\gamma}$ is defined, similar to the much used inertial number $\mathrm{I_I} = d\dot{\gamma}/\sqrt{\mathrm{P}/\rho}$ for dry systems with ideally hard particles of diameter d. Constitutive equations based on $\mathrm{I_I}$ for the stress ratio $\mu = \sigma_{xy}/\mathrm{P}$ and volume fraction have yielded striking matches with experimental results in some geometries for dry materials (Jop et al., 2006). Computational work (Trulsson et al., 2012) has predicted that the transition between dry and wet rheology (or inertial and viscous rheology) below ϕ_c is continuous, and corresponds to a shift from particle contact to fluid dominated dissipation, hinting at a shift from Bagnoldian to Newtonian rheology at low shear rate and below ϕ_c as η_f of a density matched, fully wetted, dense suspension is increased (or as the shear rate is decreased). In suspensions above ϕ_c, experimental work has demonstrated that as the interstitial fluid viscosity is increased, the onset of a transition from arrested or quasistatic, rate-independent rheology to a flowing viscous regime is found to occur at decreasing shear rate (Huang et al., 2004), though a particle-scale explanation of this behaviour is missing. While these works make considerable progress in bridging understanding between wet and dry systems, a complete picture of the rheology across flow regimes at both bulk and microscopic scales is lacking.

In the present Chapter we shed light on the transitions between flow regimes with wet and dry characteristics above and below ϕ_c, across a broad range of shear rates and fluid viscosities. Below ϕ_c, we predict that the rheology is governed by the Stokes number $\mathrm{St} = \rho\dot{\gamma}d^2/\eta_f$. We expect viscous flow below $\mathrm{St} = 1$, that is quasi-Newtonian in the sense that the stress scales linearly with shear rate at fixed volume fraction. For $\mathrm{St} > 1$, particle inertia becomes important and the flow continuously shear thickens, exhibiting Bagnoldian (Bagnold, 1954) scaling of the shear stress. Such an inertial flow regime may be considered to be highly reminiscent of dry granular flow, therefore by varying the Stokes number below ϕ_c, we effectively explore the transition from wet, fluid dominated rheology to "dry", particle contact dominated Bagnoldian rheology. For volume fractions above ϕ_c, the material has a yield stress and exhibits a quasistatic regime for low and moderate shear rates. This behaviour is reminiscent of arrested

or jammed rheology, though our fixed rate approach and *slightly* deformable grains mean flow is possible in this regime, though very large shear stresses are required. When the inverse shear rate is small relative to the characteristic timescale for contact relaxation $d/\sqrt{k_n/(\rho d)}$, large overlaps can be sustained and the flow becomes less dependent on ϕ. The rheology in this regime has been observed experimentally, for soft particle suspensions, to be intermediate (shear-thinning) (Nordstrom et al., 2010a) or viscous (Huang et al., 2004), and we demonstrate that both behaviours can be predicted computationally, dependent on the values of η_f and the particle hardness k_n. The transitions between these flow regimes are shown to consistently correlate with the variation of the stress arising from hydrodynamic lubrication. Microscopic transitions in force and contact distributions and velocity correlation length are also linked to the flow regime transitions. Finally, a constitutive model is developed to capture the transitions between regimes for all shear rates and volume fractions, serving as a unifying description.

The following section details the methods for solving particle dynamics, simulating simple shear flow and calculating bulk stresses that form this basis of all the simulation work in this thesis. The bulk rheology and microstructural analyses are presented in Sections 2.3 and 2.4, respectively. A constitutive model for the stresses in all flow regimes is proposed in Section 2.5, followed by a summary and concluding remarks in Section 2.6.

2.2 Numerical models and simulation details

Discrete element method (Cundall and Strack, 1979) simulations are carried out using the particle simulation package LAMMPS (Plimpton, 1995), an open source package maintained and distributed by Sandia National Laboratories in New Mexico. The LAMMPS simulation framework has been extensively debugged and verified for over 10 years by a large community of academic users. The positions, velocities and forces of all particles are explicitly tracked over a period of time and are calculated in a step-wise, deterministic manner according to Newton's equations of motion. Specifically, the simulation algorithm provides a numerical solution to the second order differential equation:

$$m\frac{d^2x_i}{dt^2} = F_i, \tag{2.1}$$

to determine the position x_i of a particle of mass m subjected to total force F_i across a time period t. The total force F_i may include contributions from external forces such as gravity and from contact forces arising when particles approach and interact with

each other. The numerical solution is obtained using a time-stepping algorithm, where short time increments are solved consecutively, and particle trajectories are updated accordingly during each time step. In the present work, we adopt standard techniques for optimising particle-particle contact detection and we adopt the Velocity-Verlet algorithm for updating particle positions and velocities within each time step, implemented as described in the LAMMPS documentation (Plimpton). Standard techniques are employed for choosing the time step size (O'Sullivan and Bray, 2004) based on the material parameters described below. For each type of interaction described in this Chapter (i.e. particle-particle contact and particle-fluid hydrodynamic) it has been verified using the standard benchmarking techniques described by Chung (Chung and Ooi, 2011) that the numerical solution obtained from the simulation algorithm for simple two-particle collisions in various configurations is consistent with the force equations given below, all of which are included as standard contact force models in the open source LAMMPS distribution. Included in the Appendix are example LAMMPS input scripts that provide a minimal example of the simple shearing simulations performed in this work, which may be used with a standard downloaded LAMMPS distribution to reproduce the following results. In Chapter 3 we make quantitative comparisons of the suspension viscosity predicted by the present model with relevant experimental data, while in Chapter 4 we compare the time evolution of the viscosity predicted by the present simulations with relevant experimental results, and find excellent agreement in both cases.

In accordance with recent works in dense suspension flow (Trulsson et al., 2012; Seto et al., 2013), we argue that in dense (volume fraction $\phi > 0.45$) suspension flows, the major fluid contribution to the stress can be effectively captured by resolving the normal and tangential pair-wise lubrication force (Kim and Karrila, 1991; Ball and Melrose, 1997) between neighbouring particles i and j, with diameters d_i and d_j respectively, according to

$$\mathbf{F}_i^{l,n} = \frac{3\pi\eta_f d_{ij}^2}{2}\frac{1}{h}(\mathbf{v}_i - \mathbf{v}_j)\cdot\mathbf{n}_{ij}\mathbf{n}_{ij}, \tag{2.2a}$$

$$\mathbf{F}_i^{l,t} = \frac{4\pi\eta_f d_{ij}}{5}\left(1 + \frac{d_{ij}}{d_i+d_j} + \left(\frac{d_i-d_j}{d_i+d_j}\right)^2\right) \ln\left(\frac{d_i}{2h}\right)(\mathbf{v}_i - \mathbf{v}_j)\cdot(\mathbf{I} - \mathbf{n}_{ij}\mathbf{n}_{ij}), \tag{2.2b}$$

for fluid viscosity η_f, weighted average particle diameter $d_{ij} = \frac{d_i d_j}{d_i+d_j}$, surface-to-surface separation h, velocity vectors $\mathbf{v}_i$ and $\mathbf{v}_j$, center-to-center unit vector $\mathbf{n}_{ij}$ pointing from particle j to i and identity tensor $\mathbf{I}$. We assume that at sufficiently high volume

fraction, the fluid in the narrow gaps between particles can be treated as laminar (Lemaître et al., 2009). To limit computational expense and to mitigate the contact singularity of the lubrication force, $\mathbf{F}_i^{l,n}$ and $\mathbf{F}_i^{l,t}$ are calculated for $0.001d_{ij} < h < 0.05d_{ij}$. It has been verified that an outer cut-off of $0.1d_{ij}$ does not give significantly different results. We appeal to surface roughness to justify our choice of the inner cut-off. At smaller separations, we evaluate the forces assuming $h = 0.001d_{ij}$. We find that the numerical value of the minimal h does effect the transient rheology predicted by the present model, though it does not effect the steady state rheology (demonstrated later, in Chapter 4). For homogeneous, simple shear flow in a 3-dimensionally periodic domain, described later, we find that the dissipation arising due to lubrication dominates significantly over that arising from other fluid forces, such as Stokes drag and the Archimedes force described by (Trulsson et al., 2012), so we omit other such forces from this study. Furthermore, we neglect fluid inertia from the model, assuming that (as demonstrated by (Trulsson et al., 2012)) particle interactions will dominate the dissipation for inertial flows.

In addition to the lubrication force, particles i and j interact at contact ($h < 0$) through a repulsive force, with normal and tangential components given by a linear spring-dashpot model for stiffness constants k_n and k_t, center-to-center displacement δ_{ij} and elastic shear displacement $\mathbf{u}_{ij}^t$

$$\mathbf{F}_{ij}^{c,n} = k_n \delta_{ij} \mathbf{n}_{ij}, \tag{2.3a}$$

$$\mathbf{F}_{ij}^{c,t} = -k_t \mathbf{u}_{ij}^t. \tag{2.3b}$$

A Coulomb friction coefficient μ_p is defined such that the tangential force on each particle is limited to $|\mathbf{F}^{c,t}{}_{ij}| \leq \mu_p |\mathbf{F}^{c,n}{}_{ij}|$. Energy is dissipated in the system by the lubrication forces. These forces damp out the relative velocities of approaching particles, and therefore extract kinetic energy from the system. The damping arising from the lubrication force term is sufficient to match the energy input by the driving shear flow, so further damping in the mechanical contact model (a common feature of *dry* granular material simulations) is omitted for simplicity. The particle friction coefficient is fixed at $\mu_p = 1$, which affects the critical volume fraction as discussed later. Variation of other particle parameters does not change the results presented in this chapter. The solid and fluid phases are density matched, meaning gravitational forces on the particles can be omitted.

Fluid inertia is neglected from the model for simplicity. Simulation results by Trulsson (Trulsson et al., 2012) suggest that the dissipation through particle contacts considerably outweighs that due to fluid effects in the inertial regime. In addition,

the scaling laws predicted by our simulation presented below are consistent with observations from comparable experiments (Fall et al., 2010; Bagnold, 1954) in the regime where particle and fluid inertia are likely to be coexisting, further suggesting the dominance of the particle contribution to the stress. Notably, the quadratic scaling in the inertial regime in experiments and the present simulations is also consistent with dry granular $\mu(I)$-rheology (Forterre and Pouliquen, 2008), further strengthening the argument for dominance of contacts in this regime. Future work that delineates the stress contributions from particle inertia and fluid inertia would be an extremely valuable supplement to the present results.

To achieve homogeneous simple shear flow, an assembly of spheres in a 3 dimensional periodic domain is deformed at a constant shear rate $\dot{\gamma}$. Bidispersity at a diameter ratio of 1:1.4 and volume ratio of about 1:1 is used to minimise crystallisation during flow (Ikeda et al., 2012) (and references therein). A sample assembly under shear is shown in Figure 2.1, in front and oblique projections. The particles are coloured into bands in the flow (x) direction according to their initial positions as shown in (a) and move to new positions at a later time $t = t_1$ shown in (b), conforming to the simple shear velocity profile. At a shear strain of 0.5, the deformed assembly of particles is mapped to a symmetric position with a strain of -0.5. This deformation pattern is repeated ad infinitum to reach a steady state. In practice, we find that a strain magnitude of 1 to 10 is sufficient to reach steady flow, dependent on the shear rate. Simulations at different shear rates have been performed for a range of fixed volume fractions ϕ (spanning the jamming transition) and fluid viscosities to probe the bulk rheology and microstructures. It is determined that an assembly of approximately 2000 bidisperse spheres is sufficiently large to capture the bulk rheology independently of the domain size. A larger domain is required in order to capture microstructural phenomena including correlation lengths within the material, and therefore assemblies of approximately 30,000 bidisperse spheres are used for the work presented in Section 2.4.

The bulk stress is calculated from the particle force and velocity data. It is decomposed into contributions due to the hydrodynamic interaction, the particle-particle interaction and the velocity fluctuation, given by Eqs. 2.4a, 2.4b and 2.4c, respectively,

$$\boldsymbol{\sigma}^F = \frac{1}{V}\sum_i \sum_{i\neq j} \mathbf{r}_{ij}\mathbf{F}^l_{ij}, \tag{2.4a}$$

$$\boldsymbol{\sigma}^C = \frac{1}{V}\sum_i \sum_{i\neq j} \mathbf{r}_{ij}\mathbf{F}^c_{ij}, \tag{2.4b}$$

$$\boldsymbol{\sigma}^V = \frac{1}{V}\sum_i m_i \mathbf{v}'_i \mathbf{v}'_i, \tag{2.4c}$$

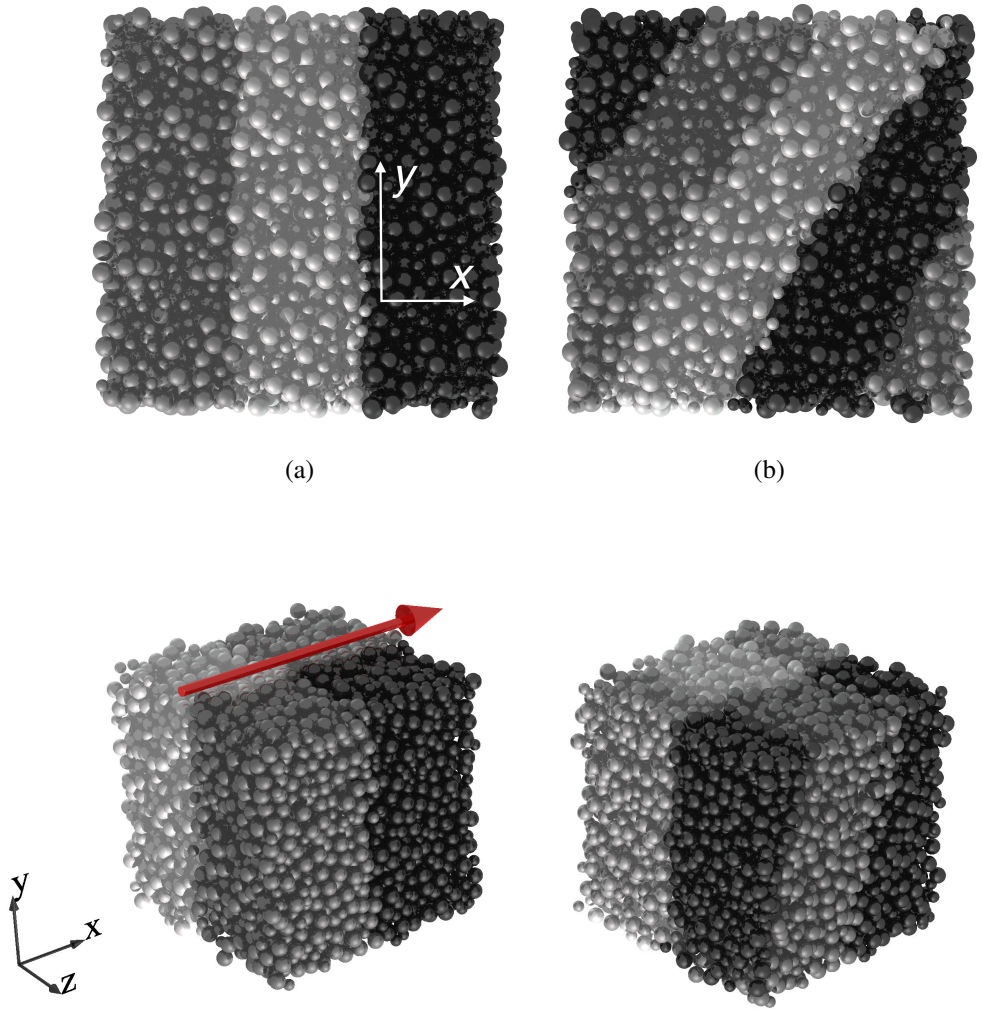

Fig. 2.1 Snapshot of a particle assembly under steady shear at some time $t = 0$ (a) and a later time $t = t_1$ (b), with a viewpoint normal to the x-y-plane where x is the flow direction and y is the velocity gradient direction. The shadings are used to illustrate the deformation being applied to the assembly. (c) The same deformation illustrated in 3d.

where $\mathbf{v}_i'$ is the particle velocity after the mean streaming velocity has been subtracted. Data from 20 realisations with randomised initial particle positions are used to obtain ensemble-averaged stresses, which are further averaged over time in the steady-state, as presented in the next section. Under simple shear flow, the relevant stresses that will be discussed are the xy components from each contribution i, σ_{xy}^i, and the mean normal stress (i.e. the pressure) from each contribution $\mathrm{P}^i = \frac{1}{3}(\sigma_{xx}^i + \sigma_{yy}^i + \sigma_{zz}^i)$. The bulk shear and normal stresses, σ_{xy} and P, can be obtained by summing the contributions σ_{xy}^i and P^i respectively (Gallier et al., 2014). We note that σ_{xy}^V is typically significantly smaller than the other contributions.

2.3 Bulk rheology

In addition to the solids volume fraction ϕ, our system is governed by 5 parameters: characteristic particle diameter d, density ρ, particle stiffness k_n, fluid viscosity η_f and shear rate $\dot{\gamma}$. From these parameters, we construct two key dimensionless numbers, $\hat{\dot{\gamma}} = \dot{\gamma} d_{ij}/\sqrt{k_n/\rho d_{ij}}$ and $\mathrm{St} = \rho \dot{\gamma} d_{ij}^2/\eta_f$. Together, these two dimensionless numbers and the volume fraction control the full rheology of the suspension.

In the absence of fluid, the shearing timescale, set by $1/\dot{\gamma}$, competes only with the relaxation time of interparticle contacts, associated with k_n, so the full rheology of the material at a given volume fraction can be explored by varying the relation between these two, using $\hat{\dot{\gamma}} = \dot{\gamma} d_{ij}/\sqrt{k_n/\rho d_{ij}}$ (Campbell, 2002; Chialvo et al., 2012), where $\hat{\dot{\gamma}}$ quantifies the departure from hard sphere rheology. The resulting shear stress can be similarly scaled according to $\hat{\sigma}_{xy} = \sigma_{xy} d_{ij}/k_n$. Such a scaling will be shown to be important to the present simulations at high shear rates (where $\hat{\dot{\gamma}} > 10^{-2}$) where particle deformations become appreciable relative to the applied flow. The fluid gives a further relevant timescale, namely a dissipative one associated with the fluid viscosity η_f, which can be related to the shearing timescale by the Stokes number $\mathrm{St} = \rho \dot{\gamma} d_{ij}^2/\eta_f$. In this case, the shear stress can be appropriately scaled with the viscous stress to give a relative suspension viscosity $\eta_s = \sigma_{xy}/\dot{\gamma}\eta_f$. A further material parameter, given by $\hat{\eta}_f = \eta_f/\sqrt{k_n \rho d_{ij}}$, is defined for convenience, to characterise the separation of the viscous dissipation and contact relaxation timescales. The role of this parameter will be demonstrated. The flow curves obtained from simple shear flow simulations are presented in terms of the k_n and η_f scalings, in Figs 2.2a and 2.2b respectively. A summary of the dimensionless parameters used in the following discussion is given in Table 2.1.

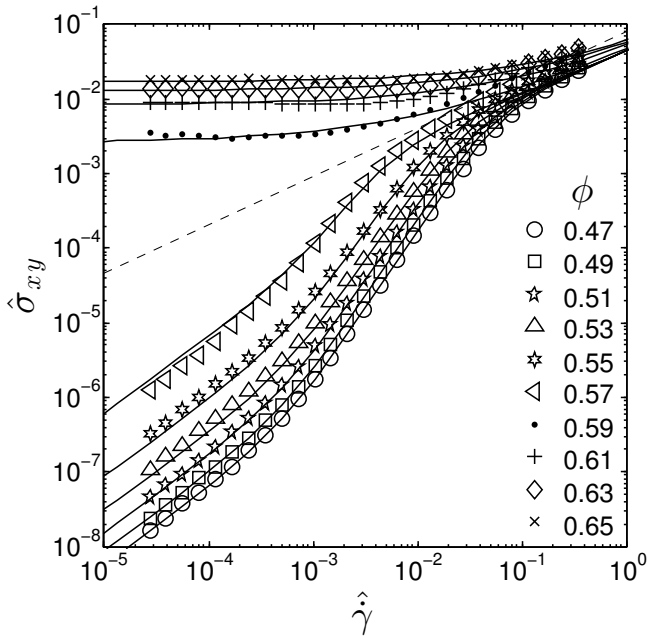

(a)

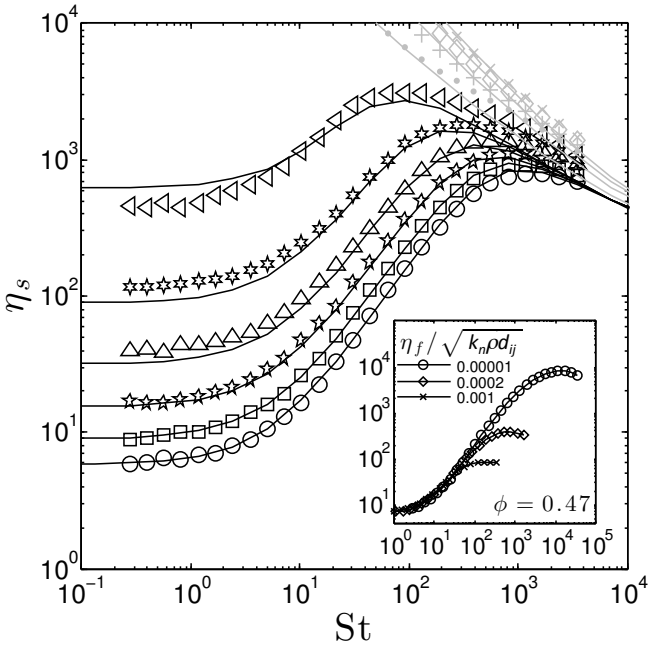

(b)

Fig. 2.2 Flow regime maps for sheared suspension with $\hat{\eta}_f = 2.15 \times 10^{-3}$, at volume fractions given by legend. (a) Scaled shear stress versus scaled shear rate. Dotted line indicates the critical flow behaviour, distinguishing rheology below and above the critical volume fraction ϕ_c; (b) Relative suspension viscosity versus Stokes number; Inset: varying $\hat{\eta}_f$ at $\phi = 0.47$, with St and η_s axes. Symbols represent DEM simulation results, solid lines are predictions from the constitutive model proposed in Section 2.5.

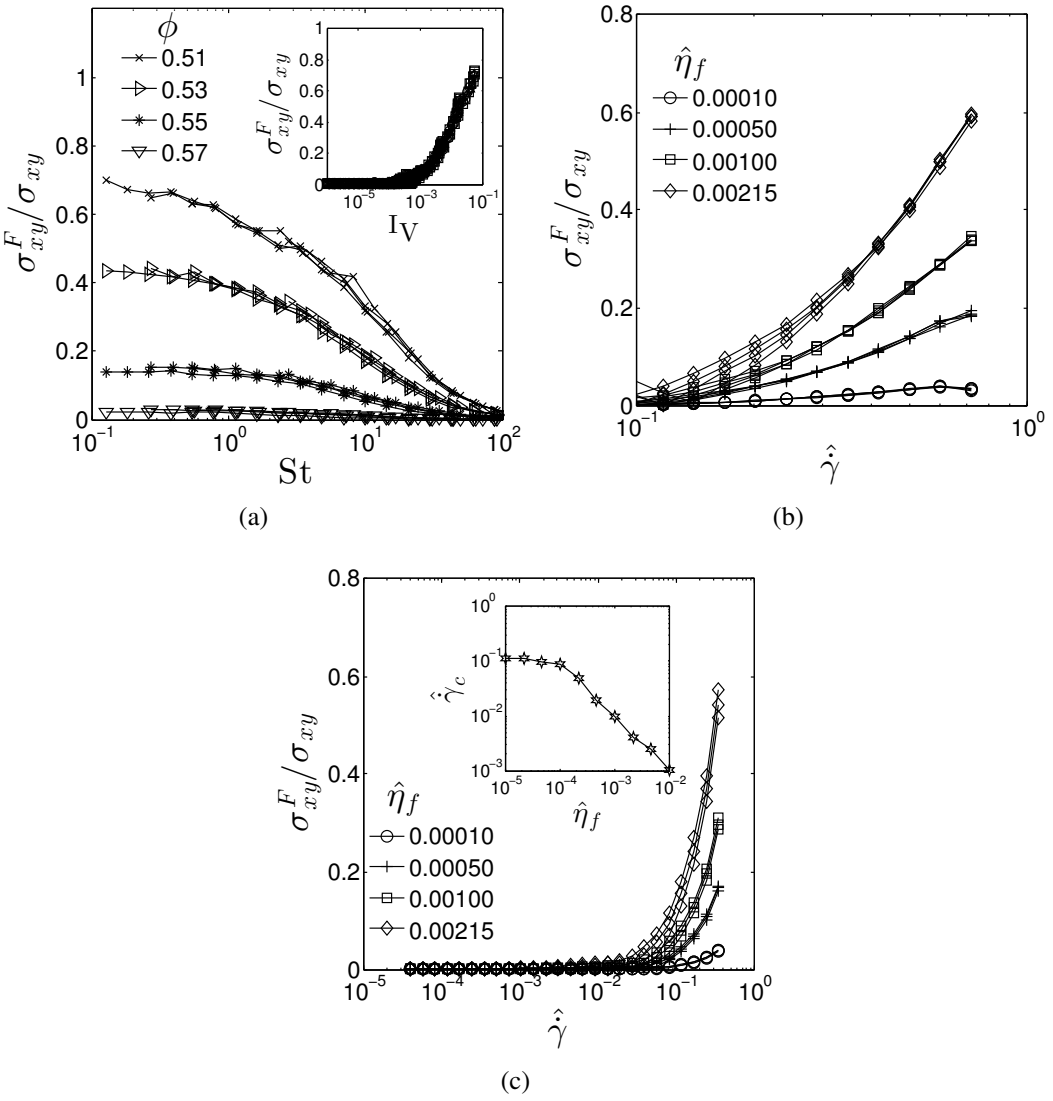

Fig. 2.3 The varying contribution of fluid stress σ^F_{xy} to the total suspension stress σ_{xy}. (a) The viscous-to-inertial transition corresponds to diminishing stress contributions from σ^F_{xy}, which collapse with St to ϕ-dependent branches. Different sets of data correspond to varying $\hat{\eta}_f$; Inset: all the data collapse as a function of I_V; (b) The inertial-to-soft particle transition corresponds to a re-emergence of σ^F_{xy} contributions, which collapse with $\hat{\dot{\gamma}}$, to $\hat{\eta}_f$ dependent (and ϕ-independent) branches. Different sets of data correspond to varying volume fraction below ϕ_c. (c) The quasistatic-to-rate-dependent transition similarly corresponds to a changing stress contribution that collapses with $\hat{\dot{\gamma}}$. Different sets of data correspond to varying volume fraction above ϕ_c; Inset: critical shear rate for the transition out of the quasistatic state.

Dimensionless parameter	Definition	Description
Reduced shear rate	$\hat{\dot{\gamma}} = \dot{\gamma} d_{ij} / \sqrt{k_n / \rho d_{ij}}$	Shear rate rescaled with particle stiffness
Stokes number	$\mathrm{St} = \rho \dot{\gamma} d_{ij}^2 / \eta_f$	Shear rate rescaled with fluid viscosity
Volume fraction	$\phi = \frac{V_{\text{particles}}}{V_{\text{particles}} + V_{\text{fluid}}}$	The fraction of the total volume occupied by solid particles
Scaled fluid viscosity	$\hat{\eta}_f = \eta_f / \sqrt{k_n \rho d_{ij}}$	A material parameter equivalent to $\mathrm{St}/\hat{\dot{\gamma}}$, controlling the separation between the viscous and soft-particle regimes
Scaled repulsive force	$\frac{3}{2} \pi \eta_f d^2 / F^{CL}$	Rescaled force required to initiate friction in the Critical Load Model, relevant to Chapter 3
Péclet number	$\mathrm{Pe} = 3\pi \eta_f \dot{\gamma} d^3 / 4kT$	Relative importance of convective streaming flow versus thermal diffusive flow, , relevant to Chapter 3

Table 2.1 The key dimensionless parameters used to describe the rheological results. The Reduced shear rate, Stokes number and Volume fraction completely govern the flow behaviour in this Chapter, while the Scaled fluid viscosity is defined for convenience when discussing the implications of the model predictions. The Scaled repulsive force and Péclet number are not relevant to this Chapter, and will be discussed further in Chapter 3.

The critical volume fraction ϕ_c is identified from Figure 2.2a as being between 0.57 and 0.59. We first consider the rheology below ϕ_c. A quasi-Newtonian regime, in which the suspension viscosity is independent of shear rate (but strongly dependent on ϕ), emerges at $\mathrm{St} < 1$. This regime, in which $\hat{\sigma}_{xy} \propto \hat{\dot{\gamma}}$, has been observed experimentally for wet granular materials (Bagnold, 1954; Petekidis et al., 2003; Coussot, 1995; Fall et al., 2010). As the shear rate is increased, the flow behaviour transitions from quasi-Newtonian to continuously shear thickening at a Stokes number of approximately 1. The $\mathrm{St} > 1$ regime, best illustrated for the range $10 < \mathrm{St} < 100$ in Figure 2.2b, is reminiscent of inertial Bagnoldian flow associated with dry granular materials, where $\hat{\sigma}_{xy} \propto \hat{\dot{\gamma}}^2$. The rheology is described as continuously shear thickening in the inertial regime, in the sense that η_s scales linearly with $\dot{\gamma}$.

The Newtonian-to-Bagnoldian (i.e. viscous-to-inertial) transition below ϕ_c is correlated with the decreasing magnitude of σ_{xy}^F relative to σ_{xy} as the Stokes number is increased (Lemaître et al., 2009) and particle inertia becomes important, as demonstrated in Figure 2.3a. The contribution from σ_{xy}^F is roughly independent of shear rate below $\mathrm{St} = 1$, but steadily drops off for $\mathrm{St} > 1$, indicating that the fluid plays a diminishing role in the suspension rheology as the particle inertia is increased. It is found that the behaviour of $\sigma_{xy}^F/\sigma_{xy}$ for varying values of material parameter $\hat{\eta}_f$ can be collapsed to volume fraction dependent branches when plotted with the Stokes number, demonstrating our previous assertion that the rheology in the viscous-to-inertial transition is governed only by the Stokes number (and the volume fraction). This result can be generalized for all ϕ, $\dot{\gamma}$ and η_f using the viscous number $\mathrm{I_V}$, as shown in the Inset of Figure 2.3a. Above some critical viscous number, the stress arising from fluid effects becomes significant. A similar result was suggested by Huang et al. (Huang et al., 2004), although they use the Leighton number ($\mathrm{Le} = \eta_f \dot{\gamma}/\sigma_{xy}$) rather than the viscous number.

This viscous-to-inertial transition can also be reconciled at the microscopic level by examining the relative magnitude of $\mathbf{F}_{ij}^l$ and $\mathbf{F}_{ij}^c$ for interacting pairs, and by appealing to the Sommerfield number associated with lubrication theory $s = \eta_f v/d\sigma_{xy}$, where v represents some relative velocity between the particle surfaces, dependent on the bulk shear rate (Fernandez et al., 2013). The general argument for viscous flow between approaching surfaces predicts that the force required to bring particles together diverges with the inverse of the gap size. For ideally smooth surfaces, this lubrication divergence may be expected to hold true until the gap size approaches the molecular dimension. For all other materials, however, there will be some asperity lengthscale larger than the molecular dimension, on which the lubrication force may break down and particle surfaces may touch, so the interaction switches from being lubrication controlled to surface contact or boundary controlled. Classical tribology uses the Sommerfeld number to distinguish between these limits. In the present work, we use a minimum cut off $h = 0.001 d_{ij}$ for the lubrication force, implying that the particles have asperities on their surfaces with height of order 0.1% of the particle diameter. Below a critical s, the lubrication films between particles rupture and mechanical contacts are initiated, at which point the stress response becomes contact-dominated rather than fluid-dominated. The critical Stokes number of 1 for the onset of the viscous-to-inertial transition relates to a critical Sommerfield number at which lubrication films begin to break down, leading to the reduction of the σ_{xy}^F magnitude.

As the shear rate is increased further ($\hat{\dot{\gamma}} > 10^{-2}$ and $\mathrm{St} > 100$ in Figs 2.2a and b respectively), the flow exits the continuously shear thickening inertial regime, and a soft

particle rheology is realised. The nature and location of this high shear rate asymptotic flow behaviour, in which the dependence on ϕ becomes small, is highly dependent on the material parameter $\hat{\eta}_f$. As discussed previously, the viscous-to-inertial transition occurs around $\mathrm{St} = 1$, and we assert here that the transition to high shear rate, soft particle rheology occurs as $\hat{\dot{\gamma}} > 10^{-2}$. The material parameter $\hat{\eta}_f$ sets the separation between the two dimensional shear rates $\dot{\gamma}$ associated with the St and $\hat{\dot{\gamma}}$ limits, effectively determining the range of shear rates over which inertial flow can be observed. For example, a suspension of very hard particles, for which $k_n \to \infty$ and $\hat{\eta}_f \to 0$, may transition between viscous and inertial flow regimes at experimentally accessible shear rates, while it would be impossible to access their "soft particle" rheology as $\hat{\dot{\gamma}} > 10^{-2}$, which would correspond to $\mathrm{St} \to \infty$. Conversely, for soft particles, $\mathrm{St} = 1$ may occur very close to $\hat{\dot{\gamma}} = 1$. Our data therefore explore the crossover from hard sphere rheology at low $\hat{\eta}_f$ in the vicinity of $\mathrm{St} = 1$ to soft sphere rheology at high $\hat{\eta}_f$ as the condition of $\mathrm{St} = 1$ approaches that of $\hat{\dot{\gamma}} = 1$. The role of $\hat{\eta}_f$ is demonstrated in the Inset of Figure 2.2b, which illustrates that inertial flow is observed over a wider range of St as $\hat{\eta}_f \to 0$.

Interestingly, the rheology (not just the location) of the soft particle limit is dependent on the value of $\hat{\eta}_f$. In the low $\hat{\eta}_f$ limit ($\hat{\eta}_f = 5 \times 10^{-5}$ data shown in Inset of Figure 2.2b), shear thinning, "intermediate" (Chialvo et al., 2012), rheology is observed as $\hat{\dot{\gamma}} > 10^{-2}$, with $\hat{\sigma}_{xy} \propto \hat{\dot{\gamma}}^{0.5}$, consistent with previous experiments in soft, highly deformable particles (Nordstrom et al., 2010a). The origin of this shear thinning scaling exponent is still uncertain, though it may relate to the large particle deformations that occur at such high shear rates. A switch back to viscous, Newtonian scaling is observed at $\hat{\dot{\gamma}} \to 1$ for high $\hat{\eta}_f$ as demonstrated in the Inset of Figure 2.2b by a shift back to rate-independent suspension viscosity for $\hat{\eta}_f = 1 \times 10^{-3}$. As with the Newtonian-to-Bagnoldian transition around $\mathrm{St} = 1$, the transition between intermediate and viscous soft particle rheology as $\hat{\dot{\gamma}} > 10^{-2}$ can be correlated with an increase in the magnitude of σ_{xy}^F relative to σ_{xy} as $\hat{\eta}_f$ is increased, Figure 2.3b. Notably, these data now collapse for different volume fractions onto $\hat{\eta}_f$ dependent branches, when plotted with $\hat{\dot{\gamma}}$, demonstrating the loss of ϕ dependence and contrasting with the St collapse observed for the viscous-to-inertial transition.

Above ϕ_c, a contact dominated, quasistatic ($\hat{\sigma}_{xy} \propto \hat{\dot{\gamma}}^0$) regime exists for $\hat{\dot{\gamma}} \ll 1$ as demonstrated in Figure 2.2a. Although the quasistatic regime is inherently a "soft" particle phenomena, in the sense that flow above ϕ_c without ordered localisation is not possible for ideally hard particles, it is not characterised by large particle deformations and volume fraction independence, except perhaps for $\phi \gg \phi_c$. As $\hat{\dot{\gamma}}$ approaches 1, however, the flow transitions to a rate-dependent, soft particle state, coinciding with that of the $\phi < \phi_c$ case, and consistent with an experimentally observed quasistatic-

to-viscous transition observed for suspensions of soft polystyrene beads (Huang et al., 2004). As with the transitions below ϕ_c, the transition out of the quasistatic regime can be well correlated with the emerging dominance of the fluid contribution relative to the contact contribution to the stress, Figure 2.3c. In all cases, the stress in the rate-independent, quasistatic regime (where $\hat{\dot{\gamma}} \ll 1$) is contact dominated, so $\sigma_{xy}^F/\sigma_{xy} \to 0$. As $\hat{\dot{\gamma}} > 10^{-2}$, and the rheology becomes rate dependent, the fluid contribution becomes significant.

The nature of the rate-dependent regime depends strongly on $\hat{\eta}_f$, as with the $\phi < \phi_c$ case. We define a critical shear rate $\hat{\dot{\gamma}}_c$ at the point where the fluid contribution begins to increase, corresponding to the quasistatic-to-rate-dependent transition. Consistent with recent experimental findings (Huang et al., 2004), the critical shear rate is found to be a linearly decreasing function of $\hat{\eta}_f$, for sufficiently high $\hat{\eta}_f$, Inset of Figure 2.3c. We extend the study to lower fluid viscosities, however, and find that at low $\hat{\eta}_f$, a plateau is observed. This plateau indicates that below a certain critical $\hat{\eta}_{fc}$ (of the order 10^{-4} from the Inset of Figure 2.3) the flow is never $\hat{\eta}_f$-dependent, providing a critical value of the material parameter to distinguish between intermediate $\hat{\sigma}_{xy} \propto \hat{\dot{\gamma}}^{0.5}$ ($\hat{\eta}_f < \hat{\eta}_{fc}$) and viscous $\hat{\sigma}_{xy} \propto \hat{\dot{\gamma}}$ ($\hat{\eta}_f > \hat{\eta}_{fc}$) rheology in the soft particle limit.

As a summary, we observe regime transitions between viscous, inertial, quasistatic, intermediate and "soft" viscous shear flow as the timescales for viscous dissipation (St) and particle contact relaxation ($\hat{\dot{\gamma}}$) are varied. The mechanism for such transitions can be ascribed to the variation of the relative importance of the fluid and contact stress contributions. The bulk flow can therefore be effectively described by considering a background dry granular rheology, governed by the $\hat{\dot{\gamma}}$ scaling, superimposed with a viscous stress, governed by the St scaling. Such a constitutive model will be presented in Section 2.5 after we further examine the microstructure of the flow in the next section.

2.4 Microstructure

Particle level dynamics and structures are studied in order to shed light on the microscale phenomena responsible for the bulk rheology in each flow regime.

The distributions of pairwise particle forces (defined in Equations 2.2 and 2.3) are plotted in Figures 2.4a-e for each of the flow regimes identified previously, illustrating the radial directions (in the *xy* (flow-gradient)-plane) and relative magnitudes of the lubrication and particle contact forces.

In the inertial regime (Figure 2.4a), there is a clear alignment of forces along the direction of compression, as expected for a collisional flow (Da Cruz et al., 2005), demonstrating that forces are transmitted through the material along a principal axis

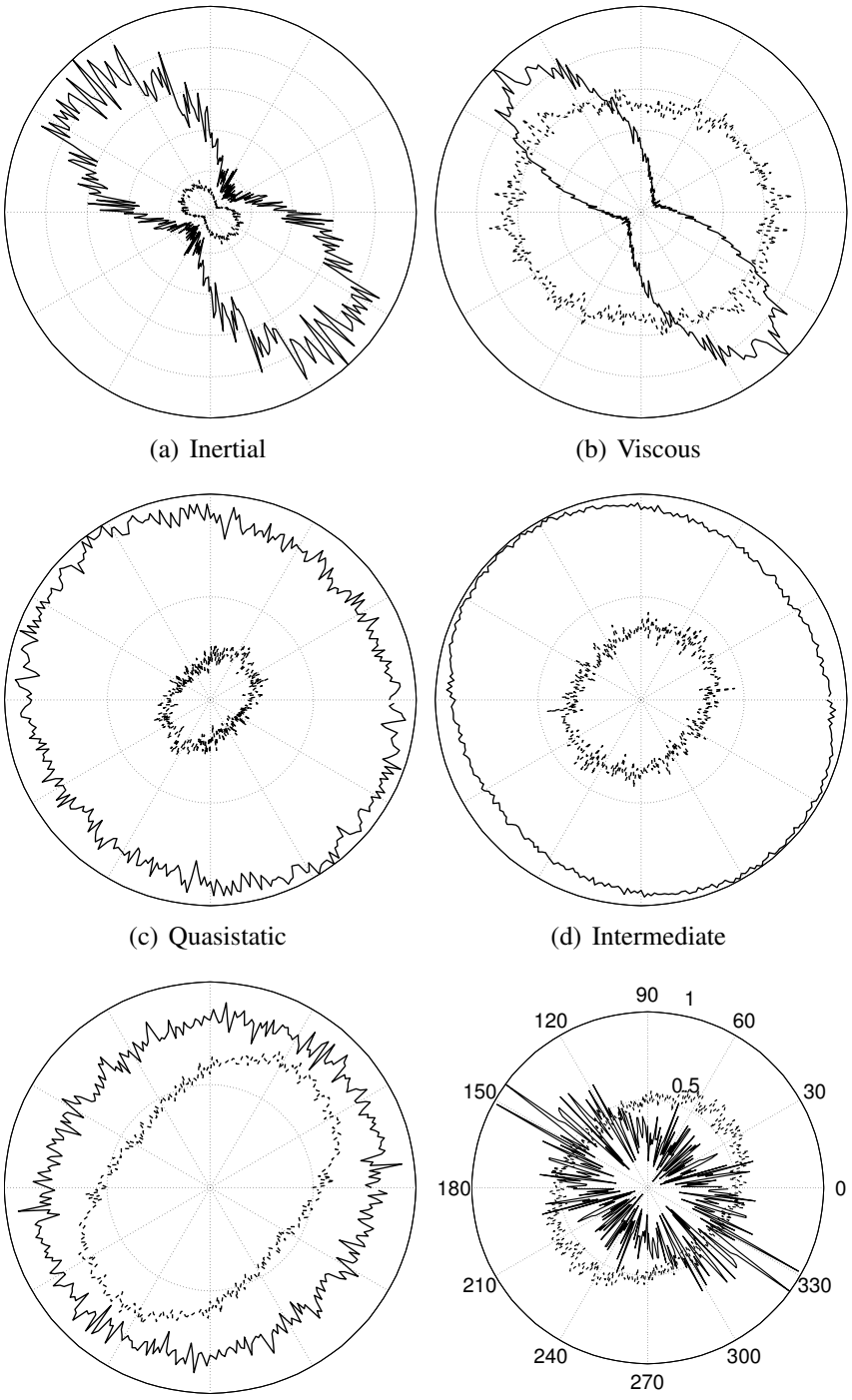

(a) Inertial (b) Viscous

(c) Quasistatic (d) Intermediate

(e) Soft viscous (f) Velocities

Fig. 2.4 (a) - (e) Flow-gradient plane radial force distributions for contact (solid line) and lubrication (dashed line) forces, for each of the flow regimes described in Section 2.3. The statistics include all particle pairs over all time steps in steady state and the forces are scaled in magnitude by the respective maximal values. (f) Radial distribution of the relative velocity between interacting particles for $\phi = 0.5$ (solid line) and $\phi = 0.65$ (dashed line).

opposing the shear flow. The contact forces dominate over the lubrication forces, consistent with observations of the bulk contact stress dominance in this regime. As the Stokes number is reduced and the role of the lubrication stress becomes dominant, the force directions are somewhat different. In the viscous regime (Figure 2.4b), the magnitude of the lubrication forces becomes comparable to that of the contacts and their orientation becomes significantly more isotropic. This suggests that the viscous lubrication films are arresting much of the rapid, inertial particle motion by suspending the particles in a more uniform, isotropic and interconnected fluid film network. Isolating the particle contact forces, we find that the contact network retains its strong alignment even though the resulting observed rheology is dominated by the stress coming from lubrication forces. In the quasistatic regime (Figure 2.4c), the contact forces become significantly more isotropic. This is attributed to the jammed state being a more interconnected network, where forces are transmitted not via collisions along a shearing direction, but through persistent contacts that compose mesoscale chains and clusters. While the contact forces appear to be completely isotropic, or perhaps aligned very slightly in the compressive axis, there is a small alignment of the lubrication force along the extensional axis, indicating that the lubrication forces are acting in an opposing direction to the contact forces. It is noted that the contact forces are significantly greater that the lubrication forces in this regime, consistent with the observations from bulk stresses that quasistatic rheology is dominated by particle contacts. The radial forces in the intermediate regime (Figure 2.4d) are consistent with those for quasistatic flow, though the role of the lubrication force becomes slightly greater, in agreement with the bulk stress contributions presented in Figure 2.3c for increasing $\hat{\dot{\gamma}}$ at low $\hat{\eta}_f$. In the soft viscous regime (Figure 2.4e), the dominance of the lubrication force increases further, again consistent with Figure 2.3c for increasing $\hat{\eta}_f$. It is also observed that the contact forces become aligned along the extensional direction, i.e. with the direction of shear, in this regime, similar to the lubrication forces.

It is further found, independently of Stokes number, that the relative velocities of interacting particles (through both lubrication and mechanical contact) are generally aligned along the compressional axis for $\phi < \phi_c$, as shown by the solid line in Figure 2.4f. The relative velocities are calculated by first subtracting the mean streaming velocity from all particles, then determining the relative magnitude and direction of the velocities between neighbouring particles (i.e. $\mathbf{v}_{\text{rel}} = \mathbf{v}'_i - \mathbf{v}'_j$). For $\phi > \phi_c$, however, a significant number of relative particle velocity vectors now align with the extensional axis (dashed line in Figure 2.4f), the opposite to what was observed for $\phi < \phi_c$. For the quasistatic and intermediate regimes, this results in the changing alignment of the lubrication forces, but since the contact forces are dominant, there is no change in alignment of

the net force. For the soft viscous regime, however, the velocity-dependent lubrication force $\mathbf{F}_{ij}^{l}$ becomes significant, and a change in both the contact and lubrication force orientations is observed.

A great wealth of information regarding the dynamics of suspension flow may be obtained from such radial plots, for example the relationships between force orientation and bulk stresses considering both compressive and tensile stresses and the precise role of the interstitial fluid, however we limit the present work to correlating the above microscopic signatures with the observed bulk rheological regimes.

To corroborate the above observations of the transitions in the microscopic dynamics, a fabric tensor characterising the contact network microstructure (Sun and Sundaresan, 2011) is constructed for each particle assembly according to

$$\mathbf{A} = \frac{1}{\mathrm{N}_c} \sum_{\alpha=1}^{\mathrm{N}_c} \mathbf{n}_\alpha \mathbf{n}_\alpha - \frac{1}{3}\mathbf{I}, \tag{2.5}$$

where N_c is the number of pairwise contacts (that have unit vector $\mathbf{n}_\alpha$) and $\mathbf{I}$ is the identity tensor. Two variants of the fabric tensor are computed. In the first, we sum over all particles that are in mechanical contact ($h < 0$), while in the second we sum over all particles that are separated by a lubrication film (those particles that are separated by a fluid layer of thickness h, where $0 < h \leq 0.05 d_{ij}$), giving two separate quantifications of the microstructure, pertaining to contact and lubrication forces respectively. The extent of the structural anisotropy can be quantified using the xy-component of the fabric tensor, A_{12}. Alignments that oppose the shear flow of the material are negative in A_{12}, while completely isotropic force networks will give $\mathrm{A}_{12} = 0$. The variation of A_{12} across volume fractions at $\mathrm{St} = 10$ and $\mathrm{St} = 0.1$ is given in Figures 2.5a and b, respectively.

At $\phi < \phi_c$ and $\mathrm{St} = 10$ (Figure 2.5a), A_{12} is negative for both the contact and lubrication network, in agreement with the significant alignment of both forces shown in the radial force plot in Figure 2.4a. As ϕ is increased above ϕ_c, A_{12} for the contact network tends to nearly zero (approximately -0.04, consistent with previous work in dry, quasistatic shear flows (Sun and Sundaresan, 2011)), while the lubrication network becomes aligned in the opposite direction. The net effect of this transition is a shift from strongly aligned to almost isotropic net force distribution (Figures 2.4a and 2.4c), since the opposite alignment occurring in the lubrication network has only a minor contribution to the total force in the quasistatic regime. At $\mathrm{St} = 0.1$ (Figure 2.5b), the same behaviour is observed in the contact network across ϕ_c, consistent with the radial contact force plots in Figure 2.4a and b. The fabric of the lubrication network

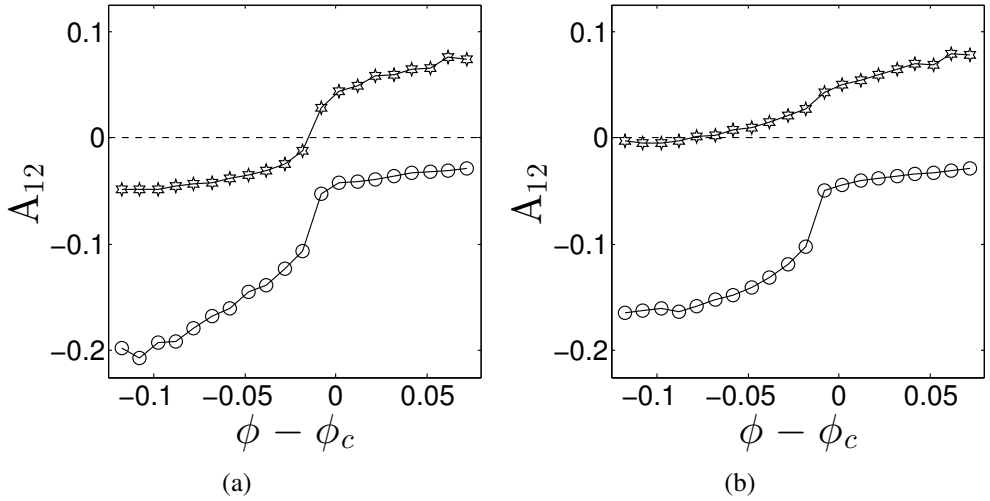

Fig. 2.5 Shear component of the fabric tensor A_{12} plotted against volume fraction at (a) $St = 10$ and (b) $St = 0.1$. Open circles show the contact network; stars show the fluid lubrication network.

is, however, different. Below ϕ_c, the lubrication fabric tends to zero in this case, corresponding to the isotropic state of the lubrication contacts presented in Figure 2.4b.

Above ϕ_c, the behaviour of the fabric appears to be independent of the Stokes number. The contact network tends towards a nearly isotropic state, while the anisotropy of the lubrication network increases in the extensional direction. This anisotropy, together with the relative velocities in the same direction, results in the lubrication force alignment along the extensional axis, which becomes dominant in the soft viscous regime.

The collective motion is further quantified by the velocity correlation length (Lois et al., 2007; Sun et al., 2006), defined according to

$$c(r) = \frac{\sum_i \sum_{j>i} \overline{\mathbf{v}}_i \cdot \overline{\mathbf{v}}_j \delta(r_{ij} - r)}{\sum_i \sum_{j>i} \delta(r_{ij} - r)}, \tag{2.6}$$

where r_{ij} is the center-to-center vector for particles i and j and $\overline{\mathbf{v}}_i$, $\overline{\mathbf{v}}_j$ are particle velocity vectors averaged over a length of time sufficient to give an averaged particle displacement due to the mean flow of approximately $0.5d$. From this expression we can quantify the extent to which the velocity of a particle is correlated with the velocities of its neighbouring particles, on average. It is found that the correlation decays approximately exponentially with the distance r (Figure 2.6a, Inset). We fit the data to an exponential function $C(r) = ke^{-r/\xi}$, characterising the correlation length according to the value of ξ (Lois et al., 2007). The dependence of this correlation length on volume fraction and Stokes number is given in Figures 2.6a and 2.6b, respectively. The correlation length increases with volume fraction, suggesting that as more particles

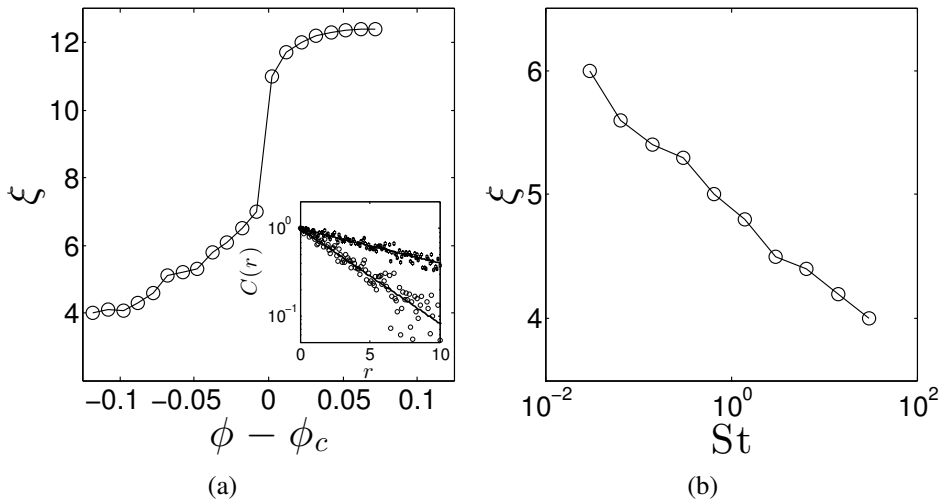

Fig. 2.6 (a) Velocity correlation length ξ at St $= 10$ as a function of volume fraction and (b) as a function of St at $\phi = 0.50$.

are added, and as gaps between particles reduce in size, there is increasing collective motion in the material. At ϕ_c there is a large jump in ξ to about half the domain length, indicating that the correlation extends across the whole domain as the material enters a quasistatic state. The forming of collectively moving clusters of particles is consistent with the radial force plots obtained above ϕ_c. Below ϕ_c, correlation lengths are short and forces are dominated by collisions along the compressive axis. Above ϕ_c, the forces are more uniformly distributed radially, as the particles move more as collective clusters.

As the Stokes number is increased, the longer range forces arising from lubrication effects become decreasingly dominant, particle inertia plays a greater role, and the correlation length decreases accordingly (Figure 2.6b). Again, this is consistent with the observed radial force distributions. As the Stokes number decreases, the particles become suspended in an increasingly strong network of lubrication films, which retard the inertial, collisional behaviour, leading to increased correlation lengths and more isotropic force distributions.

The microstructural details discussed above explain well the mechanisms underlying the transitions in the bulk rheology. When particle collisions dominate, the forces and fabric are anisotropic at the microscale and velocities are correlated over very short lengths. Such dynamics, characteristic of a collisional regime, give rise to the inertial bulk rheological response observed for $\phi < \phi_c$ at St > 1 (and away from $\hat{\dot{\gamma}} = 1$). As the Stokes number is decreased, and the fluid increasingly governs the net particle level forces, the lubrication fabric tends to be more isotropic than the contact fabric and the correlation length is increased as particles interact through increasingly strong networks of lubrication films. These conditions move the rheology away from inertial,

collisional flow to a viscous flow regime, where the bulk stress is dominated by the fluid contribution. Above ϕ_c there is a jump in the correlation length, combined with a move to a more isotropic microstructure, suggesting the presence of sustained force networks as opposed to collisional rheology. These networks dominate the behaviour in the quasistatic regime, resulting in shear rate independent rheology. As $\hat{\dot{\gamma}} > 10^{-2}$, the fluid forces, which align with the extensional axis, become significant again, coupled with the move back to rate dependent rheology in the intermediate and soft viscous regimes.

2.5 Constitutive model

Following recent discussions that the inertial and viscous numbers can characterise additive contributions to the total suspension stress from contact and fluid effects respectively (Trulsson et al., 2012), we take inspiration from a recent constitutive model (Chialvo et al., 2012) for steady, simple shear in dry granular media and propose that a similar model for the suspension pressure can be obtained simply by adding a fluid stress contribution (which is a function of the material parameter $\hat{\eta}_f$) to the particle contact stress of the flowing regimes. Chialvo et al. (Chialvo et al., 2012) define $\hat{\mathrm{P}} = \mathrm{P}d/k_n$ separately in each of the dry granular flow regimes; inertial, quasistatic and intermediate. Here we define analogous constitutive regimes, extending upon the previous model to include the σ_{xy}^F dominated rheology. For moderate shear rates below ϕ_c, we define a hard-particle regime, with characteristic pressure $\hat{\mathrm{P}}_{\mathrm{hard}}$, that captures the viscous-to-inertial rheology. Above ϕ_c we employ the previous model for $\hat{\mathrm{P}}_{\mathrm{QS}}$ directly, as it has been ascertained that the contact stress always dominates in the quasistatic region. For very high shear rates, where $\hat{\dot{\gamma}} > 10^{-2}$, we define a soft-particle regime $\hat{\mathrm{P}}_{\mathrm{soft}}$, capturing the intermediate, shear-thinning behaviour of the previous model as well as the soft viscous behaviour predicted by the above simulations. The pressure in these regimes is predicted according to the following equations

$$\hat{\mathrm{P}}_{\mathrm{hard}} = \underbrace{\alpha^{\mathrm{c}}_{\mathrm{hard}}|\phi-\phi_c|^{\beta^{\mathrm{c}}_{\mathrm{hard}}}\hat{\dot{\gamma}}^2}_{\text{inertial}} + \underbrace{\alpha^{\mathrm{f}}_{\mathrm{hard}}\hat{\eta}_f|\phi-\phi_c|^{\beta^{\mathrm{f}}_{\mathrm{hard}}}\hat{\dot{\gamma}}}_{\text{viscous}}, \tag{2.7a}$$

$$\hat{\mathrm{P}}_{\mathrm{QS}} = \underbrace{\alpha_{\mathrm{QS}}|\phi-\phi_c|^{\beta_{\mathrm{QS}}}\hat{\dot{\gamma}}^0}_{\text{quasistatic}}, \tag{2.7b}$$

$$\hat{\mathrm{P}}_{\mathrm{soft}} = \underbrace{\alpha^{\mathrm{c}}_{\mathrm{soft}}|\phi-\phi_c|^{\beta^{\mathrm{c}}_{\mathrm{soft}}}\hat{\dot{\gamma}}^{0.5}}_{\text{intermediate}} + \underbrace{\alpha^{\mathrm{f}}_{\mathrm{soft}}\hat{\eta}_f|\phi-\phi_c|^{\beta^{\mathrm{f}}_{\mathrm{soft}}}\hat{\dot{\gamma}}}_{\text{viscous}}. \tag{2.7c}$$

It should be noted that the k_n scaling of the constitutive model is maintained in order to capture all of the flow regimes within the same framework. For the hard particle branch, however, the model can be recast to capture the viscous-to-inertial transition as a function of the Stokes number and volume fraction, independently of k_n

$$\frac{\mathrm{P}_{\mathrm{hard}}}{\eta_f \dot{\gamma}} = \underbrace{\alpha^{\mathrm{c}}_{\mathrm{hard}} |\phi - \phi_c|^{\beta^{\mathrm{c}}_{\mathrm{hard}}} \mathrm{St}}_{\text{inertial}} + \underbrace{\alpha^{\mathrm{f}}_{\mathrm{hard}} |\phi - \phi_c|^{\beta^{\mathrm{f}}_{\mathrm{hard}}}}_{\text{viscous}}. \tag{2.8}$$

We demonstrate that the values (of $\alpha^{\mathrm{c}}_{\mathrm{hard}}$, α_{QS}, $\alpha^{\mathrm{c}}_{\mathrm{soft}}$, $\beta^{\mathrm{c}}_{\mathrm{hard}}$, β_{QS}, $\beta^{\mathrm{c}}_{\mathrm{soft}}$) proposed by Chialvo (Chialvo et al., 2012) in each of the flow regimes are applicable for our contact stress data, and we use the fluid stress data from our simulation results to determine suitable values for the equivalent fluid stress parameters in each regime. The value of the shear rate exponent for the contact contribution for each flow regime is consistent with our previous discussion of bulk rheology for the contact dominated regimes: $\hat{\mathrm{P}}_{\mathrm{hard}} \propto \hat{\dot{\gamma}}^2$; $\hat{\mathrm{P}}_{\mathrm{QS}} \propto \hat{\dot{\gamma}}^0$; $\hat{\mathrm{P}}_{\mathrm{soft}} \propto \hat{\dot{\gamma}}^{0.5}$. The fluid contribution to suspension pressure is linear in $\hat{\dot{\gamma}}$ in the hard and soft regimes.

The β parameter gives the divergence of the contact and fluid pressure contributions with volume fraction. As is shown in Section 2.3, there is no volume fraction dependence of the bulk stress in the soft particle limit as $\hat{\dot{\gamma}} > 10^{-2}$. We therefore take $\beta^{\mathrm{c}}_{\mathrm{soft}} = \beta^{\mathrm{f}}_{\mathrm{soft}} = 0$. In the hard particle regime, the pressure diverges with $|\phi - \phi_c|^{-2}$ in both the inertial ($\mathrm{St} = 10$) and viscous ($\mathrm{St} = 0.1$) cases, as shown in Figure 2.7a. This leads us to set $\beta^{c}_{\mathrm{hard}} = \beta^{f}_{\mathrm{hard}} = -2$. The pressure is notably higher for the inertial case, consistent with the shear thickening associated with Bagnoldian stress scaling in this flow regime. In the quasistatic regime, the pressure increases above ϕ_c according to $|\phi - \phi_c|^{\frac{2}{3} \pm 0.01}$, independently of the fluid viscosity (Figure 2.7b). It is not surprising that this behaviour is not dependent on the fluid properties, since we have already concluded that at very low shear rate and high volume fraction, i.e. in the quasistatic regime, the flow is always contact dominated for the range of fluid viscosities studied here. This further justifies the lack of a fluid contribution to $\hat{\mathrm{P}}_{\mathrm{QS}}$ in our model. A value of $\beta_{\mathrm{QS}} = 2/3$ is used for the constitutive model.

The multiplicative fitting parameters α are obtained from Chialvo et al. (Chialvo et al., 2012) for the contact terms, noting that α_{QS} is dependent on the choice of friction coefficient in the contact model. In addition, we obtain $\alpha^{\mathrm{f}}_{\mathrm{hard}} = 0.02$ and $\alpha^{\mathrm{f}}_{\mathrm{soft}} = 0.55$. A summary of all model parameters is given in Table 2.2.

A blending function is employed, identical to that proposed by Chialvo et al. (Chialvo et al., 2012), to combine the individual contributions from the limits of each flow regime,

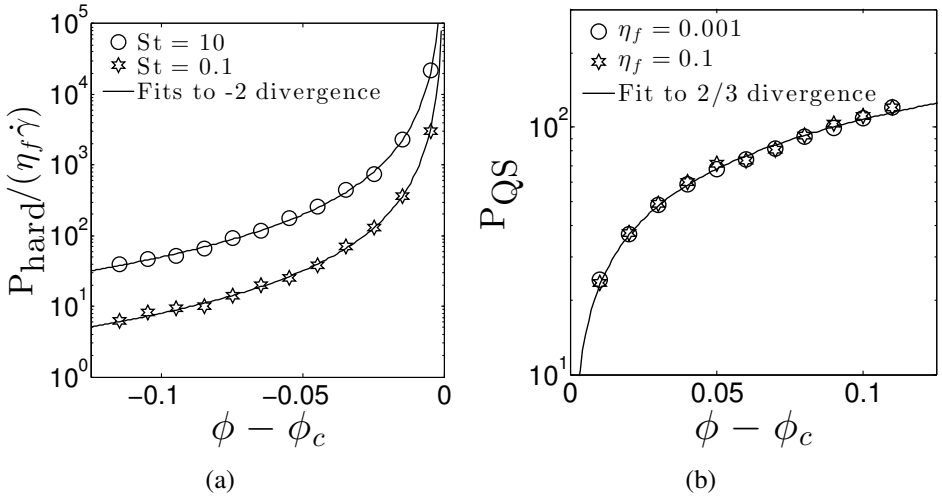

(a) (b)

Fig. 2.7 Divergence of pressure around ϕ_c in the $\hat{\dot{\gamma}} \ll 1$ limit, demonstrating the forms of the divergence for (a) $\phi < \phi_c$ and (b) $\phi > \phi_c$. Symbols represent simulation results, solid lines represent fits to the constitutive model exponents.

α^c_{hard}	α_{QS}	α^c_{soft}	α^f_{hard}	α^f_{soft}	β^c_{hard}	β_{QS}	β^c_{soft}	β^f_{hard}	β^f_{soft}
0.021	0.25	0.099	0.02	0.55	-2	2/3	0	-2	0

Table 2.2 The parameters used in the constitutive model.

giving the total pressure $\hat{\text{P}}$ as a function of $\hat{\dot{\gamma}}$, $\hat{\eta}_f$ and $|\phi - \phi_c|$ across all flow regimes:

$$\hat{\text{P}} = \begin{cases} \hat{\text{P}}_{\text{QS}} + \hat{\text{P}}_{\text{soft}} & \phi \geq \phi_c \\ \\ (\hat{\text{P}}^{-1}_{\text{hard}} + \hat{\text{P}}^{-1}_{\text{soft}})^{-1} & \phi < \phi_c \end{cases} . \tag{2.9}$$

The critical volume fraction for granular jamming ϕ_c, known to be a function of the particle-particle friction coefficient (μ_p) and the extent of bidispersity, has been determined for the present case at both macro- and microscopic levels. At the macroscopic level, a transition from viscous (or inertial) to quasistatic flow is observed for $\hat{\dot{\gamma}} \ll 1$ between $\phi = 0.57$ and $\phi = 0.59$. Furthermore, by setting $\phi_c = 0.585$ the divergence of suspension pressure with $\phi - \phi_c$ is effectively captured as $|\phi - \phi_c| \to 0$. At the micro-scale, the velocity correlation length is observed to diverge between $\phi = 0.58$ and $\phi = 0.59$. The value of ϕ_c used in this case is therefore 0.585, slightly higher than that ($\phi_c = 0.581$) reported for monodisperse particles of the same friction coefficient, as expected.

In order to calculate the shear stress from the pressure, we adopt the popular $\mu(\mathrm{I_I})$ rheology and appeal to a recent constitutive model for the stress ratio $\mu = \sigma_{xy}/\mathrm{P}$ as a function of $\mathrm{K} = \mathrm{I_V} + \alpha \mathrm{I_I^2}$ (Trulsson et al., 2012), combining inertial and viscous rheology. We find that the proposed value of $\alpha = 0.635 \pm 0.009$ is suitable for $\mathrm{K} < 10^{-2}$, but that a value of $\alpha = 0.3$ allows the rheological contributions to be combined successfully for $\mathrm{K} < 1$. Furthermore, the proposed function $\mu(\mathrm{K})$ does not take the correct form for large $\mathrm{I_V}$. As demonstrated by the experimental results and constitutive model given by Boyer (Boyer et al., 2011), μ is expected to diverge as $\mathrm{I_V} \to \infty$ at $\mathrm{I_I} = 0$, while the model of Trulsson et al (Trulsson et al., 2012) predicts a maximum in μ. We therefore propose a modified form that captures the divergence in μ with $\mathrm{K} \to \infty$,

$$\mu(\mathrm{K}) = 0.38 + 1.2\mathrm{K}^{1/2} + 0.5\mathrm{K}. \tag{2.10}$$

It is found that all the simulation data can be described by this model, with the exception of extremely high shear rates ($\hat{\dot{\gamma}} > 0.1$) where particle overlaps are expected to become unfeasibly large compared to that of granular materials under normal experimental conditions. Stress ratio data are given in Figure 2.8, along with predictions given by the present model, and that proposed previously. We note that previous $\mu(\mathrm{I})$ models (Da Cruz et al., 2005; Boyer et al., 2011) for dry granular materials predict a maximal μ for $\mathrm{I_I} \to \infty$ at $\mathrm{I_V} = 0$, while the present model diverges for $\mathrm{I_I} \to \infty$. Experimentally, the inertial number is not observed to exceed a value of around 0.3, so we conclude that our model does capture the μ dependence on $\mathrm{I_I}$ at $\mathrm{I_V} = 0$ within the experimentally accessible range, as well as the experimentally observed divergent behaviour as $\mathrm{I_V} \to \infty$.

Constitutive model predictions are given as the solid line in Figure 2.2, demonstrating good agreement with the simulation results. Furthermore, we note the ability of the model to capture the divergence of the suspension viscosity with volume fraction in the viscous, inertial and quasistatic regimes. Below ϕ_c the suspension viscosity diverges as $|\phi - \phi_c|^{-2}$ in the viscous and inertial regimes, consistent with the divergence of the bulk pressure plotted above. This result is consistent with the experimental and simulation results in (Kawasaki et al., 2015; Mari et al., 2014; Boyer et al., 2011) and also with the traditionally cited Quemada equation (Quemada, 1978), $\mu = (1 - \phi/\phi_c)^{-2}$. It has also been found that by excluding the tangential lubrication force from the present simulations, the exponent tend towards -1 for the viscous regime, which is consistent with the early theoretical derivation by Frankel and Acrivos (Frankel and Acrivos, 1967) assuming a purely normal lubrication interaction. There is still debate as to the true nature and form of this divergence, with the consensus being that the exponent is somewhere between -1 and -3 (Kawasaki et al., 2015). Above ϕ_c, the viscosity scales with

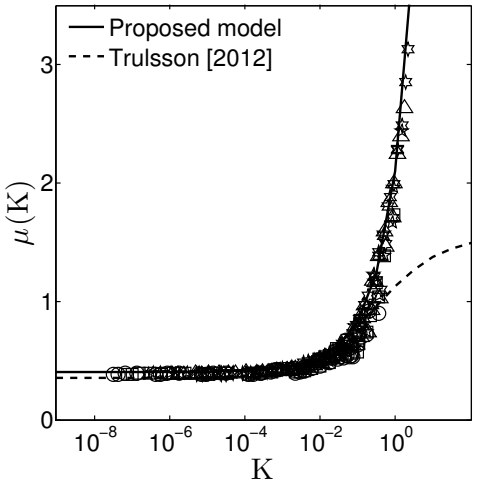

Fig. 2.8 Stress ratio μ as a function of I_I and I_V. Different symbols represent different shear rates (10^{-5} to 10^{-2}), fluid viscosities (10^{-5} to 10^{-2}) and volume fractions (0.48 to 0.68). The solid line represents the constitutive model in Equation 2.10; the dashed line represents a constitutive model proposed previously by Trulsson et al. (Trulsson et al., 2012).

$|\phi - \phi_c|^1$, giving some agreement with experimental work (Nordstrom et al., 2010a) that finds a value of around 1.35 in this regime.

Our constitutive model presented here provides a skeleton framework which enables rheological data to be mapped with respect to broad flow regimes. It is stressed that the model is applied at a phenomenological level. It has been assumed that the stress contributions (i.e. those coming from particle contacts and hydrodynamics) are additive and that the changes to their scalings can be treated by a simple numerical construct using blending functions. At a microstructural level, the particle contact and hydrodynamic stresses are in fact tightly coupled, and not simply additive. The flow map presented here is, therefore, useful for interpreting rheological data and rationalising flow behaviour with respect to specific regimes, but its construction should not be considered a literal manifestation of an additive behaviour in the suspension stresses.

2.6 Conclusions and discussion

The particle dynamics of dense granular suspensions have been simulated using the discrete element method combining particle contacts and hydrodynamic lubrication. Simulations of homogeneous simple shear flow have been performed, shedding light on the transitions between flow regimes as a function of solid volume fraction (ϕ), shear rate ($\dot{\gamma}$) and material properties ($\hat{\eta}_f$). We found that for volume fractions below a critical value, quasi-Newtonian behaviour emerges at Stokes numbers below 1, transiting to

continuously shear thickening, Bagnoldian behaviour above 1. A quasistatic, rate-independent regime exists above ϕ_c for low and moderate shear rates. At very high shear rates, which we have defined as $\hat{\dot{\gamma}} > 10^{-2}$, the flow becomes ϕ-independent and either shear thinning or viscous, depending on the value of a material parameter, $\hat{\eta}_f$. All the transitions are shown to correlate with a change in the relative importance of the lubrication contacts at the microscopic scale and their contribution to the total stress at the macroscopic scale.

The transitions in bulk rheology are well correlated with changes in microstructure, characterised by distributions of interacting forces and relative velocities, fabric and correlation length. When the viscous effect is strong, the force distribution and fabric are more isotropic and the correlation length is longer. Interestingly, the force distribution and fabric characterising mechanical contacts behave distinctly from those for the lubrication contacts. They remain anisotropic with the major principal direction aligned with the compressive axis while the lubrication contacts become more isotropic or flip the major principal direction to the extensional axis. Although the direct consequence on the bulk rheology is not clear, this distinction between the two different contact networks might have important implications for modelling more complex unsteady rheology of dense granular suspensions.

With such understanding of the rheological behaviour, constitutive equations for pressure have been established for the asymptotic flow behaviours using an additive form combining viscous effects with dry granular rheology. The equations are then bridged ad hoc using a blending function to capture the transitions between them. The shear stress-to-pressure ratio is modelled as a function of both the inertial and the viscous numbers for all flow regimes, with a form applicable to a wider parametric range than previous models. The resultant constitutive model has been shown to be able to capture all the flow curves from the DEM simulations and can predict the divergent behaviour of the suspension viscosity with respect to the solid volume fraction. The current model, with only scalar representation of stress and strain rate calibrated with data from simple shear flow, is not expected to capture different types of flow, e.g. extensional flow. Future work is warranted to generalise to a fully tensorial model supported with data from simulation and experiments of different types of flows.

Chapter 3

Shear thickening regimes of dense non-Brownian suspensions

In this chapter, we build directly upon the flow regime map obtained above, and propose a unifying rheological framework for dense suspensions of non-Brownian spheres, predicting the onsets of particle friction and particle inertia as distinct shear thickening mechanisms, while capturing quasistatic and soft particle rheology at high volume fractions and shear rates respectively (Ness and Sun, 2016b). Discrete element method simulations that take suitable account of hydrodynamic and particle-contact interactions predict all of the expected flow regimes, demonstrating both mechanisms of shear thickening, and showing that they can occur concurrently with carefully selected particle surface properties under certain flow conditions. Microstructural transitions associated with frictional shear thickening are presented. We find very distinctive divergences of both microstructural and dynamic variables with respect to volume fraction in the thickened and non-thickened states.

3.1 Review of recent shear thickening literature

Non-Newtonian rheology (Denn, 2004) has been observed and studied for centuries in numerous materials, flow regimes and applications. In this chapter we focus on shear thickening (Brown, 2013) in densely packed non-Brownian suspensions of bidisperse solid spheres, with and without inertia (Stickel and Powell, 2005; Lemaître et al., 2009; de Bruyn, 2011). This rheological phenomenon, in which the shear stress required to deform the suspension increases faster than linearly with the deformation rate, is regularly demonstrated in high volume fraction cornstarch suspensions (Fall et al., 2008), but is also observed in other particulate systems such as dry granular materials at constant volume (Chialvo et al., 2012; Forterre and Pouliquen, 2008; Jop et al.,

2006) and well characterised model suspensions (Brown and Jaeger, 2009), and has considerable industrial relevance (Benbow and Bridgwater, 1993). The non-Brownian limit arises in suspensions of both silica and polymethylmethacrylate, for example, under typical shear thickening conditions (Lin et al., 2015).

Continuous, linear shear thickening, in which the suspension viscosity is proportional to the shear rate, may arise in suspensions below jamming (Liu and Nagel, 1998) when conditions are such that particle inertia is relevant (Fall et al., 2010; Trulsson et al., 2012; Ness and Sun, 2015), much like in dry granular materials (MiDi, 2004). Other suspensions have, however, been observed to shear thicken far more severely than in these linear cases, and at Stokes numbers considerably less than 1, for which particle inertia ought to be negligible (Fall et al., 2008, 2012, 2015; Laun, 1984; Egres and Wagner, 2005; Cwalina and Wagner, 2014). This behaviour is variously known as “shear jamming", “dynamic jamming" and “discontinuous shear thickening” (DST) (Bertrand et al., 2002), and until recently has widely been thought to arise due to either the shear-induced formation of “hydroclusters” (Wagner and Brady, 2009; Cheng et al., 2011), mesoscale particle agglomerates stabilised by hydrodynamic interactions that result in massive dissipation under shear; or dilatancy, the tendency of the suspension to increase in volume upon shearing (Brown and Jaeger, 2012; Fall et al., 2008) and subsequently bifurcate into coexisting regimes of inhomogeneous solids fraction (Fall et al., 2015).

A growing body of experimental (Fernandez et al., 2013; Pan et al., 2015; Guy et al., 2015) and computational (Seto et al., 2013; Mari et al., 2014; Heussinger, 2013) work provides evidence that discontinuous shear thickening can arise because frictional particle-particle contacts appear under large loads. The suspended particles may be either charge stabilised or sterically stabilised using, for example, polymer hairs grafted to the particle surface. Under small loads, the normal repulsive forces that arise between particles due to this stabilisation are sufficient to prevent direct particle-particle contacts, so lubricating layers are maintained. Above a critical load P^*, the stabilisation is overcome and rough particle surfaces come into contact, resulting in normal and tangential forces that can be considered similar to those existing between dry granular particles (Guy et al., 2015). The increased dissipation resulting from the subsequently reorganised microstructure and the tangential contact forces means very large stresses are required to maintain flow. Under this mechanism, the shear thickened state may flow homogeneously, without velocity or volume fraction banding (Pan et al., 2015). A rheological model proposed by Wyart and Cates (Wyart and Cates, 2014) (phenomenologically reminiscient of an earlier proposal by Goddard (Goddard, 2002)) captures this transition between frictionless and frictional states, predicting the pres-

ence of continuous shear thickening at low volume fractions, and DST at high volume fractions, where S-shaped flow curves could occur with multiple flow states existing at a given shear rate but at greatly differing stresses. Such flow curves have recently been observed experimentally (Pan et al., 2015) and computationally (Mari et al., 2015a) under imposed shear stress.

In general, the rheology of suspended "nearly-hard" spheres can be broadly characterised by the interplay between the flow timescale associated with inverse of the shear rate $1/\dot{\gamma}$, and *four* competing timescales (as presented in Table 2.1): a Brownian timescale (characterised by the Péclet number $\mathrm{Pe} = 3\pi\eta_f\dot{\gamma}d^3/4kT$, for representative particle diameter d and interstitial fluid viscosity η_f); a timescale associated with the stabilising repulsion (numerically this has been referred to as $1/\dot{\gamma}_0 = \frac{3}{2}\pi\eta_f d^2/F^{CL}$, for repulsive force magnitude F^{CL}) (Mari et al., 2014); an inertial timescale (characterised by the Stokes number $\mathrm{St} = \rho d^2\dot{\gamma}/\eta_f$, where ρ is a representative suspension density and $\mathrm{St} = 1$ delineates viscous and inertial flows) and a timescale associated with the stiffness of the particles (for example $d/\sqrt{k_n/\rho d}$, where k_n is related to the Young's modulus of the particles)(Chialvo et al., 2012). So far, these diverse scales have not been probed simultaneously in a single suspension either experimentally or computationally, though there are numerous recent examples of transitions across regimes that suggest they represent isolated regions of a single rheological map for dense suspensions (Mari et al., 2015b; Ikeda et al., 2012; Kawasaki et al., 2014; Cwalina and Wagner, 2014; Guy et al., 2015; Nordstrom et al., 2010a; Fall et al., 2010).

In the present chapter, we focus on the non-Brownian limit (i.e. $\mathrm{Pe} \to \infty$), and demonstrate that constitutive models proposed for shear thickening in the non-inertial limit (Wyart and Cates, 2014) and for capturing the non-inertial (viscous) to inertial transition (Trulsson et al., 2012; Ness and Sun, 2015), can be unified to place frictional shear thickening in the wider context of dense suspension rheological regimes, also accounting for the effects of finite particle hardness. We then perform discrete element method (Cundall and Strack, 1979; Plimpton, 1995) simulations combining hydrodynamic lubrication (Ball and Melrose, 1997) with a suitable particle-particle interaction model proposed by Mari et al. (Seto et al., 2013; Mari et al., 2014) that can capture the bulk steady-state rheological behaviour associated with frictional shear thickening under imposed shear rate. We demonstrate that the timescale for *frictional* shear thickening can be made to coincide with that for *inertial* shear thickening by careful tuning of particle surface properties, hinting at novel suspension flow curves that have yet to be observed experimentally. Finally, we highlight microstructural properties associated with the frictional thickening transition, identifying very well

defined structural and dynamic signatures that may prove useful in interpretation and analysis of future rheo-imaging data for shear thickening suspensions.

3.2 Constitutive model and flow regime map

3.2.1 Model description

We first present an overview of the model proposed in the previous chapter (Ness and Sun, 2015), before extending it to incorporate the frictional thickening transition. This model is inspired by the inertial number model (Jop et al., 2006; Forterre and Pouliquen, 2008) (for inertial number $I_I = \dot{\gamma}d/\sqrt{P/\rho}$, with confining pressure P), its extension to viscous flows (Boyer et al., 2011) (for viscous number $I_V = \dot{\gamma}\eta_f/P$), and their proposed unification by Trulsson (Trulsson et al., 2012). The equation gives a prediction for the scaled (by particle hardness) pressure ($\hat{P} = Pd/k_n$) as a function of the scaled shear rate ($\hat{\dot{\gamma}} = \dot{\gamma}d/\sqrt{k_n/\rho d}$) and the departure of the solids volume fraction ϕ from its critical value for jamming (Liu and Nagel, 1998), ϕ_c, in each of three regimes: 1) the hard particle regime corresponding to viscous and inertial flows; 2) the soft particle regime corresponding to deformable particle flows; 3) the quasistatic, "jammed" regime:

$$\hat{\mathrm{P}}_{\mathrm{hard}} = \underbrace{\alpha^{\mathrm{c}}_{\mathrm{hard}}|\phi-\phi_c|^{-2}\hat{\dot{\gamma}}^2}_{\text{inertial}} + \underbrace{\alpha^{\mathrm{f}}_{\mathrm{hard}}\eta_f|\phi-\phi_c|^{-2}\hat{\dot{\gamma}}}_{\text{viscous}}, \tag{3.1a}$$

$$\hat{\mathrm{P}}_{\mathrm{soft}} = \underbrace{\alpha^{\mathrm{c}}_{\mathrm{soft}}\hat{\dot{\gamma}}^{0.5}}_{\text{intermediate}} + \underbrace{\alpha^{\mathrm{f}}_{\mathrm{soft}}\hat{\eta}_f\hat{\dot{\gamma}}}_{\text{viscous}}, \tag{3.1b}$$

$$\hat{\mathrm{P}}_{\mathrm{QS}} = \underbrace{\alpha_{\mathrm{QS}}|\phi-\phi_c|^{2/3}}_{\text{quasistatic}}, \tag{3.1c}$$

with the constants given by Ness and Sun (Ness and Sun, 2015). An arbitrary blending function is chosen, following Chialvo et al. (Chialvo et al., 2012), to combine pressure predictions from each of the expressions. The corresponding shear stresses σ_{xy} are obtained from a $\mu(K = I_V + \alpha I_I^2)$ model (Trulsson et al., 2012; Ness and Sun, 2015), an extension of the commonplace $\mu(I_I)$ rheology (Jop et al., 2006):

$$\mu(K) = \mu_1 + 1.2K^{1/2} + 0.5K. \tag{3.2}$$

The rheology predicted by Equations 3.1 and 3.2 is presented in detail in Chapter 2. We next incorporate a frictional shear thickening mechanism into this model using a stress-dependent critical volume fraction ϕ_c, following the approach used by Wyart and Cates (Wyart and Cates, 2014). A stress-dependent effective friction is introduced,

recognising that the critical volume fraction depends on the interparticle friction coefficient μ_p (Sun and Sundaresan, 2011), varying from $\phi_m \approx 0.58$ to $\phi_0 \approx 0.64$ in the limits of highly frictional ($\mu_p = 1$) and frictionless ($\mu_p = 0$) particles, respectively. Note that tangential forces saturate rapidly above $\mu_p \approx 1$, meaning rheology becomes nearly independent of μ_p for $\mu_p > 1$. From the simulation model described in Sec 3.3.1, we find that under shear flow, the rescaled pairwise particle-particle contact force magnitudes $\theta = |\mathbf{F}_{ij}^c|/Pd^2$ are distributed according to

$$\mathrm{PDF}(\theta) = a(1 - b\exp(-\theta^2))\exp(-c\theta), \tag{3.3}$$

consistent with previous authors (Mueth et al., 1998; Sun et al., 2006).

The fraction of particle contacts for which the repulsive force magnitude F^{CL} is exceeded and friction is activated is therefore given by

$$f = \int_{F^{CL}/Pd^2}^{\infty} \mathrm{PDF}(\theta)d\theta, \tag{3.4}$$

implying (except for very weak contacts) that frictional forces arise in the system above P^* according to $f \propto \exp(-P^*/P)$. We therefore use f to represent a transition from frictionless to frictional rheology with increasing P. The value set for P^* (which is directly related to the repulsive force magnitude F^{CL}) determines the critical pressure (or critical characteristic shear rate) at which the model will begin to predict frictional rheology, as described later. We subsequently calculate the (stress-dependent) critical volume fraction for jamming ϕ_c using an expression similar to the crossover function proposed by Wyart and Cates(Wyart and Cates, 2014)

$$\phi_c = \phi_m f + \phi_0(1 - f). \tag{3.5}$$

The expression for $\mu(K)$, along with that proposed by Boyer (Boyer et al., 2011), assumes a constant value for the macroscopic friction μ_1 ($= \sigma_{xy}/P = 0.38$) in the limit of $K \to 0$. As demonstrated by da Cruz (Da Cruz et al., 2005), μ_1 is actually strongly dependent on interparticle friction μ_p, particularly for μ_p close to 0, so assuming a constant value across shear thickening states is clearly not appropriate. We therefore propose a similar crossover function for μ_1 (consistent with that proposed by Sun and Sundaresan (Sun and Sundaresan, 2011) for dry granular materials) which we find gives excellent agreement with the following simulation results

$$\mu_1 = \mu_{1_m} f + \mu_{1_0}(1 - f), \tag{3.6}$$

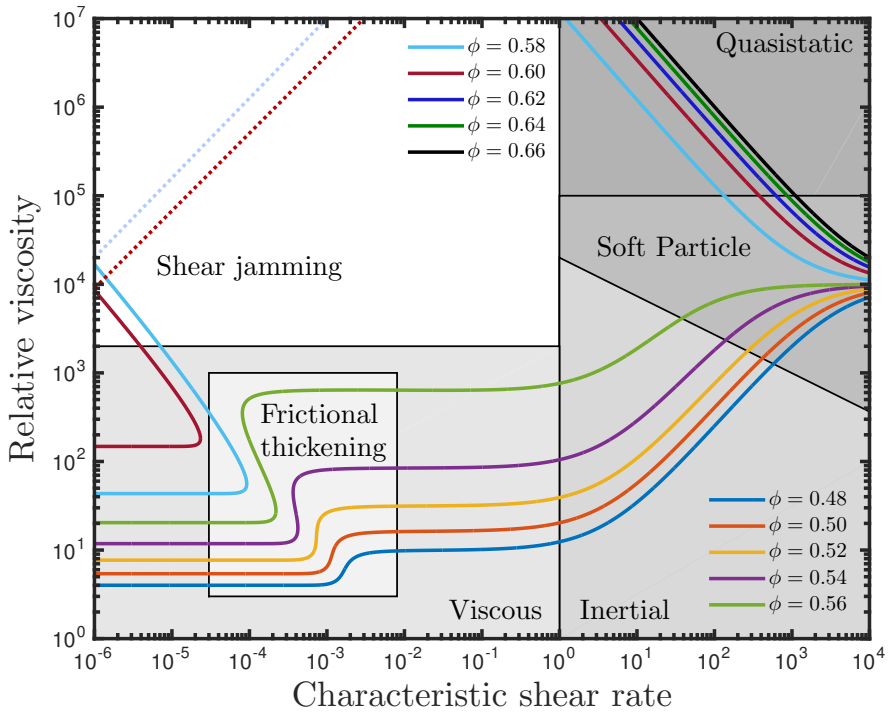

Fig. 3.1 Steady state, modular, rheological regime map for a shear thickening suspension, illustrating the frictional thickening transition within the viscous regime, shear jamming, inertial shear thickening, quasistatic behaviour and deformational behaviour associated with soft particle rheology. Solid lines represent model predictions from Equations 3.1, 3.2, 3.5 and 3.6. Dotted lines represent a schematic illustration of the possible link between the shear jammed and quasistatic states. Different colours represent different volume fractions ϕ. A thorough description of all relevant parameters is presented along with the model Equations in Section 3.2.1.

where $\mu_{1_m} = 0.41$ and $\mu_{1_0} = 0.11$ (Sun and Sundaresan, 2011). We obtain the viscosity of the suspension relative to that of the interstitial fluid according to $\eta_s = \frac{\sigma_{xy}}{\eta_f \dot{\gamma}}$.

3.2.2 Flow map and experimental evidence

We obtain the flow curves presented in Fig 3.1 from Eqs. 3.1, 3.2, 3.5 and 3.6. Below ϕ_c, the model predicts viscous rheology for Stokes numbers less than unity, inertial flow at higher Stokes numbers, and "intermediate" rheology at extremely high shear rates or for soft particle suspensions (i.e. emulsions) where large deformations are possible (Nordstrom et al., 2010a) (strictly, "soft" particle rheology is observed when $\dot{\gamma} \to d\sqrt{k_n/\rho d}$) (Chialvo et al., 2012). Above ϕ_c, quasistatic rheology is observed for low and moderate Stokes numbers, with a tendency towards soft particle rheology at very high rates. The addition of pressure dependence in ϕ_c gives rise to the frictional thickening and S-shaped flow behaviour, as shown in Fig 3.1 within the viscous flow

regime, and the hypothetical shear jamming transition that may occur between the viscous and quasistatic regimes for particles of finite stiffness.

The predicted rheology in Fig 3.1 (parameters for which are derived from our simulation data presented previously (Ness and Sun, 2015) and below) for characteristic shear rates < 1 is well corroborated by recent experimental data in shear flows of polymer-coated PMMA spheres (Guy et al., 2015). Quantitatively, comparing shear thickened relative suspension viscosities η_s at $|\phi - \phi_c| \approx 0.02$ yields around 8×10^2 for simulations versus 10^3 from experiments. The viscous-to-inertial transition at characteristic shear rate $= 1$ is well documented experimentally in the literature (Bagnold, 1954; Fall et al., 2010) and a quantitative comparison is made below. Furthermore, the quasistatic and soft particle regimes, and most notably their loss of volume fraction dependence at very large rates, are consistent with experimental results in very soft particles (Nordstrom et al., 2010a) and associated theory (Seth et al., 2011).

3.2.3 Tuning the frictional transition

The fact that the onset stress P^* varies with particle contact properties (specifically F^{CL}, the repulsive force magnitude) implies that the transition to frictional behaviour might occur at different regions of the flow map. We demonstrate this behaviour in Fig 3.3, 3.4, 3.5, by increasing the magnitude of the onset stress P^* in the definition of f, delaying the onset of the frictional behaviour governed by Eqs. 3.5 and 3.6 such that it occurs at higher Stokes numbers. We obtain the same characteristic frictional shear thickening flow curve predictions for each of Figs 3.3, 3.4, 3.5, with the added phenomena of inertia appearing at a prescribed point in relation to P^*. Such shear thickening will be demonstrated by particle simulations in the next section.

3.3 Shear flow simulations

3.3.1 Numerical method

The numerical model employed in this Chapter follows that used in Chapter 2, but we further include logarithmic terms in the lubrication force model and a critical force for the onset of friction in the particle contact model, as described fully in Equations 3.9 and 3.12. The equations of motion for non-Brownian particles suspended in a fluid can be written simply as (Brady and Bossis, 1988)

$$m\frac{d}{dt}\begin{pmatrix}\mathbf{v}\\ \boldsymbol{\omega}\end{pmatrix} = \sum\begin{pmatrix}\mathbf{F}\\ \boldsymbol{\Gamma}\end{pmatrix}, \tag{3.7}$$

for particles of mass m with translational and rotational velocity vectors $\mathbf{v}$ and $\boldsymbol{\omega}$ respectively, subjected to force and torque vectors $\mathbf{F}$ and $\boldsymbol{\Gamma}$ respectively. In this chapter we limit the forces and torques to those arising due to direct particle contacts ($\mathbf{F}^c, \boldsymbol{\Gamma}^c$) and those arising through hydrodynamic interactions ($\mathbf{F}^l, \boldsymbol{\Gamma}^l$). Full solution of the pairwise hydrodynamic forces has traditionally been done using the Stokesian Dynamics algorithm (Bossis and Brady, 1984; Brady and Bossis, 1985), though its great computational expense makes large (or very dense) simulations challenging. For highly packed suspensions, the divergent lubrication resistances that arise between extremely close particles dominate the hydrodynamic interaction, so $\mathbf{F}^l$, $\boldsymbol{\Gamma}^l$ can be approximated by summing pairwise lubrication forces among nearest neighbouring particles (Ball and Melrose, 1997; Kumar and Higdon, 2010; Trulsson et al., 2012; Mari et al., 2014; Ness and Sun, 2015). For an interaction between particles i and j, the force and torque due to hydrodynamics can therefore be expressed as

$$\begin{aligned}\mathbf{F}^l_{ij} &= -a_{sq} 6\pi\eta_f (\mathbf{v}_i - \mathbf{v}_j)\cdot \mathbf{n}_{ij}\mathbf{n}_{ij} \\ &\quad - a_{sh} 6\pi\eta_f (\mathbf{v}_i - \mathbf{v}_j)\cdot (\mathbf{I} - \mathbf{n}_{ij}\mathbf{n}_{ij}),\end{aligned} \tag{3.8a}$$

$$\begin{aligned}\boldsymbol{\Gamma}^l_{ij} &= -a_{pu}\pi\eta_f d_i^3 (\boldsymbol{\omega}_i - \boldsymbol{\omega}_j)\cdot (\mathbf{I} - \mathbf{n}_{ij}\mathbf{n}_{ij}) \\ &\quad - \frac{d_i}{2}\left(\mathbf{n}_{ij}\times \mathbf{F}^l_{ij}\right).\end{aligned} \tag{3.8b}$$

where $\mathbf{n}_{ij}$ is the vector pointing from particle j to particle i, and with squeeze a_{sq}, shear a_{sh} and pump a_{pu} resistance terms as derived by Kim and Karrila (Kim and Karrila, 1991) and given in Eq 3.9 for particle diameters d_i and d_j, with $\beta = d_j/d_i$:

$$\begin{aligned}a_{sq} &= \frac{\beta^2}{(1+\beta)^2}\frac{d_i^2}{4h_{\text{eff}}} + \frac{1+7\beta+\beta^2}{5(1+\beta)^3}\frac{d_i}{2}\ln\left(\frac{d_i}{2h_{\text{eff}}}\right) \\ &\quad + \frac{1+18\beta-29\beta^2+18\beta^3+\beta^4}{21(1+\beta)^4}\frac{d_i^2}{4h_{\text{eff}}}\ln\left(\frac{d_i}{2h_{\text{eff}}}\right),\end{aligned} \tag{3.9a}$$

$$\begin{aligned}a_{sh} &= 4\beta\frac{2+\beta+2\beta^2}{15(1+\beta)^3}\frac{d_i}{2}\ln\left(\frac{d_i}{2h_{\text{eff}}}\right) \\ &\quad + 4\frac{16-45\beta+58\beta^2-45\beta^3+16\beta^4}{375(1+\beta)^4}\frac{d_i^2}{4h_{\text{eff}}}\ln\left(\frac{d_i}{2h_{\text{eff}}}\right),\end{aligned} \tag{3.9b}$$

$$\begin{aligned}a_{pu} &= \beta\frac{4+\beta}{10(1+\beta)^2}\ln\left(\frac{d_i}{2h_{\text{eff}}}\right) \\ &\quad + \frac{32-33\beta+83\beta^2+43\beta^3}{250(1+\beta)^3}\frac{d_i}{2h_{\text{eff}}}\ln\left(\frac{d_i}{2h_{\text{eff}}}\right).\end{aligned} \tag{3.9c}$$

For each pairwise interaction, the surface-to-surface distance, h, is calculated according to $h = |\mathbf{r}_{ij}| - \frac{d_i+d_j}{2}$, for centre-to-centre vector $\mathbf{r}_{ij}$. Recent experimental (Fernandez

et al., 2013; Guy et al., 2015) and computational (Lin et al., 2015; Ness and Sun, 2016a) work indicates that direct particle-particle contacts play a significant role in determining steady state paste viscosity. To permit such contacts in the present model, we truncate the lubrication divergence and regularize the contact singularity at a typical asperity length scale $h_{\min} = 0.001 d_{ij}$ (for weighted average particle diameter $d_{ij} = \frac{d_i d_j}{d_i + d_j}$), i.e., setting $h = h_{\min}$ in the force calculation, when $h < h_{\min}$. The effective interparticle gap used in the force calculation, h_{eff}, is therefore given by

$$h_{\text{eff}} = \begin{cases} h & \text{for } h > h_{\min} \\ h_{\min} & \text{otherwise.} \end{cases} \tag{3.10}$$

For computational efficiency, the lubrication forces are omitted when the interparticle gap h is greater than $h_{\max} = 0.05 d_{ij}$. The volume fraction is sufficiently high that all particles have numerous neighbours within this range, so such an omission is inconsequential to the dynamics.

When the lubrication force is overcome and particle surfaces come into contact (this occurs when $h < 0$, and can be related to a critical Sommerfeld number at each particle-particle contact as we point out elsewhere (Ness and Sun, 2015) and as considered in more detail by Fernandez (Fernandez et al., 2013)), their interaction is defined according to a linear spring model (Cundall and Strack, 1979), with normal ($\mathbf{F}^{c,n}$) and tangential ($\mathbf{F}^{c,t}$) force and torque $\mathbf{\Gamma}^c$ given by

$$\mathbf{F}_{ij}^{c,n} = k_{\text{n}} \delta \mathbf{n}_{\text{ij}}, \tag{3.11a}$$

$$\mathbf{F}_{ij}^{c,t} = -k_{\text{t}} \mathbf{u}_{\text{ij}}, \tag{3.11b}$$

$$\mathbf{\Gamma}_{ij}^{c} = -\frac{d_i}{2} (\mathbf{n}_{ij} \times \mathbf{F}_{ij}^{c,t}), \tag{3.11c}$$

for a collision between particles i and j with normal and tangential spring stiffnesses k_n and k_t respectively, particle overlap δ (equal to $-h$) and tangential displacement $\mathbf{u}_{\text{ij}}$. We note that the damping arising from the hydrodynamics is always sufficient to achieve a steady state without employing a thermostat, and further damping in the particle-contact model is omitted for simplicity.

We employ the Critical Load Model (CLM) for inter-particle friction (Seto et al., 2013; Mari et al., 2014), to distinguish between weakly interacting particles, those that interact via the normal force deriving from stabilisation, and strongly interacting particles, those whose surfaces come into frictional contact. This model gives an additional stress scale for the particle interaction, which, numerically, is the origin of the onset stress for shear thickening P^*. An interparticle static Coulomb friction

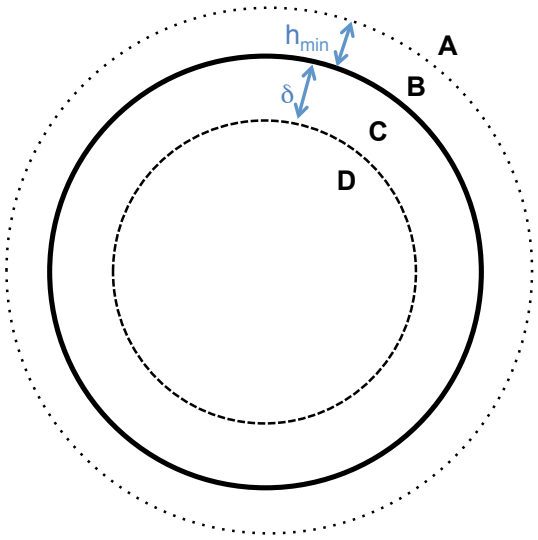

Fig. 3.2 Illustration of interaction lengthscales (not to scale). Forces resolved in region A: $\mathbf{F}^l_{ij}(h_{\text{eff}} = h)$; B: $\mathbf{F}^l_{ij}(h_{\text{eff}} = h_{\text{min}})$; C: $\mathbf{F}^l_{ij}(h_{\text{eff}} = h_{\text{min}}) + \mathbf{F}^c_{ij}(\mu_p = 0)$; D: $\mathbf{F}^l_{ij}(h_{\text{eff}} = h_{\text{min}}) + \mathbf{F}^c_{ij}(\mu_p = 1)$.

coefficient μ_p is defined according to $|\mathbf{F}^{c,t}_{i,j}| \leq \mu_p |\mathbf{F}^{c,n}_{i,j}|$, setting a maximum value for the tangential force exerted during a collision. For large tangential forces, the truncation is activated and sliding motion may occur between contacting particles; for small tangential forces, particle rotation occurs with no sliding. In granular systems, μ_p consequently determines the volume fraction at which flow arrest or jamming will occur (Chialvo et al., 2012). Such a friction model may be considered to account for roughness on the surface of near ideal spheres in model systems (Guy et al., 2015). For less idealised cases, such as cornstarch suspensions, further computational tools such as bonded-sphere complex particle shapes and rolling resistance are currently being pursued as means of accounting for severe asphericity. It is anticipated that enhanced interlocking at large volume fractions will cause shear thickening to be exaggerated even further. For each pairwise collision, the value of μ_p is dependent upon the normal force between the interacting particles and some critical normal force magnitude F^{CL}, representing the magnitude of the stabilising repulsive force, such that

$$\mu_p = \begin{cases} 1 & \text{for } |\mathbf{F}^{c,n}_{i,j}| > F^{CL} \\ 0 & \text{otherwise} \end{cases} . \tag{3.12}$$

$\mu_p = 1$ is chosen to represent a highly frictional near-upper limiting case. In practice, μ_p can be chosen to represent the roughness of any particles of interest. The primary effect of varying μ_p is to alter ϕ_m, the volume fraction at which the viscosity will diverge in the frictional limit. A secondary consequence of this is that at fixed volume fraction, the extent of shear thickening, i.e. the step change in viscosity upon exceeding P^*, will

decrease as $\mu_p \to 0$. Note that P^* and $\dot{\gamma}_0$ are not functions of μ_p. These properties of μ_p have been reported recently elsewhere (Mari et al., 2014). As a result of the CLM, particles that interact through weak forces, i.e. collisions where $\delta \to 0$, are frictionless, while interactions with large normal forces are frictional. This particle potential represents a physical scenario closer to electrostatic rather than polymer hair driven normal repulsion. The particle overlaps required to exceed F^{CL} are, at their absolute maximum, of order $10^{-5}d_{ij}$. An overview of the interaction lengthscales is given in Fig 3.2. In principle, $h_{\min}$ and δ might serve as tuning parameters that may be chosen to reflect details of a suspension of interest. For example, particles with particularly long-range repulsion or long stabilising polymer hairs or those with prominent asperities or complex surface topology might be better captured by large $h_{\min}$. In practice, however, we find that provided $h_{\min} \leq 0.005d$, steady state dynamics are little changed as $h_{\min} \to 0$ (Ness and Sun, 2016a). Similarly there is little dependence on δ, provided $0 < \delta \ll d$.

Long range hydrodynamics are justifiably omitted from the model, as discussed above. Furthermore, fluid inertia is neglected for simplicity. Trulsson (Trulsson et al., 2012) demonstrated that for inertial suspension flows, the dissipation through particle contacts considerably outweighs that due to fluid effects, a result consistent with our data in Fig 3.6a above frictional shear thickening. In addition, the scaling laws predicted by our simulations (specifically $\sigma_{xy} \propto \dot{\gamma}$ and $\sigma_{xy} \propto \dot{\gamma}^2$ for viscous and inertial flows respectively), are consistent with observations from comparable experiments (Fall et al., 2010; Bagnold, 1954). Notably, the quadratic scaling in the inertial regime in experiments and the present simulations is also consistent with dry granular $\mu(I)$-rheology (Forterre and Pouliquen, 2008), further strengthening the argument for dominance of contacts in this regime. Quantitatively, our model predicts the onset of inertia at $\phi = 0.56$ when the relative suspension viscosity $\eta_s \approx 500$. Fall (Fall et al., 2010) reports this transition for $40\mu m$ polystyrene beads at $\eta_s \approx 250$ for $\phi = 0.568$, a comparison that we consider to be acceptable. As mentioned, μ_p serves as a tuning parameter for frictional flows, so could be reduced to precisely match the experimental data.

Isotropic particle assemblies are generated in a 3-dimensional periodic domain of volume V. It is determined that approximately 5000 spheres are sufficient to capture the bulk rheology and microstructural phenomena independently of the system size. Bidispersity at a diameter ratio of 1 : 1.4 and volume ratio of 1 : 1 is used to minimize crystallization during flow (Ikeda et al., 2012). The particle assembly is sheared to steady state at constant rate $\dot{\gamma}$ and constant volume, equivalent to the application of Lees-Edwards boundary conditions (Lees and Edwards, 1972). The bulk stress, decomposed into contributions due to the hydrodynamic interaction and the particle-

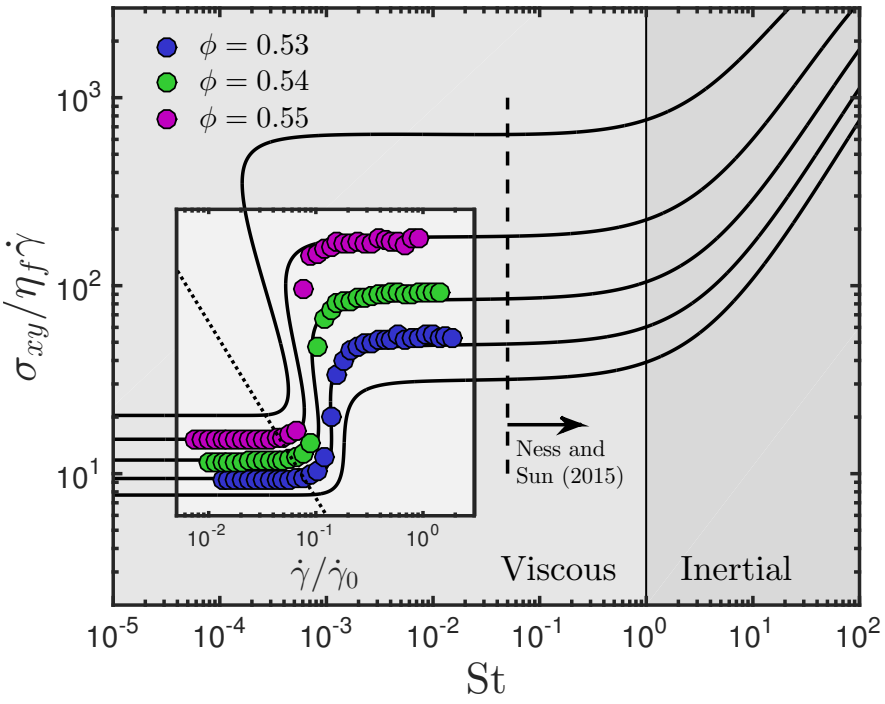

Fig. 3.3 Frictional shear thickening in the absence of inertia. Dashed line and arrow demonstrates the relative location of rheological data presented in Chapter 2 and Ness and Sun (2015); Coloured circles represent discrete element method simulation results; solid black lines represent constitutive model predictions; dotted black lines represent P^*.

particle interaction, is calculated from the particle force data (Ness and Sun, 2015), and given by Eqs. 3.13a and 3.13b

$$\boldsymbol{\sigma}^F = \frac{1}{V}\sum_i \sum_{i \neq j} \mathbf{r}_{ij}\mathbf{F}^l_{ij}, \tag{3.13a}$$

$$\boldsymbol{\sigma}^C = \frac{1}{V}\sum_i \sum_{i \neq j} \mathbf{r}_{ij}\mathbf{F}^c_{ij}. \tag{3.13b}$$

Data from 20 realizations with randomized initial particle positions are used to obtain ensemble-averaged stresses, which are further averaged over time in the steady-state. Under simple shear flow, the relevant stresses that will be discussed are the xy component σ_{xy} $(= \sigma^F_{xy} + \sigma^C_{xy})$, for flow direction x and gradient direction y, and the mean normal stress $\mathrm{P} = \frac{1}{3}(\sigma_{xx} + \sigma_{yy} + \sigma_{zz})$, for $\sigma_{xx} = \sigma^F_{xx} + \sigma^C_{xx}$ etc.

3.3.2 Macroscopic flow behaviour

Transitions between the viscous, inertial, soft particle and quasistatic regimes, as they are depicted in Fig 3.1, have been captured by discrete element method simulations

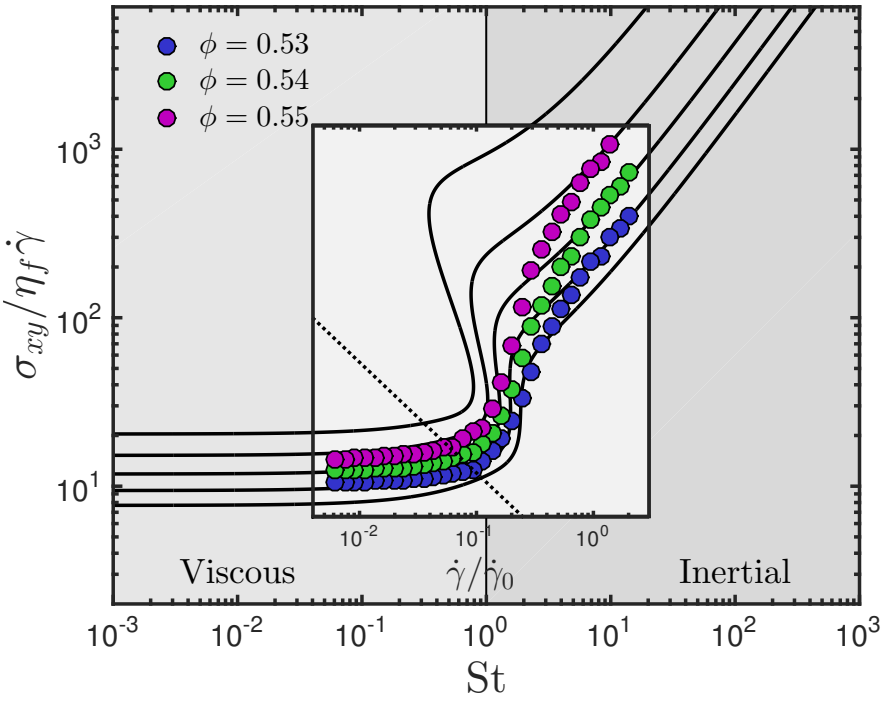

Fig. 3.4 Frictional shear thickening occurs concurrently with the onset of inertia; Coloured circles represent discrete element method simulation results; solid black lines represent constitutive model predictions; dotted black lines represent P^*.

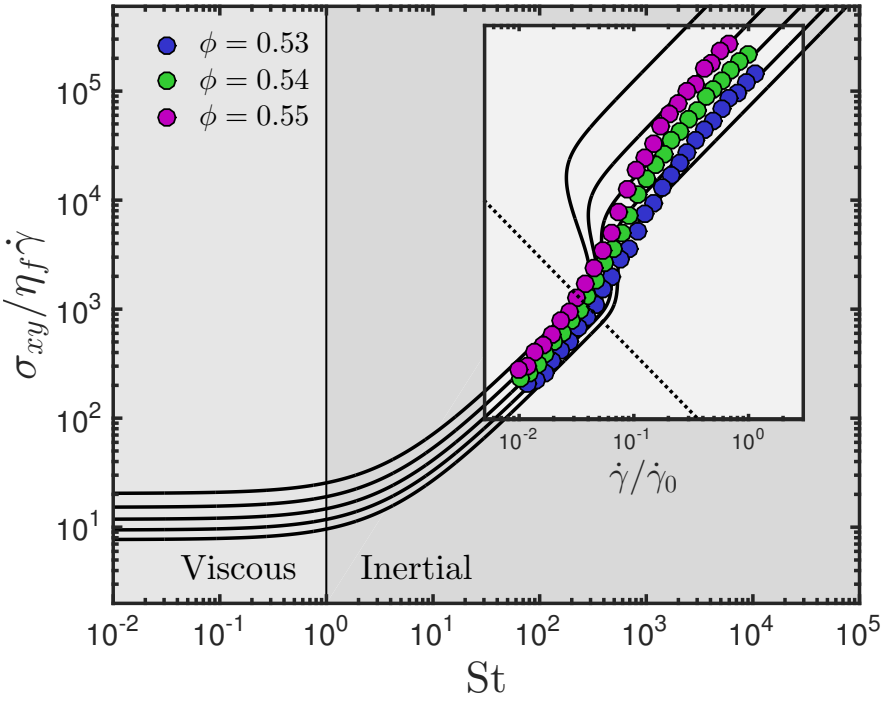

Fig. 3.5 Frictional shear thickening occurs in the presence of inertia. Coloured circles represent discrete element method simulation results; solid black lines represent constitutive model predictions; dotted black lines represent P^*.

and well characterised in Chapter 2. The steady state shear thickening behaviour predicted by the simulation model described in Sec 3.3.1 is presented as solid coloured symbols in Fig 3.3. We first focus on the results in Fig 3.3, which correspond directly to the frictional thickening transition highlighted within the viscous flow regime in Fig 3.1. Following (Mari et al., 2014), the shear rate $\dot{\gamma}$ is scaled with the reciprocal of a characteristic timescale for the relaxation of a frictional contact in a viscous fluid, given by $\dot{\gamma}_0 = F^{CL}/\frac{3}{2}\pi\eta_f d^2$. Consistent with the results obtained by Mari et al. (Seto et al., 2013; Mari et al., 2014), shear thickening between two quasi-Newtonian flow regimes is observed to occur at an onset stress P^*, independent of volume fraction and given by the dashed black line in Fig 3.3. Far below the onset stress, particles interact through forces predominantly $|\mathbf{F}_{i,j}^{c,n}| < F^{CL}$, that is, the forces are not sufficiently large to overcome the stabilisation, so frictional particle surfaces do not often come into contact. Conversely, the stabilisation is nearly always overcome (so contacts are nearly always frictional) at stresses far above the onset stress. We therefore make a distinction between purely frictionless behaviour at $\dot{\gamma}/\dot{\gamma}_0 = 0.01$ and purely frictional behaviour at $\dot{\gamma}/\dot{\gamma}_0 = 1$. The solid black lines represent predictions from the constitutive model described previously. The value of the onset stress is determined by the magnitude of F^{CL} specified in the contact potential, and is inferred from the simulation data. The annotation in Fig 3.3 illustrates the relative position of the simulation data presented in Chapter 2 and Ness and Sun (2015).

For volume fractions below approximately $\phi = 0.53$, the rheology exhibits continuous shear thickening behaviour, while between $\approx$0.53 and $\approx$0.58 the thickening is discontinuous, in that the constitutive model flow curves (solid black lines) exhibit the characteristic 'S-shaped' phenomena. The simulation data do not populate the 'S-shaped' region, probably because the simulations were performed for steady states at enforced constant shear rate, while the nature of flow in this regime is high unstable in reality. Probing the 'S-shaped' region through other simulation protocols is the subject of ongoing investigation and will be reported on in the future. For volume fractions above ϕ_m, the material "shear-jams" above P^*, as illustrated in Fig 3.1. When the onset stress is exceeded above ϕ_m, the material transitions from below to above its critical volume fraction, meaning the flow moves from a flowing, viscous state to a jammed state. Experimentally, this may be manifested as complete flow cessation, surface fracture, microstructural inhomogeneity, or volume fraction bifurcation, depending on the nature of the rheometer. Particle overlaps are allowed in the simulations, so the flow can enter a quasistatic state above jamming, in which the shear stress is rate-independent (Ness and Sun, 2015).

To bring the frictional thickening transition nearer to the inertial regime computationally, we simply reduce the viscosity of the interstitial fluid η_f, modifying $\dot{\gamma}_0 (= F^{CL}/\frac{3}{2}\pi\eta_f d_{ij}^2)$ and effectively moving the $0.01 < \dot{\gamma}/\dot{\gamma}_0 < 0.1$ window to a higher range of Stokes numbers. We can achieve an analogous effect by adjusting F^{CL}, comparable to modifying either the particle size or the particle surface chemistry experimentally. In terms of shear thickening, the effect of this adjustment is to alter the magnitude of the onset stress for frictional contacts such that it occurs in the vicinity of any desired Stokes number. Flow curves are presented for an onset stress that occurs close to $\mathrm{St} = 1$, Fig 3.4, and for an onset stress that occurs at very high St, Fig 3.5. In each case, a transition is observed between the frictionless and frictional states, similarly to the totally viscous ($\mathrm{St} \ll 0$) case. In Fig 3.4, the frictionless regime is observed for Stokes numbers up to around unity. Below this point, the suspension viscosity is independent of the Stokes number. For larger Stokes numbers, we observe frictional, inertial flow, with $\sigma_{xy}/\eta_f\dot{\gamma} \propto \dot{\gamma}$. The linear scaling of viscosity with shear rate above $\mathrm{St} = 1$ is due to inertial effects; the larger jump in viscosity (i.e. the super-linear behaviour between $\dot{\gamma}/\dot{\gamma}_0 = 0.1$ and $\dot{\gamma}/\dot{\gamma}_0 = 1$) is due to the onset of frictional contacts. We verify that the flow in each of these limits remains frictionless and frictional respectively at the microscale by examining the fraction of particle contacts that have exceeded F^{CL}. It is noted that the result in Fig 3.4 corresponds directly to the shear thickening phenomenon observed in the simulations reported by Fernandez (Fernandez et al., 2013), with a low shear rate regime in which lubrication dominates and particle friction is absent and a high shear regime dominated by friction with a viscosity that depends linearly on the shear rate. Fernandez also reports experimental findings for shear flow of polymer coated quartz miroparticle suspensions that appear qualitatively similar to Fig 3.4, though it is not clear whether the Stokes number is appropriate for such a comparison. Indeed, a similar set of experimental findings (Melrose et al., 1996) were previously attributed to enhanced *dynamic* friction due to increased resistance to fluid flow in the polymer layer. In Fig 3.5, the onset stress occurs at $\mathrm{St} \approx 300$, so both the frictionless and frictional states (again, these are verified by appealing to the frictional of individual contacts) exhibit $\sigma_{xy}/\eta_f\dot{\gamma} \propto \dot{\gamma}$ scaling, with super-linear behaviour representing the frictional transition. In each case, we obtain from the simulations excellent agreement with theoretical predictions in the limits of fully frictionless and fully frictional flow. There are, however, some differences in the transition region. We note, specifically, that the data match between simulations and theory is very good in the low Stokes number regime, but less good in the regimes for which particle inertia is relevant. Since the transition between frictionless and frictional rheology is closely related to the distribution of particle-particle contact forces (through Equation 3.4), this result implies that the

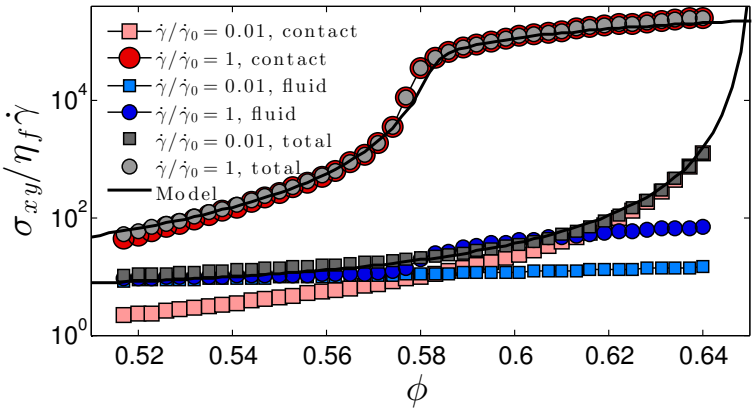

(a)

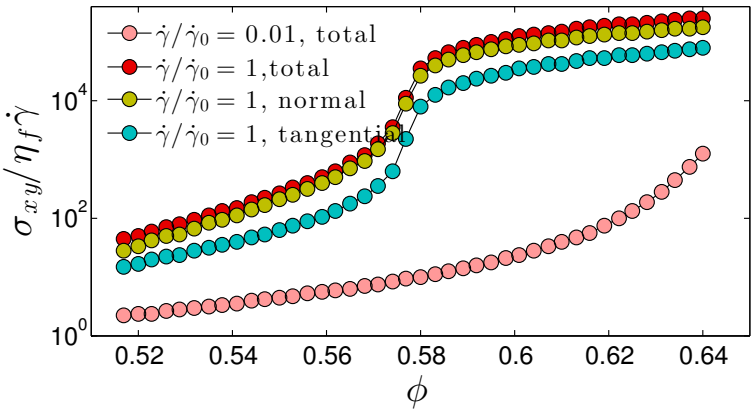

(b)

Fig. 3.6 (a) Divergence of viscosity contributions and model prediction; (b) Divergences of normal and tangential contact forces.

presence of particle inertia leads to a wider spread of particle-particle contact forces, meaning the shear-thickening transition happens over a wider range of bulk stresses.

These novel flow curves clearly illustrate the distinction between shear thickening driven by friction and by inertia. By tuning the particle and fluid properties appropriately, we have demonstrated that although (experimentally) the regimes may seem highly distinct and therefore challenging to achieve within a single system, both mechanisms might be made to arise concurrently, giving rise to new rheological behaviour. The challenge remains to achieve a sufficient understanding of the roles of particle surface chemistry, particle size and suspending fluid properties to realise and utilise these flow regimes experimentally.

For the entirely viscous case presented in Fig 3.3, we isolate the contact and fluid contributions to the viscosity and plot them against volume fraction for the frictionless ($\dot{\gamma}/\dot{\gamma}_0 = 0.01$) and frictional ($\dot{\gamma}/\dot{\gamma}_0 = 1$) limits in Fig 3.6a. It is noted that analogous results are obtained for the inertia-dominated cases, though the magnitude of the viscosity

is increased consistent with the linear viscosity scalings demonstrated in Figs 3.4 and 3.5. It is worth pointing out that the frictionless branches are entirely independent of our choice of μ_p, while the frictional branches are quantitatively dependent on μ_p, since static friction controls ϕ_m (Chialvo et al., 2012). Comparing the jumps from the frictionless to the frictional branch, it is demonstrated that the main increase in viscosity upon shear thickening is due to the contact contribution, while there is only a very minor increase in the fluid contribution (appreciable only at high volume fractions). While this suggests a configurational change leading to a change in the mean fluid film thickness or film number (resulting in a slightly increased fluid stress), it is not consistent with the notion of a large macroscopic transition to hydroclustering (Wagner and Brady, 2009) and a corresponding massive increase in viscous dissipation. We present the variation of this decomposition across intermediate shear rates (i.e. the interpolation between $\dot{\gamma}/\dot{\gamma}_0 = 0.01$ and $\dot{\gamma}/\dot{\gamma}_0 = 1$ at fixed ϕ) elsewhere (Lin et al., 2015), for the case of zero inertia. A corresponding decomposition of fluid and contact dissipation is given by Trulsson (Trulsson et al., 2012) for the onset of the inertial regime, showing even further dominance of contacts. We further decompose the contact stress into normal and tangential components, Fig 3.6b. We find that although the major difference between the frictionless and frictional limits at the individual particle level is the presence of tangential contact forces, the main contributor to the increase in the contact stress is in fact the normal component, rather than the tangential component, further corroborating the major role played by the particle configuration change induced by friction. This change can be understood from the perspective that the available degrees of freedom for particle motion decrease at the onset of frictional contacts, in that frictional particle assemblies require four contacts per particle for mechanical stability, while frictionless ones require six (Song et al., 2008). At fixed volume fraction, the transition to frictional behaviour is therefore manifested as an increased resistance to flow that necessitates greater particle overlaps and results in higher particle pressure. Interestingly, reducing the available degrees of freedom by means other than particle friction leads to the same observation. In a separate simulation we model steady shear at $\dot{\gamma}/\dot{\gamma}_0 = 0.01$, and at time t_1 we set all $z-$components of particle velocity and forces to zero, effectively imposing a 2D flow constraint. A large increase in the particle contribution to the stress is observed, consistent with the shear thickening behaviour presented here, that dissipates at a later time t_2 when the 2D flow constraint is relaxed. The dominant role of contacts, and the sensitivity to their nature (whether tangential forces may be sustained in addition to normal forces), remains a contentious issue; these results add further weight to the argument for frictional contacts as a crucial contributor to (non-inertial) shear thickening.

We have therefore demonstrated that the frictional thickening mechanism, modelled via a load-dependent particle friction in DEM and captured by the constitutive model, can occur within a variety of flow regimes and may thus couple or compete with inertial thickening. Both the DEM simulation and the constitutive model capture consistently such shear thickening phenomena. By isolating the contact and hydrodynamic contributions to the shear stress, we have shown that the shear thickening transition is heavily dominated by particle contacts as opposed to hydrodynamic effects. The large increase of contact stress upon shear thickening has been attributed mainly to normal contact forces, though we note that the tangential contact forces present in the thickened regime largely exceed the normal forces present in the non-thickened state.

3.3.3 Microscopic analysis

We use microscale information to further characterise the distinction between the thickened (frictional) and non-thickened (frictionless) states. The microstructure is quantified using the particle-particle contact number and the fabric, or net-orientation, of these contacts, while particle-level dynamics are quantified using correlation functions in displacement and velocity. Work in rheo-imaging of colloidal systems (Isa et al., 2007; Ballesta et al., 2008) has demonstrated the potential for these dynamic properties to be obtained and quantified experimentally for shear thickening materials. In addition, further experiments (Clara-Rahola et al., 2015) have led to their successful quantification for a sheared, highly polydisperse emulsion, using confocal imaging. We anticipate that future such analyses for shear thickening suspensions will benefit from, and corroborate, the results presented in this chapter.

The microstructure is characterised based on two separate length scales. For the contact number Z, we calculate (a) the average number of frictionless, $|\mathbf{F}_{i,j}^{c,n}| < F^{CL}$ interactions per particle; (b) the average number of frictional, $|\mathbf{F}_{i,j}^{c,n}| > F^{CL}$ contacts per particle. For the contact fabric, we adopt the formulation used by Sun and Sundaresan (Sun and Sundaresan, 2011) given in Equation 2.5. Under shear flow, contacts preferentially align along the compressive axis at (or close to) 45° to the $x-$ and $y-$axes (the flow and gradient directions respectively), with the corresponding shear component of $\mathbf{A}$, $|A_{12}|$ quantifying the extent of the anisotropic alignment. $A_{12} = 0.5$ represents perfect alignment of all contacts in the compressive axis, while $A_{12} = 0$ represents perfect isotropy. As with the contact number, we quantify the shear component of the fabric based on both the network of frictionless contacts and that of frictional contacts. The non-affine motion is quantified by first obtaining a coarse-grained velocity profile for the shearing flow and subtracting the appropriate value of this coarse-grained velocity (specifically the flow direction component V_x; V_y and V_z tend to 0 upon averaging) from

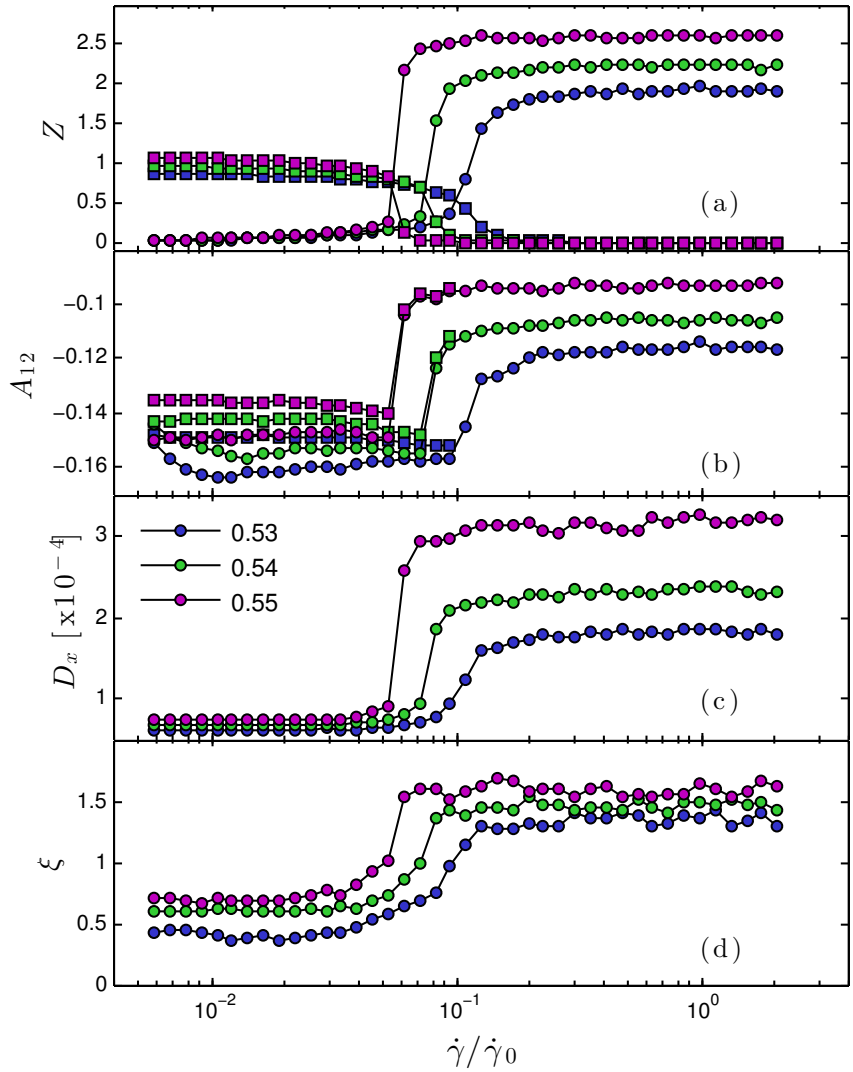

Fig. 3.7 Evolution of microscale structures and dynamics across the frictional shear-thickening transition. (a) Mean number of particle-particle contacts. Squares represent low force contacts for which friction is not activated; circles represent high force contacts for which friction is activated. (b) Shear component of the fabric tensor. Squares represent low force contacts for which friction is not activated; circles represent high force contacts for which friction is activated. (c) Effective diffusion coefficient. (d) Velocity correlation length as defined by Eq 3.14.

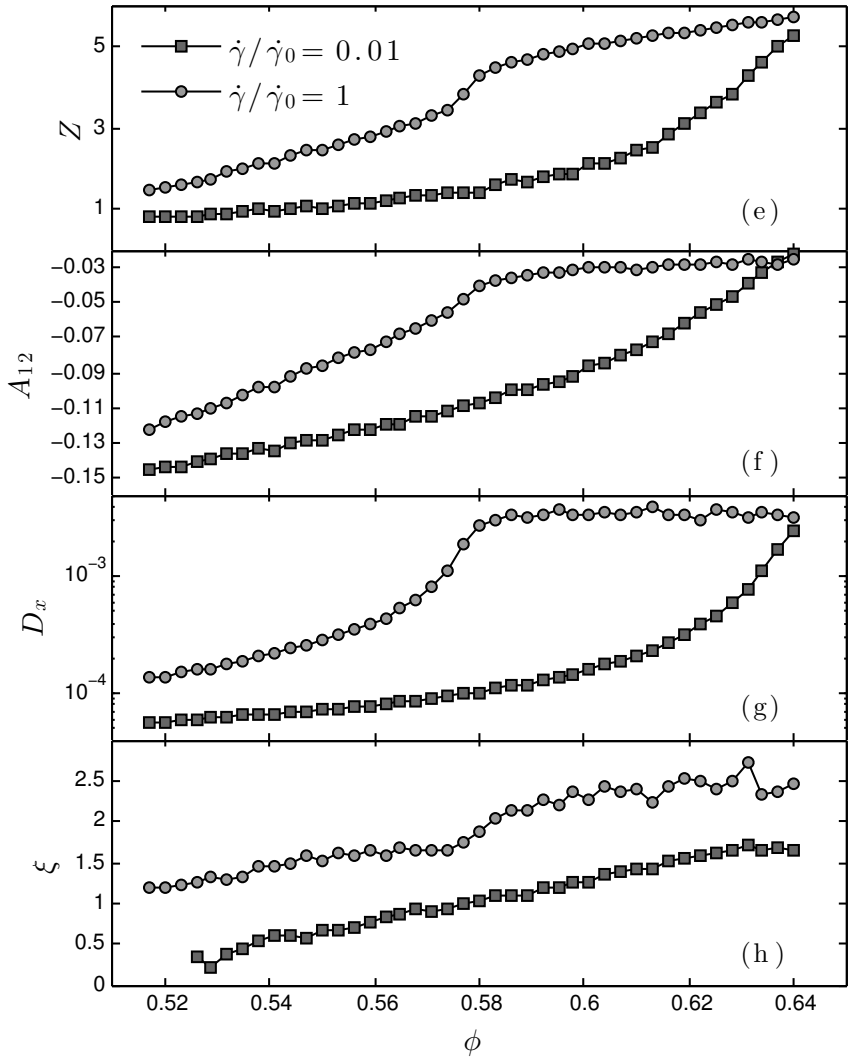

Fig. 3.8 Evolution of microscale structures and dynamics with volume fraction, for frictional and non-frictional states. (a) Mean number of particle-particle contacts. Squares represent low force contacts for which friction is not activated; circles represent high force contacts for which friction is activated. (b) Shear component of the fabric tensor. Squares represent low force contacts for which friction is not activated; circles represent high force contacts for which friction is activated. (c) Effective diffusion coefficient. (d) Velocity correlation length.

each particle's velocity vector to obtain the "fluctuating" velocity component. From these fluctuating velocities we obtain the mean squared displacement (MSD), averaged across particles and time steps. Plotting the MSD ($\langle x^2 \rangle$) versus strain magnitude ($\dot{\gamma}t$) yields a linear diffusive behaviour that is independent of Stokes number, for the case of zero inertia. We consider the evolution of diffusion coefficient D_x (*i.e.* $\langle x^2 \rangle = \mathrm{D}_x t$) with shear rate. In addition, we calculate the correlation of the fluctuating velocity vectors according to Lois (Lois et al., 2007; Sun et al., 2006; Ness and Sun, 2015)

$$c(r) = \frac{\sum_i \sum_{j>i} \overline{\mathbf{v}}_i \cdot \overline{\mathbf{v}}_j \delta(|\mathbf{r}_{ij}| - r)}{\sum_i \sum_{j>i} \delta(|\mathbf{r}_{ij}| - r)}, \tag{3.14}$$

where $\overline{\mathbf{v}}_i$, $\overline{\mathbf{v}}_j$ are particle velocity vectors averaged over a length of time sufficient to give an averaged particle displacement due to the mean flow of approximately $0.5d$. It is found that the correlation decays approximately exponentially with the distance between particle centres r. We therefore fit a simple functional form $C(r) = ke^{-r/\xi}$, where ξ takes units of particle diameter and is hereafter referred to as the "correlation length", and k is a constant prefactor. The evolution of these microscale quantities is presented in Figs 3.7 and 3.8 as a function of $\dot{\gamma}/\dot{\gamma}_0$ at three volume fractions, and as a function of volume fraction at $\dot{\gamma}/\dot{\gamma}_0 = 0.01$ (frictionless) and $\dot{\gamma}/\dot{\gamma}_0 = 1$ (frictional), for the case of zero inertia.

In Fig 3.7a we demonstrate the increasing number of frictional contacts and the diminishing of frictionless interactions as the shear rate is increased and the onset stress is exceeded. The results presented here are consistent with the evolution of the fraction of frictional contacts presented by Mari et al. (Mari et al., 2014). It is further noted that for a fixed volume fraction, the number of direct particle-particle contacts that exist in the frictional, shear thickened state exceeds the number of frictionless, normal interactions that were present in the non-thickened state. This suggests that in the process of becoming frictional, the particles have rearranged into a distinct microstructural configuration. The evolution of A_{12}, Fig 3.7b, confirms this. In the non-thickened state, we observe distinct microstructures for the networks of frictionless and frictional contacts, though the number of frictional contacts is very small. At each volume fraction, contacts for which F^{CL} is exceeded tend to be aligned more strongly with the compressive flow direction than those contacts for which friction is not activated. Upon shear thickening, however, the fabric of the frictional contact network moves closer to zero, while the frictionless fabric disappears due to an absence of such interactions far above the onset stress. The microstructural information suggests that the shear thickening transition brings the particle configuration closer to what might be expected for a quasistatic, rate-independent flow, where $Z \approx 4$ and $A_{12} \approx -0.03$ (Sun

and Sundaresan, 2011; Song et al., 2008) for the frictional cases. Shear thickening can therefore, in this sense, be considered analogous to an increase in volume fraction at constant friction, in that the central change in each case is that the departure from the critical volume fraction, quantified as $|\phi - \phi_c|$, decreases. It is noted that the inertial cases exhibit very similar behaviour with respect to the microstructural properties. The exception is a very modest increase in contact number, smaller than 10%, for the inertia-dominated flows.

Particle level dynamics are found to exhibit analogous behaviour across the thickening transition. In Fig 3.7c, we present the evolution of D_x with $\dot{\gamma}/\dot{\gamma}_0$. Rescaling D_x with $\dot{\gamma}$ we clearly demonstrate rate independence of non-affine motions (specifically $D_x \propto \dot{\gamma}$) in the frictionless and frictional limits, while there is a significant jump in the effective diffusion as the suspension shear thickens. As with the microstructure, this is consistent with the suspension becoming closer to its jamming volume fraction as the shear rate or stress is increased. As the extent of frictional behaviour increases, particles form more contacts and are required to deviate further from an affine trajectory in order to pass each other as they are subjected to shear at the same or higher rate. The average displacement deviation from the mean flow therefore undergoes a step change. A similar transition is observed in the velocity correlation length, Fig 3.7d, which indicates that in the shear thickened regime, particle trajectories tend to be more correlated with those of their immediate neighbours, suggesting a tendency towards collective motion of particle groups. Though this is, indeed, qualitatively reminiscent is some respects to the "hydroclustering" behaviour previously reported (Wagner and Brady, 2009), we note that the particle groups that collectively move in the present simulations are found to be unanimously under frictional contact, rather than separated by lubrication layers. We therefore suggest that while clustering is apparent, it is, in this case, more accurately described as *frictional*- rather than *hydro*-clustering. Indeed, experimental techniques that purportedly demonstrate hydroclustering are in fact unable to distinguish between these two mechanisms of dynamic correlation (Cheng et al., 2011).

We demonstrate in Fig 3.8 that each of the transitions presented in Fig 3.7 corresponds to a shift between distinct and well-defined branches in each of the microscale parameters investigated, in the thickened ($\dot{\gamma}/\dot{\gamma}_0 = 1$) and non-thickened ($\dot{\gamma}/\dot{\gamma}_0 = 0.01$) limits. In addition, it is observed that the differing divergences of each pair of branches with volume fraction is consistent with that observed for the bulk suspension viscosity, namely the frictional, high stress branch diverges near $\phi = \phi_m$ and is thereafter consistent with quasistatic behavior (Sun and Sundaresan, 2011), while the frictionless, low stress branch diverges towards $\phi = \phi_{RCP}$. We note that the divergence is less

clear for the correlation length ξ than for the other microscale parameters investigated, which can be attributed to the relatively small domain size, which places limits on the length scale over which correlations can be observed. The distinction between branches, however, is convincing. A demonstration of such contrasting microscale divergences in the thickened and non-thickened rheological regimes in an experimental system would prove invaluable in corroborating this work, and in highlighting the essential role of friction as the origin of the distinct rheologies below and above shear thickening.

3.4 Concluding remarks

In this chapter we have explicitly demonstrated the distinction between frictional and inertial shear thickening mechanisms, and illustrated their presence as separate regimes on the broader flow map of dense suspensions. In practice, frictional shear thickening is typically observed for colloidal ($d \lesssim 1$ μm) suspensions for which inertia is always absent (or negligible), while the inertial shear thickening typically occurs in granular $d \gtrsim 100$ μm) suspensions for which friction is always present (or more accurately starting from exceedingly low Stokes numbers). Our simulation results suggest that in principle thickening may occur in a mixed mode with both mechanisms playing a role. This may indeed be the case for a suspension of mixed colloidal and granular particles, as hinted by the recent experiments on shear thickening with intermediate particle sizes (Guy et al., 2015), which indicate that the frictional thickening onset stress scales with the inverse square of particle size. There are of course many other possible scenarios where mixed thickening could occur as suggested from our simulations, though it remains to be seen whether such rheology can be observed experimentally.

Transitions in the microstructural and dynamic variables are observed across the frictional thickening transition, and we have shown that the microstructure of the shear thickened and non-thickened states exhibit distinct divergences with respect to volume fraction, indicating the microscale mechanism for the same behaviour of the bulk suspension viscosity. We expect the results presented here to provide useful means of analysing new results obtained from particle microscopy and imaging of model experimental systems.

Chapter 4

Two-scale evolution during shear reversal in dense suspensions

The previous chapters have focussed on the *steady state* flow behaviour of dense suspensions. In order to fully understand the rheology of such materials, however, it is essential to also understand the non-steady behaviour, which may arise in practice in transient or intermittent processing conditions or during flow instabilities. Classical experiments in non-steady dense granular flows, reviewed below, have revealed puzzling temporal viscosity evolutions, which have been interpreted as representing distinct microstructurally sensitive particle-particle and particle-fluid contributions. In this chapter, we provide a detailed mechanism to explain the transient behaviour, and thereby establish a protocol for isolating the hydrodynamic and contact stresses experimentally. Shear reversal simulations are employed to explore the non-steady rheology of dense, non-Brownian suspensions. The transient stress response to an abrupt reversal of the direction of shear shows rate-independent, nonmonotonic behaviour, capturing the salient features of the corresponding classical experiments. Based on analyses of the hydrodynamic and particle contact stresses and related contact networks, we demonstrate distinct responses at small and large strains, associated with contact breakage and structural re-orientation, respectively, emphasising the importance of particle contacts. Consequently, the hydrodynamic and contact stresses evolve over disparate strain scales and with opposite trends, resulting in nonmonotonic behaviour when combined. We further elucidate the roles of particle roughness and repulsion in determining the microstructure and hence the stress response at each scale.

4.1 Introduction

The flow behaviour of dense suspensions is strongly affected by details of the microstructure and interparticle forces (Mewis and Wagner, 2012). Recent theoretical (Wyart and Cates, 2014), experimental (Fernandez et al., 2013; Guy et al., 2015) and computational (Seto et al., 2013; Mari et al., 2014) work suggests that particle surface contacts make a major contribution to suspension rheology, though their precise role, and importance relative to hydrodynamic interactions, is still debated. To this end, shear reversal experiments, in which the flow direction is suddenly reversed, prove to be an elegant means of estimating the contact stress (CS) contribution, while probing microstructural anisotropy. For example, it was shown that following a flow cessation period, the shear (Gadala-Maria and Acrivos, 1980) (or normal (Kolli et al., 2002)) stress in a suspension of ~ 40 μm polystyrene spheres reaches an "immediate" peak upon reversal, then evolves nonmonotonically over a strain of ≈ 3 to its steady state. The large-strain evolution was attributed to microstructural realignment (Gadala-Maria and Acrivos, 1980); the initial stress peak was hypothesized to represent the hydrodynamic stress (HS), leading to a suggestion of the larger role played by particle contacts in denser suspensions (Kolli et al., 2002). It remains difficult to isolate the evolution of the CS and HS contributions and link the microstructural effect to the puzzling nonmonotonic behaviour. In the present chapter, we reveal responses at two disparate strain scales, an elegent manifestation of the microfragile vs. macrofragile distinction proposed by Cates et al. (Cates et al., 1998). The small strain stress peak is shown to be a hydrodynamic response to surface-contact breakage, but is distinct from the steady state HS. The large strain scale is determined by microstructural reorientation, as predicted (Gadala-Maria and Acrivos, 1980). The nonmonotonic behaviour is a combined effect of the CS and HS evolutions. We show that different surface characteristics control the stress response at different strain scales, meaning our two-scale explanation, and hence the micro- versus macro- fragility paradigm, can be applied usefully to a wide range of suspended systems.

4.2 Simulation model

The numerical model employed in this Chapter follows that used in Chapter 2, but we further include logarithmic terms in the lubrication force model as described fully in Equation 4.2. We solve the equations of motion numerically (Plimpton, 1995) for neutrally buoyant suspended non-Brownian particles, subject to forces and torques arising due to hydrodynamics and particle surface contact (Cundall and Strack, 1979).

For dense suspensions, in which the average surface separation between neighbouring particles becomes very small, the full hydrodynamic resistance matrix (Brady and Bossis, 1988) can be suitably approximated by resolving pairwise, frame-invariant lubrication forces (Ball and Melrose, 1997), which diverge at contact and significantly exceed the long-range force components. Such a simplification has been proven to be effective in capturing the behaviour of dense suspensions (Trulsson et al., 2012; Mari et al., 2014; Kumar and Higdon, 2010). For an interaction between particles i and j, (with particle and fluid density ρ) the force and torque on particle i due to hydrodynamic lubrication can be expressed as

$$\begin{aligned} \boldsymbol{F}^l_{ij} &= -a_{sq} 6\pi\eta_f (\mathbf{v}_i - \mathbf{v}_j)\cdot \mathbf{n}_{ij}\mathbf{n}_{ij} \\ &\quad - a_{sh} 6\pi\eta_f (\mathbf{v}_i - \mathbf{v}_j)\cdot (\boldsymbol{I} - \boldsymbol{n}_{ij}\boldsymbol{n}_{ij}), \end{aligned} \tag{4.1a}$$

$$\begin{aligned} \boldsymbol{\Gamma}^l_{ij} &= -a_{pu}\pi\eta_f d_i^3 (\boldsymbol{\omega}_i - \boldsymbol{\omega}_j)\cdot (\boldsymbol{I} - \boldsymbol{n}_{ij}\boldsymbol{n}_{ij}) \\ &\quad - \frac{d_i}{2}\left(\boldsymbol{n}_{ij}\times \boldsymbol{F}^l_{ij}\right), \end{aligned} \tag{4.1b}$$

for particle diameter d_i, fluid viscosity η_f, particle translational and rotational velocity vectors $\boldsymbol{v}_i$ and $\boldsymbol{\omega}_i$ respectively, centre-to-centre unit vector $\boldsymbol{n}_{ij}$ pointing from particle j to i and identity tensor $\boldsymbol{I}$, with the squeeze a_{sq}, shear a_{sh} and pump a_{pu} resistance terms as derived by (Kim and Karrila, 1991), for $\beta = d_j/d_i$, as:

$$\begin{aligned} a_{sq} &= \frac{\beta^2}{(1+\beta)^2}\frac{d_i^2}{4h} + \frac{1+7\beta+\beta^2}{5(1+\beta)^3}\frac{d_i}{2}\ln\left(\frac{d_i}{2h}\right) \\ &\quad + \frac{1+18\beta-29\beta^2+18\beta^3+\beta^4}{21(1+\beta)^4}\frac{d_i^2}{4h}\ln\left(\frac{d_i}{2h}\right), \end{aligned} \tag{4.2a}$$

$$\begin{aligned} a_{sh} &= 4\beta\frac{2+\beta+2\beta^2}{15(1+\beta)^3}\frac{d_i}{2}\ln\left(\frac{d_i}{2h}\right) \\ &\quad + 4\frac{16-45\beta+58\beta^2-45\beta^3+16\beta^4}{375(1+\beta)^4}\frac{d_i^2}{4h}\ln\left(\frac{d_i}{2h}\right), \end{aligned} \tag{4.2b}$$

$$\begin{aligned} a_{pu} &= \beta\frac{4+\beta}{10(1+\beta)^2}\ln\left(\frac{d_i}{2h}\right) \\ &\quad \frac{32-33\beta+83\beta^2+43\beta^3}{250(1+\beta)^3}\frac{d_i}{2h}\ln\left(\frac{d_i}{2h}\right). \end{aligned} \tag{4.2c}$$

The separation between particles i and j is calculated according to $h = |\boldsymbol{r}_{ij}| - \frac{d_i+d_j}{2}$ for centre-to-centre vector $\boldsymbol{r}$. We calculate the lubrication force when the interparticle gap h is smaller than $h_{\max} = 0.05d$ (where d is the harmonic average particle diameter). An increasing body of evidence (Fernandez et al., 2013; Guy et al., 2015) shows that direct particle-particle surface contacts can play a major role in suspension rheology; indeed,

simulations that strictly resolve lubrication forces (treating particles as ideally hard and ideally smooth) (Bossis and Brady, 1989) have proven to be inadequate for capturing dense suspension rheology for cases where particle-particle contacts are presumed to be important. We therefore truncate the lubrication divergence and regularize the contact singularity at a typical asperity length scale $h_{\min}$ ($= 0.001d$ unless specified otherwise), i.e., setting $h = h_{\min}$ in the force calculation, when $h < h_{\min}$. We use a value of $\eta_f = 0.1$ [viscosity unit: $\rho d^2/t$].

Mechanical contact occurs at $h \leq 0$, giving normal repulsive and tangential forces described by a linear spring model and related through a Coulomb friction coefficient μ_p ($= 0.2$ unless specified otherwise) (Cundall and Strack, 1979). A linear (as opposed to Hertzian) spring is chosen for convenience, though we expect Hertzian results to lead to identical conclusions reagarding the respective roles of contacts and lubrication. The normal ($\boldsymbol{F}^{c,n}$) and tangential ($\boldsymbol{F}^{c,t}$) contact force and torque $\boldsymbol{\Gamma}^c$ are given by

$$\boldsymbol{F}^{c,n}_{ij} = k_{\mathrm{n}}\delta\boldsymbol{n}_{\mathrm{ij}}, \tag{4.3a}$$

$$\boldsymbol{F}^{c,t}_{ij} = -k_{\mathrm{t}}\boldsymbol{u}_{\mathrm{ij}}, \tag{4.3b}$$

$$\boldsymbol{\Gamma}^{c}_{ij} = -\frac{d_i}{2}(\boldsymbol{n}_{ij} \times \boldsymbol{F}^{c,t}_{ij}), \tag{4.3c}$$

for a collision between particles i and j with normal and tangential spring stiffnesses k_n and k_t respectively [$k_n = 20000$, unit: $\rho d^3/t^2$ and $k_t = (2/7)k_n$], particle overlap δ and tangential displacement $\boldsymbol{u}_{\mathrm{ij}}$.

The bulk stress tensor is calculated from the particle force and velocity data. It is decomposed into contributions due to the hydrodynamic lubrication interaction and the particle-particle interaction, given by Eqs. 6.6a and 6.6b, respectively,

$$\boldsymbol{\sigma}^{l}_{ij} = \frac{1}{V}\sum_i \sum_{i \neq j} \boldsymbol{r}_{ij}\boldsymbol{F}^{l}_{ij}, \tag{4.4a}$$

$$\boldsymbol{\sigma}^{c}_{ij} = \frac{1}{V}\sum_i \sum_{i \neq j} \boldsymbol{r}_{ij}(\boldsymbol{F}^{c,n}_{ij} + \boldsymbol{F}^{c,t}_{ij}). \tag{4.4b}$$

In the following discussion, we consider the shear components of the above stress tensors corresponding to the direction of the applied deformation, σ^l and σ^c, as well as the mean of the diagonal components, namely the "pressures" P^l and P^c. The hydrodynamic stress σ^l is further decomposed in two ways. In the first, we isolate the contributions from normal forces (the squeeze a_{sq} terms) and tangential forces (the shear a_{sh} and pump a_{pu} terms) (Ball and Melrose, 1997) as $\sigma^l_{\mathrm{normal}}$ and $\sigma^l_{\mathrm{tangential}}$ respectively. In the second, we isolate contributions from opening and closing particle pairs (pairs for which

$dh/dt > 0$ and $dh/dt < 0$ respectively), presented as $\sigma^l_{\text{opening}}$ and $\sigma^l_{\text{closing}}$. It is noted that $\sigma^l_{\text{opening}} + \sigma^l_{\text{closing}} = \sigma^l$ and $\sigma^l_{\text{normal}} + \sigma^l_{\text{tangential}} = \sigma^l$. Assemblies of 5000 spheres are sufficiently large to achieve system size independence, and bidispersity with diameter ratio 1 : 1.4 prevents crystallisation (Ikeda et al., 2012). Simulation results are ensemble-averaged over 20 realisations with different initial particle configurations. We note that although the overlap is exceedingly small, typically of order $10^{-7}d$ in the Stokesian regime (Ness and Sun, 2015), it can lead to qualitatively different rheology from that produced using the "ideal" hard-sphere model, as demonstrated later. The present technique produces results at the dense limit (solid volume fraction $\phi \gtrsim 0.45$) closely approximating those that would be obtained by fully resolving the hydrodynamics (e.g. (Brady and Bossis, 1985)), but assuming particles co-move with fluid at the mean flow level (Ball and Melrose, 1997), valid for shear flows. We verify this by incorporating an additional drag force, similar to (Trulsson et al., 2012), which leads to a negligible increase in the calculated suspension viscosity. The particle assemblies are subjected to rate ($\dot{\gamma}$) controlled simple shear flow in a 3-dimensional periodic domain at constant ϕ ($= 0.54$) and Stokes numbers St ($= \rho\dot{\gamma}d^2/\eta_f$) $< 10^{-2}$, inhibiting particle inertia. The suspension is first sheared from $\dot{\gamma}t = -8 \rightarrow -2$, reaching steady flow. No shear is applied for $\dot{\gamma}t = -2 \rightarrow 0$. From $\dot{\gamma}t = 0$, the suspension is sheared in the opposite direction until a new steady state is obtained.

4.3 Stress and microstructure evolution

The total stress ($\boldsymbol{\sigma} = \boldsymbol{\sigma}^c + \boldsymbol{\sigma}^l$) evolution, Fig 4.1(a), is strikingly reminiscent of classical experiments (Gadala-Maria and Acrivos, 1980; Narumi et al., 2002; Kolli et al., 2002). Rate-independence is demonstrated by collapsing stress components with the respective steady state total stress $\bar{\boldsymbol{\sigma}}$, for multiple $\dot{\gamma}$. Fig. 4.2 shows the microstructural evolution, characterised by a mechanical coordination number Z_c, the mean number of per particle contacts which support a contact stress greater than 10^{-6} of the mean steady-state stress $\bar{P}$, a surface coordination number $Z_{\text{h}_{\text{min}}}$ counting all pairs with $h < h_{\text{min}}$ and a fabric tensor (Sun and Sundaresan, 2011; Ness and Sun, 2015), $\boldsymbol{A} = 2/(Z_{\text{h}_{\text{max}}}N)\sum_{h<h_{\text{max}}} \boldsymbol{n}_\alpha\boldsymbol{n}_\alpha - \frac{1}{3}\boldsymbol{I}$ (see also Equation 2.5). Under shear flow, particles preferentially align along the compressive axis at 45° with the shear component of $\boldsymbol{A}$, $|A_{12}| = 0.5$ representing perfect alignment of all contacts and $A_{12} = 0$ representing perfect isotropy.

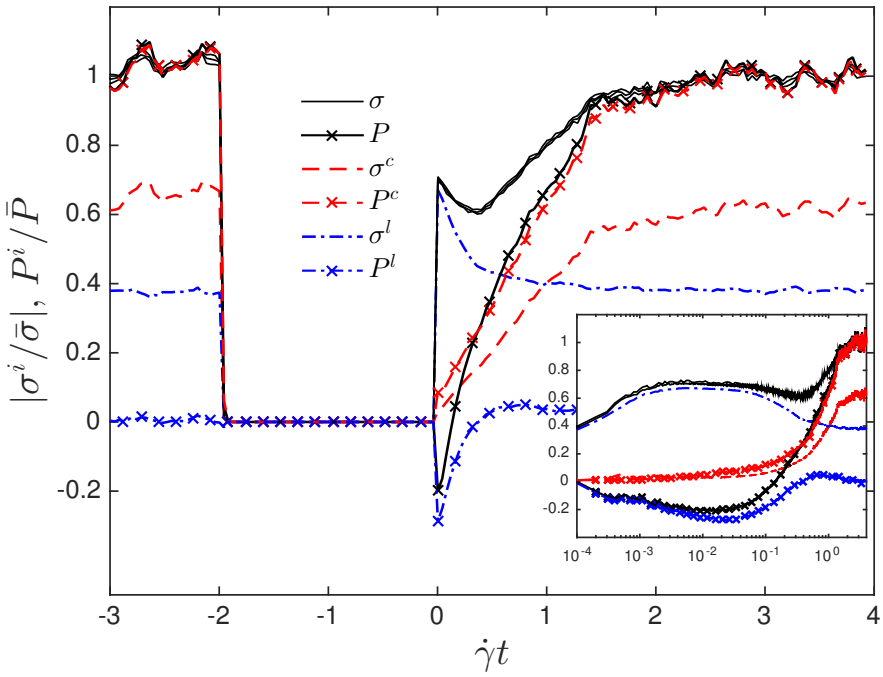

(a)

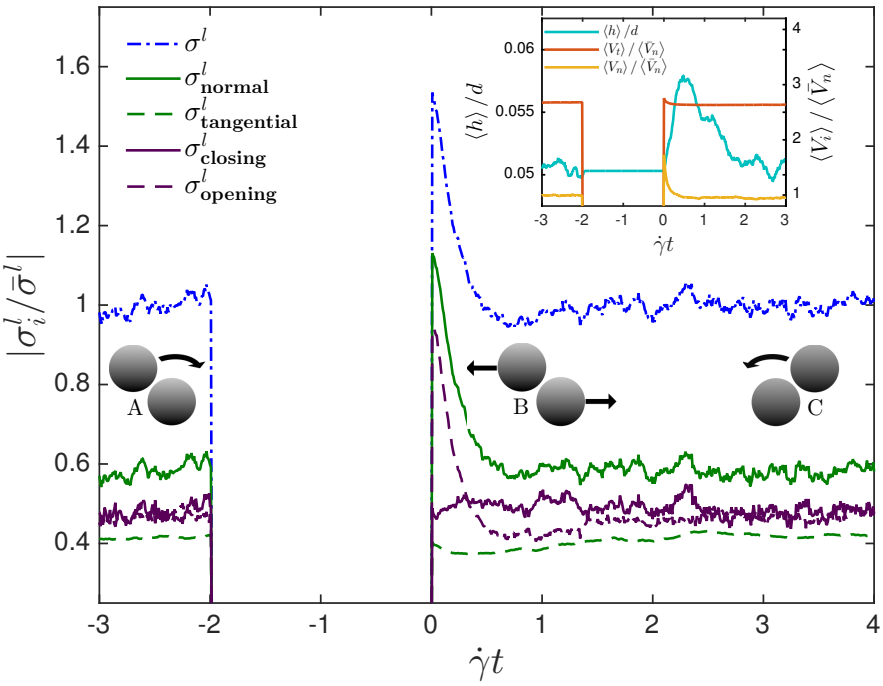

(b)

Fig. 4.1 (a) Evolution of stresses following reversal at $\dot{\gamma}t = 0$, showing total (σ, P), contact (σ^c, P^c) and fluid (σ^l, P^l) contributions, each scaled by the steady state total stress ($\bar{\sigma}$, $\bar{P}$). Multiple lines for σ illustrate $\dot{\gamma}$ independence. Inset: Same data with logarithmic x-axis; (b) σ^l components arising from (i) normal and tangential forces; (ii) opening and closing interparticle gaps. Inset: Evolution of the mean fluid film thickness $\langle h\rangle$ and scaled mean neighbouring-particle normal $\langle V_n\rangle / \langle\bar{V}_n\rangle$ and tangential $\langle V_t\rangle / \langle\bar{V}_n\rangle$ velocity magnitudes. Embedded: particle-pair configurations corresponding to different times.

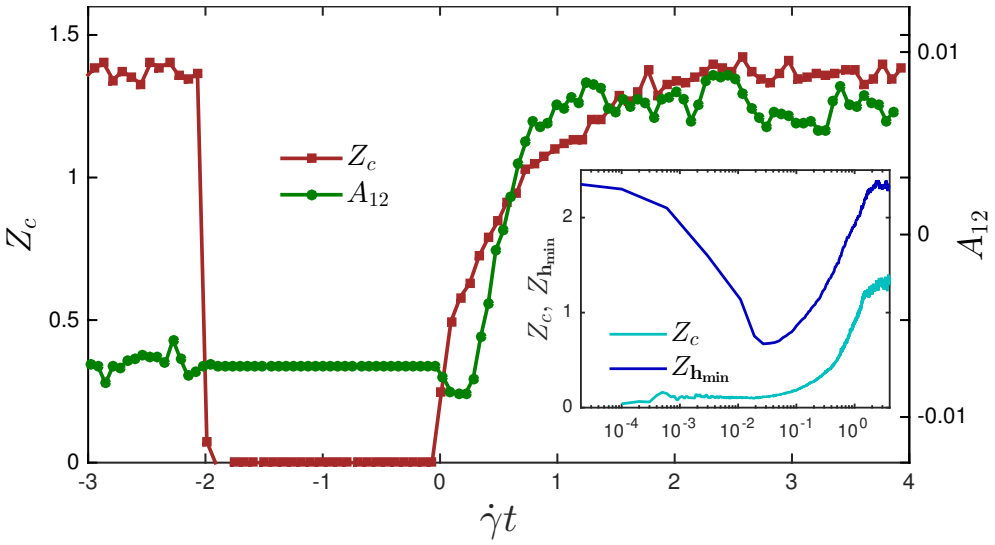

Fig. 4.2 Evolution of coordination number Z_c and shear fabric component A_{12}. Inset: Coordination Z_c and surface coordination $Z_{\mathrm{h_{min}}}$ evolution, with logarithmic x-axis.

4.3.1 Steady flow and cessation

In the steady state ($\dot{\gamma}t < -2$, Fig 4.1(a)), the contact stress contribution is surprisingly large given the small contact overlaps, representing 60% of the total shear stress. The relative contribution is ϕ-dependent, e.g., at $\phi = 0.47$, we found $\sigma^c \approx 0.3\sigma$ (Ness and Sun, 2015). We find $Z_c \approx 1.5$ and the shear component of $\boldsymbol{A}$, $A_{12} \approx -0.01$, indicating persistent mechanical contacts and an anisotropic network of lubrication films. In this condition, relative particle motions are as illustrated in particle-pair diagram A, Fig 4.1(b), a configuration that results in the mean relative normal velocity of neighbouring particles $\langle V_n \rangle$ being smaller than the mean relative tangential velocity $\langle V_t \rangle$, highlighted in Fig 4.1(b) Inset, which gives these quantities scaled by the steady state value of $\langle V_n \rangle$, $\langle \bar{V}_n \rangle$. This leads to comparable normal and tangential lubrication forces (and corresponding stress contributions $\sigma^l_{\mathrm{normal}}$ and $\sigma^l_{\mathrm{tangential}}$ as decomposed in Fig. 4.1(b)), in spite of the order of magnitude difference expected from their respective $1/h$ versus $\ln(1/h)$ dependence. The average number of particle pairs moving together or apart is equal at steady state, as required to satisfy the constant volume constraint, resulting in constant mean lubrication film thickness $\langle h \rangle$, Fig. 4.1(b) Inset, equal stress contributions $\sigma^l_{\mathrm{opening}}$ and $\sigma^l_{\mathrm{closing}}$, Fig. 4.1(b), and $\bar{P}$ dominated by P^c, Fig 4.1(a).

Upon flow cessation ($\dot{\gamma}t = -2$), the contact stress relaxes together with the hydrodynamics stress, suggesting that caution should be exercised when interpreting the "instantaneous" stress loss as entirely hydrodynamic in such experiments (Mewis and Wagner, 2012; O'Brien and Mackay, 2000). Correspondingly, Z_c drops to zero in the relaxation period, though a small portion of weak contacts relax more slowly due to

confinement and fluid overdamping. The shear-induced anisotropic microstructure pertaining to hydrodynamics, however, remains intact throughout the relaxation period, evidenced by constant A_{12} and $Z_{\mathrm{h}_{\min}}$ (Fig 4.2 and Inset, $Z_{\mathrm{h}_{\min}}(\dot{\gamma}t \to 0) = Z_{\mathrm{h}_{\min}}(\dot{\gamma}t = 4)$), implying the steady state HS can be recovered instantaneously (with opposite sign) upon shear reversal.

4.3.2 Shear reversal: micro- and macro-strain responses

Indeed, σ^l does resume its steady state magnitude upon reversal for strains $\leq 10^{-4}$, Fig. 4.1(a) Inset. It then surges to a significant peak, around 50% greater than the steady value, at strain 10^{-3}, sustaining until about 10^{-2} where it starts to subside. Resumption of the steady value followed by a demonstrable peak is also observed for P^l over the same strain scale. We attribute this small-strain surge, the manifestation of a microfragile response (Cates et al., 1998), to the pulling apart of particle surfaces at the $h_{\min}$ ($= 10^{-3}d$) scale due to the new (reversed) load being incompatible with the present microstructural alignment. This is clearly demonstrated by the coincident decrease of $Z_{\mathrm{h}_{\min}}$, which reaches a minimum near 10^{-2}. The mechanism is further evidenced by the significantly greater $\langle V_n \rangle$ than under steady flow, the dominance of $\sigma^l_{\mathrm{normal}}$ and $\sigma^l_{\mathrm{opening}}$, and the tensile nature of P^l. Relative particle motions during this time are illustrated in particle-pair diagram B, Fig. 4.1(b). Such microfragile events in, e.g., a dry granular system, would be subtle to detect or difficult to distinguish from the macroscopic process. These events in dense suspensions, *nonhydrodynamic* in nature, however, lead to the spectacular *hydodynamic* responses, which have been measured robustly in experiments (Gadala-Maria and Acrivos, 1980; Kolli et al., 2002). We note that a microfragile hydrodynamic response is absent in Stokesian Dynamics simulations of shear reversal that strictly inhibit fluid films smaller than $0.01d$ (Bricker and Butler, 2007), strengthening the argument for direct surface contacts *in addition* to hydrodynamics, as a crucial contributor to the rheology observed by (Gadala-Maria and Acrivos, 1980; Kolli et al., 2002).

The subsequent building up of $Z_{\mathrm{h}_{\min}}$ after a strain of 0.01 is coupled to re-orientation of the microstructural anisotropy A_{12}, corresponding to macrofragile evolution at a larger strain scale of order unity. The initial subsidence of σ^l from its peak until $\dot{\gamma}t \approx 0.5$ (while $A_{12} < 0$), corresponds to a net opening of lubrication films (see $\langle h \rangle$ and $\sigma_{\mathrm{opening}}$, Fig 4.1(b)), consistent with the leading $1/h$ dependence of the lubrication forces, combined with a reduction in $\langle V_n \rangle$. At larger strains, a new contact network establishes in the now-compatible, oppositely aligned, compressive direction (evidenced by $A_{12} > 0$) with net repulsive lubrication forces during $0.5 < \dot{\gamma}t < 2$, restoring $\langle h \rangle$ to its steady value thereby producing positive P^l and a marginally dominant $\sigma^l_{\mathrm{closing}}$.

The consequent mean relative particle motion is highlighted in particle-pair diagram C, Fig 4.1(b). Although σ^l evolves continuously during this large-scale period, the responsible mechanism therefore switches as the anisotropy changes sign. The stress presented by (Bricker and Butler, 2007) has a comparable macrofragile evolution but the microfragile response does not follow the experimental behaviour as well as the present work, most probably due to the inadequate modelling of the frictional particle-particle surface contact.

The contact stresses (σ^c, P^c) follow a similar macrofragile evolution, their associated microfragile contact breakage having occurred at flow cessation as discussed. The stress evolution is closely correlated with the building up of the mechanical coordination number Z_c, which occurs on a similar strain scale as the fabric reorientation described above, as illustrated in Fig 4.2. The separation of scales in the evolution of the contact stress and the hydrodynamic peak ensures dominance of the hydrodynamic stress at small strains after reversal, an assertion made in (Gadala-Maria and Acrivos, 1980; Kolli et al., 2002), though overlooking the microfragile hydrodynamic response. Combining the increasing σ^c with the decreasing σ^l at $\dot{\gamma}t > 0.01$ gives rise to the nonmonotonic total stress, meaning microfragility in the hydrodynamic response is crucial in capturing the experimental behaviour.

The above analysis sheds light on the two-scale nature of the stress evolution, linked to configurational change at small strains and anisotropy re-orientation at large strains. The importance of particle contacts in achieving the nonmonotonic stress response naturally leads to the question of the sensitivity of the evolution at each scale to particle interactions and surface properties.

4.4 Role of particle properties

In order to test the applicability of the above described mechanism to a wide range of particle systems, we address two factors pertaining to well studied suspensions, namely surface roughness and stabilising repulsion. For suspensions of large particles (e.g., $d > 10$ μm), such as the $40-50\mu m$ polystyrene spheres suspended in density matched silicon oils studied in (Gadala-Maria and Acrivos, 1980), surface roughness is perhaps the more relevant factor; for those of small particles (e.g., $d < 10$ μm) steric or electrostatic repulsion may give well-defined repulsive forces.

4.4.1 Surface roughness

Surface roughness is represented numerically by an asperity length scale (by means of $h_{\min}$) and the friction coefficient μ_p. $h_{\min}$ contributes to the strain scale of the

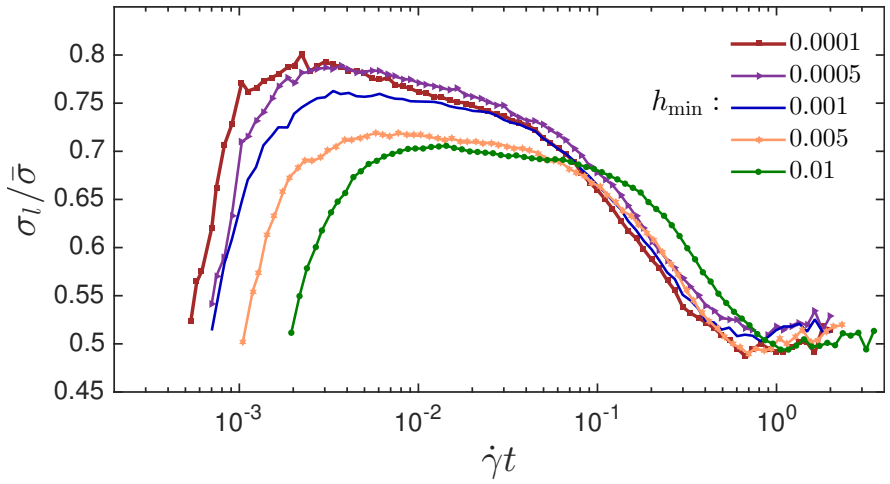

(a)

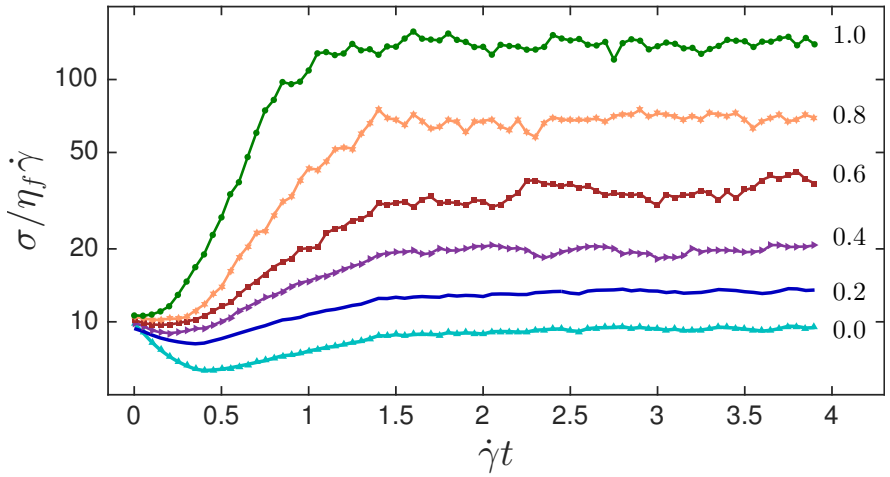

(b)

Fig. 4.3 Stress response to reversal as a function of (a) asperity length scale $h_{\min}$, with the numerical values of $h_{\min}$ given in the legend in units of d; (b) friction coefficient μ_p, with the numerical values of μ_p given;

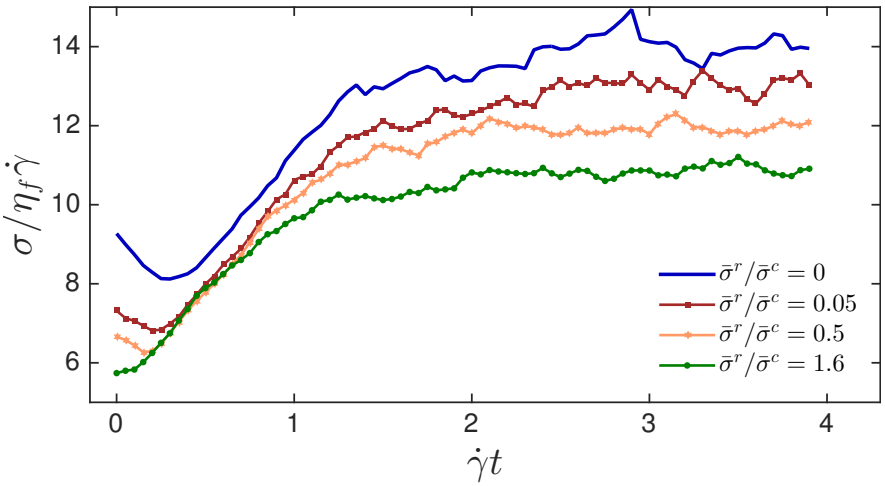

Fig. 4.4 Stress response to reversal as a function of repulsive force magnitude $|\boldsymbol{F}^r|$, quantified as the relative magnitude of the repulsive stress $\bar{\sigma}^r$ to the contact stress $\bar{\sigma}^c$.

microfragile HS response and should also affect the HS magnitude. We explore such effects by varying $h_{\min}$ between $10^{-4}d$ and $10^{-2}d$, considering the physical size of surface asperities and bounded numerically by the singularity and the overdamping requirement at the lower and upper limits, respectively. The resulting σ^l scaled by the steady state total stress $\bar{\sigma}$, following a reversal at $\dot{\gamma}t = 0$, is plotted against strain on a log-linear scale in Fig. 4.3(a). The strain scale of the microfragile peak decreases with decreasing $h_{\min}$ in the $0.01d$ to $0.001d$ range, but saturates approaching $10^{-4}d$. We verified that the saturation is not due to inertial effects, but is perhaps due to the nonlinear coupling between particle configuration and dynamics. Decreasing $h_{\min}$ also significantly increases the peak magnitude, but only weakly affects the macrofragile HS response, the evolution of which interestingly collapses relative to $\bar{\sigma}$. The surface roughness effect of $h_{\min}$ thus controls the microfragile, but not the macrofragile HS response.

In a manner often employed in dry granular studies (see e.g. (Srebro and Levine, 2003)), we vary the friction coefficient μ_p incrementally between 0 and 1, exploring particle surfaces from ideally frictionless to very frictional. The total shear stress evolution is given on a linear x-scale in Fig. 4.3(b). On the contrary to the effects of varying $h_{\min}$, the microfragile response is largely insensitive to μ_p, which is unsurprising given the small scale stress is dominated by attractive/tensile lubrication forces. The invariance of the hydrodynamic stress gives strong support to the central role of particle contacts in achieving the very different viscosities observed in such systems. The stresses differ hugely at larger strains, however, indicating that the μ_p-dependent contact stress is important during $0.3 < \dot{\gamma}t < 2$, coinciding with recovery of Z_c to its steady value. The increase of the contact stress with increasing friction can be understood

from the increase of tangential contact forces and the decreased departure from the jamming volume fraction ϕ_c (Liu and Nagel, 1998), which is known to decrease as friction increases (Chialvo et al., 2012; Sun and Sundaresan, 2011). The latter effect is also consistent with the experimental observation that the peak immediately after reversal becomes lower relative to the steady state stress when increasing volume fraction (Kolli et al., 2002). The interparticle friction thus mainly affects the large scale microstructure and contact stress and hence the macrofragile response. In reality, μ_p and $h_{\min}$ are probably simultaneously coupled to the surface roughness variation, though the combined effect may be deduced from the present separate analyses, exploiting the marked separation of scales associated with our two-scale description.

4.4.2 Surface stabilisation

We next probe the effect of a generic stabilising repulsive force, extending the above analysis to consider particles in the size range $d < 10\mu$m. It is assumed, based on previous simulation results (Mari et al., 2014; Seto et al., 2013), that a static, short range, normal repulsive potential is sufficient to capture the essence of a stabilising mechanism such as electrostatic repulsion or a grafted polymer hair coating. Enhanced dissipation in the lubrication forces, a phenomena described by (Melrose and Ball, 2004), is neglected for simplicity. A generic form of the repulsive force model derived by Fredrickson et al. (Fredrickson and Pincus, 1991) is used, $\boldsymbol{F}^r = k\left(\frac{1}{h}\right)^{5/4}\boldsymbol{n}_{ij}$, where k is some constant that encapsulates (among other things) the chemical properties of the hairs and their density on the surface, essentially quantifying the "strength" of the static repulsion. We apply the same singularity regularisation as in the lubrication model, and the same values $h_{\min}$, h_{max}. Coupling to the mechanical contact model is as before. The total shear stress response to reversal is given in Fig. 4.4, for k spanning 2 orders of magnitude (quantified by the relative magnitude of the steady-state repulsive $\bar{\sigma}^r$ and contact $\bar{\sigma}^c$ stresses). As expected for small k, the additional static repulsion is insufficient to separate particles, so the stress response closely resembles that for the base case in Fig. 4.1(a). As k (or $\bar{\sigma}^r/\bar{\sigma}^c$) is increased, we note that while the large strain scale for the evolution appears to be unchanged, the steady value of σ decreases. This is attributed to increasing inhibition to mechanical contacts (for which $h < 0$) as the repulsion becomes stronger. We note that this trend is valid when $\bar{\sigma}^c$ is of comparable magnitude to $\bar{\sigma}^r$. For very large $\bar{\sigma}^r/\bar{\sigma}^c$, an opposite trend is observed (Mari et al., 2014) due to a shear thinning mechanism—the polymer hair length can begin to contribute to an effectively larger total particle diameter, leading to a higher effective volume fraction and therefore a higher shear stress, as explained in detail by (Mari et al., 2014) and references therein. This then leads to shear thinning behaviour with *reducing* k, rather

than with *increasing* k as we observe here. For small strains after reversal, we observe a marked loss of the microfragile stress peak as k is increased.

To further understand this loss, we present the full evolution of shear stress contributions for large k and a flow cessation period sufficient to relax to steady state, Fig. 4.5(a), with $\langle h \rangle$ increasing from around $0.06d$ to $0.08d$ and $Z_{\mathrm{h_{min}}}$ decreasing modestly (middle Inset). Upon reversal, some remaining h_{min} contacts are opened, resulting in a $Z_{\mathrm{h_{min}}}$ decrease and a HS response over a 10^{-3} strain scale (middle and right Insets, respectively), consistent with the microfragile response in Fig. 4.1. In this sense, a microfragile HS response still occurs; though it starts from a "loosened" microstructure, producing a HS lower than its steady value, rather than the surge noted previously. Following this reasoning, a HS peak would be recovered if the relaxation period were shortened sufficiently to disallow any increase in $\langle h \rangle$. We verify this in Fig 4.5(b) using a very short relaxation period $\dot{\gamma}t = -0.01 \rightarrow 0$. A HS surge of about 100% of its steady value is observed, although it does not result in an appreciable peak in the total stress since the HS contribution is small. The repulsion and contact stresses similarly follow a macrofragile evolution. This again creates a strain window for the HS to be measured separately from other components. In short, the repulsive force magnitude together with the associated scales provides extra control over particle configurations and hence the stress response. The two-scale evolution concept is, however, still robustly helpful in understanding this more complicated behaviour.

4.5 Shear reversal with thickening

We next demonstrate a practical application of this two-scale evolution understanding by considering the shear thickening behaviour discussed in the previous chapter. As discussed, there is currently much contention surrounding the respective contributions of hydrodynamics and particle-particle contacts to shear thickening. Here we show that our two-scale mechanism can resolve the dispute. Since we have demonstrated that the small strain scale microfragile response is dominated by hydrodynamic forces, while the large strain scale macrofragile response is dominated by particle-particle contact forces, it follows that we can infer the relative magnitudes of hydrodynamic and contact forces by careful interpretation of shear reversal experimental data.

We therefore carry out shear reversal simulations similar to those described above, but employing the Critical Load Model for particle friction described in the previous Section. Increasing the shear rate relative to the characteristic timescale $1/\dot{\gamma}_0$ reveals an increasing macrofragile response, that we know to be dominated by the particle-particle contact stress, as shown in Figure 4.6(a).

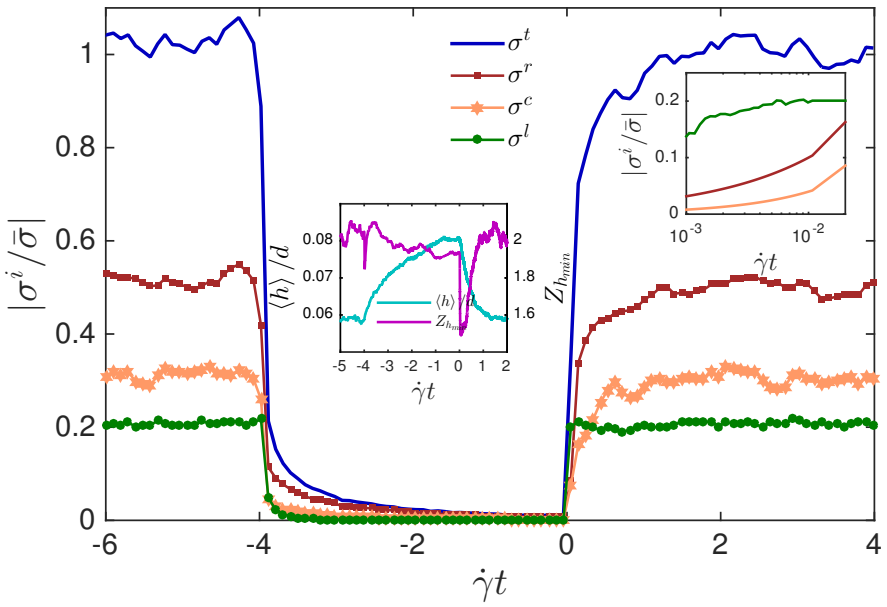

(a)

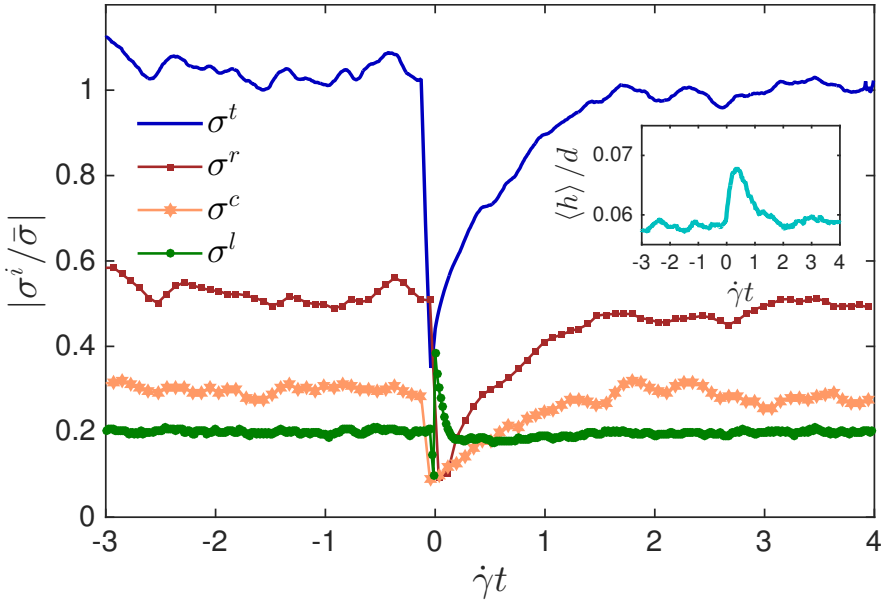

(b)

Fig. 4.5 (a) Response to shear reversal, showing the total σ, contact σ^c, fluid σ^l and repulsive stress σ^r contributions, each scaled by the steady state total stress $\bar{\sigma}$; Right Inset: Same data with logarithmic x-axis. Middle Inset: Evolution of mean fluid film thickness $\langle h\rangle$ and surface coordination $Z_{\mathrm{h_{min}}}$. (b) Analogous result for very short relaxation period.

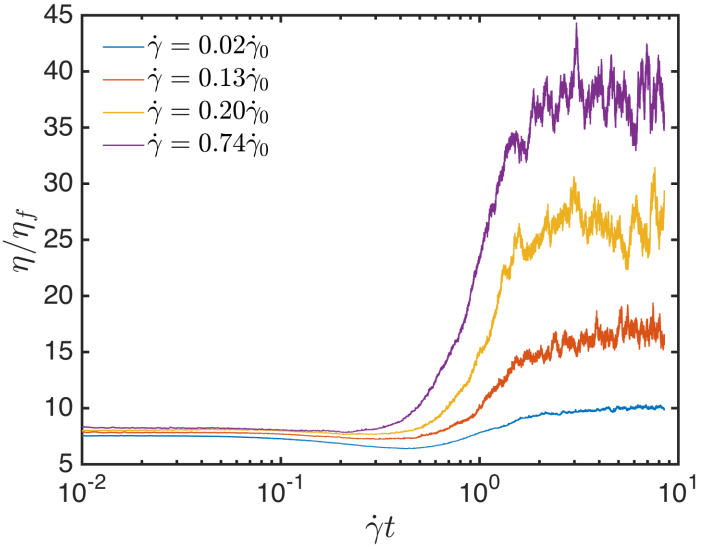

(a)

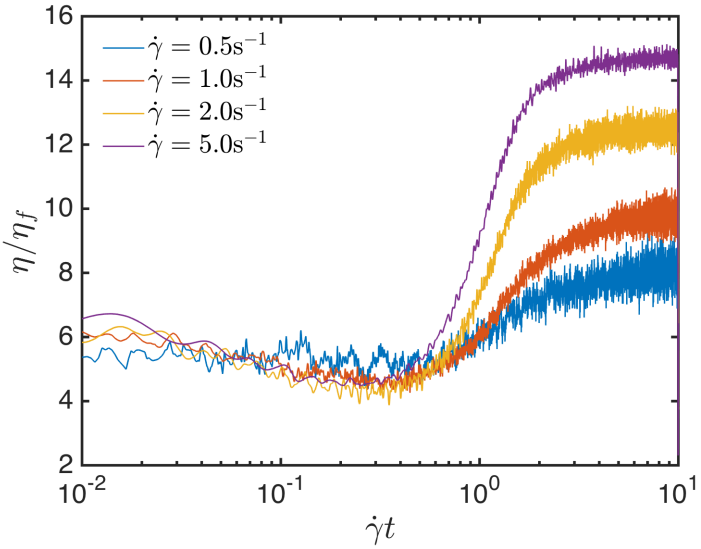

(b)

Fig. 4.6 (a) Response to shear reversal at four shear rates, relative to $\dot{\gamma}_0$. Across the shear thickening transition, the microfragile response is unchanged, while the macrofragile response is significantly increased. (b) Response to shear reversal for a dense suspension of silica particles. As with the simulation, the microfragile response is independent of shear rate, while the macrofragile response is highly sensitive to shear rate. Experiments carried out by Neil Lin as described in (Lin et al., 2015). The particle-particle friction coefficient serves as a tuning parameter for the quasi-Newtonian suspension viscosity in the simulation, at large strains. It is therefore expected that very close quantitative matches can be made between computational and experimental systems by optimising the friction coefficient for specific suspensions. Furthermore, the necessary value of the friction coefficient for matching experimental behaviour may reveal details about the surface properties and true frictional nature of real suspensions.

For comparison, experiments are carried out by collaborator Neil Lin. Experiments involve controlled rate shear flow tests using a dense suspension of density matched silica particles as described in Lin et al. (2015). Results are presented in Figure 4.6(b). The close correspondence between simulation and experimental results is remarkable. Indeed, analogous results are also obtained for a suspension of polymer coated PMMA spheres. Considered within the framework of our two-scale evolution description, the experimental data, most notably the clear independence and dependence of the micro- and macro- fragile responses respectively, strongly support the argument that particle contacts dominate shear thickening.

4.6 Concluding remarks

We provide a robust characterisation of a two-scale response to shear reversal in dense suspensions, that is highly reminiscent of the micro- versus macro- fragility proposed by Cates et al. (Cates et al., 1998). Links are established between stress responses at small and large strains with *microfragile* contact breakage and *macrofragile* microstructural (re-)building respectively, resolving the hitherto unexplained nonmonotonic stress evolution following shear reversal. This substantiates the emerging understanding about the importance of particle contacts in suspension rheology – they not only provide a significant contact stress at steady state, but also give rise to a pronounced small strain transient hydrodynamic response. This understanding provides a sound theoretical framework from which to formulate constitutive models with appropriate two-scale characteristics, and previous attempts at such models (Goddard, 2006) might be revised to correctly link the stress and microstructure at each scale. The evidence that different microstructural features control the contact and hydrodynamic stresses respectively and in an analogous way to that in dense granular flows (Sun and Sundaresan, 2011), supports further unification of dense suspension and granular rheology extending from steady (Boyer et al., 2011) to unsteady state. The findings on surface features and interactions also open doors to either devising new experiments and protocols, e.g., varying relaxation time, to characterise particle surface properties and stress contributions; or designing new particles, e.g., with different grafted polymer hairs, to realise certain desired rheological properties. Finally, we demonstrate that in shear thickening suspensions, the large viscosity increase occurs during the macrofragile response, and is dominated by particle-particle contacts. A remarkable similarity to corresponding experimental results leads us to conclude that particle-particle contacts are indeed the main contributor to shear thickening in many dense suspensions.

Chapter 5

Flow regimes of dry and wet grains in a narrow channel

In this chapter, we assess the extent to which the flow regime map described in Chapter 2 can be applied to non-homogeneous flow conditions, such as those that may arise under industrial flows. We use discrete element simulations to study the rheological regimes of dense packings of inertial ("dry") and non-inertial ("wet") grains as they flow through a narrow channel. Generic behaviour is observed in the velocity and volume fraction profiles. A simple model is therefore constructed that combines a spatial-cooperativity function for the particle number distribution near the boundaries with an established model for the flow-rate independent velocity profile. The model, combined with the flow map in Chapter 2, successfully predicts the pressure drop versus flow rate relation, for all flow regimes and particle types.

5.1 Introduction

While large steps have recently been made towards a complete description of the rheological regimes of suspended materials under shear flow (Guy et al., 2015; Ness and Sun, 2015; DeGiuli et al., 2015; Jop et al., 2006), transferring this understanding to more complex geometries, in which stress distributions become non-trivial, remains challenging. Among the most simple configurations that requires further consideration is Poiseuille flow: pressure driven flow through a narrow (in this case) capillary or channel. Experimental study of dense particulate material in narrow channels spans both non-Brownian (Pouliquen and Gutfraind, 1996) and Brownian (Isa et al., 2007) flow, with surprisingly similar results, that are also consistent with the near-wall flow behaviour during discharge of grains from silos. It is found that a sheared region establishes at the bounding walls, the width of which is independent of the pressure

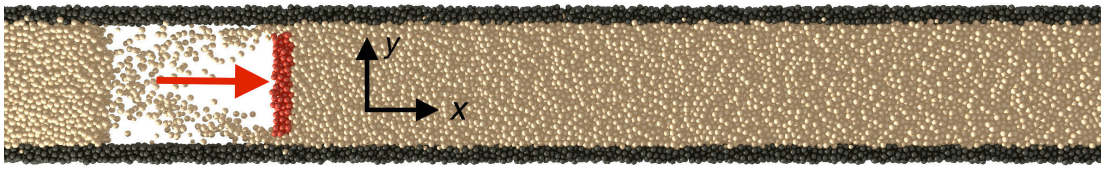

Fig. 5.1 Channel flow geometry. Black particles represent stationary walls; red particles represent a force-controlled driving ram; brown particles represent the grains under consideration.

drop applied across the channel. This result is contrary to what might be expected for e.g. a material obeying the Herschel-Bulkley constitutive relation, in which the extent of shearing increases with increasing stresses. The anomaly is explained in terms of a stress fluctuation model, proposing that, while the mean shear stress in the material is insufficient for flow (i.e. it is below the yield stress), large, pressure-drop-independent fluctuations result in the stress instantaneously exceeding the yield stress, with a probability that rapidly decays away from the channel wall.

More recently, the failure of the material to adhere to a local rheological model (i.e. the emergence of non-local behaviour) has been quantified by appealing to the cooperative nature of such materials, assuming a cooperatively length scale that can characterise the *fluidity* of the material (Goyon et al., 2008), i.e. the propensity for stresses to be generated as a result of particle rearrangements due to long-range cooperativity, rather than through local convecting flow. Successful predictions of granular flow features have been obtained using these (Kamrin and Koval, 2012; Kamrin and Henann, 2014) and similar (Bouzid et al., 2013) ideas.

In the present chapter, we present an alternative viewpoint, using discrete element method simulations to study pressure driven flow though a narrow channel. We find universal scalings of the velocity and volume fraction profiles, that we model using the stress-fluctuation term proposed by (Isa et al., 2007) and a simple geometric construction (introducing spatial cooperativity), respectively. Local shear rates and volume fractions predicted by these models are subsequently "plugged-in" to the previously described regime map for the shear rheology of granular materials (Chialvo et al., 2012; Ness and Sun, 2015), yielding convincing predictions of the mass flow rate through the channel across particle types and applied pressure drops.

5.2 Simulation Method

5.2.1 Geometry and contact model

An assembly of bidisperse (diameters d and $1.4d$, harmonic average (weighed by respective number fractions) $\hat{d}$), spherical particles (highlighted *brown*, Fig 5.1) flows through a channel formed between rigid, parallel walls (highlighted *black*, Fig 5.1) with centres of mass located at $y \pm 12.5d$. The channel has periodic boundaries in x, at $x = 0$ and $x = 200d$ and in z at $z \pm 2.5d$. Flow is driven by the application of a constant force F_{app} to a rigid assembly, a "ram", of particles (highlighted *red*, Fig 5.1) that may translate in x only (with instantaneous and time-averaged velocities V_{r} and $\bar{V}_{\text{r}}$ respectively), and may not rotate. A clearance of $2d$ between ram and wall prevents blockages and allows "recycling" of particles. The stress required to shear particles within this clearance region is negligible compared to that required to drive the main flow. The volume fraction is not constrained; the system dynamically adopts an "equilibrium" volume fraction dependent on particle properties and F_{app}. Flow is in the $+x$ direction as indicated by the red arrow in Fig 5.1. Particle-particle and particle-fluid forces are calculated as described in Chapter 4.

5.2.2 Post processing

To coarse-grain the simulation results and obtain pseudo-continuous data, an array of cuboidal cells of dimensions $d \times d \times 5d$ and volume V is generated across the entire channel. At each time step, particles are assigned to bins based on the location of their centres. Pseudo-continuous velocity and volume fraction profiles are then obtained by time-averaging the properties of particles existing within each bin. Similarly, the stress tensor within each bin is obtained from the contact data corresponding to that bin, according to Equations 2.4a and 2.4b. The following discussion focusses on the mean normal stress, the particle pressure, calculated as $P = -\frac{1}{3}(\sigma_{11} + \sigma_{22} + \sigma_{33})$.

5.3 Results

We simulate five cases, varying the particle-particle friction coefficient μ_p and the fluid viscosity η_f, as detailed in Table 5.1. For each case we perform simulations for 10 realisations of the channel, and calculate ensemble-averaged results. Fluid viscosities and friction coefficients are chosen to explore the inertial and viscous limits, and the distinction between very smooth and very rough particles. Bulk flow behaviour is assessed by considering the F_{app} *vs.* $\bar{V}_r$ relationship, Fig 5.2. Coarse grained velocity

Case	$\mu_p = 0$ $\eta_f = 0.1$	$\mu_p = 0$ $\eta_f = 0$	$\mu_p = 1$ $\eta_f = 0.1$	$\mu_p = 1$ $\eta_f = 0$	$\mu_p = 0.2$ $\eta_f = 0$
ϕ	0.629	0.624	0.600	0.597	0.609

Table 5.1 Summary of simulation Cases studied

and volume fraction profiles are presented in Fig 5.3 and Fig 5.4 respectively. The underlying rheology of the material is probed using the coarse grained velocity and stress profiles, from which we obtain the data presented in Fig 5.5.

5.3.1 Bulk flow characterisation

The F_{app} *vs.* $\bar{V}_r$ relationship is given for frictionless particles in Fig 5.2(a) and for frictional particles in Fig 5.2(b). Corresponding spatially and temporally averaged volume fractions are given in Table 5.1. A distinction is drawn between $F_{\text{app}} \to 0$, for which the grains approximate perfectly "hard" spheres and $F_{\text{app}} \to \infty$, for which overlaps between neighbouring grains become large and the particles behave as "soft" spheres. This distinction was noted in previous chapters for the shear flow regimes. In the hard particle limit, $\bar{V}_r = k_1 F_{\text{app}}^{1/2}$ scaling is observed in the limit of $\eta_f = 0$, with k_1 dependent on μ_p, implying an underlying shear rheology with form $\sigma \propto \dot{\gamma}^2$, consistent with Bagnold scaling for dry granular materials. By contrast, overdamped flows (with $\eta_f = 0.1$) exhibit $\bar{V}_r = k_2 F_{\text{app}}$ scaling, implying an underlying shear rheology with form $\sigma \propto \dot{\gamma}$, consistent with quasi-Newtonian viscous behaviour for granular particles in a viscous fluid. It is noted that for the case where $\mu_p = 0$ and $\eta_f = 0.1$, the scaling exponent begins to shift $1 \to 1/2$ for $F_{\text{app}} > 0.01$, corresponding to local Stokes numbers ($\text{St} = \rho \dot{\gamma} d^2 / \eta_f$) approaching unity within the channel. This is highlighted by the Viscous and Inertial labels on Fig 5.2a In all cases, super-linear scaling exists in the "soft" particle region, corresponding to enhanced particle deformability and approaching emulsion-type shear-thinning rheology (Nordstrom et al., 2010a). For frictional particles, a "jammed" (Liu and Nagel, 1998) region exists at small F_{app}, corresponding to yield stress behaviour. It is uncertain whether a similar yield stress exists for frictionless particles, though the magnitude of F_{app} for which it might be observed renders the dynamics excessively slow for observation in the present work.

5.3.2 Underlying rheology

Velocity profile

In all cases, the velocity profile clearly exhibits a central region with minimal y-dependence, which we identify as the plug, and sheared regions near the boundaries

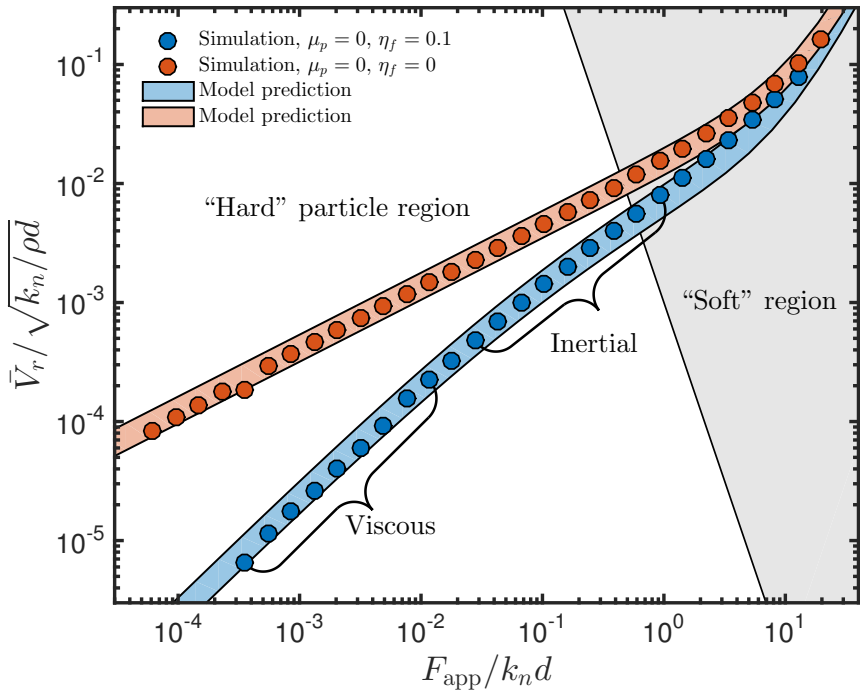

(a)

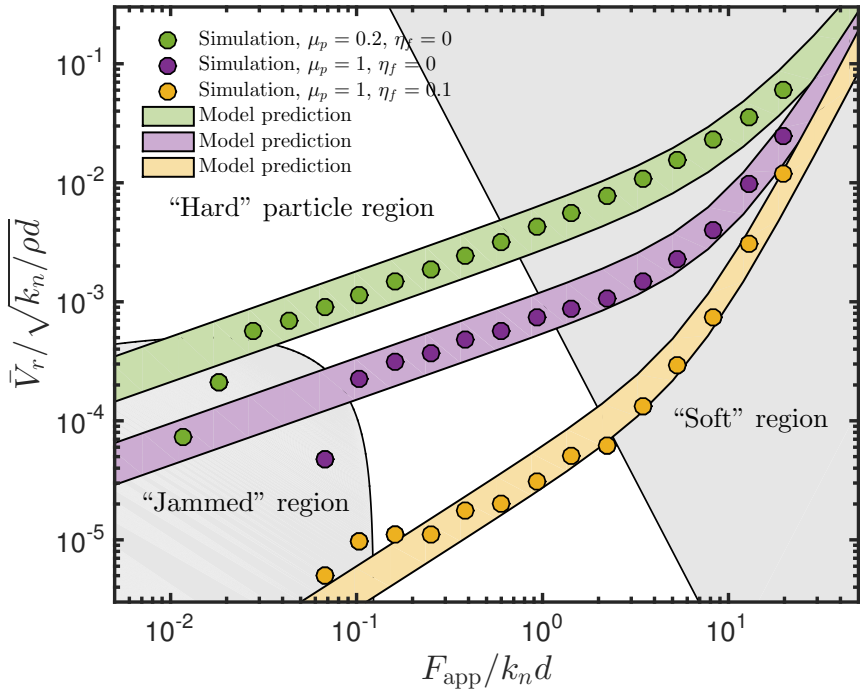

(b)

Fig. 5.2 Time averaged scaled ram velocity versus scaled applied force, for (a) frictionless particles under viscous and inertial conditions and (b) frictional particles under viscous and inertial conditions, with $\mu_p = 1$ and $\mu_p = 0.2$.

(coloured regions, Fig 5.3). Normalising the velocity profiles in each case by their respective centreline values, we demonstrate that the width of the sheared region is approximately $5d$ in all cases, independent of pressure drop and particle properties. This is contrary to what would be expected from such a material, the bulk rheology of which might typically be described by a Herschel-Bulkley type model, suggesting a deviation from homogeneous rheology. Comparable pressure drop independence of the velocity profile has been observed in flows of both colloidal (Isa et al., 2007) and granular (Pouliquen and Gutfraind, 1996) systems, suggesting a universal behaviour that spans broad particle types. A stress fluctuation model proposed by (Isa et al., 2007) provides a satisfactory fit for all velocity profiles, Fig 5.3(f), meaning for any flow within the computational channel, the range of effective shear rates can be obtained directly from the mass flow rate.

Volume fraction profile

In further agreement with experimental work (Isa et al., 2007), a volume fraction inhomogeneity is observed across the channel, there being a marked decrease in solid content in the shear zones, relative to that in the plug. Consistent with the velocity profiles, it is observed that for each set of simulation parameters (μ_p, η_f), the volume fraction profiles collapse to a single curve when scaled by their respective centreline value. The volume fraction profile is, however, dependent upon μ_p and η_f. It is widely acknowledged that the critical volume fraction of a dense suspension is sensitive to the frictional properties of the particles (Sun and Sundaresan, 2011; Guy et al., 2015), so for the present simulations, in which the system is free to adopt a volume fraction that is consistent with the flowability of the material, it is expected that different values of μ_p will lead to different volume fractions. Spatially averaged volume fractions are calculated for the bulk volume of the material, away from the ram and the downstream extremity, and presented in Table 5.1 for each case.

As expected, frictionless particles (which have $\phi_c \approx 0.64$) attain volume fractions notably higher than frictional particles (that have $\phi_c \approx 0.59$). At a given friction coefficient, we note a minor increase in volume fraction with increasing η_f. Differing values of the mean volume fraction are reflected in the volume fraction profiles in Fig 5.4. Comparing Cases (a) and (c), we note a considerable reduction in the shear zone volume fraction with increasing friction coefficient, for example.

To elucidate the volume fraction inhomogeneity in more detail, a finer coarse-graining is carried out, using a bin width of $0.1d$ in Y. In all cases, we find decaying fluctuations near the boundary that are independent of statistical averaging, indicating the presence of a layering effect. Such an effect has been demonstrated in colloids

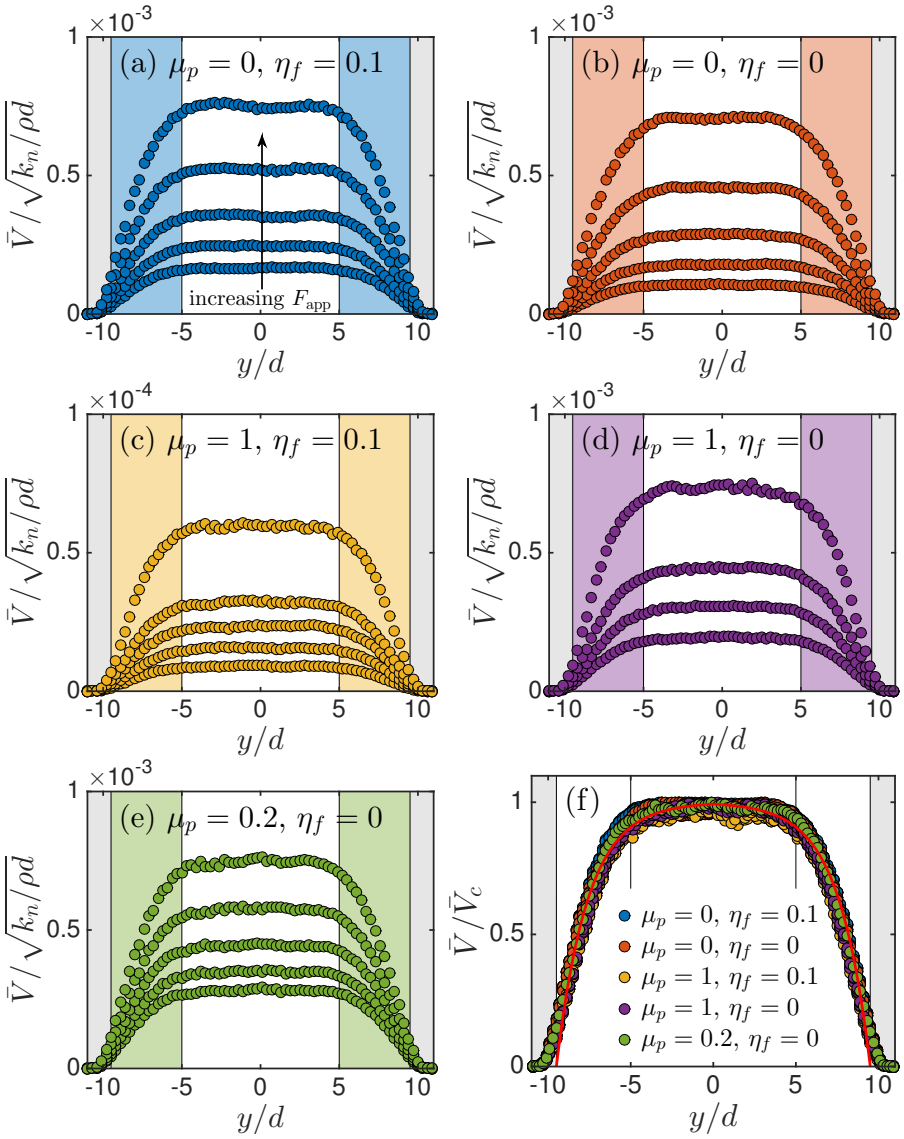

Fig. 5.3 (a)-(e) Velocity profiles for a range of applied ram forces F_{app}, for each set of simulation parameters. Highlighted coloured regions indicate sheared zones; (f) Velocity profiles scaled by centreline value. Results collapse to a single curve for all simulation cases. Solid red line: model prediction (Isa et al., 2007).

using confocal imagery (Isa et al., 2009). These well defined fluctuations largely disappear by a distance of $5d$ from the wall (notably corresponding to the transition from shear zone to plug), suggesting that the boundary effect is dissipated and the particle distribution becomes closer to homogeneous beyond this point. In spite of the considerable differences in bulk volume fraction between simulation cases, it is observed that the finely coarse-grained volume fraction profiles collapse surprisingly well, when scaled by the centreline value, illustrated in Fig 5.4(f). Similarly to the velocity profile, this suggests a universal behaviour across particle types, and poses the question of whether a single model can provide a unified description.

A geometric model is proposed for the formation of the fluctuating volume fraction inhomogeneity that can successfully predict the length scale of decay, and is independent of the dynamics of the system. We begin by considering the details of the bounding walls of the channel. The inner surfaces of the bounding walls are composed of particles with centres of mass normally (approximately) distributed about $|y| = 10d$. Therefore, the probability that a boundary particle is located at position y, $p_1(y)$, may be given by

$$p_1(y) = \frac{1}{\Sigma\sqrt{2\pi}} e^{-(y-10d)^2/(2\Sigma^2)}. \tag{5.1}$$

Subsequently, a flowing particle adjacent to the boundary will be centred at approximately $\hat{d}$ from its neighbouring boundary particle, though with some variation (we use a single value of Σ throughout, for simplicity), where the position of that boundary particle is given by p_1. For every possible position of the first layer particle, y, we evaluate the location probability density for the second layer particle, p_2, and scale this by $p_1(y)$. The location probability distribution of the $(n+1)th$ particle, p_{n+1}, is therefore related to that of the nth particle, p_n, by Eq 5.2, where the denominator ensures the total probability per particle is unity

$$p_{n+1}(y) = \frac{\sum_Y p_n(Y) \frac{1}{\Sigma\sqrt{2\pi}} e^{-(y-(10d-n\hat{d}))^2/(2\Sigma^2)}}{\int_y \sum_Y p_n(Y) \frac{1}{\Sigma\sqrt{2\pi}} e^{-(y-(10d-n\hat{d}))^2/(2\Sigma^2)}}. \tag{5.2}$$

The $(n+1)th$ distribution is centred at $\hat{d}$ from the nth, and has a greater resultant variance. A prediction for the number density as a function of the distance from the wall is then obtained by summing the contributions from each layer of particles, where N is the number of particle layers existing before the system reaches a homogeneous state.

$$P(y) = \sum_{k=1}^{N} p_k(y). \tag{5.3}$$

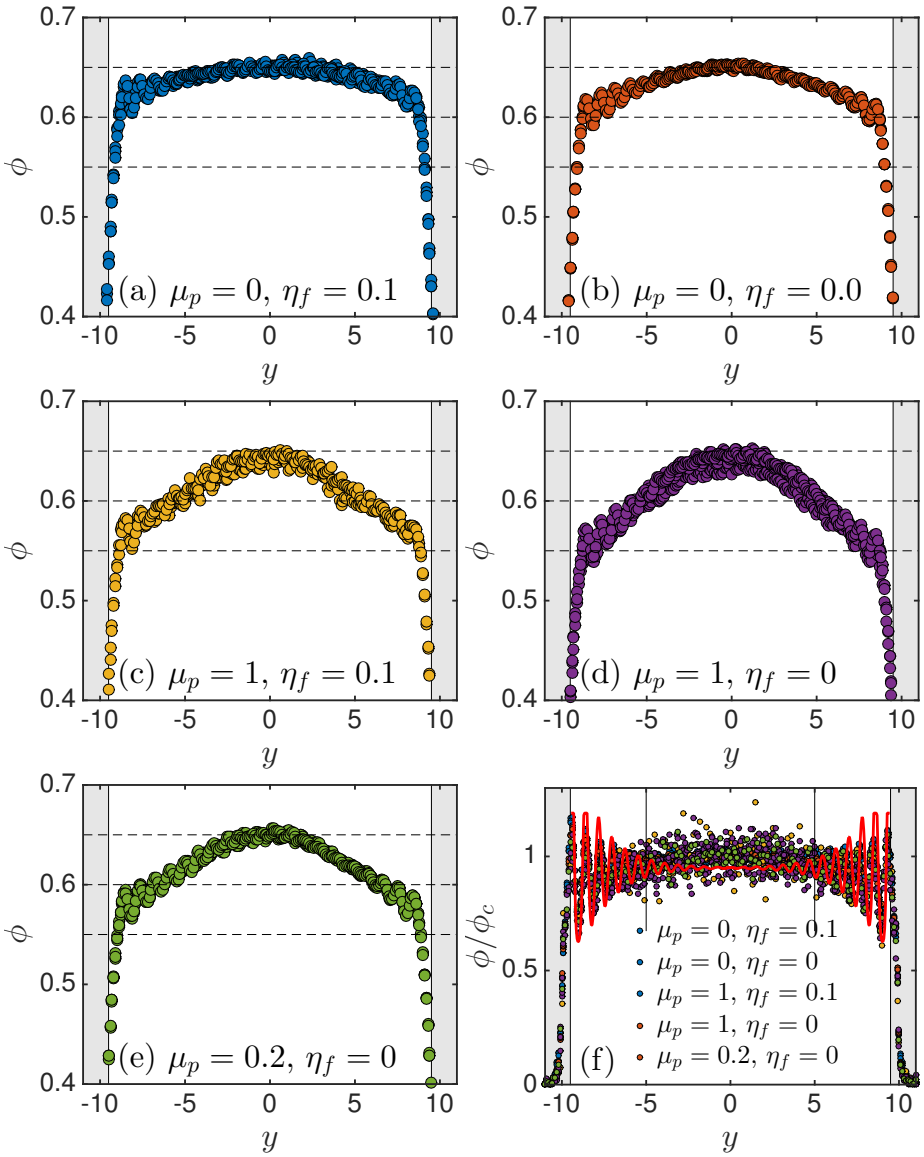

Fig. 5.4 (a)-(e) Volume fraction profiles for a range of applied ram forces F_{app}, for each set of simulation parameters; (f) Volume fraction profiles coarse-grained on a $0.1d$ grid, and scaled by centreline value. Results collapse for all simulation cases, showing characteristic "layering" at the boundaries. Solid red line: model prediction Eqs 5.1, 5.2 and 5.3.

The resulting profile, for a suitable value of Σ (which might be linked to, for example, the solids volume fraction and the particle shape), shows oscillations that approximate those observed in the simulation data. Based on particle and system properties, i.e. the values of mean and variance in our probabilistic model, we are able to obtain a good approximation of the boundary volume fraction inhomogeneity in the channel, illustrated in Fig 5.4(f). This model introduces the notion of non-locality into the analysis, through a co-operativity effect in the particle distribution.

The predicted profiles are subsequently rescaled by the known bulk volume fractions from Table 5.1, and truncated such that $\phi < \phi_c$ in each case. Applying a coarse-graining function to this volume fraction prediction at the $1d$ scale, consistent with our presentation of volume fraction profiles in Figs 5.4(a)-(e), we recover good predictions of the volume fraction profiles for all cases. From a knowledge of the mass flow rate and the bulk solids content of the material, we are therefore able to use two simplistic models to correctly predict the local volume fractions and shear rates within the channel.

Constitutive relation

Next, we demonstrate that the material within the sheared regions of the channel consistently conforms to a local rheology model, namely the Inertial (Jop et al., 2006; Forterre and Pouliquen, 2008) and Viscous (Boyer et al., 2011) models, unified for general flows of dry and wet grains as we described in Chapter 2 (Trulsson et al., 2012; Ness and Sun, 2015). Figs 5.5(a) and (b) show local (coarse grained) stress-strain data for frictionless and frictional particles respectively, for the sheared regions only (those regions highlighted in Figs 5.3(a)-(e)), each scaled by the respective distance from the jamming point ϕ_c as proposed by (Chialvo et al., 2012). The result is consistent with the bulk flow behaviour observed in Fig 5.2. At very high shear rates (corresponding to large F_{app}), the material adheres to "intermediate" or "soft-particle" rheology (Chialvo et al., 2012; Ness and Sun, 2015), while at lower shear rates, hard-particle rheology is observed, with the stress (P) exhibiting either viscous or inertial scaling, dependent on η_f (or, more correctly, on the local Stokes number). The data correspond well to the model predictions from Chapter 2. It is noted that the scatter of the data is considerably greater for the frictional case (we omit the $\mu_p = 0.2$ case for simplicity, though it occupies an inertial branch that is intermediate in stress between those for $\mu_p = 0$ and $\mu_p = 1$), though the consistency with the model prediction remains convincing.

From the velocity and volume fraction profile models described above, we are able to obtain predictions of the local shear rates and volume fractions within the sheared regions. Using the constitutive model proposed in Chapter 2, which we now know to capture the rheology in the sheared region, we can obtain a prediction of the stress (P)

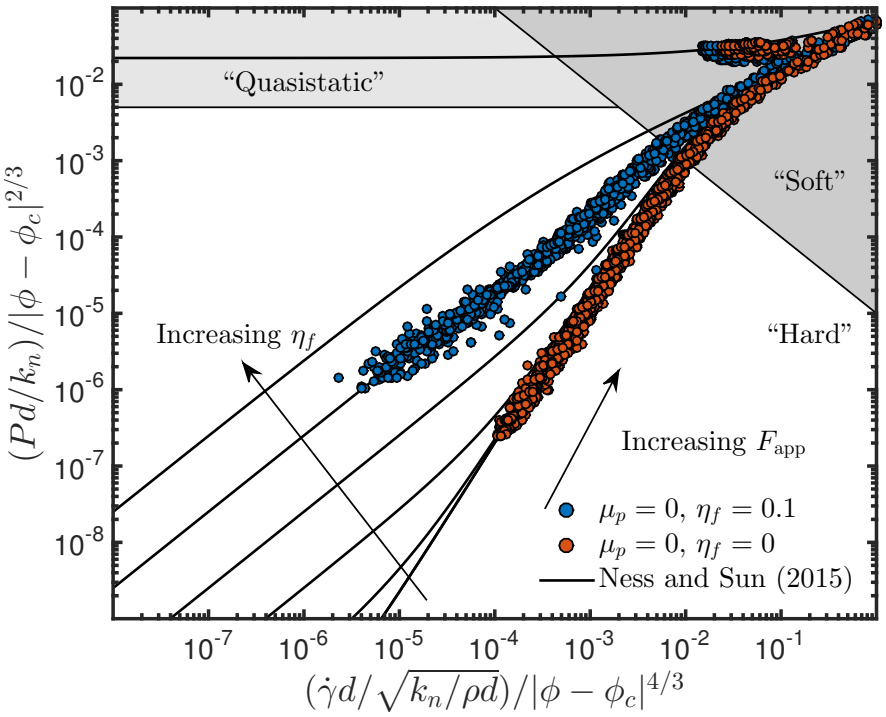

(a)

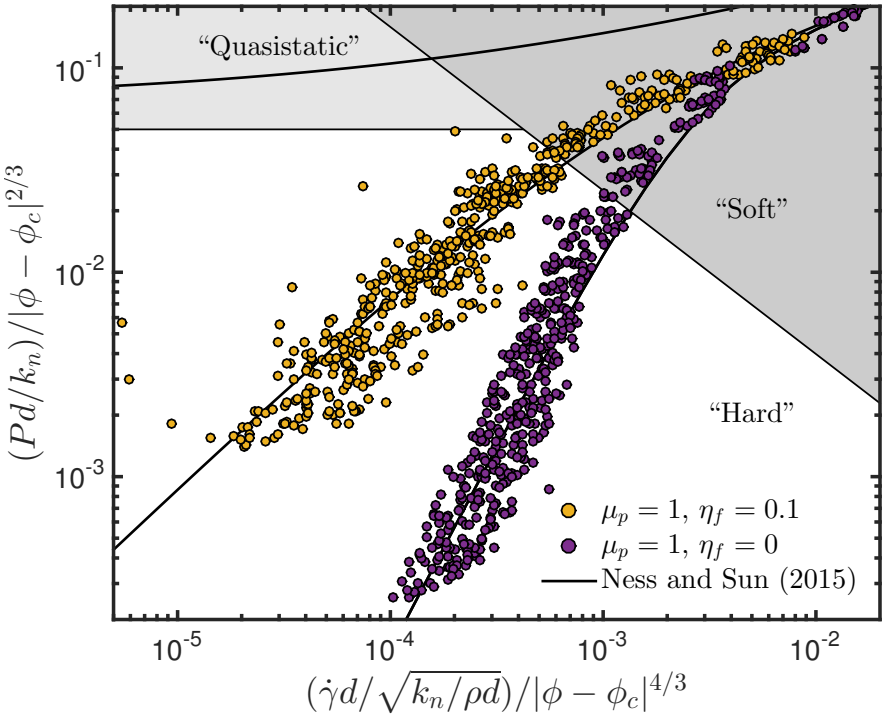

(b)

Fig. 5.5 Time averaged scaled local pressure versus time averaged scaled local shear rate, for all coarse-grained cells within the sheared region of the channel, for (a) frictionless particles under viscous and inertial conditions and (b) frictional particles under viscous and inertial conditions.

across the sheared region. A basic momentum balance across the channel (i.e. parallel walls bounded by periodicity in z) predicts a uniform mean normal stress (pressure P) profile (which we verify in the simulation data), meaning the pressure P in the sheared regions maybe be considered to be the pressure across the full channel width at a given x location. The maximum value of the pressure prediction can subsequently be taken to be the most upstream pressure, near the ram, and is used to predict the required force on the ram. Model predictions are given in Fig 5.2 including error bounds, and are shown to convincingly capture the flow behaviour for all simulation cases.

5.4 Concluding remarks

The present simulations of dense suspensions in confined channels predict flow rate independence in the velocity profile, consistent with previous experimental work, and also in the volume fraction profile. Adopting a model for the shear rate variation from the literature (Isa et al., 2007), and using a simple cooperativity function for the volume fraction near the walls, we can obtain good estimates of these profiles. For a desired mass flow rate through the channel, of a suspension with known global solids fraction, we can therefore obtain radial shear rate and volume fraction profiles that can be input into the regime map in Chapter 2 to closely predict the required pressure drop.

While this chapter gives some predictions of the behaviour of suspensions under inhomogeneous shearing conditions, future work is required before this approach may be utilised with confidence. Specifically, the volume fraction is not fixed, meaning the suspension is free to dilate and contract under intermittent flows in a manner that might normally be inhibited by the finite liquid pore flow rate of an incompressible liquid. Furthermore, at particularly high volume fractions, the particle packing is free to "loosen" to allow flow, in cases where the material would normally be below yielding under constant volume conditions. These issues might be resolved by coupling the particle-particle interaction solver to an explicit liquid phase solver at each time step, to take into account an incompressible interstitial fluid with finite viscosity subjected to the arising pore pressure distributions.

Chapter 6

Paste extrusion through a square entry die

In this chapter, we use discrete element method simulations to study the flow of a dense suspension through a square entry extrusion die. Particle-fluid interactions are accounted for by resolving hydrodynamic lubrication forces, and a linear spring contact model accounts for direct particle-particle interactions as in Chapter 2. Flow through the die is driven by a constant applied force. We give a qualitative and quantitative description of the resulting flow behaviour, focussing on the resulting stress and velocity fields. The roles of fluid viscosity, particle softness, particle-particle and particle-wall friction are considered, and potentially predictive links are made with the semi-empirical parameters of the traditional Benbow-Bridgwater equation.

6.1 Introduction

Extruded monolithic honeycomb catalyst supports have played a major role in automotive emissions control since the 1970s. As automobile manufacture soars in developing parts of the world, the need for emissions control is now greater than ever before. It is therefore essential that such catalyst supports can be manufactured rapidly, cost effectively, and to a consistently high standard. Forming these supports involves extrusion of a ceramic paste through a die of complex geometry, giving a honeycomb structure with many narrow channels. Increasing the extrusion rate can lead to defects such as phase maldistribution, cracking and other unpredictable flow instabilities. To better understand the cause of such instabilities, and to facilitate future design and optimisation of extrusion processes, simulations are used to model and predict the behaviour of pastes as they are extruded. The models currently employed in industry use single-phase constitutive equations to represent complex, multicomponent ceramic pastes. While

often qualitatively predicting extrusion pressure drop vs velocity relationships, they fail to fully capture the complex internal stress and phase distributions associated with multiphase paste flow in extrusion die geometries, limiting their predictive power and their value to the engineer. In this chapter we address these issues by using particle-level simulations of pastes under extrusion to understand how both particle-particle and particle-fluid interactions contribute to the bulk stresses under flow.

Paste extrusion is a central processing step in the manufacture of many consumer and industrial products. Such extrusion processes involve applying a force to a dense suspension of solid particles in liquid (a paste) in order to drive flow through a constricting geometry, giving a product of desired composition and dimensions. The pastes being extruded are complex solid-liquid assemblies and will typically exhibit many of the rheological properties examined previously in this work, such as yield stress behaviour and shear thickening. Benbow and Bridgwater outline some of the most common methods of generating and applying extrusion pressures in *Paste Flow and Extrusion* (Benbow and Bridgwater, 1993). They go on to derive Equation 6.1, an expression for the driving pressure P required to achieve a desired extrusion velocity V in a standard die extrusion geometry

$$P = 2(\sigma_0 + \alpha V^m)\ln\left(\frac{D_0}{D}\right) + 4(\tau_0 + \beta V^n)\frac{L}{D}, \tag{6.1}$$

for a square-entry extruder with barrel diameter D_0, die diameter D, die length L. The first term represents the die-entry pressure drop, while the second term represents the die pressure drop, where α, β, m, n, σ_0 and τ_0 are empirical parameters that treat the paste as an approximate Herschel-Bulkley fluid. This expression has become very popular for both industrial and academic extrusion pressure calculations, despite being semi-empirical and hence requiring calibration through experiment or using historical data (Wilson and Rough, 2006). Furthermore, this expression is purely based on bulk rheology and assumes the material can be characterised simply by a bulk yield stress σ_0 and a zero velocity wall shear stress τ_0, therefore failing to take into account the complex rheology and particle interactions that really govern paste extrusion. As a result, it can offer a sound practical determination of the energy input required for specific extrusion processes, but does not necessarily have great predictive capability in terms of new material or new process design, when a constitutive model is lacking.

Benbow and Bridgwater give examples of extrusion instabilities, cases where the above model breaks down or fails to predict extrusion behaviour. It is emphasised that in thoroughly describing the paste extrusion process, microstructural constitutive equations are invaluable (Coussot, 2007) in predicting, preventing and utilising instabilities such

as wall slip, surface fracture and liquid phase migration (Wilson and Rough, 2006), which cannot be characterised by the pressure term given above alone.

While the expression for extrusion pressure requirement proposed by Benbow and Bridgwater has found many practical applications, its simplicity means that it cannot necessarily capture complex particle interactions that occur during the extrusion process, and as such it fails to predict extrusion instabilities, which can be devastating.

Other predictive techniques for extrusion involve direct solution of the Navier-Stokes equations for viscous flow in a cylindrical geometry using, for example, a Herschel-Bulkley constitutive model (Li et al., 2011). Again, while offering a robust approximation of extrusion pressure that in simple cases can deliver quantitative agreement with experiment, these methods lack a deep appreciation of particle level interactions, meaning they neglect physics that potentially leads to instabilities.

Here we give some examples of CFD-DEM coupling and constitutive approaches to predicting paste extrusion behaviour that aim to take particle level properties and interactions into account, before focussing particularly on modelling techniques that have addressed the phenomenon of liquid phase migration during extrusion.

As an alternative to continuum modelling, solid-liquid flows have been simulated using coupled CFD-DEM solvers (Sun et al., 2009; Xiao and Sun, 2011; Hu and Joseph, 1992). These approaches treat the solid and liquid phases as separate and interpenetrating, solving the low-Reynolds, laminar liquid phase flow field on a volume mesh and the solid phase interactions explicitly using a DEM code. In a two-way coupled simulation, the particle-fluid interaction is taken into account by calculating the drag on the particles and the momentum transferred from particles to fluid at each time step. Yuan *et.al*. (Yuan et al., 2001) adopted this approach to model the ram extrusion of dense pastes. A DEM solver was coupled with a Darcy's Law-type porous flow model for the liquid phase. The model was able to qualitatively capture some of the experimentally observed flow features during the extrusion process. This approach appears to offer some insight into the particle interactions and their role in flow behaviour, for example by potentially being able to predict phase migration and other extrusion instabilities without the need to rely on a constitutive equation based on a continuum approximation of particle dynamics. However, without considerable experimental validation, as well as great understanding of the DEM model and the appropriate form of contacts models, it is unwise to make process design decisions based on the results of these coupled simulations. Furthermore, coupled simulations are significantly more computationally expensive than single phase CFD simulations (Hu and Joseph, 1992), particularly for industrial geometries.

Semi-empirical constitutive models specifically for extrusion flow have been proposed for many complex industrial and consumer materials (Aydin et al., 2000), using experimentally observed flow features to build upon traditional constitutive equations such as the Herschel-Bulkley and Bingham Plastic models (Roussel, 2005; Engmann and Mackley, 2006). Such constitutive models typically correlate microstructural changes during extrusion to bulk rheological properties. For example, Engmann and Mackley (Engmann and Mackley, 2006) modelled chocolate during cold extrusion as a Bingham Plastic by relating the work done during the process to the energy input required to convert the constituent crystalline particles to a liquid state which evolves throughout the process. This energy input required for flow corresponds to a Bingham Plastic yield stress. The Carreau Model, a constitutive equation typically used for describing the rheology of polymers, has been adapted (Patil et al., 2006, 2008) to successfully describe the microstructural evolution of PTFE paste during extrusion, giving remarkable agreement with experimental data. The proposed model includes the evolution of a microstructural parameter ξ with strain, which characterises the extent of fibril formation in the material as extrusion proceeds. This allows the model to begin to predict shear-thickening behaviour as the microstructure develops during extrusion. These examples give a small indication of the great efforts being made to incorporate microstructural dynamics into paste extrusion models.

Liquid phase migration has proven to be a sometimes disastrous consequence of poorly understood paste dynamics (Benbow and Bridgwater, 1993). While phase-maldistribution can be advantageous (Elhweg et al., 2009; Wilson and Rough, 2006) in the case of apparent wall-slip (where reduced particle concentration at boundary walls can lead to a significant reduction in apparent viscosity at the wall and hence a reduction in pressure drop in pipe-flow geometries), when misunderstood or unpredicted it can very negatively impact extrusion success (Yu, 1999).

Flow geometries that result in sharp pressure gradients, for example the stagnant regions between die entry and die land in a ram extruder (Benbow and Bridgwater, 1993), promote “dewatering”, where the liquid phase moves through the solid structure. This movement of liquid down a pressure gradient through stagnated or slower-moving solid particles results in localised regions of increased solids volume fraction. Depending on the rheology of the components, this can result in regions of significantly increased viscosity, or even regions of undesired quasistatic behaviour in an otherwise viscous flow (Yu, 1999; Rough et al., 2000). This can give rise to issues such as extrudate compositional inhomogeneity (Rough and Wilson, 2004) and subsequent structural weakness, that can prove difficult to predict.

A number of studies of ram extrusion have found strong evidence that the onset of phase migration is correlated with ram velocity (Rough and Wilson, 2004; Mascia et al., 2006; Zhang et al., 2011; Liu and Leu, 2009). Phase migration has been proven to be occuring both by post-extrusion drying, weighing and analysis of extrudate samples, and by ram force profiles. The required extrusion force for a certain extrusion velocity is found to increase rapidly in the presence of liquid migration, presumably due to the increased viscosity and/or entry in to the quasi-static regime associated with increased localised solid volume fraction. Phase migration is found to be more likely to occur at low extrusion velocities (Rough and Wilson, 2004; Liu and Leu, 2009), where the convection of liquid through the slower moving solid matrix is more prevalent. As extrusion velocity is increased from a value at which migration definitely occurs, there is a critical velocity associated with the material properties and geometry, above which liquid phase migration will not occur (Liu and Leu, 2009). This critical velocity has been found to increase as solid volume fraction in the paste is increased (Mascia et al., 2006), in a number of extrusion geometries. It is therefore proposed that liquid phase migration can be mitigated to some extent by operating at extrusion velocities above a certain critical value. It is not always possible to operate at high extrusion velocities, however, as other instabilities such as surface fracture impose upper limits (Benbow and Bridgwater, 1993). It has been proposed that in addition to localised pressure gradients, liquid phase migration during extrusion can also be caused by suction effects due to the extensional strain rate imposed on the paste at the die entry (Mascia et al., 2006; Patel et al., 2007; Zhang et al., 2011). It has been suggested that liquid phase migration due to suction at the die entry could be mitigated by using multi-holed dies rather than single holed ones. In the case of extrusion-spheronisation, this has been shown to yield equal product quality, while reducing the limiting velocity at which liquid phase migration begins (Zhang et al., 2011).

A number of approaches to modelling phase migration have been proposed. A continuum constitutive equation accounting for phase migration in dense granular materials that couples a Newtonian constitutive equation with a diffusive model for flow induced particle motion (Phillips et al., 1992; Leighton and Acrivos, 1987), has been assimilated into a finite element code, and found to qualitatively predict phase migration in steady, two-dimensional Couette Flow (Fang and Phan-Thien, 1995), and in laminar pipe flow (Zhang and Acrivos, 1994). Later work (D'Avino et al., 2010) examined the behaviour of a single particle in a sheared viscoelastic fluid, and found the presence of migratory effects is independent of fluid properties. This work has been extended (Subia et al., 1998) to axi-symmetric three-dimensional flows, and shown to yield qualitative agreement with experimental data that is significantly better than previous

continuum approaches. In these cases, the model has been benchmarked using analytical solutions based on the constitutive model. Microstructurally-considerate constitutive approaches such as these are advantageous over CFD-DEM coupled approaches as the computational expense is greatly reduced.

One-dimensional models for phase migration during ram extrusion have also been developed (Rough et al., 2000, 2002). Such models have been grounded more in soil mechanics, utilising Janssen-Walker stress analysis, while describing the liquid flow using a Darcy-type model (Darcy, 1856). While they are able to achieve some qualitative agreement with experiment and are potentially useful in predicting threshold extrusion velocities for phase migration, they are limited in that they fail to account for suction effects, which as mentioned previously are thought to be significant, and they require experimentally determined parameters.

In another approach, Patel *et. al.* (Patel et al., 2007) developed a two-dimensional modelling technique that treats the solid and liquid phases separately, and implemented it in the commercial finite element code ABAQUS. The solid phase is treated as a matrix that is subject to deformations resulting from the large strains associated with the extrusion process. As with previous models, the liquid phase is described using Darcy's Law, as though it is flowing through a static solid porous medium. Again, a limitation of this method is that considerable experimental validation is essential.

In the present chapter, we address the shortcomings of existing extrusion modelling techniques by establishing a particle-based simulation that accounts for particle-particle and particle-liquid effects explicitly as described throughout this thesis.

6.2 Model description

6.2.1 Contact model

We employ the model described in Chapter 4. The paste is bidisperse, being composed of a 1:1 mixture (by number) of particles with diameters d and $1.5d$. Such a particle size distribution is adopted to prevent crystallisation (as occurs for sheared monodisperse particles (Ikeda et al., 2012) (and references therein)), and to approximate a bimodal distribution that may be encountered in a real paste. For simplicity, the paste is assumed to be non-Brownian, meaning particle thermal diffusion is negligible compared to advection under the driving flow. This non-Brownian limit, corresponding to Péclet number $\mathrm{Pe}(=3\pi\eta_f\dot{\gamma}d^3/4kT) > 1$ for characteristic shear rate $\dot{\gamma}$, arises in dense suspensions of both silica and polymethylmethacrylate, for example, under typical processing conditions (Lin et al., 2015). For an interaction between particles i and j, the force and

torque on particle i can be expressed as

$$\begin{aligned}\mathbf{F}_{ij}^{h} &= -a_{sq}6\pi\eta_f(\mathbf{v}_i-\mathbf{v}_j)\cdot\mathbf{n}_{ij}\mathbf{n}_{ij} \\ &\quad - a_{sh}6\pi\eta_f(\mathbf{v}_i-\mathbf{v}_j)\cdot(\mathbf{I}-\mathbf{n}_{ij}\mathbf{n}_{ij}),\end{aligned} \tag{6.2a}$$

$$\begin{aligned}\mathbf{\Gamma}_{ij}^{h} &= -a_{pu}\pi\eta_f d_i^3(\boldsymbol{\omega}_i-\boldsymbol{\omega}_j)\cdot(\mathbf{I}-\mathbf{n}_{ij}\mathbf{n}_{ij}) \\ &\quad - \frac{d_i}{2}\left(\mathbf{n}_{ij}\times\mathbf{F}_i^{l}\right).\end{aligned} \tag{6.2b}$$

for particle diameter d_i, fluid viscosity η_f [viscosity unit: $\rho d^2/t$], centre-to-centre unit vector from j to i $\mathbf{n}_{ij}$ and identity tensor $\mathbf{I}$. The squeeze a_{sq}, shear a_{sh} and pump a_{pu} resistance terms, derived by (Kim and Karrila, 1991) for $\beta = d_j/d_i$, are given by

$$\begin{aligned}a_{sq} &= \frac{\beta^2}{(1+\beta)^2}\frac{d_i^2}{4h_{\text{eff}}} + \frac{1+7\beta+\beta^2}{5(1+\beta)^3}\frac{d_i}{2}\ln\left(\frac{d_i}{2h_{\text{eff}}}\right) \\ &\quad + \frac{1+18\beta-29\beta^2+18\beta^3+\beta^4}{21(1+\beta)^4}\frac{d_i^2}{4h_{\text{eff}}}\ln\left(\frac{d_i}{2h_{\text{eff}}}\right),\end{aligned} \tag{6.3a}$$

$$\begin{aligned}a_{sh} &= 4\beta\frac{2+\beta+2\beta^2}{15(1+\beta)^3}\frac{d_i}{2}\ln\left(\frac{d_i}{2h_{\text{eff}}}\right) \\ &\quad + 4\frac{16-45\beta+58\beta^2-45\beta^3+16\beta^4}{375(1+\beta)^4}\frac{d_i^2}{4h_{\text{eff}}}\ln\left(\frac{d_i}{2h_{\text{eff}}}\right),\end{aligned} \tag{6.3b}$$

$$\begin{aligned}a_{pu} &= \beta\frac{4+\beta}{10(1+\beta)^2}\ln\left(\frac{d_i}{2h_{\text{eff}}}\right) \\ &\quad + \frac{32-33\beta+83\beta^2+43\beta^3}{250(1+\beta)^3}\frac{d_i}{2h_{\text{eff}}}\ln\left(\frac{d_i}{2h_{\text{eff}}}\right).\end{aligned} \tag{6.3c}$$

For each pairwise interaction, the interparticle gap, i.e. the surface-to-surface distance, h is calculated according to $h = |\mathbf{r}_{ij}| - \frac{d_i+d_j}{2}$ for centre-to-centre vector $\mathbf{r}_{ij}$. We truncate the lubrication divergence and regularize the contact singularity at a typical asperity length scale $h_{\min} = 0.001d_{ij}$ (for weighted average particle diameter $d_{ij} = \frac{d_i d_j}{d_i+d_j}$), i.e., setting $h = h_{\min}$ in the force calculation, when $h < h_{\min}$. The effective interparticle gap used in the force calculation, h_{eff}, is therefore given by

$$h_{\text{eff}} = \begin{cases} h & \text{for } h > h_{\min} \\ h_{\min} & \text{otherwise.}\end{cases} \tag{6.4}$$

For computational efficiency, the lubrication forces are omitted when the interparticle gap h is greater than $h_{\max} = 0.05d_{ij}$. The volume fraction is sufficiently high that all particles have numerous neighbours within this range, so such an omission is inconsequential to the dynamics. When a lubrication film between two particle surfaces

ruptures, for example below some critical Sommerfeld number (Fernandez et al., 2013) (this occurs when $h < 0$), the particle interaction is defined according to a purely repulsive linear spring model (Cundall and Strack, 1979), with normal ($\mathbf{F}^{c,n}$) and tangential ($\mathbf{F}^{c,t}$) force and torque $\mathbf{\Gamma}^c$ given by

$$\mathbf{F}_{ij}^{c,n} = k_\mathrm{n}\delta\mathbf{n}_\mathrm{ij}, \tag{6.5a}$$

$$\mathbf{F}_{ij}^{c,t} = -k_\mathrm{t}\mathbf{u}_\mathrm{ij}, \tag{6.5b}$$

$$\mathbf{\Gamma}_i^c = -\frac{d_i}{2}(\mathbf{n}_{ij} \times \mathbf{F}_{i,j}^{c,t}), \tag{6.5c}$$

for a collision between particles i and j with normal and tangential spring stiffnesses k_n and k_t respectively, particle overlap δ and tangential displacement $\mathbf{u}_\mathrm{ij}$. We note that the damping arising from hydrodynamic interactions is always sufficient to achieve a steady state without employing a thermostat, so further damping in the particle-particle contact model is omitted for simplicity. A Coulomb particle-particle friction coefficient μ_p is defined according to $|\mathbf{F}_{i,j}^{c,t}| \leq \mu_p|\mathbf{F}_{i,j}^{c,n}|$, setting a maximum value for the tangential force exerted during a collision. This friction coefficient sets a critical force value for which contacting particles will slide past each other rather than role over each other. In addition, a particle-wall friction coefficient μ_w is defined, regulating the maximum tangential force that may be exerted by the wall on any particle.

Hydrodynamic and contact stress tensors are calculated according to

$$\boldsymbol{\sigma}^H = \frac{1}{V}\sum_i\sum_{i\neq j}\mathbf{r}_{ij}\mathbf{F}_{ij}^h, \tag{6.6a}$$

$$\boldsymbol{\sigma}^C = \frac{1}{V}\sum_i\sum_{i\neq j}\mathbf{r}_{ij}\mathbf{F}_{ij}^c, \tag{6.6b}$$

respectively (Ness and Sun, 2015), where $\mathbf{F}_{ij}^c = \mathbf{F}_{ij}^{c,n} + \mathbf{F}_{ij}^{c,t}$ and V is a characteristic volume in which the stress is being evaluated. The relevant stress components that we discuss in this work are the hydrodynamic and contact shear components in the velocity-gradient plane (the *xy* plane, see Figure 6.1), σ^h and σ^c respectively, and the mean normal stresses, or the pressures, P^h and P^c respectively. The total stresses σ and P are obtained by summing the contributions $\sigma^h + \sigma^c$ and $P^h + P^c$ respectively (Gallier et al., 2014).

6.2.2 Geometry and boundary conditions

A model paste described by the above set of interaction forces flows through a pseudo-2D square entry extrusion die with geometry and dimensions given in Figure 6.1. A

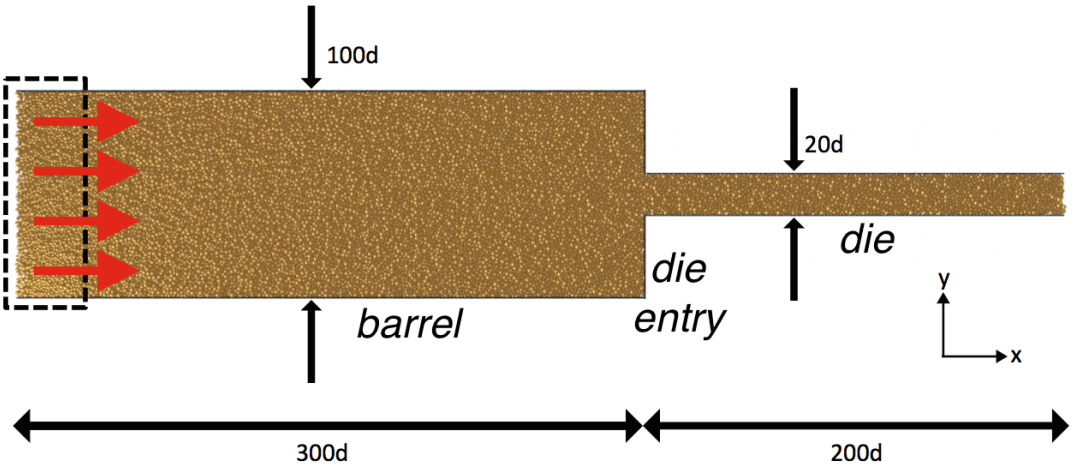

Fig. 6.1 Schematic of the extrusion geometry used in the present work, with flow from left to right. Dimensions shown in units of d. The geometry is $5d$ thick in the z-direction, with a periodic boundary condition on front and back. The dashed box illustrates the particle insertion and force application region.

barrel width of $100d$ and a die width of $20d$ are used to approximate a very narrow confinement such as may arise in an industrial extrusion application, for example the extrusion geometry pertaining to the inner honeycomb walls of a monolithic ceramic catalyst support. While the die width of $20d$ may be realistic for the narrowest industrially employed extrusion dies, the corresponding barrel width in such an apparatus would generally be considerably larger than $100d$. The present dimensions are chosen, however, to reduce computational expense while retaining relevant features of the geometry such that the resulting velocity and stress profiles may be indicative of those that arise in reality. The geometry is periodic in the $z-$direction, with a depth of $5d$.

Extruder walls are composed of particles of diameter $0.5d$ at very high area fraction, giving an inherent wall "bumpiness" that will offer some resistance to flow by allowing the walls to support non-zero loads in the $x-$direction. An identical contact model to that presented in Section 6.2.1, comprising hydrodynamic and contact forces, is used to describe the interaction between paste particles and wall particles, though a separate friction coefficient μ_w is defined independently of μ_p, allowing the frictional behaviour between particle and wall to be different to that for particle-particle contacts.

A pressure drop along the axial ($x-$direction) length of the extruder is generated by applying a constant body force F in the positive $x-$direction at each timestep to all particles that are inside the dashed box in Figure 6.1. These particles will consequently move downstream out of the dashed box, where they will exert contact forces on neighbouring particles that eventually percolate the extruder and result in mass flow through the die. The flow rate through the extruder is therefore dependent on the

magnitude of the constant force applied in the dashed box. In order to achieve steady flow over large displacements, particles are generated inside the dashed box at each timestep, such that the particle volume fraction (defined as the volume of particle divided by the total volume) within this region remains at approximately $\phi = 0.5$. Note that there is no imposed volume fraction or particle number in the extruder: a constant volume fraction and driving force are maintained only within the dashed box. Downstream of this region the system dynamically reaches an "equilibrium" state with a driving-force-dependent flow rate, pressure drop and volume fraction. The downstream end of the geometry is open, so particles flowing out of the end of the die are removed from the simulation and subsequently omitted from contact force and stress calculations.

Simulations can then be run ad infinitum, meaning time averaged as well as instantaneous flow features can be studied. The imposed force magnitudes F that will be implemented in the present work are chosen such that the flow remains close to the "hard particle" limit (practically this means particle overlaps, quantified by δ, remain $\ll 0.01d$) and such that overdamping arising due to particle-fluid interactions is sufficiently thorough that particle inertia can be neglected. Simple shear flow simulations of an analogous paste (Chapter 2) (Ness and Sun, 2015) suggest that the rheology should consequently be Newtonian (i.e. stresses scale linearly with shear rates) though exquisitely sensitive to particle volume fraction. Violation of the above criteria would lead to "soft-particle", shear thinning rheology and inertial, Bagnoldian, shear thickening rheology respectively, both of which may be captured by the present model but are beyond the scope of the present study.

For post-processing, we adopt a simple binning protocol to coarse grain the particle information and obtain pseudo-continuous velocity (V_x, V_y, V_z), volume fraction (ϕ) and stress (σ, P) fields. Bins are generated with dimensions $d \times d \times 5d$ on a regular grid in the $x-y$ plane. The properties of each particle are accumulated in a bin based on the coordinates of centre of that particle. We then obtain a coarse grained map of the velocity, volume fraction and stress profiles at each timestep which can be used to generate temporally-averaged profiles or to study transient features of the flow.

6.2.3 Simulation cases studied

In the present study, we give a general description of the flow features predicted by the above model, followed by an overview of the sensitivity of these features to the model parameters. From the particle-fluid interaction, the available parameters are the magnitude of the fluid viscosity η_f and the limiting surface separation constants $h_{\min}$ and $h_{\max}$. As discussed above, h_{max} is chosen to be sufficiently large that all immediate neighbours will be considered when calculating the lubrication forces for a particle.

Case	Particle friction μ_p	Wall friction μ_w	Fluid viscosity η_f	Particle stiffness k_n
A	1	0	0.05	10000
B	1	0.1	0.05	10000
C	0.1	0	0.05	10000
D	0.1	0.1	0.05	10000
E	1	0	0.0005	10000
F	1	0	0.05	20000

Table 6.1 Summary of particle and wall properties investigated

It has been confirmed that setting $h_{max} = 0.1d_{ij}$ does not give significantly different rheological behaviour. Furthermore, it has been demonstrated in Chapter 4 (Ness and Sun, 2016a) that the size of $h_{\min}$ is important in determining the "microfragile" (Cates et al., 1998) response of model pastes to minute deformations, but that its influence during large paste deformations and in flows close to steady state is minor. Therefore, the primary fluid parameter available for investigation is the Newtonian viscosity η_f.

The parameters present in the particle-particle interaction are the particle stiffness k_n and the particle-particle and particle-wall friction coefficients μ_p and μ_w respectively. Each of these parameters is varied independently, and the influence on flow behaviour is studied. A summary of each of the simulation Cases explored is given in Table 6.1.

As argued above, the paste flow regime investigated in this work is a "hard-particle", viscous regime. It is therefore anticipated that, provided we remain in this regime, varying the parameters η_f and k_n will have a quantitative, but not qualitative, influence, since the relative paste viscosity (i.e. the paste viscosity divided by the fluid viscosity η_f) is independent of both when driving forces are scaled appropriately (Chialvo et al., 2012; Ness and Sun, 2015; Lin et al., 2015).

6.3 Results

6.3.1 General description of flow features

For each Case, simulations are carried out for driving forces F spanning two orders of magnitude. In addition, five simulations are carried out for each value of F, each with different precise configurations of wall particles but representing the same large-scale geometry. The following results represent ensemble- and time-averages.

We first present a general picture of the flow features obtained using an initial set of parameters, Case A (see Table 6.1). Starting with an empty extruder, the paste flows in at the upstream end as particles are generated, and flow initiated, in the dashed box. There

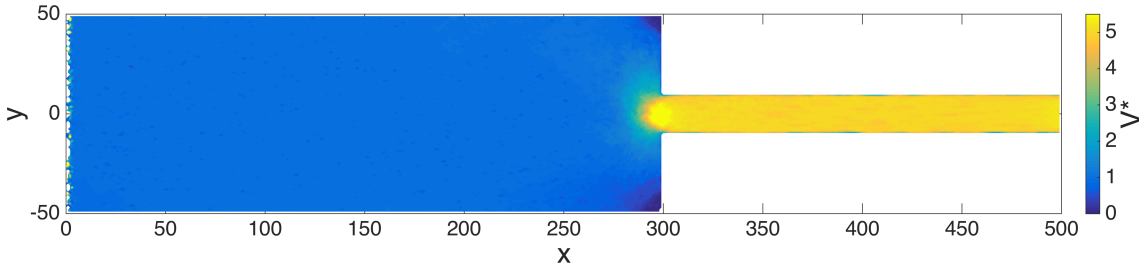

(a) Velocity contour

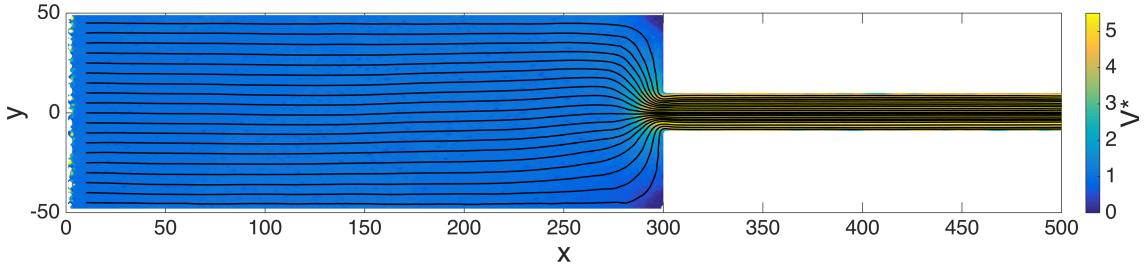

(b) Velocity contour, with superimposed streamlines

Fig. 6.2 (a) Velocity contour plot for Case A showing V^*, the velocity magnitude V scaled by the mean centreline downstream velocity in the barrel V^{barrel}; (b) Same data, with streamlines superimposed.

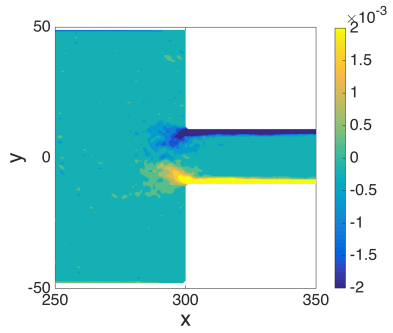

(a) dV_x/dy

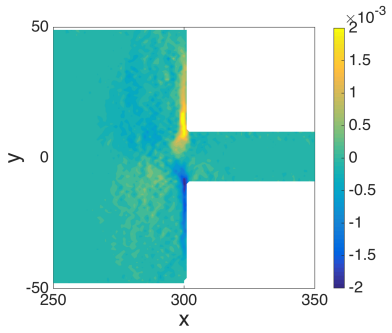

(b) dV_y/dx

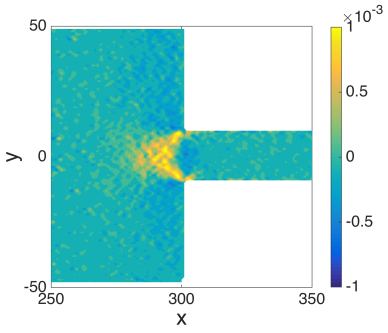

(c) dV_x/dx

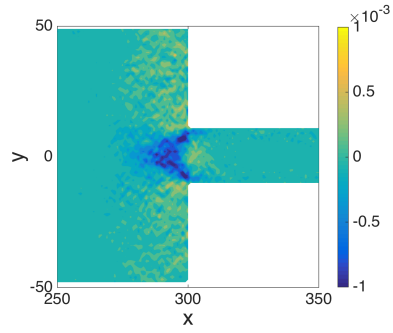

(d) dV_y/dy

Fig. 6.3 Contour plots showing the velocity gradients in the vicinity of the die entry.

is no flow out of the die during this time, so the particle number increases steadily. Once the extrusion barrel fills up and uninterrupted "chains" of contacts establish between the barrel inlet and the die entry, particles begin to flow into, and through, the die to the outlet, eventually establishing a steady state. It is verified that a steady state has been reached by checking that the mass balance is satisfied such that the total number of particles present inside the extruder is approximately constant with time. Since the particle number is not fixed, the outlet flow minus the inlet flow fluctuates with time around zero.

Velocity profiles

A contour plot of the time-averaged velocity magnitude ($V = (V_x^2 + V_y^2 + V_z^2)^{1/2}$) profile is given in Figure 6.2a (with superimposed streamlines added for clarity in Figure 6.2b) for a typical driving force magnitude F^*. Such a profile allows a clear qualitative overview of the flow behaviour within the extruder, which is built upon with more detail later. For simplicity of interpretation, the velocity magnitude is scaled according to $V^* = V/V^{\text{barrel}}$, where V^{barrel} is the mean centreline (i.e. at axial position $y = 0$) downstream velocity in the barrel. Furthermore, we include plots of the velocity gradients in the region of the die entry, Figure 6.3, to elucidate the shearing and extensional flows in the location where high strain rates are generated. We plot the shearing terms dV_x/dy and dV_y/dx and the extensional terms dV_x/dx and dV_y/dy.

Together, the velocity contours and streamlines illustrate that there is a highly laminar, viscous and uniform flow profile inside the extruder, that is qualitatively reminiscent of experimental velocity profiles measured using positron emission particle tracking (Wildman et al., 1999). It is observed that there is very little variation in V along the $x-$direction length of the barrel, in the region between the inlet and around 10-20d upstream of the die entry. Similarly, the $x-$direction flow along the length of the die is highly uniform from around 5-10d downstream of the die entry, to the outlet. To clarify this observation, the centreline velocity magnitude $V(x, y = 0)$ is plotted in Figure 6.4, which shows absolute velocities (Figure 6.4a) as well as velocities scaled by V^{barrel} (Figure 6.4b), for a range of applied forces F. Consistent with expectation, velocity magnitudes increase with increasing F. It is observed in Figure 6.4b that the die velocity is approximately $5\times$ larger than that in the barrel, consistent with the diameter ratio of these regions, satisfying mass conservation. Error bars in Figure 6.4 represent the standard deviation of the velocity fluctuations with time. It is noted that velocity fluctuations in the die appear to be larger for slower-flowing cases. For all values of F, a good collapse of velocity profiles is observed, suggesting a rate-independent rheological deformation behaviour, perhaps consistent with the previously stated constraint of

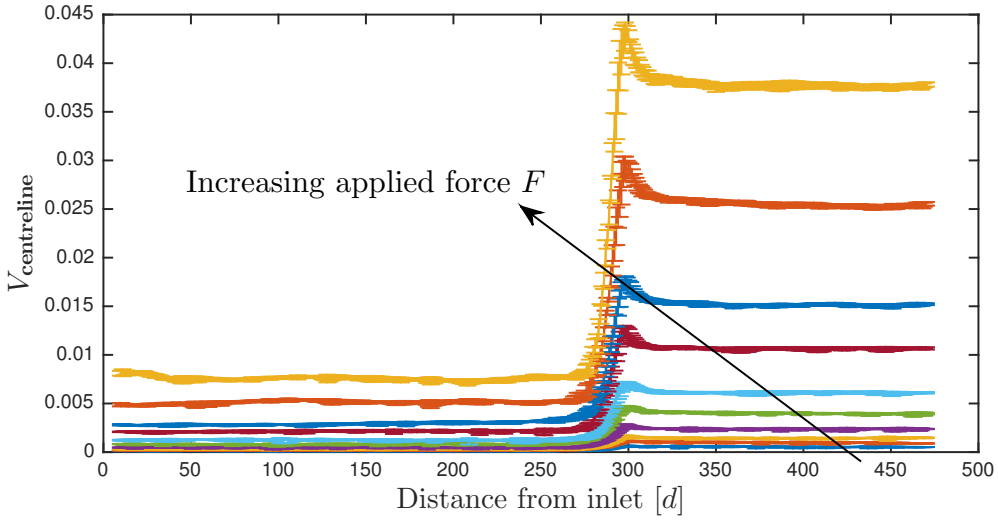

(a)

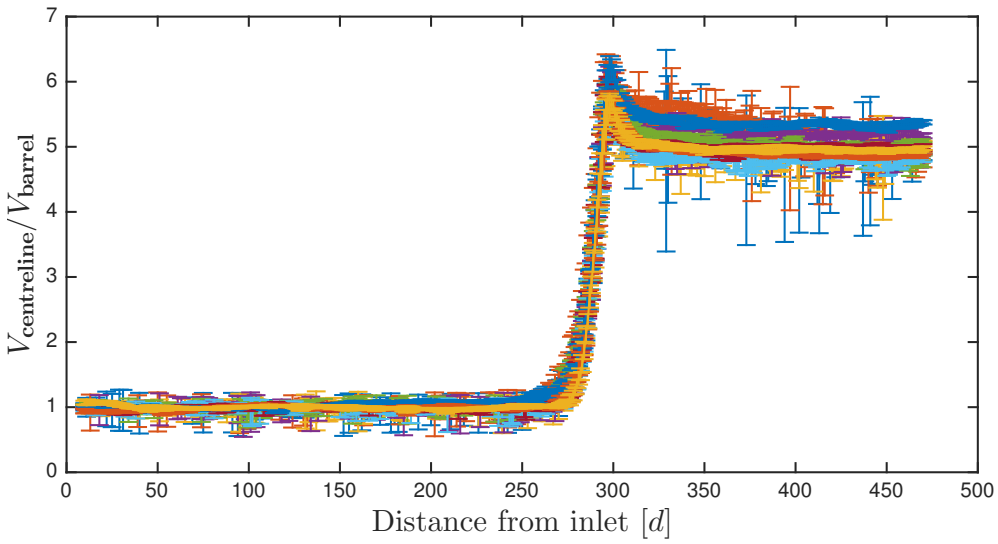

(b)

Fig. 6.4 Centreline velocity magnitude corresponding to Figure 6.2, for a range of applied forces F. (a) Absolute value of the centreline velocity [distance/time units]; (b) Centreline velocity scaled by the mean centreline downstream velocity in the barrel V^{barrel}.

entirely overdamped flow. It is therefore concluded that, while there may be shearing of the paste near the barrel and die walls, the majority of the deformation, that is, the extensional part of the flow, is concentrated within a very narrow region close to the die entry for all paste flow rates.

In both the barrel and the die, the velocity appears to be largely independent of $y-$coordinate, indicating the presence of near-perfect plug flow throughout the extruder, away from the die entry. The particle-wall friction coefficient μ_w is set to zero in this Case (see Table 6.1), meaning any deviation from ideal plug flow, which would represent perfect wall slip, must be attributable to the inherent bumpiness of the boundary (that derives from its particle-based composition), which offers some resistance to flow and can support loads with non-zero $x-$components. Radial velocity profiles are presented for the barrel (y-variation of velocity magnitude V averaged across $50 < x < 200$) and the die (y-variation of velocity magnitude V averaged across $350 < x < 450$) in Figures 6.5 and 6.6 respectively. In each case, the absolute value of the velocity magnitude V is presented along with the scaled values (V/V^{barrel} and V/V^{die}, respectively). From Figure 6.5b, we observe near ideal plug flow in the barrel, while in Figure 6.6b there is some evidence of sheared zones close to the walls. For the purposes of industrial paste processing, it is desirable to minimize the extent of shearing flow, thus moving the system as close to ideal plug-flow as possible. Perfect slip flow can lead to smoothly flowing extrudates with minimal surface defects, whereas shear flow close to the paste surface might result in instabilities in the paste surface being generated at the die outlet.

We next focus on the flow near the die entry. To elucide the deformation modes acting in this region, we present the velocity gradient in Figure 6.3, for shearing (dV_x/dy, dV_y/dx) and extensional (dV_x/dx, dV_y/dy) flows. In each case, we give the velocity gradient scaled by $\rho d^2/\eta_f$, so that the numerical values represent approximated Stokes numbers. The velocity gradients reveal considerable shear flow, both along the inner edges of the die, extending to the outlet (not shown) and, surprisingly, along the vertical inner edges of the die entry, where there is considerable shearing flow in dV_y/dx. The liquid phase migration paradigm suggests that pressure gradients culminating at the die entry corners lead to liquid migration away from this area. There is a consequent increase in particle concentration leading to jamming or solidification at these regions of the extruder. Instead, the present model suggests that a net flow of particles can be achieved along the inner edge of the die entry. We note also that no significant spatial variations in the solids fraction are identified in the present study. The flow at the entrance point to the die exhibits significant extension and compression, as indicated by the dV_x/dx and dV_y/dy profiles. It is observed that the flow entering the die along

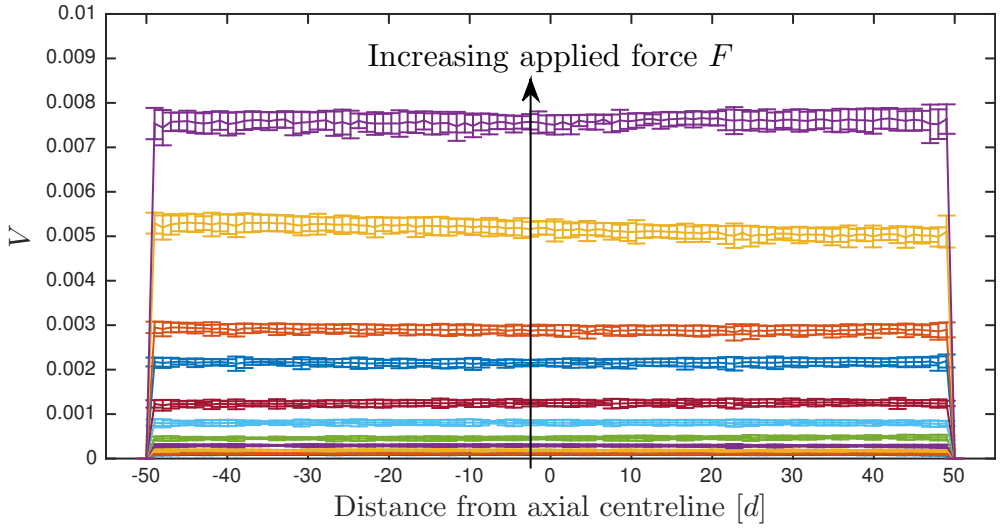

(a)

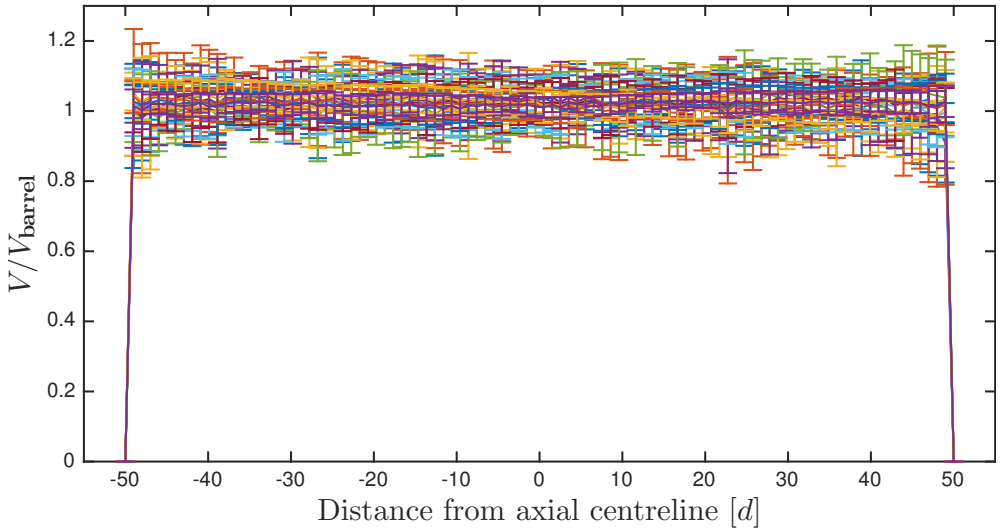

(b)

Fig. 6.5 Radial velocity profiles in the barrel for Case A. (a) Absolute value of the velocity magnitude; (b) Velocity magnitude scaled by the mean centreline downstream velocity in the barrel V_x^{barrel}.

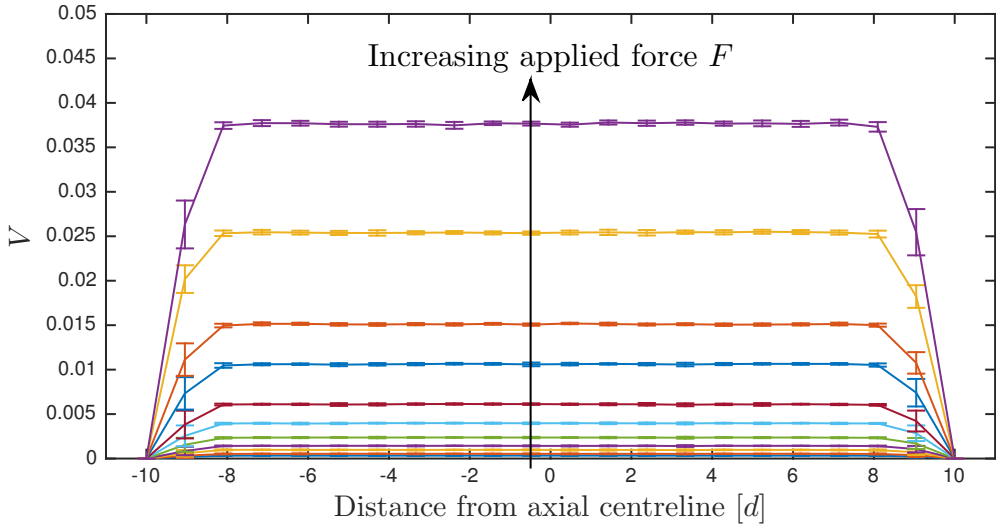

(a)

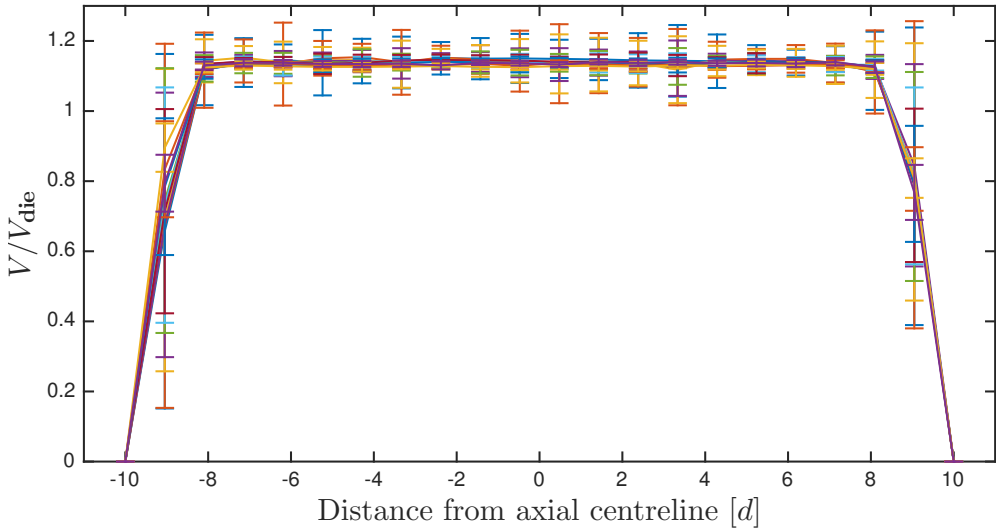

(b)

Fig. 6.6 Radial velocity profiles in the die for Case A. (a) Absolute value of the velocity magnitude; (b) Velocity magnitude scaled by the mean centreline downstream velocity in the die V_x^{die}.

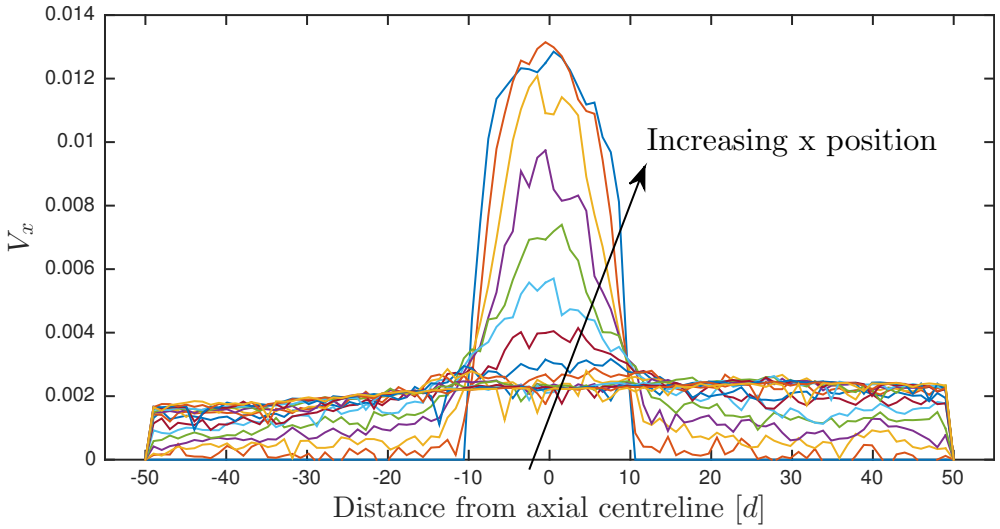

(a)

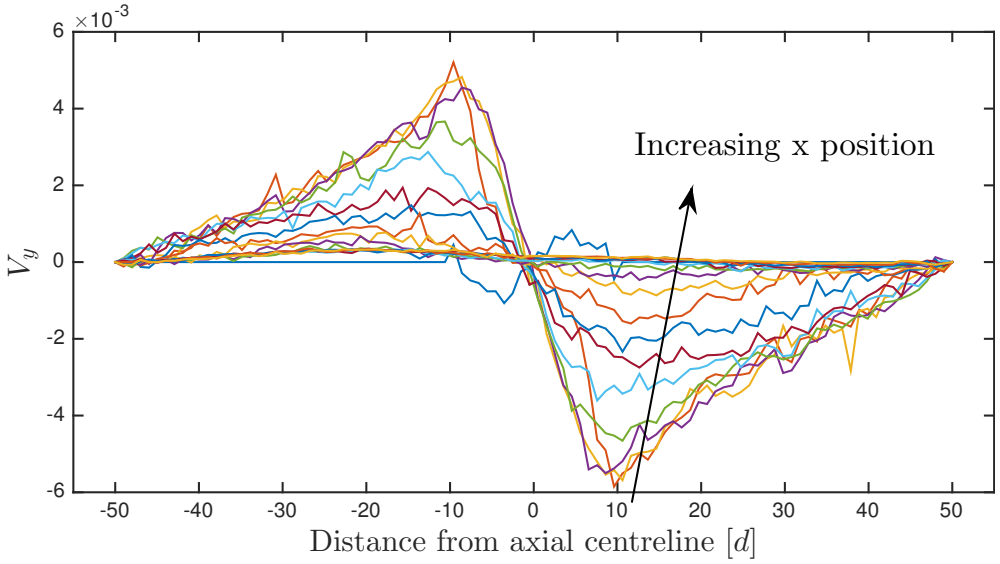

(b)

Fig. 6.7 Velocity profiles at the die entry for a single applied force F, as a function of $x-$coordinate. (a) $x-$component of velocity; (b) $y-$component of velocity;

the vertical extruder walls at the die entry is subject to compression, indicated by the 'squeezing' of the streamlines at this point and the negative dV_y/dy. Simultaneously, the flow entering the die along the extruder axis (near to $y = 0$) undergoes almost pure extension, as shown by the positive dV_x/dx. This stretching of the paste entering the die may be indicative of the above mentioned suction effect that is responsible for drawing liquid out of slower flowing die entry corners into the main extruding flow. These velocity gradients serve to offer a thorough qualitative description of the main deformational flow at the die entry at steady state. Figure 6.7 gives x and y velocity profiles determined at increasing $x-$coordinate (for $250 < x < 300$) for a single value of F. The $x-$component of the velocity exhibits an evolving profile that switches from a wide near-perfect plug across the full barrel width to a distinctly parabolic shape as the paste enters the die. Near-plug flow in the die, consistent with Figure 6.6, is recovered from around $10d$ downstream of the die entry. The $y-$velocity profile illustrates an inward radial mass flow of particles across the barrel width, which diminishes very close to the die entry. Consistent with the steady state nature of the flow and the principle of conservation of mass, the flow is symmetric about the $y = 0$ axis when averaged over time. It is noted, particularly in Figure 6.2, that the lateral flowing regions do not extend fully to the bounding walls at $y = \pm 50$ for $x \to 300$, demonstrating that there are completely stagnant regions in the corners.

For convenience, the extent of these stagnant regions near the die entrance is (somewhat arbitrarily) quantified by counting the number of coarse-grained cells near the square-entry corners for which the local velocity $V^l < 0.25V^{\text{barrel}}$. Each of these cells represents a $d \times d \times 5d$ volume. The variation of this stagnant region size with extrusion velocity is presented in Figure 6.8. Results are presented for each of the five realisations for Case A, as well as the ensemble average. The simulation results suggest that the static zone size decreases consistently with increasing mass flow rate through the extruder. A static zone represents a region in which the solid contact network composed of paste particles is nearly stationary, while the liquid phase may remain mobile by engaging in a porous-media type flow if the pressure field allows. In general, the larger a stagnant region is, the greater the potential for phase migration within the paste. For paste processing purposes, it is therefore desirable to minimize static region formation. The present results would suggest that liquid phase migration deriving from such static zones may be reduced by operating at increased extrusion velocities.

Stress profiles

We next focus on the steady state pressure P and shear stress σ profiles, which are presented in Figures 6.9a and 6.9b respectively. The pressure and shear stress are scaled

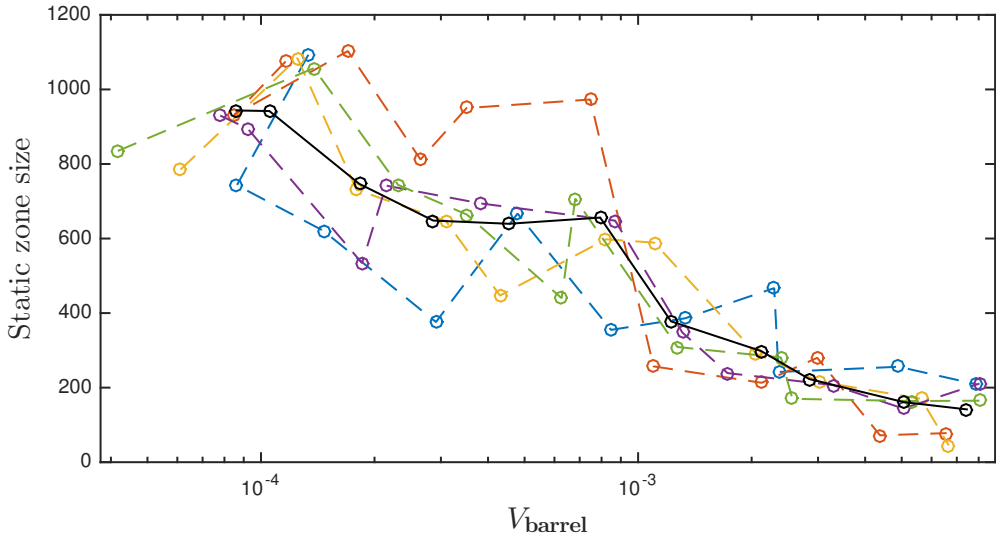

(a)

Fig. 6.8 Time-averaged static zone size, in terms of number of static coarse-grained cells, as a function of F. Coloured lines: individual extrusion realisations. Black line: ensemble-averaged static zone size.

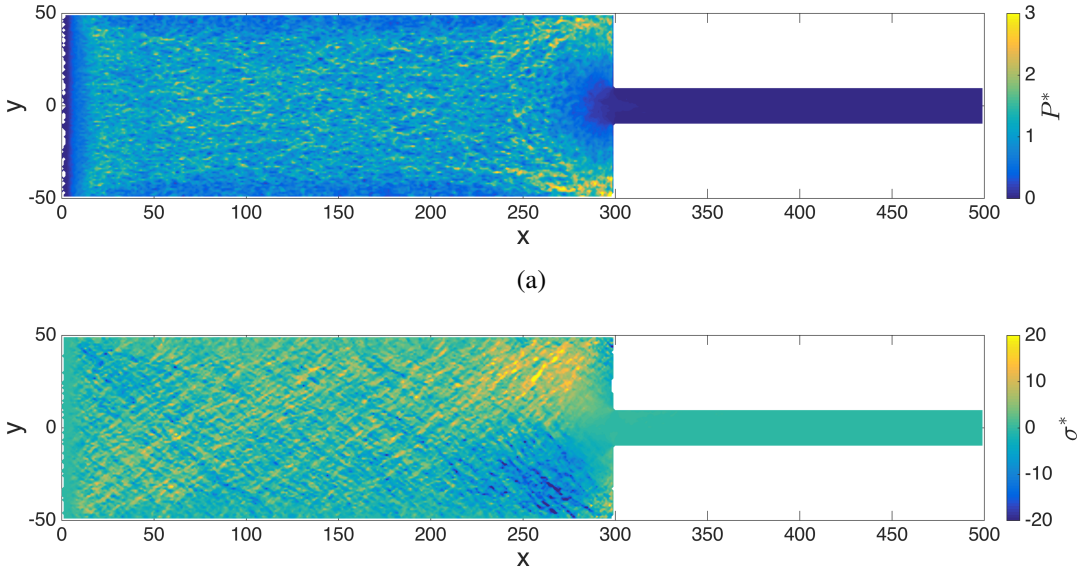

(a)

(b)

Fig. 6.9 Stress profiles for Case A. (a) Pressure profile. The pressure P is scaled by the mean pressure at the upstream end ($25 < x < 50$) of the barrel; (b) Shear stress profile. The shear stress σ is scaled by the mean pressure at the upstream end ($25 < x < 50$) of the barrel.

according to $P^* = P/P^{\text{barrel}}$ and $\sigma^* = \sigma/P^{\text{barrel}}$ respectively, where P^{barrel} is the mean pressure at the upstream end of the barrel in the region $25 < x < 50$ and P and σ are as defined previously. It is noted that erroneous (i.e. particularly low) stresses are found for $0 < x < 10$ due to the boundary condition being implemented within this region.

Mean normal stress (pressure) profile Consistent with the velocity profile, a rather uniform pressure profile is observed in the main flowing regions of the barrel (for $50 < x < 200$) and the die (for $350 < x < 450$), away from the die entry. This is illustrated in the radial pressure profile plots for barrel and die, given in Figure 6.10. A slight pressure reduction is observed within 10-20d from the barrel walls in Figure 6.10a, though the pressure remains largely uniform across the majority of the barrel width. The pressure behaves similarly in the die, with a largely uniform value across the width that increases with increasing applied force F. In Figure 6.11a we plot the pressure along the extruder centreline (where $y = 0$) for a range of flow rates. It is found that the variation in x within the barrel ($x < 250$) is minimal, suggesting that, for the present Case of $\mu_w = 0$, the pressure drop resulting from the inherent wall bumpiness is negligible. A significant pressure drop, typically around an order of magnitude, is then observed immediately upstream of the die entry, in the region $250 < x < 300$. There is a minimal pressure drop, between one and two orders of magnitude though the absolute value is already considerably reduced following flow through the die entry, along the length of the die. The pressure then drops to zero at the outlet. This pressure evolution along the channel length is further elucidated in Figure 6.11a. It is notable that pressure fluctuations (given as error bars in Figure 6.11a that represent the standard deviation of pressure with time) are observed to increase considerably with increasing flow rate, and that the relative magnitude of the fluctuations in the die are larger than those in the barrel. This axial pressure drop is essentially the driving force for the net flow of paste through the extruder.

A marked deviation from uniform pressure distribution is observed in the region $250 < x < 300$. An arching effect is observed, whereby regions of high pressure extend from just upstream of the die entry into the corner stagnant zones. The pressure reaches a maximum at these points. This arching pressure appears to be transmitted inhomogeneously through force chains that can be observed as narrow regions of high pressure protruding from near the corners of the square die entry region into the central part of the barrel. Such arching behaviour is reminiscient of simulations of gravity-driven silo discharges (Rotter et al., 1998), in which normal and tangential loads supported by frictional walls allow stable “bridges” to transiently form and collapse. For the nearly-frictionless walls considered in the present simulation, it is expected that

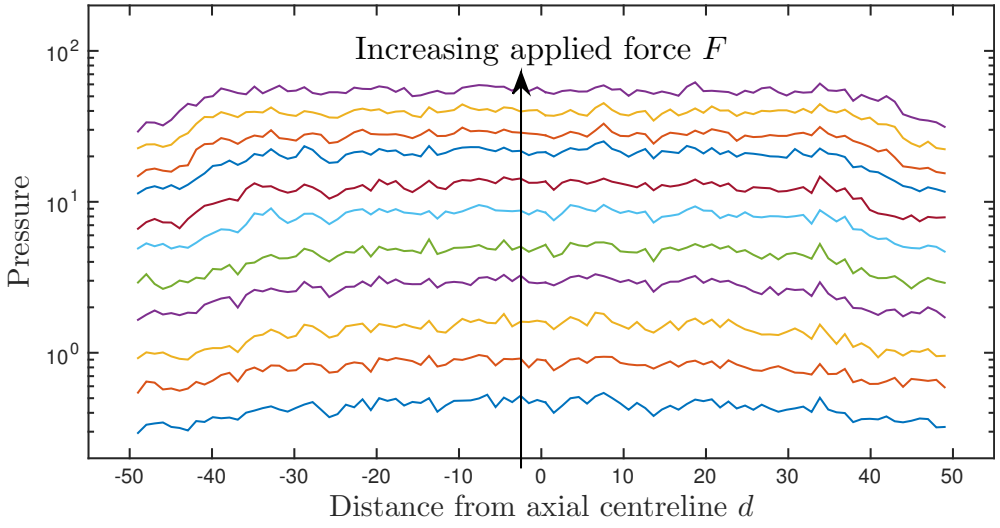

(a)

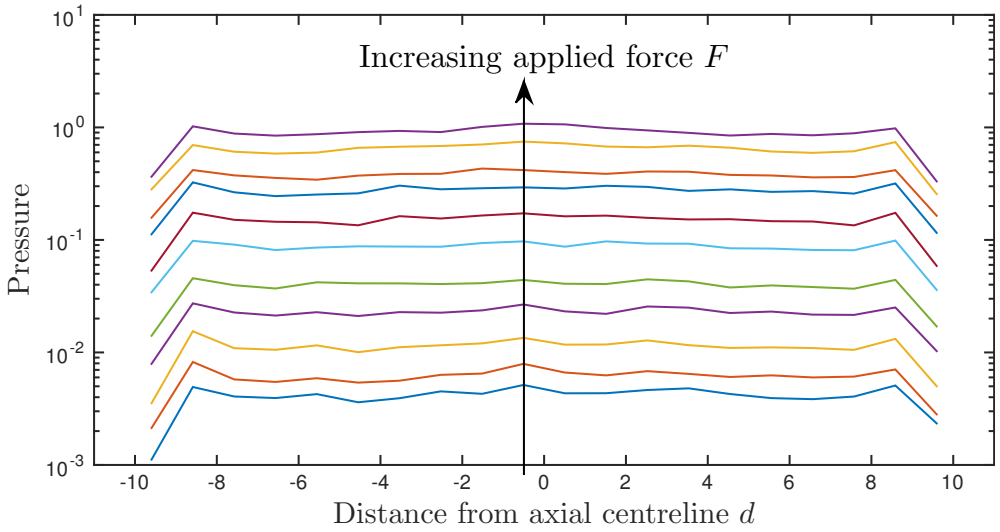

(b)

Fig. 6.10 Radial pressure profiles for Case A, for a range of applied forces F. (a) Radial pressure at the upstream end of the barrel ($25 < x < 50$); (b) Radial pressure at the upstream end of the die ($325 < x < 350$).

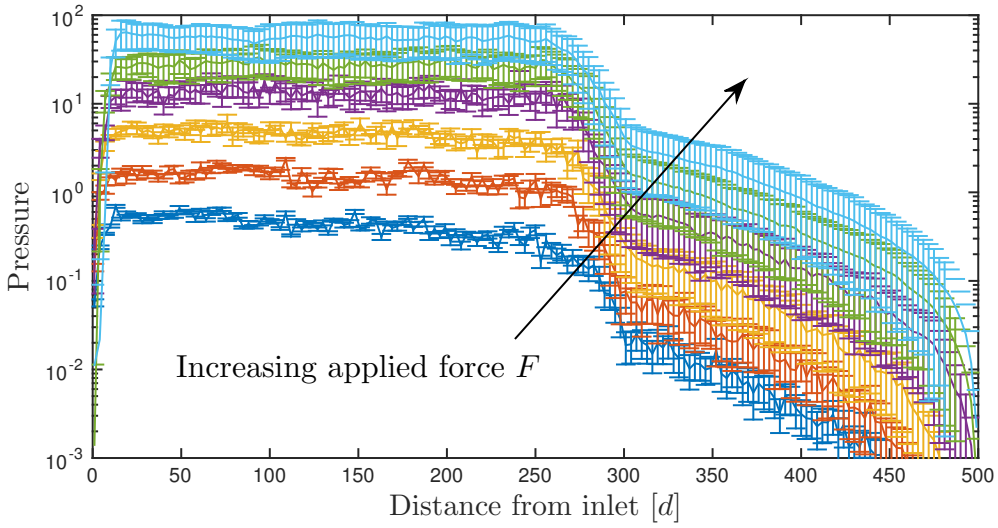

(a)

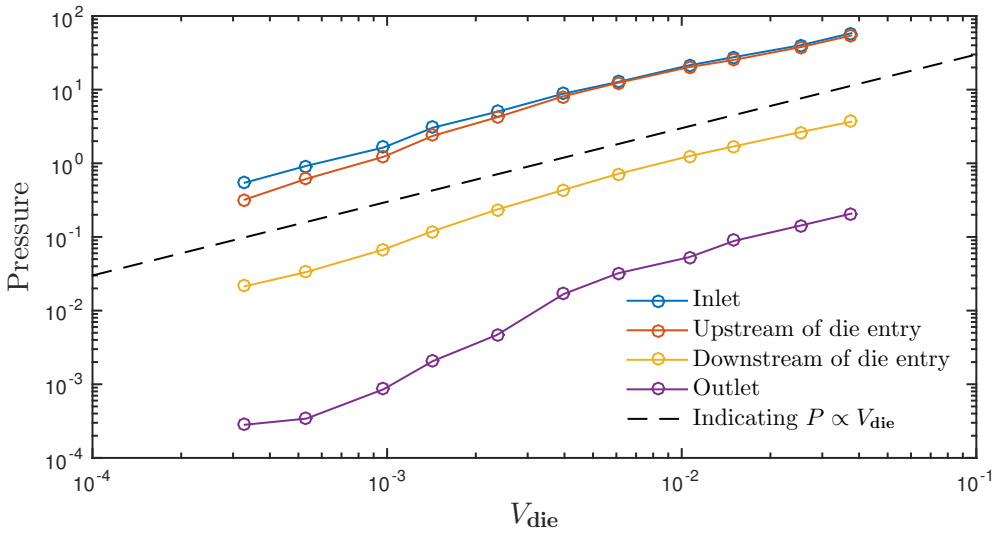

(b)

Fig. 6.11 (a) Axial pressure profiles for Case A, for a range of applied forces F. (b) Local centreline pressure at four points across the length of the extruder.

the focussing of normal stresses on the square end walls at $x = 300$ will be exaggerated, since only minimal $x-$direction loads can be supported by the barrel walls. There is a significant pressure drop in the $y-$direction at the die entry, for $275 < x < 300$. This radial pressure drop between the corners of the die entry and the die entry itself is responsible for the lateral mass flow of paste observed in this region.

Shear stress profile Shear stress profiles evaluated in the barrel ($25 < x < 50$) and the die ($325 < x < 350$) are presented in Figure 6.12. For both the barrel and the die, the observed shear stress profiles are symmetric (in terms of magnitude) about $y = 0$, as expected. The radial shear stress profile across the die is approximately linear, while that in the barrel is approximately linear in the region $|y| < 20d$, but curves off significantly, leaving an almost flat profile for $20 < |y| < 40$. In both cases, the shear stress drops close to zero at the bounding walls. The shear stress contour plot in Figure 6.9 shows a profile that is comparable to that previously discussed for the pressure. Notably, there are regions of significantly higher shear stress that correspond to the local arching effects. The shear stress in these regions is, consistent with the pressure, focussed into narrow bands, or chains, that propagate from the central point of the arch to close to the square die corners. These pressure and stress profiles clearly emphasise the inherently discrete nature of the flow, highlighting the challenge of successfully and adequately capturing the flow behaviour using a single phase continuum level constitutive model.

6.3.2 Role of model parameters

The bulk flow behaviour of the paste with respect to the previously identified model parameters is assessed by considering the relationship between the velocity in the die during extrusion and the extrusion pressure drop, the velocity profiles in the die, and the extent of static zone formation.

Pressure drop versus velocity relationship

The variation of pressure drop along the extruder with extrudate (i.e. die) velocity is presented in Figures 6.13 and 6.14. We present the total pressure drop ΔP, the pressure drop in the barrel ΔP^{barrel}, the pressure drop due to paste deformation at the die entry $\Delta P^{\text{die-entry}}$, and the pressure drop in the die ΔP^{die}. For each pressure drop, results are presented for each of simulation Cases A - F. In addition, a dashed line is included to indicate a gradient of unity.

In all Cases, each of the pressure drops are found to vary approximately linearly with barrel velocity, for the entire range of velocities considered. This linear variation of

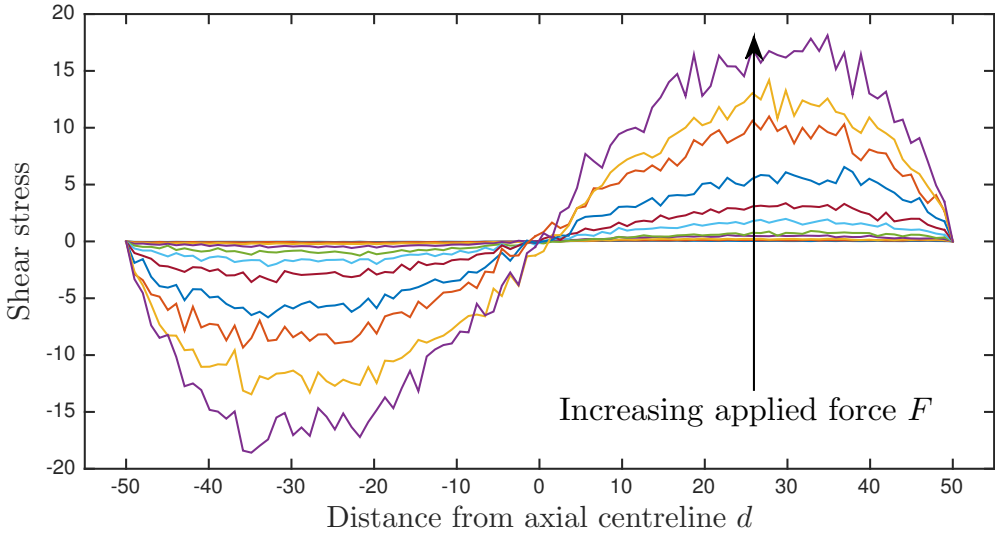

(a)

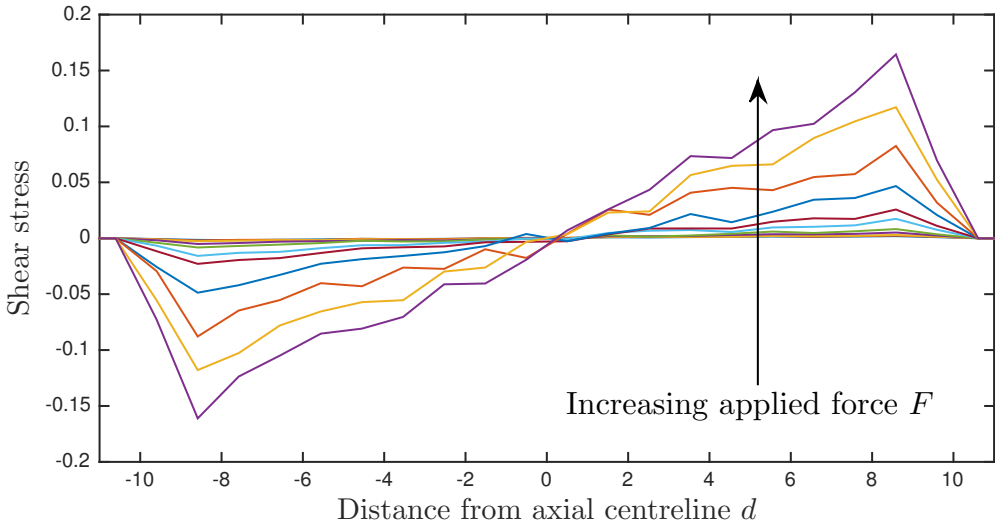

(b)

Fig. 6.12 Radial shear stress profiles for Case A, for a range of applied forces F. (a) Radial shear stress at the upstream end of the barrel ($25 < x < 50$); (b) Radial shear stress at the upstream end of the die ($325 < x < 350$).

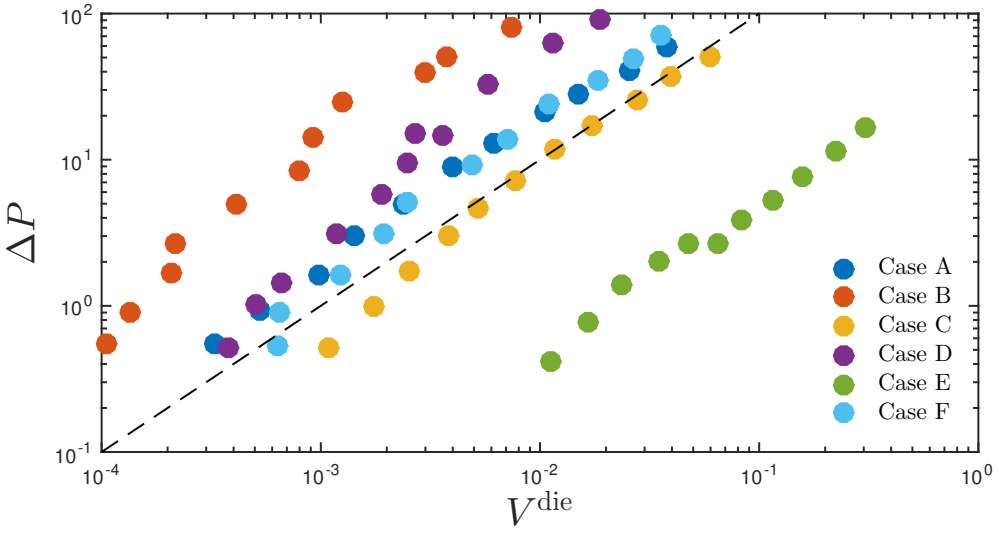

(a)

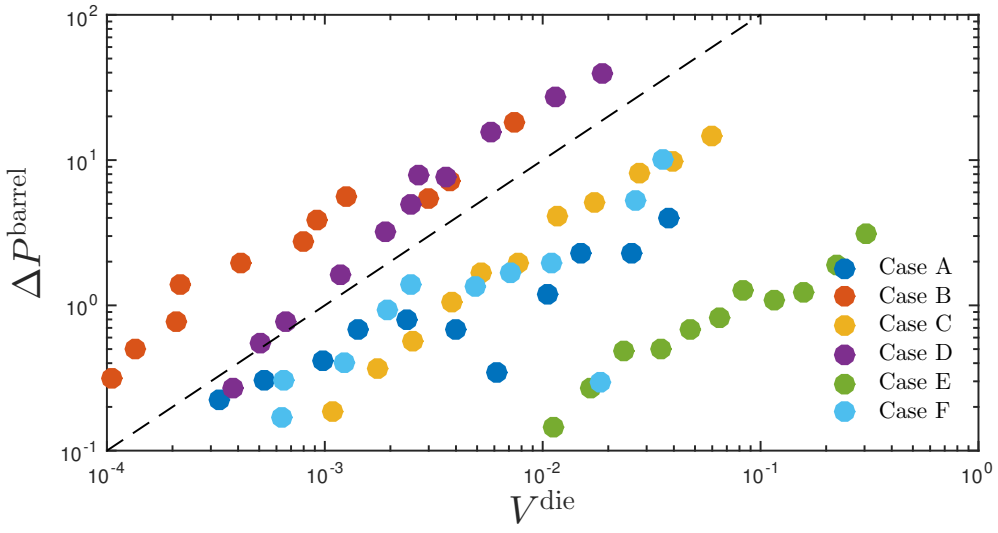

(b)

Fig. 6.13 Pressure drop versus die velocity [simulation units] for Cases A - F, as described in Table 6.1. (a) Total pressure drop across extruder; (b) Barrel pressure drop;

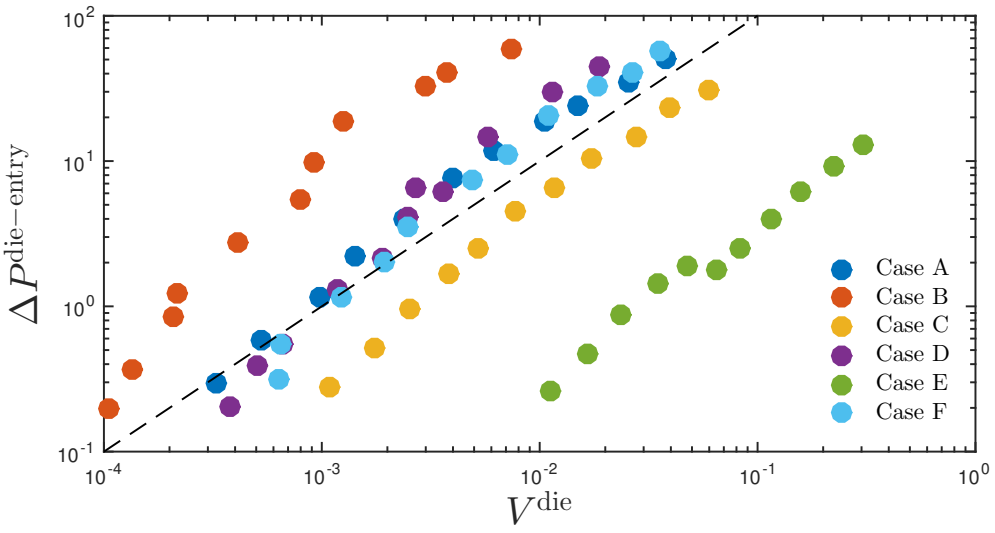

(a)

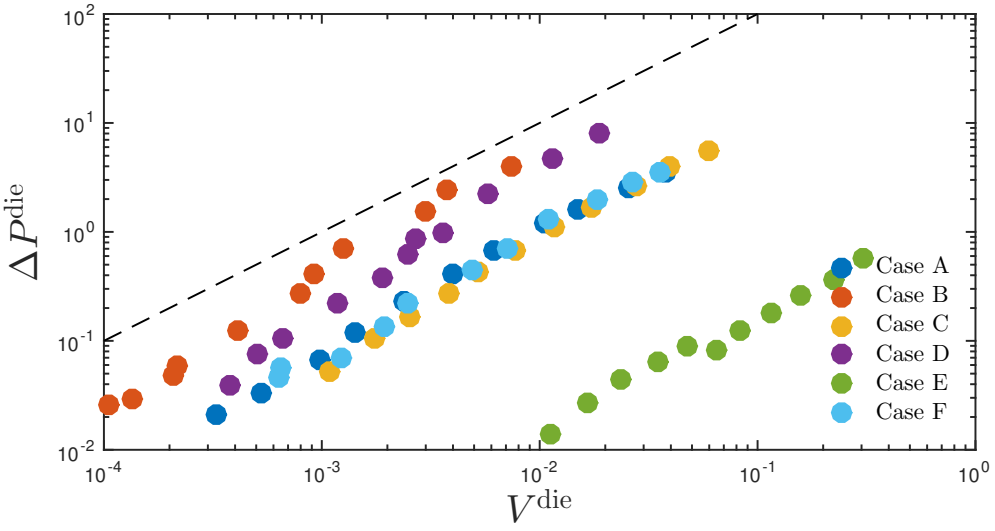

(b)

Fig. 6.14 Pressure drop versus die velocity [simulation units] for Cases A - F, as described inTable 6.1. (a) Die-entry pressure drop; (b) Die pressure drop. Dashed black line indicates a gradient of unity.

pressure with velocity implies that the material obeys $\sigma \propto \dot{\gamma}$, i.e. quasi-Newtonian ($\eta \neq f(\dot{\gamma})$) behaviour under shear flow. Such behaviour stems directly from the nature of the lubrication contact model described in Section 6.2.1, which, assuming sufficiently hard particles and particle Stokes numbers considerably less than unity, leads to suspension stresses that scale linearly with shear rate under steady state shear flow (Ness and Sun, 2015).

It is observed that no yield-stress behaviour is predicted by the present model. This can be explained by the boundary conditions of the simulation, in which the global volume fraction within the extruder is not fixed. Therefore, for any applied force at the barrel inlet, the volume fraction within the extruder evolves over time and eventually adopts a value such that flow may occur. In all Cases, therefore, the volume fraction throughout the extruder is found to be approximately uniform, with a value that lies marginally below the respective critical volume fraction for jamming (Liu and Nagel, 1998) for the relevant set of model parameters. It is widely acknowledged that the critical volume fraction for jamming is crucially dependent on the particle-particle friction coefficient (Da Cruz et al., 2005; Sun and Sundaresan, 2011; Guy et al., 2015). Simulations in a comparable geometry (not shown in the present work) indicate that a precompaction process, whereby the paste volume fraction is forced to be above its critical value for jamming or flow arrest, introduces yield stress behaviour into the material.

Consistent with the previous discussion regarding the independence of rheology on particle stiffness k_n provided the hard-particle limit is adhered to, it is observed in Figures 6.13 and 6.14 that the results for Cases A and F, corresponding to particle stiffnesses k_n and $2k_n$ respectively, are nearly identical.

Comparing Cases A and E, a dramatic increase in extrusion flow rate is observed for reduced suspending fluid viscosity, at fixed ΔP, as expected. It is noted, however, that this increase in flow rate is approximately two orders of magnitude, for a reduction in η_f of the same proportion. Considering the paste flow behaviour in terms of viscous number rheology (Jop et al., 2006; Forterre and Pouliquen, 2008; Boyer et al., 2011) (applicable for hard-particle and entirely non-inertial flows), therefore, it is determined that Cases A and E represent identical flow states, for which the parameter $\eta_f \dot{\gamma}/P$ is approximately constant.

Total pressure drop predictions (Figure 6.13a) for Cases B to D are in line with expectation: increasing particle-particle friction (compare Cases A and C) increases total pressure drop; increasing particle-wall friction (compare Cases A and B or Cases C and D) increases total pressure drop. Comparing the relative barrel, die-entry and die pressure drops is, however, more revealing. For flow within the barrel, the pressure drop

ΔP^{barrel}, is found to be remarkably insensitive to the particle-particle friction, illustrated by comparison between Cases A and C or Cases B and D. Barrel flow is, however, highly sensitive to particle-wall friction, showing that the entirety of the dissipation within this region is driven by particle-wall interactions, regardless of the frictional properties of the particles. Analogous behaviour is observed for ΔP^{die}, though the pressure drop magnitudes are considerably lower than those in the barrel.

The pressure drop at the die-entry, $\Delta P^{\text{die}-\text{entry}}$, dominates the total pressure drop within the extruder. Comparing Cases A to D reveals that the pressure drop magnitude is sensitive to both the particle-particle μ_p and particle-wall μ_w friction coefficients. From the velocity profile contour plot in Figure 6.2, it can be deduced that the pressure drop at the die entry derives from both a predominantly elongational paste deformation across $275 < x < 300$, and a lateral ($y-$direction) flow of material along the bounding wall at $x = 300$. The former may be dominated by details of particle-particle interaction, whereas the latter may be more sensitive to the particle-wall behaviour.

These results provide quantitative guidance about how future constitutive models, for example those based on the traditional Benbow-Bridgwater equation, might be linked more explicitly to the physical properties of the constituent paste particles. For example, the present results exhibit linear scaling of the pressure drop with respect to extrusion velocity, indicating that the m and n parameters may be dropped from the Benbow-Bridgwater equation (Equation 6.1), reducing it from 6- to 4-parameters, and meaning it would approximate the paste as a Bingham plastic rather than a Herschel-Bulkley fluid. Our results suggest this simplification is suitable for pastes of repulsive (nearly-)hard spheres in the viscous regime, though this may be dependent upon the unconstrained ϕ nature of the simulations.

Furthermore, direct links can be made between particle properties and the α and β parameters that quantify the gradient of $\Delta P \propto V^{\text{die}}$. Specifically, we have shown that the die pressure drop is sensitive to particle-wall friction but independent of particle-particle friction, implying a link between β and μ_w, whereas the die-entry pressure drop is sensitive to both particle-particle and particle-wall friction, suggesting a more complex relationship between α and μ_p, μ_w.

Velocity profiles

It is assumed that the nature of the velocity profile near the die exit is indicative of the propensity for flow instability in the extrudate. Profiles with large shear zones might indicate a tendency to form surface defects, whereas idealised plug flow might indicate a smooth and uniform extrusion product. Radial velocity profiles, averaged across the die length, are presented in Figure 6.15 for Cases A - F. In general, the extrusion die velocity

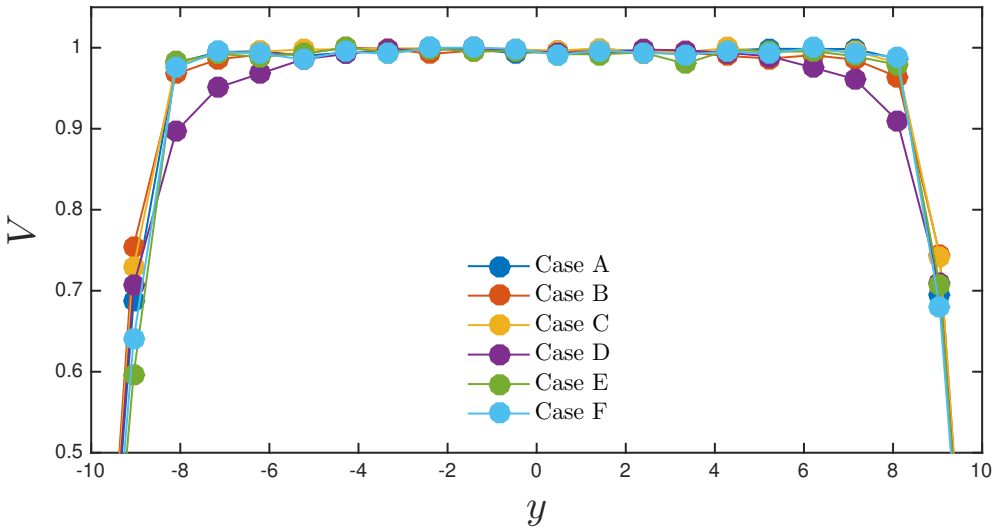

Fig. 6.15 Radial velocity profile in the die for Cases A - F, at fixed mass flow rate.

profile exhibits near ideal plug-flow, with sheared zones extending to a maximum of $2d$ from the die wall. The exception is Case D ($\mu_p = 0$, $\mu_w = 0.1$), which shows a considerable increase in shear zone width, extending to around $4d$ into the die. These is also a very slight indication of similar behaviour for Case B ($\mu_p = 1$, $\mu_w = 0.1$), though it is less pronounced. Rougher walls tend to lead, therefore, to enhanced shear flow near the walls, with the phenomena being more dominant for lower-friction particles, perhaps because the decreased resistance to flow for $\mu_p = 0$ particles allows sheared regions to form more easily, and to endure more stabily.

These results indicate that the velocity profile in the die is quite highly sensitive to the extruder wall roughness, though not very dependent on the frictional properties of the paste particles themselves. It would therefore be preferential, in terms of manufacturing processes, to minimize paste-extruder friction.

Static zone formation

We finally consider the effect of particle and wall properties on the propensity for static zone formation in the extruder. Time-averaged static zone sizes, in terms of number of static coarse-grained cells, as a function of V^{die}, are presented in Figure 6.16 for each of Cases A-F. As with the analysis of pressure drops, we find that the effect of varying k_n is negligible on static zone formation, while varying η_f shifts the results to higher velocities (while maintaining consistent I_V rheology) but retains qualitatively similar behaviour. Though the uncertainty appears to be large, it is observed that the static region size approximately obeys two distinct behaviours: one for Cases A and B, and another for Cases C and D. This would therefore suggest that the propensity for static zone formation is sensitive to details of particle-particle interaction, but not particle-

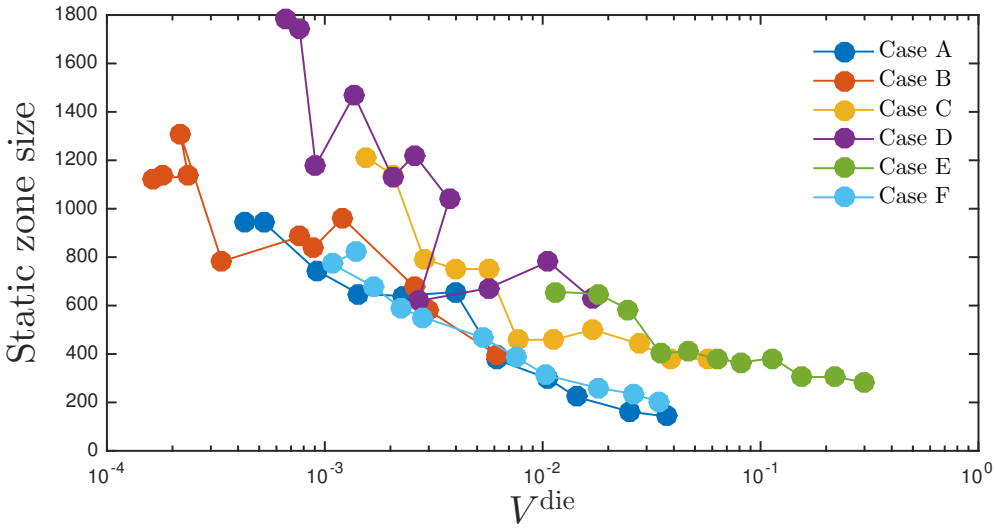

Fig. 6.16 Time-averaged static zone size, in terms of number of static coarse-grained cells, as a function of V^{die}, for each of Cases A-F.

wall interaction, where significantly larger static regions are predicted for "smooth" particles compared to "rough" particles. An explanation for this might be that for smooth particles, a stable slip layer may establish between the static region and the flowing region, allowing the static region to persist with a stable static-flowing interface. For frictional particles, tangential forces may lead to enhanced shear stress transmission between the flowing and static regions, leading to a less stable static-flowing boundary and consequently smaller static regions. The present results predict that in order to minimize stagnant region formation, and hence the potential propensity for liquid phase migration, it is preferable to use particles with enhanced surface roughness.

6.4 Discussion and Concluding remarks

In this chapter, we have established a simulation model for paste extrusion that accounts for particle-particle and particle-liquid effects. The model may be used directly by industrialists to inform design and optimisation of extrusion processes, since its implementation is considerably less computationally expensive than alternative solid-liquid approaches that resolve individual particles. Furthermore, the strong understanding of fundamental shear flow regimes developed in previous chapters allows the constitutive or bulk level extrusion flows to be understood at a microscopic level, bringing suitable microscale constitutive relations into closer reach.

There are, however, a number of limitations of the model that must be considered when interpreting flow predictions. First, the model does not explicitly conserve the mass of the fluid. This means that in regions of volume fraction gradient (which, as we

point out above, are very small or negligible in the present case) it is assumed that the fluid may permeate the solid matrix at infinitely high rate. Further work is necessary to test whether this assumption is valid. A further consequence of our neglecting the fluid phase is that anomalous stresses may arise close to flat boundaries (Figure 6.12), where the particle concentration tends to zero. The bounding walls of the present extruder are frictionless (Case A) and composed of particles much smaller than the bulk paste particles. As a result, the paste particles essentially see the wall as a flat, smooth surface, meaning there will be a fluctuating particle concentration adjacent to the wall, tending to zero at the contact point. Furthermore, the low paste-wall friction coefficient means that the particle contribution to the stress will be extremely low at this point, so an accurate determination of the fluid stress is expected to be paramount to correctly obtaining the overall wall shear stress. Another limitation of the model is its inability to capture free surface flows. Specifically, we are unable to capture the flow behaviour of the paste when it exits the extruder. This is a crucial region of flow, where the engineer typically determines the outcome and success of the extrusion process, i.e. smooth, flowing extrudate or unstable, inhomogeneous, poorly mixed paste. The present model, being composed of repulsive spheres, simply relaxes when the confinement is removed, causing the paste to disintegrate.

Future work is therefore required to properly couple the fluid and solid stresses within the extruder, to address the necessity of capturing liquid phase migration, to account for the anomalous stress behaviour near the extruder walls upstream of the die-entry, and to capture the true outlet flow behaviour. In spite of these present shortcomings, the model can successfully capture the complex and inhomogeneous stress and contact distributions around the die entry region that govern the large extrusion pressures necessary for flow. In this respect, the model is able to account for the inherently discrete nature of the paste, making it a valuable and practicable tool for studying extrusion processes in industry.

Outlook

Mapping flow regimes

Hatano (2008) and Otsuki and Hayakawa (2008) initially presented data in the stress versus strain rate framework to demonstrate the critical stress scalings of frictionless, dry granular media, with respect to solids volume fraction and shear rate. It is now widely accepted that the shear and normal stresses of a sheared granular material *diverge* as $(\phi_c - \phi) \to 0$, in the hard particle limit. Stresses for different volume fractions *converge*, however, when the hard particle limit is violated at large shear rates, where $\dot{\gamma} \to \sqrt{k_n}$. This work was continued by Chialvo et al. (2012), who simulated frictional particles, finding qualitatively consistent behaviour.

The work in Chapters 2 and 3 of this thesis has similarly served to rationalise the numerous flow regimes of suspensions, extending the existing picture by the inclusion of hydrodynamic lubrication forces. This introduces an additional shearing timescale, the Stokes number, adding a further dimension to the established dry granular flow map. Furthermore, we incorporated the emerging notion of *frictional* shear thickening into this picture, giving yet another governing timescale (or stress scale), that associated with the stabilising repulsive force. Our extended regime map in Figure 3.1 proposes how of all the above timescales might be incorporated into a regime map for a single material, though an experimental realisation is challenging.

Other authors have developed the understanding further, for example through the inclusion of cohesive forces. Gu et al. (2014) extended the regime map of Chialvo et al. (2012) to include particle-particle cohesion, finding an onset of yield stress behaviour below ϕ_c, and potentially bridging understanding between the rheology of dry granular materials, and that of agglomerating or gelating colloidal dispersions. Furthermore, Haeri and Sun (2015) mapped the flow regimes of dry granular materials of arbitrary shapes, again finding universal scalings with respect to ϕ and $\dot{\gamma}$.

This unifying understanding of the rheology of diverse materials might now be utilised to develop predictive design principles, to achieve desirable mechanical properties in suspensions for industrial applications. With sufficient knowledge of the material properties of constituent particles and liquid, one might make predictions as to the relative importance of particle inertia and cohesion, for example, or make predictions as to whether shear thickening ought to be considered or whether it will be masked by a large yield stress due to particle cohesion.

There remain several areas in which the regime maps may continue to be extended. We are currently exploring the influence of particle polydispersity on shear thickening rheology. Specifically, the results in Chapter 3 along with the experimental results

of our collaborators (Guy et al., 2015) suggest an onset stress for shear thickening that scales with the inverse square of the particle size. This suggests that desired shear thickening behaviour may be predicted and obtained by tuning particle size distributions. Furthermore, it implies that mixtures of particles of greatly differing sizes might exhibit a multi-moded or a much broader shear thickening transition, as particles of different sizes shear thicken at different stresses. Demonstrating such behaviour, and resolving the rheology of suspensions with great polydispersity, will be invaluable to the design of, for example, future industrial pastes. In addition, recent work addressing the instability of shear thickening flows (Hermes et al., 2015) poses challenges for future computational work, that we hope to address by building upon the work in this thesis.

Further utilising shear reversal

Using shear reversal (Chapter 4), we have elucidated the distinct roles of contact and hydrodynamic stresses under transient flow in a suspension of *nearly* hard spheres, and consequently provided a means of isolating the respective magnitudes of these stresses experimentally. This collaborative work (Lin et al., 2015) has successfully settled an ongoing dispute (e.g. Wagner and Brady (2009) versus Seto et al. (2013)) regarding the origin of shear thickening, by demonstrating that upon shear thickening, the large suspension viscosity increase can be attributed entirely to particle-particle contacts, rather than hydrodynamic stresses. This has important consequences for both the design of suspensions for industrial applications (i.e. particle surface details, such as frictional properties, are of utmost importance) and for the development of future constitutive models for these materials.

There are a number of areas where the shear reversal protocol might be employed to shed further light on suspension rheology. For example, there is a sustained effort among the suspension community to achieve a first-principles understanding of the divergence of the viscosity as $\phi_c - \phi \to 0$ (see, for example, Frankel and Acrivos (1967), Andreotti et al. (2012), Kawasaki et al. (2015) and Suzuki and Hayakawa (2015)). It is now possible to execute the shear reversal protocol at increasing solids volume fraction, to isolate the individual divergences of the particle contact and hydrodynamic stresses as ϕ_c is approached from below. Such insight would prove invaluable to obtaining a complete description of the critical behaviour.

The shear cessation and reversal protocol may also be employed as a diagnostic tool, for obtaining the nature of the particle-particle interaction for a given "test" suspension. The flow cessation period could, for example, reveal whether long range repulsive forces are important: suspensions of purely hard spheres relax instantaneously upon cessation; those with long range repulsion might relax over a longer time scale dependent on the

ease of particle rearrangements. The stress evolution upon reversal and subsequent magnitude of the contact (or general non-hydrodynamic) stress might reveal the relative importance of particle-particle interactions in different suspensions of similar volume fraction, informing the predictive design of pastes by extrusion scientists, who aim to maximise solids fraction without reducing flowability.

Extending the work in complex geometries

Some preliminary results in simple engineering geometries have been presented in Chapters 5 and 6, to extend the shear flow regime maps to inhomogeneous conditions. The results of our simulations of engineering geometries are promising, demonstrating that in regions where shear flow exists, the above described regimes maps can be locally applied. There remain many problems to explore, for example addressing the issue of the compressibility of the interstitial fluid as mentioned in Chapter 6, incorporating the critical load model for particle friction into these flows to predict the propagation of friction under inhomogeneous stresses and linking both the Poiseuille and extrusion rheology to the emerging picture of fluidity of non-local flows.

Chapter 7

Appendix: LAMMPS input script for simple simulation example

The following input scripts represent a minimal example that can be run consecutively to perform simple shear of a particle assembly. These scripts represent the input structure that has been employed throughout this thesis and can be used to reproduce the simple shear rheology results presented. No modifications are required to run these using the standard distribution of LAMMPS, available from the Sandia National Laboratories website.

Input script to generate an assembly of particles:

```
atom_style sphere
boundary p p p
newton off
comm_modify mode single vel yes
region reg prism 0 10 0 10 0 10 0 0 0 units box
create_box 2 reg
lattice  sc 1
create_atoms 1 random 500 400000 NULL
create_atoms 2 random 500 400001 NULL
set type 1 diameter 1
set type 2 diameter 0.7
neighbor 0.2 bin
neigh_modify delay 0
pair_style      gran/hooke/history 10000 NULL 200 NULL 0 0
pair_coeff * *
```

```
timestep 0.0001
velocity all create 100 123456 dist gaussian
fix 1 all nve/sphere
compute 1 all erotate/sphere
compute 3 all temp
compute 4 all pressure 3
thermo_style custom step c_4 vol
thermo 1000
thermo_modify lost ignore norm no
compute_modify thermo_temp dynamic yes
run 100000
write_restart restart.restart
```

Input script to apply a fixed rate shear flow to the assembly of particles:

```
read_restart restart.restart
newton off
comm_modify mode single vel yes
neighbor 0.2 bin
neigh_modify delay 0
pair_style      hybrid/overlay gran/hooke/history 10000 NULL ...
200 NULL 0 1 lubricate/poly 0.1 1 1 1.001 1.05
pair_coeff      * * gran/hooke/history
pair_coeff      * * lubricate/poly
timestep 0.0001
velocity all zero linear
velocity    all zero angular
fix 1 all nve/sphere
compute 1 all erotate/sphere
compute 3 all temp/profile 1 0 0 y 20
compute 4_0 all pressure 3 pair
thermo_style custom step c_4_0[4]
thermo_modify lost ignore norm no
compute_modify thermo_temp dynamic yes
fix 2 all deform 1 xy erate 0.01 remap v
thermo 1000
```

```
run 100000
```

References

L. Aarons and S. Sundaresan. Shear flow of assemblies of cohesive and non-cohesive granular materials. *Powder Technology*, 169(1):10–21, 2006.

L. Aarons and S. Sundaresan. Shear flow of assemblies of cohesive granular materials under constant applied normal stress. *Powder Technology*, 183(3):340–355, 2008.

L. Aarons, J. Sun, and S. Sundaresan. Unsteady shear of dense assemblies of cohesive granular materials under constant volume conditions. *Industrial and Engineering Chemistry Research*, 49(11):5153–5165, 2009.

N. Al-Din and D. J. Gunn. The flow of non-cohesive solids through orifices. *Chemical Engineering Science*, 39(1):121–127, 1983.

L. Anand and C. Gu. Granular materials: constitutive equations and strain localization. *Journal of the Mechanics and Physics of Solids*, 48(8):1701–1733, 2000.

B. Andreotti, J.-L. Barrat, and C. Heussinger. Shear flow of non-brownian suspensions close to jamming. *Phys. Rev. Lett.*, 109:105901, Sep 2012.

I. S. Aranson and L. S. Tsimring. Patterns and collective behavior in granular media: Theoretical concepts. *Reviews of Modern Physics*, 78:641–692, 2006.

P. Arp and S. G. Mason. The kinetics of flowing dispersions. *Journal of Colloid and Interface Science*, 61(1):44–61, 1977.

I. Aydin, F. Biglari, B. Briscoe, C. Lawrence, and M. Adams. Physical and numerical modelling of ram extrusion of paste materials: conical die entry case. *Computational Materials Science*, 18:141–155, 2000.

E. Azema, F. RadjaÏ, and G. Saussine. Quasistatic rheology, force transmission and fabric properties of a packing of irregular polyhedral particles. *Mechanics of Materials*, 41(6):729–741, 2009.

R. A. Bagnold. Experiments on a gravity-free dispersion of large solid spheres in a Newtonian fluid under shear. *Proceedings of the Royal Society A Mathematical Physical and Engineering Sciences*, 225(1160):49–63, 1954.

R. C. Ball and J. R. Melrose. A simulation technique for many spheres in quasi-static motion under frame-invariant pair drag and Brownian forces. *Physica A Statistical and Theoretical Physics*, 247(1-4):444–472, 1997.

P. Ballesta, R. Besseling, L. Isa, G. Petekidis, and W. C. K. Poon. Slip and flow of hard-sphere colloidal glasses. *Physical Review Letters*, 101:258301, 2008.

H. A. Barnes. Shear-Thickening ("Dilatancy") in Suspensions of Nonaggregating Solid Particles Dispersed in Newtonian Liquids. *Journal of Rheology*, 33:329, 1989.

G. K. Batchelor. The effect of Brownian motion on the bulk stress in a suspension of spherical particles. *Journal of Fluid Mechanics*, 83(01):97–117, 1977.

K. J. Bathe and H. Zhang. Finite element developments for general fluid flows with structural interactions. *International Journal for Numerical Methods in Engineering*, 60(1):213–232, 2004.

K.-J. Bathe, E. Ramm, and E. L. Wilson. Finite element formulations for large deformation dynamic analysis. *International Journal for Numerical Methods in Engineering*, 9(2):353–386, 1975.

R. P. Behringer, D. Howell, L. Kondic, S. Tennakoon, and C. Veje. Predictability and granular materials. *Physics D*, 133:1–17, 1999.

J. Benbow and J. Bridgwater. *Paste Flow and Extrusion*. Clarendon Press, 1993.

E. Bertrand, J. Bibette, and V. Schmitt. From shear thickening to shear-induced jamming. *Physical Review E*, 66:060401, 2002.

R. Besseling, L. Isa, P. Ballesta, G. Petekidis, M. E. Cates, and W. C. K. Poon. Shear banding and flow-concentration coupling in colloidal glasses. *Physical Review Letters*, 105(26):268301, 2010.

W. A. Beverloo, H. A. Leniger, and J. Van De Velde. The flow of granular solids through orifices. *Chemical Engineering Science*, 15(3-4):260–269, 1961.

E. C. Bingham. Plasticity. *Journal of Physical Chemistry*, 29(10):1201–1204, 1925.

L. Bocquet, W. Losert, D. Schalk, T. C. Lubensky, and J. P. Gollub. Granular shear flow dynamics and forces: experiment and continuum theory. *Physical Review E*, 65: 011307, 2001.

G. Bossis and J. F. Brady. Dynamic simulation of sheared suspensions. I. General method. *The Journal of Chemical Physics*, 80(10):5141, 1984.

G. Bossis and J. F. Brady. The rheology of Brownian suspensions. *The Journal of Chemical Physics*, 91(3):1866, 1989.

M. Bouzid, M. Trulsson, P. Claudin, E. Clément, and B. Andreotti. Nonlocal rheology of granular flows across yield conditions. *Physical Review Letters*, 111(23):1–5, 2013.

F. Boyer, E. Guazzelli, and O. Pouliquen. Unifying suspension and granular rheology. *Physical Review Letters*, 107:188301, 2011.

J. F. Brady and G. Bossis. The rheology of concentrated suspensions of spheres in simple shear flow by numerical simulation. *Journal of Fluid Mechanics*, 155(1): 105–129, 1985.

J. F. Brady and G. Bossis. Stokesian Dynamics. *Annual Review of Fluid Mechanics*, 20 (1):111–157, 1988.

J. M. Bricker and J. E. Butler. Correlation between stresses and microstructure in concentrated suspensions of non-Brownian spheres subject to unsteady shear flows. *Journal of Rheology*, 51(4):735, 2007.

E. Brown. Friction's Role in Shear Thickening. *Physics*, 6:125, 2013.

E. Brown and H. M. Jaeger. Dynamic jamming point for shear thickening suspensions. *Physical review letters*, 103:086001, 2009.

E. Brown and H. M. Jaeger. The role of dilation and confining stresses in shear thickening of dense suspensions. *Journal of Rheology*, 56(4), 2012.

W. H. H. Bulkley and R. Konsistenzmessungen von Gummi-Benzollosungen. *Kolloid Zeitschrift*, 39:291–300, 1926.

C. Campbell. Granular material flows – An overview. *Powder Technology*, 162(3): 208–229, 2006.

C. S. Campbell. Granular shear flows at the elastic limit. *Journal of Fluid Mechanics*, 465:261–291, 2002.

C. S. Campbell. Stress-controlled elastic granular shear flows. *Journal of Fluid Mechanics*, 539(1):273, 2005.

P. J. Carreau. Rheological equations from molecular network theories. *Journal of Rheology*, 16(1):99–127, 1972.

C. Cassar, M. Nicolas, and O. Pouliquen. Submarine granular flows down inclined planes. *Physics of Fluids*, 17(10):1–11, 2005.

M. E. Cates, J. P. Wittmer, J.-P. Bouchaud, and P. Claudin. Jamming, force chains, and fragile matter. *Physical Review Letters*, 81:1841–1844, 1998.

M. E. Cates, W. C. K. Poon, and P. Bartlett. Colloids, grains and dense suspensions: under flow and under arrest. *Philosophical transactions. Series A, Mathematical, physical, and engineering sciences*, 367(1909):4989–4991, 2009.

P. Chaudhuri, L. Berthier, and S. Sastry. Jamming transitions in amorphous packings of frictionless spheres occur over a continuous range of volume fractions. *Physical Review Letters*, 104(16):165701, 2010.

X. Cheng, J. H. McCoy, J. N. Israelachvili, and I. Cohen. Imaging the microscopic structure of shear thinning and thickening colloidal suspensions. *Science*, 333(6047): 1276–1279, 2011.

S. Chialvo and S. Sundaresan. A modified kinetic theory for frictional granular flows in dense and dilute regimes. *Physics of Fluids*, 25(7), 2013.

S. Chialvo, J. Sun, and S. Sundaresan. Bridging the rheology of granular flows in three regimes. *Physical Review E*, 85(2):21305, 2012.

Y. C. Chung and J. Y. Ooi. Benchmark tests for verifying discrete element modelling codes at particle impact level. *Granular Matter*, 13(5):643–656, 2011.

J. Clara-Rahola, T. A. Brzinski, D. Semwogerere, K. Feitosa, J. C. Crocker, J. Sato, V. Breedveld, and E. R. Weeks. Affine and nonaffine motions in sheared polydisperse emulsions. *Physical Review E*, 91:010301, 2015.

C. Coulomb. *Essai sur une application des règles des maximis et minimis à quelques problèmes de statique relatifs à l'architecture*. Paris, 1773.

P. Coussot. Structural similarity and transition from newtonian to non-Newtonian behavior for clay-water suspensions. *Physical Review Letters*, 74:3971–3974, 1995.

P. Coussot. Rheophysics of pastes: a review of microscopic modelling approaches. *Soft Matter*, 3(5):528, 2007.

M. M. Cross. Rheology of Non-Newtonian Fluids: A new flow equation for pseudo-plastic Systems. *Journal of Colloid Science*, 20:417–437, 1965.

P. A. Cundall and O. D. L. Strack. A discrete numerical model for granular assemblies. *Geotechnique*, 29(1):47–65, 1979.

C. D. Cwalina and N. J. Wagner. Material properties of the shear-thickened state in concentrated near hard-sphere colloidal dispersions. *Journal of Rheology*, 58(4): 949–967, 2014.

F. Da Cruz, S. Emam, M. Prochnow, J.-N. Roux, and F. Chevoir. Rheophysics of dense granular materials : Discrete simulation of plane shear flows. *Physical Review E*, 72 (2 Pt 1):21309, 2005.

R. Daniel, a. Poloski, and a. Eduardosaez. A continuum constitutive model for cohesionless granular flows. *Chemical Engineering Science*, 62(5):1343–1350, 2007.

H. Darcy. *Les fontaines publiques de la ville de Dijon*. Dalmont, 1856.

J. de Bruyn. Unifying Liquid and Granular Flow. *Physics*, 4:86, 2011.

E. DeGiuli, G. Düring, E. Lerner, and M. Wyart. Unified theory of inertial granular flows and non-Brownian suspensions. *Physical Review E*, 91(6):1–12, 2015.

M. M. Denn. Fifty years of non-Newtonian fluid dynamics. *AIChE Journal*, 50: 2335–2345, 2004.

J. Dijksman, E. Wandersman, S. Slotterback, C. R. Berardi, W. D. Updegraff, M. Van Hecke, and W. Losert. From Frictional to Newtonian Flows: Three Dimensional Imaging and Rheology of Gravitational Suspensions. *Physical Review E*, 82(6):1–4, 2010.

T. Divoux and J.-C. Géminard. Friction and dilatancy in immersed granular matter. *Physical Review Letters*, 99(25):258301, 2007.

P. G. Drazin and N. Riley. *The Navier-Stokes equations: a classification of flows and exact solutions*. Cambridge University Press, 2006. ISBN 9780521681629.

G. D'Avino, T. Tuccillo, P. L. Maffettone, F. Greco, and M. Hulsen. Numerical simulations of particle migration in a viscoelastic fluid subjected to shear flow. *Computers & Fluids*, 39(4):709–721, 2010.

R. G. Egres and N. J. Wagner. The rheology and microstructure of acicular precipitated calcium carbonate colloidal suspensions through the shear thickening transition. *Journal of Rheology*, 49(3):719, 2005.

A. Einstein. (4), 19, 1906,. *Annalen der Physik*, 4(19):289–306, 1906.

A. Einstein. *Investigations on the theory of Brownian movement*. Dover publications, 1956.

B. Elhweg, I. W. Burns, Y. M. J. Chew, P. J. Martin, a. B. Russell, and D. I. Wilson. Viscous dissipation and apparent wall slip in capillary rheometry of ice cream. *Food and Bioproducts Processing*, 87(4):266–272, 2009.

J. Engmann and M. R. Mackley. Semi-solid processing of chocolate and cocoa butter - Modelling rheology and microstructure changes during extrusion. *Food And Bioproducts Processing*, 84(C2):102–108, 2006.

A. Fall, N. Huang, F. Bertrand, G. Ovarlez, and D. Bonn. Shear thickening of cornstarch suspensions as a reentrant jamming transition. *Physical Review Letters*, 100:018301, 2008.

A. Fall, A. Lemaître, F. Bertrand, D. Bonn, and G. Ovarlez. Shear thickening and migration in granular suspensions. *Physical Review Letters*, 105:268303, 2010.

A. Fall, F. Bertrand, G. Ovarlez, and D. Bonn. Shear thickening of cornstarch suspensions. *Journal of Rheology*, 56(575), 2012.

A. Fall, F. Bertrand, D. Hautemayou, C. Mezière, P. Moucheront, A. Lemaître, and G. Ovarlez. Macroscopic Discontinuous Shear Thickening versus Local Shear Jamming in Cornstarch. *Physical Review Letters*, 114(9):98301, 2015.

L. Fan and Y. Chen. Recent developments in solids mixing. *Powder Technology*, 61(3): 255–287, 1990.

Z. Fang and N. Phan-Thien. Numerical simulation of particle migration in concentrated suspensions by a finite volume method. *Journal of Non-Newtonian Fluid Mechanics*, 58(1):67–81, 1995.

N. Fernandez, R. Mani, D. Rinaldi, D. Kadau, M. Mosquet, H. Lombois-Burger, J. Cayer-Barrioz, H. J. Herrmann, N. D. Spencer, and L. Isa. Microscopic mechanism for shear thickening of non-brownian suspensions. *Physical Review Letters*, 111: 108301, 2013.

R. a. Fisher. On the capillary forces in an ideal soil; correction of formulae given by W. B. Haines. *The Journal of Agricultural Science*, 16(03):492, 2009.

Y. Forterre and O. Pouliquen. Flows of Dense Granular Media. *Annual Review of Fluid Mechanics*, 40(1):1–24, 2008.

R. T. Fowler and J. R. Glastonbury. The flow of granular solids through orifices. *Chemical Engineering Science*, 10(3):150–156, 1959.

N. Frankel and A. Acrivos. On the viscosity of a concentrated suspension of solid spheres. *Chemical Engineering Science*, 22:847–853, 1967.

G. H. Fredrickson and P. Pincus. Drainage of compressed polymer layers: dynamics of a "squeezed sponge". *Langmuir*, 7:786–795, 1991.

F. Gadala-Maria and A. Acrivos. Shear-Induced Structure in a Concentrated Suspension of Solid Spheres. *Journal of Rheology*, 24(6):799–814, 1980.

S. Gallier, E. Lemaire, F. Peters, and L. Lobry. Rheology of sheared suspensions of rough frictional particles. *Journal of Fluid Mechanics*, 757:514–549, 2014.

V. Garzó and J. W. Dufty. Dense fluid transport for inelastic hard spheres. *Physical Review E*, 59(5):5895–5911, 1999.

J. Goddard. Dissipative Materials as Constitutive Models for Granular Media. *Acta Mechanica*, 13(1):3–13, 1986.

J. D. Goddard. Continuum modeling of dry granular media. In *Physics of dry granular media*, chapter 1. Springer, 1998.

J. D. Goddard. Material instability with stress localization. *Journal of Non-Newtonian Fluid Mechanics*, 102(2):251–261, 2002.

J. D. Goddard. A dissipative anisotropic fluid model for non-colloidal particle dispersions. *Journal of Fluid Mechanics*, 568:1, 2006.

J. Goyon, a. Colin, G. Ovarlez, a. Ajdari, and L. Bocquet. Spatial cooperativity in soft glassy flows. *Nature*, 454(7200):84–87, 2008.

M. Gross, T. Kruger, and F. Varnik. Rheology of dense suspensions of elastic capsules: normal stresses, yield stress, jamming and confinement effects. *Soft Matter*, 10: 4360–4372, 2014.

Y. Gu, S. Chialvo, and S. Sundaresan. Rheology of cohesive granular materials across multiple dense-flow regimes. *Physical Review E*, 90:032206, Sep 2014.

N. Guicciardini. Isaac newton, philosophiae naturalis principia mathematica, first edition (1687). In *Landmark Writings in Western Mathematics 1640-1940*, pages 59–87. Elsevier, 2005. ISBN 9780444508713.

B. M. Guy, M. Hermes, and W. C. K. Poon. Towards a Unified Description of the Rheology of Hard-Particle Suspensions. *Physical Review Letters*, 115(8):88304, 2015.

S. Haeri and J. Sun. On the effects of particle shape on shear flow of non-spherical particles. *IV International Conference on Particle-Based Methods*, 2015.

D. Harris. A unified formulation for plasticity models of granular and other materials. *Mathematical and Physical Sciences*, 450(1938):37–49, 1995.

D. Harris. Some Properties of a New Model for Slow Flow of Granular Materials. *Meccanica*, 41(3):351–362, 2006.

D. Harris. Ill and well-posed models of granular flow. *Acta Mechanica*, 146(3):199–225, 2010.

T. Hatano. Scaling properties of granular rheology near the jamming transition. *Journal of the Physical Society of Japan*, 77(12):123002, 2008.

T. K. Haxton, M. Schmiedeberg, and A. J. Liu. Universal jamming phase diagram in the hard-sphere limit. *Physical Review E*, 83, 2011.

M. Hermes, B. Guy, G. Poy, M. Cates, M. Wyart, and W. Poon. Unsteady flow and particle migration in dense, non-brownian suspensions. *arXiv*, 1511(08011), 2015.

C. Heussinger. Shear thickening in granular suspensions: Interparticle friction and dynamically correlated clusters. *Physical Review E*, 88:050201, 2013.

H. H. Hu and D. D. Joseph. Theoretical and Computational Fluid Dynamics Direct Simulation of Fluid Particle Motions I. *Theoretical Computational Fluid Dynamics*, 3:285–306, 1992.

N. Huang, G. Ovarlez, F. Bertrand, S. Rodts, P. Coussot, and D. Bonn. Flow of wet granular materials. *Physical Review Letters*, 94(2):28301, 2004.

M. L. Hunt, R. Zenit, C. S. Campbell, and C. E. Brennen. Revisiting the 1954 suspension experiments of R. A. Bagnold. *Journal of Fluid Mechanics*, 452(1):1–24, 2002.

A. Ikeda, L. Berthier, and P. Sollich. Unified study of glass and jamming rheology in soft particle systems. *Physical Review Letters*, 109(1):18301, 2012.

L. Isa, R. Besseling, and W. C. K. Poon. Shear zones and wall slip in the capillary flow of concentrated colloidal suspensions. *Physical Review Letters*, 98(19):198305, 2007.

L. Isa, R. Besseling, E. R. Weeks, and W. C. K. Poon. Quantitative imaging of colloidal flows. *Advances in Colloid and Interface Science*, 146, 2009.

R. Jackson. Some Features of the Flow of Granular Materials and Aerated Granular Materials. *Journal of Rheology*, 30(5):907, 1986.

H. M. Jaeger, S. R. Nagel, and R. P. Behringer. Granular solids , liquids , and gases. *Reviews of Modern Physics*, 68(4):1259–1273, 1996.

J. T. Jenkins and M. W. Richman. Kinetic theory for plane flows of a dense gas of identical, rough, inelastic, circular disks. *Physics of Fluids*, 28(12):3485, 1985.

J. R. Johanson. A Rolling Theory for Granular Solids. *Journal of Applied Mechanics*, 32(4):842–848, 1965.

P. C. Johnson and R. Jackson. Frictional-collisional constitutive relations for granular materials, with application to plane shearing. *Journal of Fluid Mechanics*, 176(1):67, 1987.

P. Jop, Y. Forterre, and O. Pouliquen. A constitutive law for dense granular flows. *Nature*, 441(7094):727–730, 2006.

P. P. Jose and I. Andricioaei. Similarities between protein folding and granular jamming. *Nature communications*, 3:1161, 2012.

K. Kamrin and D. Henann. Modeling the nonlocal behavior of granular flows down inclines. *Soft Matter*, 11:179–185, 2014.

K. Kamrin and G. Koval. Nonlocal constitutive relation for steady granular flow. *Physical Review Letters*, 108(17), 2012.

T. Kawasaki, A. Ikeda, and L. Berthier. Thinning or thickening? Multiple rheological regimes in dense suspensions of soft particles. *Europhysics Letters*, 107:28009, 2014.

T. Kawasaki, D. Coslovich, A. Ikeda, and L. Berthier. Diverging viscosity and soft granular rheology in non-brownian suspensions. *Physical Review E*, 91:012203, 2015.

S. Kim and S. Karrila. *Microhydrodynamics: Principles and selected applications*. Dover publications, 1991.

V. G. Kolli, E. J. Pollauf, and F. Gadala-Maria. Transient normal stress response in a concentrated suspension of spherical particles. *Journal of Rheology*, 46(1):321, 2002.

I. M. Krieger. Rheology of monodisperse lattices. *Advances in Colloid and Interface Science*, 3(1):111–132, 1972.

I. M. Krieger and T. J. Dougherty. A Mechanism for Non-Newtonian Flow in Suspensions of Rigid Spheres. *Journal of Rheology*, 3:137–152, 1959.

A. Kumar and J. J. L. Higdon. Origins of the anomalous stress behavior in charged colloidal suspensions under shear. *Physical Review E*, 82(5):51401, 2010.

P. Langevin. On the theory of Brownian motion (Sur la theorie du mouvement Brownien). *C. R. Acad. Sci*, 146:530–533, 1908.

H. M. Laun. Rheological properties of aqueous polymer dispersions. *Macromolecular Materials and Engineering*, 123:335–359, 1984.

A. W. Lees and S. F. Edwards. The computer study of transport processes under extreme conditions. *Journal of Physics C Solid State Physics*, 5(15):1921–1928, 1972.

D. Leighton and A. Acrivos. The shear-induced migration of particles in concentrated suspensions. *Journal of Fluid Mechanics*, 181(1):415–439, 1987.

A. Lemaître, J.-N. Roux, and F. Chevoir. What do dry granular flows tell us about dense non-Brownian suspension rheology? *Rheologica Acta*, 48(8):925–942, 2009.

E. Lerner, G. Düring, and M. Wyart. A unified framework for non-Brownian suspension flows and soft amorphous solids. *Proceedings of the National Academy of Sciences of the United States of America*, 2012(1):1–6, 2012.

M. Li, L. Tang, F. Xue, and R. Landers. Numerical Simulation of Ram Extrusion Process for Ceramic Materials. *Twenty Second Annual Solid Freeform Fabrication Symposium*, 2011.

C. J. Lin. Simple shear flow round a rigid sphere: inertial effects and suspension rheology. *Journal of Fluid Mechanics*, 44:1–17, 1970.

N. Y. C. Lin, B. M. Guy, M. Hermes, C. Ness, J. Sun, W. C. K. Poon, and I. Cohen. Hydrodynamic and contact contributions to continuous shear thickening in colloidal suspensions. *Physical Review Letters*, 115:228304, 2015.

A. J. Liu and S. R. Nagel. Jamming is not just cool any more. *Nature*, 396:21–22, 1998.

H. Liu and M. C. Leu. Liquid phase migration in extrusion of aqueous alumina paste for freeze-form extrusion fabrication. *International Journal of Modern Physics B*, 23: 1861–1866, 2009.

G. Lois, A. Lemaître, and J. M. Carlson. Spatial force correlations in granular shear flow. II. Theoretical implications. *Physical Review E*, 76:021303, 2007.

S. Luding and H. J. Herrmann. Cluster-Growth in Freely Cooling Granular Media. *Chaos*, 9(3):673–681, 1999.

C. K. K. Lun, S. B. Savage, D. J. Jeffrey, and N. Chepurniy. Kinetic theories for granular flow: inelastic particles in Couette flow and slightly inelastic particles in a general flowfield. *Journal of Fluid Mechanics*, 140:223–256, 1984.

M. Mackley. Engineering the future of rheology within the UK. *Journal of Non-Newtonian Fluid Mechanics*, 157(3):145–146, 2009.

T. S. Majmudar and R. P. Behringer. Contact force measurements and stress-induced anisotropy in granular materials. *Nature*, 435(7045):1079–1082, 2005.

C. Mankoc, A. Janda, R. Arévalo, J. Pastor, I. Zuriguel, A. Garcimartín, and D. Maza. The flow rate of granular materials through an orifice. *Granular Matter*, 9(6):407–414, 2007.

R. Mari, R. Seto, J. F. Morris, and M. M. Denn. Shear thickening, frictionless and frictional rheologies in non-Brownian suspensions. *Journal of Rheology*, 58(6): 1693–1724, 2014.

R. Mari, R. Seto, J. F. Morris, and M. M. Denn. Nonmonotonic flow curves of shear thickening suspensions. *Physical Review E*, 91(5):52302, 2015a.

R. Mari, R. Seto, J. F. Morris, and M. M. Denn. Discontinuous Shear Thickening in Brownian Suspensions By Dynamic Simulation. *arXiv*, 1508:01243(1-7):1–7, 2015b.

S. Mascia, M. J. Patel, S. L. Rough, P. J. Martin, and D. I. Wilson. Liquid phase migration in the extrusion and squeezing of microcrystalline cellulose pastes. *European Journal of Pharmaceutical Sciences*, 29(1):22–34, 2006.

J. R. Melrose and R. C. Ball. Continuous shear thickening transitions in model concentrated colloids—The role of interparticle forces. *Journal of Rheology*, 48(5):937, 2004.

J. R. Melrose, J. H. van Vliet, and R. C. Ball. Continuous shear thickening and colloid surfaces. *Physical Review Letters*, 77:4660–4663, Nov 1996.

J. Mewis and A. J. B. Spaull. Rheology of concentrated dispersions. *Advances in Colloid and Interface Science*, 6:173–200, 1976.

J. Mewis and N. J. Wagner. *Colloidal Suspension Rheology*. Cambridge Series in Chemical Engineering. Cambridge University Press, 2012. ISBN 9780521515993.

G. D. R. MiDi. On dense granular flows. *The European Physical Journal E*, 14(4): 341–365, 2004.

S. Miller and S. Luding. Cluster growth in two- and three-dimensional granular gases. *Physical Review E*, 69:031305, 2004.

R. Mittal and G. Iaccarino. Immersed Boundary Methods. *Annual Review of Fluid Mechanics*, 37(1):239–261, 2005.

J. F. Morris and J. F. Brady. Pressure-driven flow of a suspension: Buoyancy effects. *International Journal of Multiphase Flow*, 24:105–130, 1998.

D. M. Mueth, H. M. Jaeger, and S. R. Nagel. Force distribution in a granular medium. *Physical Review E*, 57:3164–3169, 1998.

T. Narumi, H. See, Y. Honma, T. Hasegawa, T. Takahashi, and N. Phan-Thien. Transient response of concentrated suspensions after shear reversal. *Journal of Rheology*, 46: 295–305, 2002.

R. Nedderman. *Statics and kinematics of granular materials*. Cambridge University Press, 2005. ISBN 9780521404358.

S. Nemat-Nasser. A micromechanically-based constitutive model for frictional deformation of granular materials. *Journal of the Mechanics and Physics of Solids*, 48 (6-7):1541–1563, 2000.

S. Nemat-nasser and J. Zhang. Constitutive relations for cohesionless frictional granular materials. *International Journal of Plasticity*, 18(4):531–547, 2002.

C. Ness and J. Sun. Flow regime transitions in dense non-Brownian suspensions: Rheology, microstructural characterization, and constitutive modeling. *Physical Review E*, 91:012201, 2015.

C. Ness and J. Sun. Two-scale evolution during shear reversal in dense suspensions. *Physical Review E*, 93:012604, 2016a.

C. Ness and J. Sun. Shear thickening regimes of dense non-brownian suspensions. *Soft Matter*, (12):914, 2016b.

K. N. Nordstrom, E. Verneuil, P. E. Arratia, A. Basu, Z. Zhang, a. G. Yodh, J. P. Gollub, and D. J. Durian. Microfluidic rheology of soft colloids above and below jamming. *Physical Review Letters*, 105(17):175701, 2010a.

K. N. Nordstrom, E. Verneuil, W. G. Ellenbroek, T. C. Lubensky, J. P. Gollub, and D. J. Durian. Centrifugal compression of soft particle packings: theory and experiment. *Physical Review E*, 82(4 Pt 1):41403, 2010b.

P. R. Nott and J. F. Brady. Pressure-driven flow of suspensions: simulation and theory. *Journal of Fluid Mechanics*, 275(-1):157, 1994.

V. T. O'Brien and M. E. Mackay. Stress components and shear thickening of concentrated hard sphere suspensions. *Langmuir*, 16(21):7931–7938, 2000.

C. S. O'Hern, S. A. Langer, A. J. Liu, and S. R. Nagel. Random packings of frictionless particles. *Physical Review Letters*, 88(7):75507, 2002.

C. S. O'Hern, L. E. Silbert, A. J. Liu, and S. R. Nagel. Jamming at zero temperature and zero applied stress: The epitome of disorder. *Physical Review E*, 68:011306, 2003.

P. Olsson and S. Teitel. Critical scaling of shear viscosity at the jamming transition. *Physical Review Letters*, 98(17):245701, 2007.

J. Ooi and K. She. Finite element analysis of wall pressure in imperfect silos. *International Journal of Solids and Structures*, 34(16):2061 – 2072, 1997.

C. O'Sullivan and J. D. Bray. Selecting a suitable time step for discrete element simulations that use the central difference time integration scheme. *Engineering Computations*, 21(2/3/4):278–303, 2004.

M. Otsuki and H. Hayakawa. Universal scaling for the jamming transition. *Progress of Theoretical Physics*, 121(3):9, 2008.

M. Otsuki and H. Hayakawa. Critical behaviors of sheared frictionless granular materials near the jamming transition. *Physical Review E*, 80:011308, 2009.

M. Otsuki and H. Hayakawa. Critical scaling near jamming transition for frictional granular particles. *Physical Review E*, 83:051301, 2011.

Z. Pan, H. de Cagny, B. Weber, and D. Bonn. <math> <mi mathvariant="sans-serif">S</mi> </math> -shaped flow curves of shear thickening suspensions: Direct observation of frictional rheology. *Physical Review E*, 92(3):032202, 2015.

M. J. Patel, S. Blackburn, and D. I. Wilson. Modelling of paste flows subject to liquid phase migration. *International Journal for Numerical Methods in Engineering*, 72 (10):1157–1180, 2007.

P. D. Patil, J. J. Feng, and S. G. Hatzikiriakos. Constitutive modeling and flow simulation of polytetrafluoroethylene (PTFE) paste extrusion. *Journal of Non-Newtonian Fluid Mechanics*, 139:44–53, 2006.

P. D. Patil, I. Ochoa, J. J. Feng, and S. G. Hatzikiriakos. Viscoelastic flow simulation of polytetrafluoroethylene (PTFE) paste extrusion. *Journal of Non-Newtonian Fluid Mechanics*, 153(1):25–33, 2008.

G. Petekidis, D. Vlassopoulos, and P. N. Pusey. Yielding and flow of colloidal glasses. *Faraday discussions*, 123:287–302, 2003.

R. J. Phillips, R. C. Armstrong, R. a. Brown, A. L. Graham, and J. R. Abbott. A constitutive equation for concentrated suspensions that accounts for shear-induced particle migration. *Physics Of Fluids A Fluid Dynamics*, 4(1):30, 1992.

S. Plimpton. LAMMPS Molecular Dynamics Simulator, http://lammps.sandia.gov/.

S. Plimpton. Fast Parallel Algorithms for Short – Range Molecular Dynamics. *Journal of Computational Physics*, 117:1–42, 1995.

O. Pouliquen and R. Gutfraind. Stress fluctuations and shear zones in quasistatic granular chute flows. *Physical Review E*, 53(1), 1996.

C. Pozrikidis. Dynamical Simulation of the Flow of Suspensions : Wall-Bounded and Pressure-Driven Channel Flow. *Ind. Eng. Chem. Res*, 41:6312–6322, 2002.

D. Quemada. Rheology of concentrated disperse systems II. A model for non-newtonian shear viscosity in steady flows. *Rheologica Acta*, 17:632–642, 1978.

K. A. Reddy and V. Kumaran. Dense granular flow down an inclined plane: A comparison between the hard particle model and soft particle simulations. *Physics of Fluids*, 22(11):113302, 2010.

G. P. Roberts, H. a. Barnes, and P. Carew. Modelling the flow behaviour of very shear-thinning liquids. *Chemical Engineering Science*, 56(19):5617–5623, 2001.

P. G. Rognon, J.-N. Roux, M. Naaïm, and F. Chevoir. Dense flows of cohesive granular materials. *Journal of Fluid Mechanics*, 596(18):21–47, 2008.

L. Rothenburg. Critical state and evolution of coordination number in simulated granular materials. *International Journal of Solids and Structures*, 41(21):5763–5774, 2004.

J. Rotter, J. Holst, J. Ooi, and A. Sanad. Silo pressure predictions using discrete–element and finite–element analyses. *Philosophical Transactions of the Royal Society of London A: Mathematical, Physical and Engineering Sciences*, 356(1747):2685–2712, 1998.

S. L. Rough and D. I. Wilson. The production of homogeneous extrudates of microcrystalline cellulose pastes. *International Journal of Pharmaceutics*, 276(1-2):185–189, 2004.

S. L. Rough, J. Bridgwater, and D. I. Wilson. Effects of liquid phase migration on extrusion of microcrystalline cellulose pastes. *International Journal of Pharmaceutics*, 204(1-2):117–126, 2000.

S. L. Rough, D. I. Wilson, and J. Bridgwater. A model describing liquid phase migration within an extruding microcrystalline cellulose paste. *Trans IChemE*, 80, 2002.

N. Roussel. Steady and transient flow behaviour of fresh cement pastes. *Cement and Concrete Research*, 35(9):1656–1664, 2005.

G. Ryskin. The extensional viscosity of a dilute suspension of spherical particles at intermediate microscale Reynolds numbers. *Journal of Fluid Mechanics*, 99:513–529, 1980.

S. B. Savage. Streaming motions in a bed of vibrationally fluidized dry granular material. *Journal of Fluid Mechanics*, 194:457–478, 1988.

S. B. Savage, R. M. Nedderman, and U. Tuzun. The Flow of Granular Materials. *Chemical Engineering Science*, 38(2):195–198, 1983.

P. Schall and M. Van Hecke. Shear Bands in Matter with Granularity. *Annual Review of Fluid Mechanics*, 42(1):67–88, 2010.

A. Schofield and P. Wroth. Critical State Soil Mechanics. *Soil Use and Management*, 25:105–128, 1968.

J. R. Seth, L. Mohan, C. Locatelli-Champagne, M. Cloitre, and R. T. Bonnecaze. A micromechanical model to predict the flow of soft particle glasses. *Nature Materials*, 10(11):838–843, 2011.

R. Seto, R. Mari, J. F. Morris, and M. M. Denn. Discontinuous Shear Thickening of Frictional Hard-Sphere Suspensions. *Physical Review Letters*, 111:218301, 2013.

R. H. Shertzer. *Fabric Tensors and Effective Properties of Granular Materials with Application to Snow*. PhD thesis, Montana State University, 2011.

R. Shield. On Coulomb's law of failure in soils. *Journal of the Mechanics and Physics of Solids*, 4(1):10–16, 1955.

A. O. N. Siemens and M. Van Hecke. Jamming: A simple introduction. *Physica A: Statistical Mechanics and its Applications*, 389(20):4255–4264, 2010.

L. E. Silbert, D. Ertaş, G. S. Grest, T. C. Halsey, D. Levine, and S. J. Plimpton. Granular flow down an inclined plane: Bagnold scaling and rheology. *Physical Review E*, 64: 17, 2001.

P. Sollich, F. m. c. Lequeux, P. Hébraud, and M. E. Cates. Rheology of soft glassy materials. *Physical Review Letters*, 78:2020–2023, 1997.

C. Song, P. Wang, and H. A. Makse. A phase diagram for jammed matter. *Nature*, 453 (7195):629–632, 2008.

M. Sperl. Experiments on corn pressure in silo cells - Translation and comment of Janssen's paper from 1895. *Granular Matter*, 8:59–65, 2006.

Y. Srebro and D. Levine. Role of friction in compaction and segregation of granular materials. *Physical review. E, Statistical, nonlinear, and soft matter physics*, 68: 061301, 2003.

J. J. Stickel and R. L. Powell. Fluid Mechanics and Rheology of Dense Suspensions. *Annual Review of Fluid Mechanics*, 37(1):129–149, 2005.

J. J. Stickel, R. J. Phillips, and R. L. Powell. A constitutive model for microstructure and total stress in particulate suspensions. *Journal of Rheology*, 50(4):379, 2006.

S. R. Subia, M. S. Ingber, L. Mondy, S. Altobelli, and L. Graham. Modelling of concentrated suspensions using a continuum constitutive equation. *Journal of Fluid Mechanics*, 373(1998):193–219, 1998.

J. Sun and S. Sundaresan. A constitutive model with microstructure evolution for flow of rate-independent granular materials. *Journal of Fluid Mechanics*, 682:590–616, 2011.

J. Sun, F. Battaglia, and S. Subramaniam. Dynamics and structures of segregation in a dense, vibrating granular bed. *Physical Review E*, 74:061307, 2006.

J. Sun, H. Xiao, and D. Gao. Numerical study of segregation using multiscale models. *International Journal of Computational Fluid Dynamics*, 23(2):81–92, 2009.

K. Suzuki and H. Hayakawa. Divergence of viscosity in jammed granular materials: A theoretical approach. *Phys. Rev. Lett.*, 115:098001, Aug 2015.

B. P. Tighe, E. Woldhuis, J. J. C. Remmers, W. Van Saarloos, and M. Van Hecke. Model for the Scaling of Stresses and Fluctuations in Flows near Jamming. *Physical Review Letters*, 105(8):4, 2010.

M. Trulsson, B. Andreotti, and P. Claudin. Transition from the Viscous to Inertial Regime in Dense Suspensions. *Physical Review Letters*, 109(11):118305, 2012.

L. Vanel, D. Howell, D. Clark, R. P. Behringer, and E. Clément. Memories in sand: experimental tests of construction history on stress distributions under sandpiles. *Physical Review E*, 60(5):5040–5043, 1999.

V. Vedachalam. *Discrete Element Modelling Of Granular Snow Particles Using LIGGGHTS*. PhD thesis, University of Edinburgh, 2011.

N. J. Wagner and J. F. Brady. Shear thickening in colloidal dispersions. *Physics Today*, 62:27–32, 2009.

M. Wang and J. F. Brady. Constant stress and pressure rheology of colloidal suspensions. *Physical Review Letters*, 115:158301, 2015.

J. F. Wendt. *Computational Fluid Dynamics - An Introduction*, volume 44. Springer, 2009. ISBN 9783540850557.

R. D. Wildman, S. Blackburn, D. M. Benton, P. A. McNeil, and D. J. Parker. Investigation of paste flow using positron emission particle tracking. *Powder Technology*, 103 (3):220–229, 1999.

D. Wilson and S. Rough. Exploiting the curious characteristics of dense solid–liquid pastes. *Chemical Engineering Science*, 61(13):4147–4154, 2006.

J.-H. Wu, J.-S. Lin, and C.-S. Chen. Dynamic discrete analysis of an earthquake-induced large-scale landslide. *International Journal of Rock Mechanics and Mining Sciences*, 46(2):397–407, 2009.

M. Wyart and M. E. Cates. Discontinuous shear thickening without inertia in dense non-brownian suspensions. *Physical Review Letters*, 112:098302, 2014.

H. Xiao and J. Sun. Algorithms in a robust hybrid CFD-DEM solver for particle-laden flows. *Communications in Computational Physics*, 9:297–323, 2011.

N. Xu and C. S. O'Hern. Measurements of the yield stress in frictionless granular systems. *Physical Review E*, 73:61303, 2006.

N. Xu, T. K. Haxton, A. J. Liu, and S. R. Nagel. Equivalence of glass transition and colloidal glass transition in the hard-sphere limit. *Physical Review Letters*, 103(24): 245701, 2009.

A. Yu. Liquid maldistribution in particulate paste extrusion. *Powder Technology*, 103 (2):103–109, 1999.

W. X. Yuan, A. S. Burbidge, S. Blackburn, K. A. Fisher, and P. A. Langston. A Micro scale Model of Paste Flow in the Ram Extrusion Process. *6th World Congress of Chemical Engineering*, 2001.

K. Zhang and A. Acrivos. Viscous resuspension in fully developed laminar pipe flows. *International Journal of Multiphase Flow*, 20:579–591, 1994.

M. Zhang, S. L. Rough, R. Ward, C. Seiler, and D. I. Wilson. A comparison of ram extrusion by single-holed and multi-holed dies for extrusion-spheronisation of microcrystalline-based pastes. *International Journal of Pharmaceutics*, 416(1): 210–222, 2011.

W. Zhang, R. Noda, and M. Horio. Evaluation of lubrication force on colliding particles for DEM simulation of fluidized beds. *Powder Technology*, 158(1-3):92–101, 2005.

Z. Zhang, N. Xu, D. T. N. Chen, P. Yunker, A. M. Alsayed, K. B. Aptowicz, P. Habdas, A. J. Liu, S. R. Nagel, and A. G. Yodh. Thermal vestige of the zero-temperature jamming transition. *Nature*, 459(7244):230–233, 2009.

H. Zhou and C. Pozrikidis. The flow of suspensions in channels: Single files of drops. *Physics of Fluids A: Fluid Dynamics*, 5(2):311, 1993.

H. Zhu, M. M. Mehrabadi, and M. Massoudi. Incorporating the effects of fabric in the dilatant double shearing model for planar deformation of granular materials. *International Journal of Plasticity*, 22(4):628–653, 2006.